UC Merced

UC Merced Electronic Theses and Dissertations

Title

The Non-Additive Kinetic Potential: Features, Singularities, and Routes to Improvement of Density Functional Theory

Permalink

https://escholarship.org/uc/item/6pr9m0tr

Author

Banafsheh, Mojdeh

Publication Date

2022

Supplemental Material

https://escholarship.org/uc/item/6pr9m0tr#supplemental

UNIVERSITY OF CALIFORNIA, MERCED

The Non-Additive Kinetic Potential: Features, Singularities, and Routes to Improvement of Density Functional Theory

A dissertation submitted in partial satisfaction of the
requirements for the degree
Doctor of Philosophy

in

Physics

by

Mojdeh Banafsheh

Committee in charge:

    Professor Jay Sharping, Chair
    Professor David A. Strubbe, Advisor
    Professor Aurora Pribram-Jones
    Professor Leeor Kronik

2022

The dissertation of Mojdeh Banafsheh is approved, and it is acceptable in quality and form for publication on microfilm and electronically:

_____

(Professor Aurora Pribram-Jones)

_____

(Professor Leeor Kronik)

_____

(Professor David A. Strubbe, Advisor)

_____

(Professor Jay Sharping, Chair)

University of California, Merced

2022

DEDICATION

To my beloved dog, Napoleon Banafsheh.

EPIGRAPH

"Religion and Science are inter-twined with each other and cannot be separated. These are the two wings with which humanity must fly. One wing is not enough. Every religion which does not concern itself with Science is mere tradition, and that is not the essential. Therefore science, education and civilization are most important necessities for the full religious life."

—'Abdu'l-Bahá ,

'Abdu'l-Bahá in London, p. 28

MY EPIGRAPH

''Dans chaque épreuve et lors de chaque tyrannie de votre vie, apprenez des erreurs de vos ennemis et enseignez-les à vos amis."

"In every trial and in every tyranny of your life, learn from the mistakes of your enemies and teach them to your friends."

—*Mojdeh Banafsheh*

TABLE OF CONTENTS

List of Figures

xiii

List of Tables

ACKNOWLEDGEMENTS

It can be very common for almost everyone to have difficulty recognizing everything. It has been about six years in which I have faced difficulties and barriers in my path. Today, I am so grateful to have had the chance to be surrounded by incredible beings who supported me in trouble.

Every day of my life since the first day I started my studies in physics has been blessed with divine assistance, so my greatest appreciation goes to Bahá'u'lláh the founder of the Bahá'í Faith. My university life was strewn with pitfalls from the first day I moved alone to Switzerland. But all the obstacles were miraculously removed in his time. Some may believe that if God decides to speak with his creatures, he can choose to make a phone call or send an email. Instead, I see it differently. He/She was constantly assisting me through his/her other creatures which I want to recall here chronologically.

First of all and everyone, I need to say thousands of "Thank you" to my adorable dog, Napi. If the tears allow me to continue writing, I want to say thank you for accompanying me in almost all the courses during my bachelor's and master's. Thank you for asking my teacher to be nicer during the final oral exam of astronomy class by constantly barking at him. Thank you for licking my face in my sad times and bringing me joy, strength, and hope whenever you found me on the verge of giving up. Thank you for being the reason I adopted three adorable kittens. Now is the time to enjoy my kittens. I still don't know if I would have fewer bugs in my codes if Tina wasn't there frequently to catch the mouse cursor on the monitor. Or could I do more analytical derivations if Heeda stopped grabbing my pencil every time I derived the formula on paper? Could I work more hours a day if Billy stopped occupying my desk chair every time I tried to take a 10-minute break? I do not know. The only thing I know for sure is that I work much better when I'm happier. So here I have my little kittens to thank for keeping me happy and busy all these years.

Of course, there were not only my adored four-paw beloved ones who kept me up.

I desire to express my special appreciation to Mrs. Mahchid Fatio. She has been supporting me in a priceless manner each time she found me in difficulties. I will never forget her help to make my father, and I see each other after being

far from each other for seven years. It is never enough to appreciate my sister-in-heart Ines El-Shikh who has been by my side to support me to overcome the obstacles on my way. I was very lucky to have Katayoon Shahroozi, a generous soul who without her by my side I could not achieve my exploits. I would like to thank Emilie Chemineau-Chalaye for her encouragement not to give up on my scientific dreams during the most difficult part of my graduate program. I appreciate Dr. Siamak Alimirzazadeh for reading a few chapters of this work to help to find the typos.

Incredible friends have not only spoiled me in Switzerland. I was grateful to be surrounded by lovely people in the United States. Among these, I thank Arabi Seshappan and her beloved parents for their kindness and support towards me. Without her, I would never have my kitties on this adventure. Special thanks to Matthew William Robinson, who made my return home possible with his inexplicable support and help. Without him, I couldn't have a happy ending to my degree.

I have struggled for days to find the words and sentences that can express my gratitude, love, respect and appreciation to these two unique and remarkably respected persons: Professor Leeor Kronik and Professor David Alan Strubbe. Leeor was not only my thesis director or my scientific collaborator. He and his beloved wife, Dr. Natalie Kronik, made me feel like part of their family. They became my older brother and sister, showing me the right path to my private and professional life. They never left my hand as I walked.

Today, if I decide to give an example of a perfect family, I will talk about his family. They were the true example of love, unity, generosity, bravery, hard work, respectful and successful unity of the society. These two great souls have made the world a better place through the very successful education of two other amazing people, their children.

Doing physics for about twelve years has been one of my most amazing acts because it has answered thousands of questions that have occupied my brain exaggeratedly since my childhood. This of course brought me more questions. As I know myself very well, I will find answers to these questions sooner or later except for one. The only question I'm afraid I can't find the answer to is how such a young professor can behave the way that all his students have routinely

shouted on campus that "Our Professor, Professor Strubbe is THE BEST!" ?

I had a lot of ups and downs during my graduate program. He was the one who pulled me up when I was down. He was the only one who gave me hope when I was helpless. He made me believe in myself. He was omnipresent to answer my questions and encourage me to progress. He taught me to ask for help. The latter has changed my life to an incredible one.

Thank you very much for accepting me into your group Professor Strubbe.

Can we really use words to appreciate our parents? My beloved adorable parents, the most courageous, I will never be able to thank you as you deserve. At the time within a society which was not yet receptive to adoption, you adopted me a few hours after my birth. You raised me with love, affection and wisdom. I keep wondering what could happen to me if I wasn't adopted by you. I found about your exceptional and brave act when I was four years old. I have kept this secret in my heart and I hide it from you to protect you. I have witnessed your fear of I understand one day the reality. I cried in hidden every time your tears flowed from your beautiful eyes for fear of losing me. I tried my best to be your good daughter and I know that I failed it partially but at least I tried. You never lose me, I'm yours forever. What I have achieved in my life before anyone else but after Baha'u'llah is thanks to you two. Thank you for accepting me as your child and showering me with your blessings. You will forever be in my prayers.

VITA

Last Version: April 2022

Mojdeh Banafsheh

Physicist

Theoretical Particle and Nuclear Physicist, Computational theoretical Condensed Matter Physicist, System Analyser and Designer, Cosmologist, Computational Chemical Physicist, Project Manager, Research Manager, Computer Engineer, Data Analyser, Researcher

Educations

2019– 2022	**PhD in Physics**, *University of California*.
2015–2018	**Professor Assistant in Theoretical Physics and Graduate Research**, *University of Geneva*, Geneva.
	Teaching Quantum mechanics course, in the second year of Bachelor's; Doing research in analytical solutions of FDET equations and improvements of approximations to the density functional of the embedding potential, Computer simulations studies of the electronic structure of chemical species in their realistic condensed-phase environment
2012–2015	**Master of Science**, *University of Geneva*, Geneva.
	Specialised in theoretical particle and nuclear Physics and Cosmology
2008–2012	**Bachelor of Science**, *University of Geneva*, Geneva.
	Specialised in Physics
July 2004	**Bachelor of engineering**, *Sharif University of Technology-BIHE University*, Tehran.
	Computer Science
July 2003	**Bachelor of Social Science**, *BIHE University*, Tehran.
	Philosophy and Theology

Ph.D. Thesis

Title	*The Non-Additive Kinetic Potential: Features, Singularities, and Routes to Improvement of Density Functional Theory.*.
Advisor	Professor David Alan Strubbe

Description   Analytical solutions of FDET equations and improvements of approximations to the density functional of the embedding potential, Computer simulations studies of the electronic structure of complex systems

Masters Thesis

Title   *Magnetic Fields in the Large Scale Structure from Faraday Rotation measurements*
Supervisors   Professor Andrii Neronov
Description   We search for magnetic fields outside galaxies and galaxy clusters by investigating the redshift evolution of Faraday rotation measures (RM) of extragalactic radio sources. Our analysis reveals strong evidence for the redshift dependence of the mean of the absolute value of the RM. The evidence is further strengthened if the Galactic contribution to the RM is subtracted. The hypothesis of the absence of the redshift evolution of residual RM is ruled out at the 5 sigma level. The observed redshift dependence of RM is consistent with the possibility of the presence of nano-Gauss strength magnetic fields with correlation length shorter than 0.1 Mpc in the weakly over-dense elements of the Large Scale Structure traced by the Ly-alpha clouds.

Academical Experiences

2022   **Paper Reviewer Expert** , *Invited by Optic Express Journal*.
Technical and Scientific evaluation of manuscript for publications.

2015–2019   **Theoretical Physics-Prof-Assistant of Quantum Mechanics**, *University of Geneva*, Geneva.
Teaching and Assisting the students for Quantum Mechanics courses.

2015–2019   **Bachelor and Master Graduation Project Supervisor**, *University of Geneva*, Geneva.
Teaching and Assisting the students for Quantum Mechanics courses.

2018   **BSc Project Supervisor**, *BIHE*.

2013–2014   **Particle Physics Data Analysing**, *University of Geneva*, Geneva.
Geneva, Department of Nuclear and Corpuscular physics. Working on the data of IceCube project in the research group of Prof. Teresa Montaruli.

2012–2013   **Physics Teacher**, *Madame de Stael High School*, Geneva.
Geneva, Department of public Instruction of Geneva (DIP). Teacher of physics laboratory in 3d year of gymnasium.

2012–2013   **Physics Teacher**, *Henry-Dunant High School*, Geneva.
Geneva, Department of public Instruction of Geneva (DIP). Teacher of physics laboratory in 3d year of gymnasium.

2011–2012   **Data Analysing for the Construction of the POLAR instrument**, *University of Geneva*, Geneva.
Geneva, Department of Nuclear and Corpuscular physics. Working on the simulated data in the research group of the Senior lecturer Silvio Orsi for Gamma Ray Bursts experience

2010–2011   **Physics Supervisor**, *University of Geneva*, Geneva.
Department of public Instruction of Geneva (DIP). Supervision of General Physics course for medical students.

Professional Experiences

1996–Present — **Private Teacher/Professor**, *Maths and Physics*, Worldwide.
Private courses of Math and Physics from High-school level to PhD level, Research Supervising of thesis for Masters and Bachelors Students

March 2022–Present — **President of the Academie Lab SARL**, *AI based Educational and Professional Skill Development Platform*, Vaud.
Innovator and Project manager and application developer.

2018– 2020 — **Project manager and application developer**, *Public Health Environment*, Geneva.
Project manager and application developper, Public Health Environment , Geneva. Development and design of a new application based on artificial intelligence and management of a small group of 5 people. Confidential private side project.

2018–2019 — **Business Support and General Management-Modelling, Simulation and Data Analyst**, *UBS*, Zurich.
Business Risk Management UBS Switzerland (BRM UBS CH) supports front units and a variety of stakeholders in the implementation and maintenance of business risk analysis and controls. The Data Analytics, Solutions, and Reporting The team is part of BRM UBS CH and is responsible for analysis, data sourcing, operation, and further development of BRM applications. Mathematical modelling and strategy proposals to optimise investment prediction algorithms. Reading different formats of reports from all national banks around the world through a Python script and providing excel-format reports for numerical analysis. Data analysing was done equally by Mathematica and Python.

2003–2005 — **Project Manager**, *IT Xagross SA.*, Tehran-Ir.
Manager of a group of 14 analysts located across the country. Automation and mechanisation of National Spring Factory of DAMGHAN, using Oracle and ERP. Designing the large systems like industrial and high-tech companies from A to Z to reach them to expected international standards (ISO...). As a system engineer, I was charged mainly with managing complexity by doing system architecture, system modelling, optimisation, system analysing, statistical analysing, and decision making. For that purpose, I charged and hired 14 engineers including industrial engineers, computer engineers, and environmental scientists. During these periods I did automation of the three biggest national factories for the first time in the country.

2003–2005 — **System Analyser- System Designer**, *IT Xagross SA.*, Tehran-Ir.
Primary technical contact for critical for a global IBM internet application used for opportunity management and global sales forecasting.

2002–2003 — **Web Developer and System Analyser**, *Iran Khodro-Andisheh-Karan SA.*, Tehran-Ir.
Technical support and creation of the website of Mehrabad international airport. Database administration of Sarcheshmeh copper mine using SQL-Server.

Skills

- **Research:** Scientific simulations and modelling of Maths and Physics theories, Theoretical Particle physics, Nuclear Physics, Magnetic Field Properties, EM-Matter Interactions, DFT, TDDFT, Embedding Theory, Many-body Theory, Data analysing, Strategic planning, Statistics
- **Teaching:** Physics, Mathematics University level
- **Programing:** Root, Fortran 90, C, C#, C++, Mathematica, Matlab, Python, HTML
- **Computational Many-Body Solvers** DARSEC, Octopus, Gaussian, GW
- **Informatics:** LaTeX, Linux, Parallel Processing, Distributed system
- **Data Analysing:** Mathematica, Gnuplot, Python

○ **Project Managing:** Machine Learning, Deploying Machine Learning, Data Engineering, AI, Data Revolution, Business Strategy, System Modelling, Security, Neural network architectures

Certificates

2015 **Mathematics-Chemistry High Performance Computing**, University Pierre et Marie Curie.

2016 **TDDFT**, Spain.

2016 **Advanced Quantum Field Theory and Renormalisation Group**, EPFL.

2017 **Reduced Density Matrix Functional Theory**, EPFL.

Publications and Talks

○ **Publications:**

2013 **Magnetic Fields in the Large Scale Structure from Faraday Rotation measurements**, *A. Neronov, D.Semikoz, M.Banafsheh*, arXiv:1305.1450 astro-ph.CO.

We search for magnetic fields outside galaxies and galaxy clusters by investigating redshift evolution of Faraday rotation measures (RM) of extragalactic radio sources. Our analysis reveals a strong evidence for the redshift dependence of the mean of the absolute value of the RM. The evidence is further strengthened if the Galactic contribution to the RM is subtracted. The hypothesis of the absence of the redshift evolution of residual RM is ruled out at 5 sigma level. The observed redshift dependence of RM is consistent with the possibility of the presence of nano-Gauss strength magnetic fields with correlation length shorter than 0.1 Mpc in the weakly overdense elements of the Large Scale Structure traced by the Ly-alpha clouds.

2018 **Nonadditive kinetic potentials from inverted Kohn–Sham problem**, *Mojdeh Banafsheh , Tomasz Adam Wesolowski*, International Journal of Quantum Chemistry, 118(1), e25410.

The nonadditive kinetic potential is a key element in density-dependent embedding methods. The correspondence between the ground-state density and the total effective Kohn–Sham potential provides the basis for various methods to construct the nonadditive kinetic potential for any pair of electron densities. Several research groups used numerical or analytical inversion procedures to explore this strategy which overcomes the failures of known explicit density functional approximations. The numerical inversions, however, apply additional approximations/simplifications. The relations known for the exact quantities cannot be assumed to hold for quantities obtained in numerical inversions. The exact relations are discussed with special emphasis on such issues as: the admissibility of the densities for which the potential is constructed, the choice of densities to be used as independent variables, self-consistency between the potentials and observables calculated using the embedded wavefunction, and so forth. The review focuses on how these issues are treated in practice. The review is supplemented with the analysis of the inverted potentials for weakly overlapping pairs of electron densities—the case not studied previously.

○ **Publications under preparation:**

2022 **Nuclear Cusp and singularities in Non-Additive Kinetic Potential bi-Functional from Analytical Inversion**, *Phys. Rev. A.*

The non-additive kinetic potential functional Vnad is a key issue in density-dependent embedding methods, such as Frozen Density Embedding Theory and Partition-DFT. Vnad is bifunctional of pairs of specific electron densities ρ_B and ρ_B. We previously reported the exact analytical inversion procedure to generate reference Vnad for weakly overlapping ρ_A and ρ_B (M. Banafsheh, T. A. Wesolowski, Int. J. Quant. Chem. 118 (2018): e25410). The behaviour of V^{nad} at the vicinity of the nuclei has been questioned since the beginning. Available computational tools and methods in the past led to a derivative discontinuity of the potential at nuclei. We demonstrate the non-existence of derivative discontinuity V^{nad} mathematically, whereas it respects the nuclear cusps condition of ground-state density. We show the agreement of numerical calculations to this fact for various diatomic model systems of two and four electrons. We discuss the constraints on the choice of electron densities to ensure their admissibility. The results are compared to the von Weizsäcker functional, which is exact for particular densities. In addition, the well-known step structure associated with molecular dissociation is studied from the behaviour of V^{nad} in the region of weakly overlapping subsystems' density.

2022 **Non-additive kinetic potential functional V^{nad} from analytic inversion: All-electron Calculations vs Pseudopotential Calculations**, *Mojdeh Banafsheh , David A. Strubbe*.

Non-additive kinetic potential functional is the key issue of embedding DFT theory, Partition DFT and Average atom model. It needs to be approximated. Different attempts to such approximation have been suggested through numerical approaches in the past. All approximations carry numerical errors and consequently, lack of uniqueness between ground state charge density and inverted potential. Knowing the electron density of a system ρ_{tot}, once we could define a sub-density ρ_A with one electron or two spin-compensated electrons, Non-additive kinetic potential could be analytically inverted since it concerns a bifunctional of an appropriate pair of electron density $v_t^{nad}[\rho_A, \rho_{tot}](\mathbf{r})$. In this work we show the feature of exact v_t^{nad} calculated from a Kohn-Sham equation solver in real space, for four-electron systems and $2 + N$-electron systems in which we could localise two spin-compensated electrons in the space with very high accuracy. We used a Kohn-Sham solver which is basis-set independent and psudo-potential independent. The advantage of our tool compared to all numerical solvers which are basis-set dependent is the fact that the uniqueness of correspondence between density ρ_A and v_t^{nad} is assured.

2022 **Relation between Interatomic Steps Structure on the Analytical V^{nad} and Derivative Discontinuity of The Energy**, *Mojdeh Banafsheh , Leeor Kronik, David A. Strubbe*.

Step Structure is important attribute of exact exchange-correlation (xc) potentials. Analytically inverted Non-Additive kinetic Potential Functional bi-Functional from an admissible pair of ground-state densities tempts to be exact. In our previous publications we reported the existence of the step structure at the expected location in the space. The exact fundamental gap energy, related to the Ionisation Potential (IP) and the Electron Affinity (EA) originate from the step structure on the potential curve. In this paper we construct the relation between those quantities and the step structure physical properties such as: width, hight, and the position of the step on the potential curve.

2022 **Improvement of popular Kinetic Functionals with the aide of the exact V^{nad}**, *Mojdeh Banafsheh , David A. Strubbe.*

○ **International Talks:**

2011 **Detection of gamma-ray bursts using POLAR**, *ICPS.*

2012 **NEMO (The Neutrino Mediterranean Observatory) Project**, *ICPS.*

2014 **Relic Cosmic Magnetic Fields from Faraday Rotation measurement and reduction of Magnetic field of Galaxy calculated through a new model**, ***Invited talk at ETHZ***, *Astroparticle department.*

2017 **Analytically inverted non-additive kinetic potential functional at small density overlapsl**, *17th International Conference on Density-Functional Theory and its Applications*, Sweden .

2017 **Analytically inverted non-additive kinetic potential functional at small density overlapsl**, *International Workshop on 'New challenges in Reduced Density Matrix Functional Theory: Symmetries, time-evolution and entanglement'*, EPFL. Switzerland

2020 **Analytic inversion procedure for the exact non-additive kinetic potential functional V^{nad}**, *APS March Meeting 2020*, USA .

2021 **Non-additive kinetic potential functional V^{nad} from analytic inversion: all-electron and pseudopotential calculations**, *APS March Meeting 2021*, USA .

2022 **Investigation of cusps and steps in the non-additive kinetic potential functional V^{nad} from analytic inversion**, *APS March Meeting 2022*, USA .

Academic Awards

1997 National Champion: Physics Olympiad

1995 National Champion: Science Competition for high-school students

Awards

2021 Wild-life photography: 2nd award.

2000-2004 National Champion of Judo: 4 years.

1999 National Vice-Champion of Judo

Languages

Persian	**Mothertongue**
French	**Bilingual**
English	**Fluent-Professional**
Tabari	**Fluent**
Modern Standard Arabic	**Fluent**
Spanish	**B2**
German	**B1**

Interests

- Human rights and animal rights Activities
- General director of Paradis-Terrestre Association of Animal rights
- Art, Sport, Lecture, photography

Side Activities

- President of Paradis Terrestre Association of Animal Rights
- Member of Spiritual Local Assembly of the Bahai community of Merced in USA and Lausanne in Switzerland

References

David Alan Strubbe, *dstrubbe*@ucmerced.edu, University of California, Merced.

Francesco Aquilante, *francesco.aquilante*@EPFL.ch, EPFL, Lausanne.

Leeor Kronik, *leeor.kronik*@weizmann.ac.il, Weizmann Institute.

Jay E. Sharping, *jsharping*@ucmerced.edu, University of California, Merced.

Aurora Pribram-Jones, *apribram-jones*@ucmerced.edu, University of California, Merced.

PREFACE

This work emerged from research in Density Functional Theory (DFT). The attempts to achieve this level of valuable scientific precision were initially launched to provide a not-expensive computationally method to solve precisely many-body quantum systems. My interest in DFT and TDDFT started after my master's thesis in particle physics and cosmology. I saw that cosmological and astronomical observations and theories are mainly based on precisely calculated views in the standard model of cosmology and the standard model of particle physics. Although those latter turned out to be very successful, their theories remain restrained in the frame of imposed assumptions. The standard model of particle physics assumes solving the problem separately within each interaction. As the energy regime of each interaction varies significantly from the energy of the other interactions, one can be taken as having zero impact on a regime. For instance, when I solve the problems, including the quarks, I use the strong force field and ignore the weak force's possible effect. On a larger scale, when I study the electronic structure, I mainly remain in Bohr-Oppenheimer's frame. I ignore the impact of the relativistic electromagnetic, electro-weak and strong interactions entirely. To me, physics can be understood if and only if I take account of the totality of phenomena. Nothing must remain ignored if I seek the exact solution to a problem. My philosophical challenges were mainly to find a way to answer two questions: 1) How can the standard model of particle physics (or other models) can help the domain of electronic-structure-related works? 2) How can our actual understanding of many-body problems can help us to discover more in Astroparticle physics and cosmology?

Later on, when I heard about Density Functional Theory, I asked myself if this could be a correct assumption to say: "Knowing the exact density of any fundamental particles can lead us to their interacting energy"? Or, can I also suggest a model of non-interacting fundamental particles that provides the total energy of interacting particles? Of course, those questions were asked for high-energy physics. At the time, what I was missing was all about DFT and TDDFT.

I started to work at the University of Geneva with Prof. Tomasz Adam Wesolowski on Analytical solutions to Frozen Embedding Density Functional

Theory in April 2015. Some initial results of our attempts were more importantly, published in 2017 in the International Journal of Quantum chemistry. During my three first years, I managed to form several collaboration groups. The first collaboration started with the group of Prof. Leeor Kronik at the Weizmann Institute of technology. This collaboration provided a very fruitful impact on the numerical developments of the theory. Connected to this latter group another collaboration with Griffiths University was developed through interesting scientific communications with Prof. Tim Gould. He provided a valuable mathematical approach to a scientific claim I had made two years prior to our collaboration. The research continued after a gap of one and half years within the group of Prof. David A. Strubbe at the University of California in September 2019.

This work addresses the amount of hard work during five and half years to the reader interested in the related fields. The chapters are prepared in an independent form that helps the reader to have access to the fundamental definitions and information without crossing the other chapters. Chapters 2 to 6 concern whether the already published paper, soon submitted paper, or papers under preparation are to be published in close future. The latest group of chapters includes important information in their "outlook" sections. Tim's beautiful work is inserted in the theory section of chapter 3.

This work includes the analytical methods used for the first time to produce the results for solving certain model systems under specific conditions. Some existing ambiguities about the feature of so-called exact analytically inverted potential bi-functional were clarified precisely for the first time. The results in this work are the essential tools for the improvement of successful theories in orbital-free DFT.

During my graduate program, I gained a deep understanding of nuclear DFT and QED-DFT and developed calculations in Lagrangian DFT. I still don't have a clear answer to the questions that led me into this field. The only thing I know for sure is that even if it still takes more trying, there are sure answers to these questions. Secondary interests sometimes bring more miracles than the main stake of the work. So I can invite readers to think about these questions and maybe add some follow-up questions to this problem.

LIST OF NOTATION

- **Analytically inverted non-additive potential bi-Functional:**
  $v^{NAD/INV}[\rho_B, \rho_{tot}](\mathbf{r})$,

- **Numerically inverted non-additive potential bi-Functional:**
  $v^{\mathrm{nad'}}[\rho_A, \rho_B](\mathbf{r})$,

- **Numerically Approximated non-additive potential bi-Functional:**
  $\tilde{v}^{\mathrm{nad'}}[\rho_A, \rho_B](\mathbf{r})$,

- **Analytically inverted non-additive potential bi-Functional from one-orbital formula:**
  $v^{NAD/INV}[\rho_B, \rho_1](\mathbf{r})$,

- **Analytically inverted potential Functional:** $v_s[\rho_i](\mathbf{r})$

- **Approximated non-additive kinetic potential bi-Functional:**
  $v_t^{\mathrm{NAD}}[\rho_B, \rho_{tot}](\mathbf{r})$.

- **von Weizsäcker Kinetic Functional:**
  $T_s^{\mathrm{vW}}[\rho](\mathbf{r})$. (also written as $T_s^{\mathrm{vW}}[\rho](\mathbf{r})$)

- **von Weizsäcker non-additive potential bi-Functional:**
  $v^{\mathrm{NAD/vW}}[\rho_B, \rho_{tot}](\mathbf{r})$.

- **Thomas-Fermi Kinetic Functional:**
  $T_s^{TF}[\rho](\mathbf{r})$.

- **Effective potential:**
  $v_{eff}(\mathbf{r})$.

- **Fermi-Dirac Distribution Function:**
  $F(z)$.

- **Density Obtained from variational calculations using approximated non-additive kinetic potential:**
  $\tilde{\rho}$

Acronyms

AAM Average Atom Model

DARSEC Diatomic Real-Space Electronic Calculation

DD Derivative Discontinuity

DFT Density Functional Theory

EA Electron Affinity

FDET Frozen Density Embedding Theory

GGA Generalized Gradient Approximation

HOMO Highest Occupied Molecular Orbital

KEDF Kinetic Energy Density Functional

KLI Krieger-Li-Iafrate

KS Kohn-Sham

LDA Local Density Approximation

LKT Luo-Karasiev-Trickey

LUMO Lowest Un-Occupied Molecular Orbital

OEP Optimised Effective Potential

OF-DFT Orbital Free Density Functional Theory

PBE Perdew-Burke-Ernzerhof

PDFT Partitioning Density Functional Theory

PGS-KE Pauli-Gaussian Kinetic Energy Functionals

SCAN Strongly Constrained and Appropriately Normed

SS Step Structure

TDDFT Time-Dependent Density Functional Theory

TF Thomas-Fermi

xc exchange-correlation

Chapter 1

Introduction

In this chapter, a brief explanation of the main approaches to the calculations of this work is provided. A general idea and necessary background to understand the attempts of this work can be extracted in the introduction. For further knowledge and information, the readers can turn to the references indicated in the text. In this chapter, they can also find the motivations before this research and the practical applications of the reported discoveries.

All chapters include the required information for optimal understanding, so those with a strong background related to the theories used in this work can skip the introduction chapter. The chapter 2 is already published and the chapter 3 is under preparation to be submitted. The other chapters are part of two up coming publications under preparation.

1.1 Background and Motivation

Research on large and complex systems is often required to meet the demands of industry, as well as to add to the fundamental scientific-based domains. In important numbers of those works, the main system in question is fragmented into subsystems to understand the physical properties of the elements of the system or modelling properties of chemical species and chemical reactions. Those studies require usually the quantum-mechanical level of description. For instance, chemists are interested in the physical and chemical properties of a solution in which the molecules of the solvent (i.e. water) cannot penetrate the interior of the solute. Another example is the attempts

to understand the properties of an atom within a molecule from partitioning-based theories. Orbital-free-density-functional-based attempts are promising and computationally affordable methods for calculating the electronic structure of such complex systems. Among these theories, Frozen Density Embedding Theory (FDET)[217, 212, 213, 166] is the main focus of this work. The choice of FDET is mainly because of its computationally low cost for such calculations, like in QM/MM because of not treating the whole system just a part. In the partition-based frameworks of density functional theory (DFT) similarly to FDET, the main challenge concerns the formulation of the interaction between sub-densities. The exchange of energy between sub-densities or between a frozen density and the whole density of a system is provided by the "non-additive potentialfunctional", (v^{NAD}). In numerical simulations based on FDET or subsystem formulation of density functional theory (subsystem DFT)[178, 35], the non-additive kinetic potential needs to be approximated.

Explicit semi-local approximations to the functional v^{NAD} in numerical simulations are doomed to fail [9]. Such failures prompted the interest in the implicit functionals for the non-additive kinetic potential constructed by means of numerical inversion (of Kohn-Sham equation) procedures. Unfortunately, numerical inversion of Kohn-Shame quation is an ill-defined problem if finite basis sets are used. It results in numerical instabilities or multiple solutions. A more recent analysis of the non-uniqueness of the numerical inversion and an approach to deal with it can be found in the work by Jacob [100].

In the general case, Kohn-Sham equations must be inverted twice to obtain the v^{NAD} for a given pair of densities. The two-step inversion procedure aggravates the problems. Only for some model systems can v^{NAD} be expressed analytically[214]. The analytical inversion of v^{NAD} for some toy models was used to discuss the relation between the pseudopotential theory[169] and FDET.

De Silva and Wesolowski[36] explored the construction of v^{NAD} for various partitioning of the ground-state electron densities using analytical inversion from the lowest Kohn-Sham orbital density. Their study was confined by basis-set-depended numerical tool and for the strongly overlapping densities. This latter leads to violation of constraints required for precise calculation of analytical inversion which will be discussed later in this work. I and Wesolowski

published a complete review of the construction of v^{NAD} within approximations and inversion procedures[9].

Unfortunately, in all previous attempts toward the construction of v^{NAD} some holes remained unfilled that concluded low understanding of v^{NAD}. In addition, the exact analytical inversion of the potential remained unknown as those who studied this case were limited by basis-set-dependent numerical tools which spoil the accuracy of the calculations due to numerical issues. This problem is similarly the case for the construction of the exact v^{NAD} from numerical iterative inversion procedures[60]. After all, no works was published for weakly overlapping densities nor the cases in which the admissibility of the input density was satisfied (means one or two electrons were precisely localised in the space. This is explained clearly later in this work.)

Among the different strategies to calculate the non-additive potential functional, this work is distinct from previous work in terms of:

- using the basis-set-independent numerical tool for

- weakly overlapping partitioned densities

- with choice of density-to-potential inversion

- from exact analytical inversion calculation.

Finally, thanks to the framework itemised above, the clear understanding of v^{NAD} is ready to be published and explained in this work. The clear feature of v^{NAD} brought up other useful properties of exact potential that turns it into a good candidate for wider use in various domain of research. I will see that v^{NAD} has the capacity to explain molecular dissociation, molecular ionisation and atomic ionisation. These quantities expand the application of v^{NAD} in different domains such as:

- **C**ondensed matter: Study the defect/s within a crystal (Fig.[1.1]). The defect/s can be partitioned and studied separately from the rest of the system and its interaction with the environment can be explained by v^{NAD}.

- **M**etal Insulator transition: Where metal hybrids are formed by the transition of metal and alloys from the homolytic dissociation of H_2 to H.

Similarly to the previous example, v^{NAD} can provide the required information related to such dissociation.

- **P**hoto-Chemistry: v^{NAD} has the capacity to explain the dissociation happening on excited potential via photo-excitation.

- **E**nvironmental science: Acid-Chemistry: In researches where acids are used to release hydrogen ions from a solution. Such ion separation crosses the molecular-dissociation-like actions again in which v^{NAD} appears very useful.

One possible motivation for studying the inverse problem of DFT is to benchmark the many approximate exchange-correlation functionals[82]. In this work, it will be explained how the properties of the exact potential appearing in v^{NAD}, can make from it a correction to frequently used kinetic functional approximations in DFT framework.

During five years of hard-working I managed to formulate and understand interesting questions such as theoretically expected feature and physical interpretation of non-additive potential bi-functional of a pair of densities. I found out the further application of my works in the wide domain of research and highlighted the properties of the exact potential in my results. I developed my research in different codes within various frameworks of DFT calculations. Those accomplishments were extracted in the calculation of v^{NAD} from the analytical inversion procedure of admissible pair of densities to provide analytical solutions of FDET equations. I suggested specific numerical tricks for preparing the admissible required densities for my calculations.

Theoretical explanations required to understand this work together with numerical tools and developments are given in the next chapter. The verified results are presented in current progress and the steps required to be developed to accomplish the program are clarified in Future work. More complete and historical information is available in our previous publication[9].

1.2 Theoretical Methods

1.2.1 Density Functional Theory

Prior to introducing the Frozen Density Embedding Theory (FDET) the basic concepts of Density Functional Theory (DFT) is provided. The advantage of DFT is that it can perform calculations relatively quickly with high enough accuracy. It can therefore be used to find the properties of large molecules and many crystalline solids. A computationally fast enough calculation such as DFT is known inexpensive calculation. Approximately, for N-interacting electrons, the cost of time scales is about N^3 although that raises exponentially for other methods.

The quantum Many-Body problem is solved in terms of electron density in DFT framework. The latter distinguishes DFT from Schrödinger framework that solves the problem in terms of the wavefunction. The original idea was formulated first by Thomas and Fermi [193, 50], in 1927 that expresses representation of the energy in terms of the electron density. Theoretical model of Thomas-Fermi promoted in 1964 by Hohenberg and Kohn into the theoretical DFT [93] through which Kohn and Sham in 1965 introduced the "one-electron-system approach" to non-interacting many-electron system that satisfies the problem [114]. The corresponding functional reads:

$$E[\rho] = T_s[\rho] + E_{ext}[\rho] + J[\rho] + E_{xc}[\rho] \tag{1.1}$$

where $T_s[\rho]$ is the kinetic functional of non-interacting electrons, $E_{ext}[\rho]$ the coulomb interaction potential between the electrons and local nuclei, $J[\rho]$ the electron-electron coulomb repulsion and $E_{xc}[\rho]$ known as "exchange-correlation" functional is the reminder of the total energy.

In Kohn-Sham formulation of the DFT, the energy functional of the entire system is minimised with respect to the ground-state charge density:

$$\left[-\frac{1}{2}\nabla^2 + v_{KS}(\mathbf{r}) \right] \psi_i(\mathbf{r}) = \epsilon_i \psi_i(\mathbf{r}) \tag{1.2}$$

with ϵ_i the energies of Kohn-Sham orbitals $\psi_i(\mathbf{r})$. Kohn-Sham effective potential (written either v_{KS} or v_{eff}) needs to be constructed, such that the

ground-state density of a non-interacting electrons confined by that potential is equal to a given density $\rho(\mathbf{r})$. Where:

$$\rho(\mathbf{r}) = \sum_i^N n_i \psi_i^2(\mathbf{r}) \qquad (1.3)$$

where n_i is the occupation number corresponding to the solution $\psi_i(\mathbf{r})$. In Eq.[1.2], the effective Kohn-sham potential reads:

$$v_{KS}[\rho](\mathbf{r}) = v_{ext}(\mathbf{r}) + v_H[\rho](\mathbf{r}) + v_{xc}[\rho](\mathbf{r}) \qquad (1.4)$$

where $v_H[\rho](\mathbf{r}) = \int \frac{\rho(\mathbf{r}')}{|\mathbf{r}'-\mathbf{r}|} d\mathbf{r}'$ known as Hartree potential represents the mean-field part of electron-electron repulsion energy whereas $v_{xc}[\rho](\mathbf{r}) = \frac{\delta E_{xc}[\rho](\mathbf{r})}{\delta\rho(\mathbf{r})}$ reads the exchange-correlation potential. By exchange-correlation potential, I simply mean the difference between the exact total energy of a system and the classical Hartree energy. In DFT formulation of many-body problems, the quality of calculation is determined by how close the approximate exchange and correlation comes to the exact value. The developments of approximations to $E_{xc}[\rho](\mathbf{r})$ can be found in different works (see for example [112, 31, 104, 78]).

1.2.2 Partitioned System
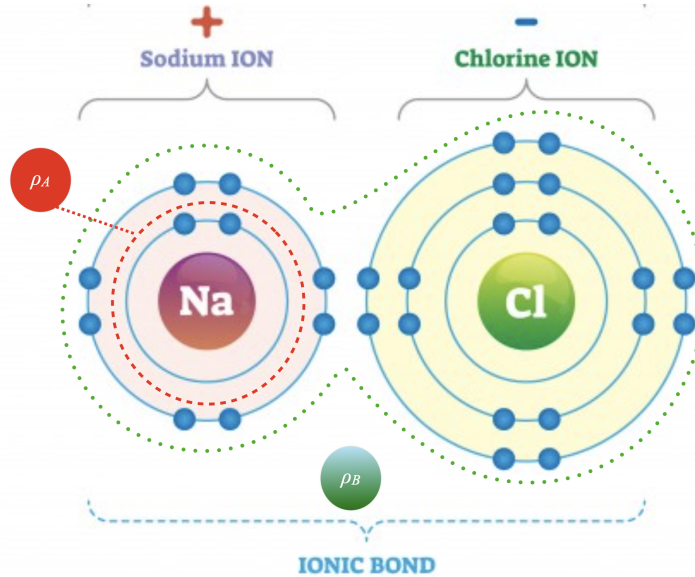
Figure 1.1: Illustrates the partitioning of a molecule. Red dashed circle represent the Na+ cation, and the green dashed circle represent the Cl- cation; in a crystal or bulk system of NaCl a missing, or defect, Cl- position is denoted with the electron cloud (e-) in its position. This system is partitioned such that an ion is enclosed by the red box and represented by density ρ_A. The system could be partitioned to exclude the reminder site (Cl), and represented with density ρ_B.

As already mentioned earlier it is costly favourable to partition the complex systems for quantum-mechanically treatments. Since the electron density is possible to be introduced as an additive quantity, the system is eligible for petitioning within a DFT framework [47, 153]. Cortona [35] introduced the idea of Partition DFT for a system in which the electrons density is partitioned in the way that the density of the full system is thus a sum over the "m" subsystems' density:

$$\rho(\mathbf{r}) = \sum_j^m \rho_j(\mathbf{r}) \tag{1.5}$$

The kinetic energy of the full system is similarly the sum over the kinetic energy of all subsystems, plus a "non-additive" term (T_s^{NAD}) which is the result of the interactions between subsystems[[153]]. The ground-state solution due

to each subsystem is obtained by a one-electron equation:

$$\left[-\frac{1}{2}\nabla^2 + v_{\text{eff}}^{\text{sub}}[\rho, \rho_j](\mathbf{r}) \right]\psi_{ij}(\mathbf{r}) = \epsilon_{ij}\psi_{ij}(\mathbf{r}) \tag{1.6}$$

where,

$$v_{\text{eff}}^{\text{sub}}[\rho, \rho_j](\mathbf{r}) = v_{\text{eff}}[\rho](\mathbf{r}) + \frac{\delta T_s[\rho]}{\delta\rho(\mathbf{r})} - \frac{\delta T_s[\rho_j]}{\delta\rho_j(\mathbf{r})}. \tag{1.7}$$

The last two terms at the right-hand side of Eq.[1.7] is called "Non-Additive Kinetic Potential bi-Functional". Those required to be approximated as the partitioning of other energy terms are straightforward. Numerical approaches to "Non-Additive Kinetic Potential Functional" face a double self-consistency problem as they depend on the densities generated from the orbitals of the subsystems. Frozen Density Embedding Theory (FDET) was first suggested to cure the "double" self-consistency problem.

1.2.3 Frozen-Density DFT

In FDET the subsystems are classified either as "environment" which represents the frozen subsystem or "Active subsystem" (called in this paper respectively ρ_B and ρ_A). The last two terms at the right of Eq.[1.7] are replaced by a new quantity, "Embedding Potential", $v^{emb}[\rho_A, \rho_B]$:

$$\begin{aligned}
v^{emb}[\rho_A, \rho_B](\mathbf{r}) = {} & v_{ext}^B(\mathbf{r}) + \int \frac{\rho_B(\mathbf{r}')}{|\mathbf{r}' - \mathbf{r}|}d\mathbf{r}' + \left.\frac{\delta E_{xc}[\rho](\mathbf{r})}{\delta\rho(\mathbf{r})}\right|_{\rho=\rho_A+\rho_B} \\
& -\left.\frac{\delta E_{xc}[\rho](\mathbf{r})}{\delta\rho(\mathbf{r})}\right|_{\rho=\rho_A} + \left.\frac{\delta T_s[\rho](\mathbf{r})}{\delta\rho(\mathbf{r})}\right|_{\rho=\rho_A+\rho_B} - \left.\frac{\delta T_s[\rho](\mathbf{r})}{\delta\rho(\mathbf{r})}\right|_{\rho=\rho_A}
\end{aligned} \tag{1.8}$$

where two first terms on the right-hand side of the equation are external (ionic) and Coulomb repulsion potentials respectively and, terms 3 and 4 represent together, so-called Non-Additive-Exchange-Correlation bi-Functional ($\frac{\delta E_{xc}^{\text{NAD}}[\rho_A,\rho_B](\mathbf{r})}{\delta\rho_A(\mathbf{r})} = \frac{\delta E_{xc}[\rho](\mathbf{r})}{\delta\rho(\mathbf{r})} - \frac{\delta E_{xc}[\rho_A](\mathbf{r})}{\delta\rho_A(\mathbf{r})}$). The last two terms in blue are the main terms of interest in this work, "Non-Additive Kinetic Energy bi-Functional":

$$\frac{\delta T_s^{\text{NAD}}[\rho_A, \rho_B](\mathbf{r})}{\delta\rho_A(\mathbf{r})} = \frac{\delta T_s[\rho](\mathbf{r})}{\delta\rho(\mathbf{r})} - \frac{\delta T_s[\rho_A](\mathbf{r})}{\delta\rho_A(\mathbf{r})} \tag{1.9}$$

The flowchart of FDET in the applications can be summarised as following:

- The density of environment ρ_B can be constructed whether by numerical tricks of partitioning or KS-DFT calculations

- Once the embedding is performed Eq. [1.10] will be solved with Constrained Electron Density for ρ_A while the environment is frozen

$$\left[-\frac{1}{2}\nabla^2 + v^{emb}[\rho_A, \rho_B](\mathbf{r}) \right] \psi_i(\mathbf{r}) = \epsilon_i \psi_i(\mathbf{r}) \qquad (1.10)$$

The double Self-Consistency is thus avoided but the calculation of "Non-Additive Kinetic Energy bi-Functional" and consequently Eq. [1.10] remain $\rho_B - dependent$. For the complex system, the environment that provides the embedding potential can be approximated while ensuring the efficiency of FDE calculation. This latter brings up the choice of the environment density as a key issue in FDET-based calculations ([166, 212, 213, 217]).

1.2.4   Analytical Inversion of Density

Inverse problems are common in science and have been central in quantum mechanics since their inception. Much of what I know about the structure of matter has come from scattering experiments, [140] which can be described mathematically as inverse problems. In the direct problem of DFT I use an approximate exchange-correlation potential to solve the KS equations (Eq. 1.11) for the unknown density. So, the problem is suffered by two unknown interrelating quantities: the density and the wavefunctions (the unknown quantities are shown with red in Eqs.[1.11,1.13]). The advantage of the inverted problem is dealing with only one unknown quantity as the density is known (Eq. 1.13).

The strategy of the inversion procedure relies on the unique correspondence between the Kohn-Sham potential $(v_s[\rho](\mathbf{r}))$ (we denote the inverted Kohn-Sham potential from density by v_s which is not the explicit expression for the Kohn-Sham effective potential) and the ground-state density The Kohn-Sham equation for a system of N electrons can be written as :

$$\epsilon_i^\alpha \psi_i^\alpha(\mathbf{r}) = \left[-\frac{\nabla^2}{2} + v_s[\rho_{tot}](\mathbf{r}) \right] \psi_i^\alpha(\mathbf{r}) \qquad (1.11)$$

$$\rho_{tot}(\mathbf{r}) = \sum_{i,\alpha}^{N} n_i^{\alpha} |\psi_i^{\alpha}(\mathbf{r})|^2$$

$$i = 1, 2, \ldots$$

$$\alpha = \uparrow, \downarrow$$

(1.12)

where n_i^{α} is the occupation number and α is the spin index. Eq [1.12] must respect the condition $\int_v \rho_{tot}(\mathbf{r}) d\mathbf{r} = N$.

The inversion procedures are categorised mainly into analytical inversion and numerical inversions. In numerical inversions, Kohn-Sham equations must be inverted twice. In first step the inverted kinetic functional $T_s[\rho_{in}(\mathbf{r})]$ is used to find the solutions which minimised the kinetic energy $T_s[\rho_{in}](\mathbf{r}) = \sum_{i=1}^{N} \int \psi_i^*(\mathbf{r}) \left(-\frac{\hbar^2}{2m} \nabla^2 \right) \psi_i(\mathbf{r}) d(\mathbf{r})$ and from those solutions, the potential will be inverted.

Numerical inversions are suffering from the lack of the uniqueness. As they are formulated in an iterative procedure, two slightly different solutions will eventuate the same inverted potential. Also, the iterative inversion is significantly expensive in terms of computational calculations. Above all, numerical inversions are based on two-step inversion, one that provides $T_s[\rho_{in}]$ which through the minimisation of the kinetic energy concludes the solutions ϕ_i to produce ρ and in the next step $v_t[\rho]$ will be calculated to solve the whole system again to obtain $\rho = \rho_{in}$. Both steps are done in an iterative procedure. For more information you can read my published review [9] in chapter 2. Analytical inversion doesn't require iterative procedures and respects the uniqueness condition of potential-wavefunction.

$$\epsilon_i^{\alpha} \psi_i^{\alpha}(\mathbf{r}) = \left[-\frac{\nabla^2}{2} + v_{KS}[\rho_{tot}](\mathbf{r}) \right] \psi_i^{\alpha}(\mathbf{r})$$

(1.13)

$$\rho_{tot}(\mathbf{r}) = \sum_{i,\alpha}^{N} n_i^{\alpha} |\psi_i^{\alpha}(\mathbf{r})|^2$$

$$i = 1, 2, \ldots$$

$$\alpha = \uparrow, \downarrow$$

(1.14)

Only under specific conditions, the potential could be inverted analytically and in one step. I describe below those conditions.

One-Orbital Formula

The one-orbital formula for one electron or two spin compensated electrons where the solution is real and positive (means $\psi_i(\mathbf{r}) = \sqrt{\rho_i(\mathbf{r})}$) Eq. [1.2] could be rearranged as:

$$v_{KS}(\mathbf{r}) = \frac{\nabla^2 \psi_i(\mathbf{r})}{2\psi_i(\mathbf{r})} + \epsilon_i \tag{1.15}$$

If the wavefunction is real and positive, the Kohn-Sham potential reads:

$$v_{KS}(\mathbf{r}) = \frac{\nabla^2 \sqrt{\rho_i(\mathbf{r})}}{2\sqrt{\rho_i(\mathbf{r})}} + \epsilon_i = v_s[\rho_i(\mathbf{r})] \tag{1.16}$$

where i defines is orbital index.

Analytical Inversion of Non-Additive Potential Functional of Pair of Density

Non-Additive potential bi-Functional (v^{NAD}) denotes the difference of the energy between two given partitioned densities or one partitioned density (called ρ_A in this work) the total ground-state density in a system. The latter is defined in Eq. [1.17].

$$v^{\mathrm{NAD}}[\rho_A, \rho_{tot}](\mathbf{r}) = v_s[\rho_A(\mathbf{r})] - v_{KS}(\mathbf{r}) \tag{1.17}$$

In order that v^{NAD} be expressed entirely in functional notion, the last term of Eq.[1.17] could be replaced by its definition from Eq.[3.5]:

$$v^{\mathrm{NAD}}[\rho_A, \rho_{tot}](\mathbf{r}) = v_s[\rho_A(\mathbf{r})] - v_s[\rho_i(\mathbf{r})] \tag{1.18}$$

Such Analytical inversion is correct under specific constraints. The density used as an independent variable of analytically inverted potential functional has to integrate to integers 1 or 2 in whole space for one-electron or two spin-compensated electrons respectively.

1.2.5 Numerical Simulations

The theory of this work has been numerically developed in two programs developed in real space one based on all-electron calculation and the other with pseudopotential approach. The advantage of the real grid approach compared to other approaches such as spectrum algorithm[203] is the possibility of controlling the quality of the discretisation with changes in the spacing of the grids and the entire size of the system. That provides fast calculation while multiple tests during the implementation of theories and high accuracy with decreased errors for solving the problems. Below a brief explanation on all-electron calculation with DARSEC[135].

All-electron Calculations

For all-electron-based calculations of this work code, DARSEC was used[134]. This code allows for spin-polarized all-electron DFT calculations for single atoms and diatomic molecules, using a real-space prolate-spheroidal grid (Fig.[1.2]). One or two atoms in question are sited at the centres of elliptic-like coordinates (blue dots in Fig.[1.2]). The grids are very dense near the centres and get distant far from the atoms. Clearly, the advantage of DARSEC is the high precision of the calculations due to the better sampling at the vicinity of the atoms where the atomic potential is singular and the orbitals oscillate rapidly.

The prolate-spheroidal coordinates $(\mu, \nu, \phi)[0, \infty][0, \pi][0, 2\pi]$ for centres at $A(0, 0, -R/2)$ and $B(0, 0, -R/2)$, are defined by:

$$
\begin{aligned}
x &= \frac{R}{2} \sinh(\mu) \sin(\nu) \cos(\phi) \\
y &= \frac{R}{2} \sinh(\mu) \sin(\nu) \sin(\phi) \\
z &= \frac{R}{2} \cosh(\mu) \cos(\nu)
\end{aligned}
\tag{1.19}
$$

Similarly, the Prolate-spheroidal coordinates in terms of Cartesian coordinates are defined as:

$$
\begin{aligned}
\mu &= \cosh^{-1}\left(\frac{r_A + r_B}{R}\right) \\
\nu &= \cos^{-1}\left(\frac{r_A - r_B}{R}\right) \\
\phi &= \tan^{-1}\frac{y}{x}
\end{aligned}
\tag{1.20}
$$

where $r_A(r)$ and $r_B(r)$ are the Euclidean distances of a general point (x, y, z) from the centres A and B, respectively, and ϕ is the angle of rotation around the interatomic axis, i.e., the z-axis.

Another advantage of DARSEC is its computational cost, knowing that the code is not yet parallelised. The problem could be solved in 2D in DARSEC due to the cylindrical symmetry of diatomic molecules. This is true while the angle ϕ can be treated analytically.

Formally, this means that all physical entities (i.e., charge density, potentials, squared absolute wave functions, etc.) are ϕ-independent and that the one-particle wave functions are of the form $\psi(\mu, \nu, \phi) = \psi(\mu, \nu, 0)e^{im\phi}$ for $m = 0, \pm 1, \pm 2, ...$, where m is an integer corresponding to the quantum number of angular momentum with respect to the interatomic axis.
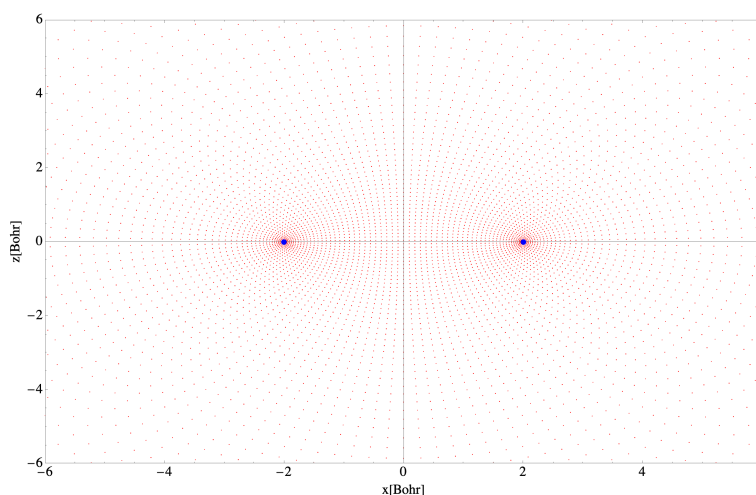
Figure 1.2: DARSEC visualization the grids in real-space. The blue dots represent position atom centres, with red dots denoting the grid of the coordinate system. DARSEC employs the use of a real-space prolate-spheroidal grid.

Graphical Representation of the Results

The results are shown graphically in 1D or 2D representations. The outputs of the calculations done within DARSEC are available to be plotted in 1D or 2D as the DARSEC reduces the calculations into 2D based on axial symmetry of the parabolic coordinates and symmetry of the diatomic systems. As it is manifested in Fig.[1.2], the atoms are sited on the center of the coordinate system along the z-axis. The $z = 0$ has no grid points. When I show graphically

the data in 1D, the plots represent the values of the grid points in first coming (ν, μ) to the inter atomic axis in the half positive part of the space. In fact the 1D representation of the results are the value found on the grid points siting on the red line in Fig.[1.3]
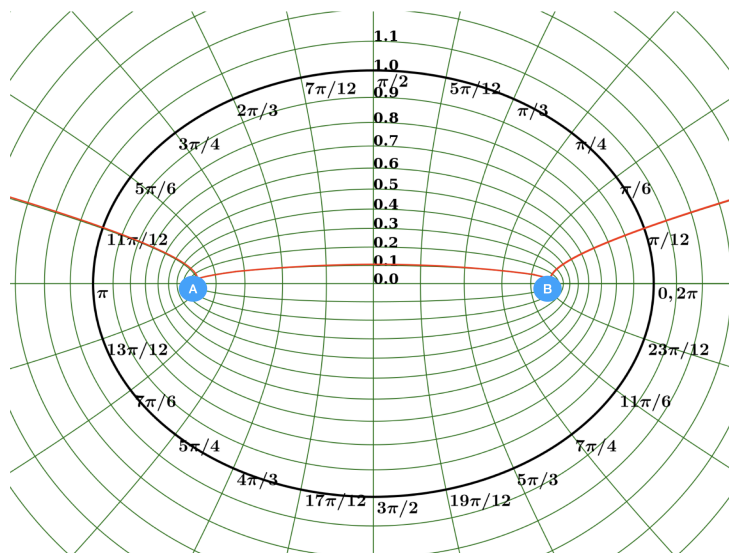
Figure 1.3: Schematic of the prolate-spheroidal coordinates. The red line represents the grids from which the values of the calculations are extracted for the 1D representation of the results.

The 2D plots contain the value of entire grid points in the space as it is illustrated in Fig.[1.2].

Chapter 2

non-additive kinetic potentials from inverted Kohn-Sham problem

2.1 Abstract

This chapter is the expansion of my published work[9]. The non-additive kinetic potential is a key element in density-dependent embedding methods. The correspondence between the ground-state density and the total effective Kohn-Sham potential provides the basis for various methods to construct the non-additive kinetic potential for any pair of electron densities. Several research groups used numerical or analytical inversion procedures to explore this strategy which overcomes the failures of known explicit density functional approximations. The numerical inversions, however, apply additional approximations/simplifications. The relations known for the exact quantities cannot be assumed to hold for quantities obtained in numerical inversions. The exact relations are discussed with special emphasis on such issues as: the admissibility of the densities for which the potential is constructed, the choice of densities to be used as independent variables, self-consistency between the potentials and observables calculated using the embedded wavefunction, and so forth. The review focuses on how these issues are treated in practice. The review is supplemented with the analysis of the inverted potentials for weakly overlapping pairs of electron densities – the case not studied previously.

2.2 Introduction

The non-additive kinetic energy (T_s^{NAD}) and potential ($v_t^{\mathrm{NAD}}(\mathbf{r})$) are key ingredients in numerical simulation methods exploring the density embedding strategy (see Section 2.2.2). Both quantities are defined as functionals of admissible pairs of electron densities:

$$T_s^{\mathrm{NAD}}[\rho_A, \rho_{tot}] = T_s[\rho_{tot}] - T_s[\rho_{tot} - \rho_A] - T_s[\rho_A] \tag{2.1}$$

and

$$v_t^{\mathrm{NAD}}[\rho_A, \rho_{tot}](\mathbf{r}) = \left. \frac{\delta T_s[\rho]}{\delta \rho} \right|_{\rho(\mathbf{r}) = \rho_{tot}(\mathbf{r})} - \left. \frac{\delta T_s[\rho]}{\delta \rho} \right|_{\rho(\mathbf{r}) = \rho_A(\mathbf{r})} \tag{2.2}$$

where the functional $T_s[\rho]$ is defined via the constrained search [127]:

$$T_s[\rho] = \min_{\Psi_s \to \rho} \left\langle \Psi_s \left| \hat{T} \right| \Psi_s \right\rangle = \left\langle \Psi_s^{opt} \left| \hat{T} \right| \Psi_s^{opt} \right\rangle \tag{2.3}$$

where Ψ_s denotes a N-electron single-determinant trial wavefunction. Atomic units are used throughout this work.

In practical applications, $\rho_A(\mathbf{r})$ is the density corresponding to the wavefunction Ψ_{emb} associated with the embedded subsystem and $\rho_{tot}(\mathbf{r})$ is electron density of the total system comprising the part represented by Ψ_{emb} and its "environment". Usually, explicit density functionals approximate the functionals $v_t^{\mathrm{NAD}}[\rho_A, \rho_{tot}](\mathbf{r})$ and/or $T_s^{\mathrm{NAD}}[\rho_A, \rho_{tot}]$. Simulations and studies on model systems reported by several researchers revealed many cases where that the currently known explicit density functionals fail (see section 2.2.2). These failures resulted in recent interest in an alternative - implicit - strategy to construct $v_t^{\mathrm{NAD}}[\rho_A, \rho_{tot}](\mathbf{r})$ (and $T_s^{\mathrm{NAD}}[\rho_A, \rho_{tot}]$) for arbitrarily chosen pairs of densities $\rho_A(\mathbf{r})$ and $\rho_{tot}(\mathbf{r})$. Such constructions are based on the Levy correspondence [127] between the Kohn-Sham potential [115] and the electron density. This correspondence exists for admissible electron densities but using it in practice relies on the *numerical inversion*, i.e., the construction of the Kohn-Sham potential (and orbitals) for a given target density.

(see Section 2.2.1 for the exact relations between the quantities, which are obtained from the inversion procedures and $v_t^{\mathrm{NAD}}[\rho_A, \rho_{tot}](\mathbf{r})$ are given in.)

The non-additive kinetic potentials obtained from the inversion procedures are presently being constructed by several authors for various purposes. To

our knowledge, the numerically inverted potentials where introduced into the general field of density based embedding methods to generate local atomic pseudopotentials [229]. Other authors used accurate inverted potentials to detect flaws of explicit approximations to $v_t^{\mathrm{NAD}}[\rho_A, \rho_{tot}](\mathbf{r})$ and to determine their limits of applicability [176, 215, 37, 55]. Reports on using inverted potentials in practical simulations started appearing in the literature [229, 179, 171, 172, 173, 61, 62, 63, 6]. Such studies provide frequently direct or indirect (through calculated observables) inrormation about the quality of the inverted non-additive kinetic potential.

The present work overviews these developments. Section 2.2.1 provides the basic definitions and exact relations between the discussed quantities. These relations provide the basis for various possible practical constructions of non-additive kinetic potentials for a given pair of densities. Section 2.2.2 provides key examples of failures of explicit functionals in approximating the exact potential. The review of the literature concerning the non-additive kinetic potentials obtained from various inversion techniques is given in Section 2.3. The literature examples are supplemented by our own new results concerning inverted potentials at a special case of weak overlap between subsystem densities. The inverted potentials for such a case were not discussed in the literature so far and are provided here as a supplement.

2.2.1 Implicit definition of the functional for non-additive kinetic potential

Up to a constant, Kohn-Sham equation provide the exact correspondence between the total Kohn-Sham effective potential (the last three terms in the operator in the right-hand-side of Eq. 2.4) and the ground-state electron density $\rho_o(\mathbf{r})$ obtained for this potential:

$$\left(-\frac{1}{2}\nabla^2 + v_{ext}(\mathbf{r}) + \int \frac{\rho_o(\mathbf{r}')}{|\mathbf{r}' - \mathbf{r}|} d\mathbf{r}' + v_{xc}[\rho_o](\mathbf{r}) \right) \phi_i = \epsilon_i \phi_i \ \text{ for } \ i = 1, \ N \quad (2.4)$$

where $\rho_o(\mathbf{r}) = \sum_i^N n_i |\phi_i|^2$, and n_i to be the obital occupation number.

This correspondence will be denoted hereafter as the functional $v_s[\rho_o](\mathbf{r})$. This functional makes it possible to cast Eq. 2.4 into the form which does not

involve explicitly the external potential:

$$\left(-\frac{1}{2}\nabla^2 + v_s[\rho_o](\mathbf{r})\right)\phi_i[\rho_o] = \epsilon_i[\rho_o]\phi_i[\rho_o] \text{ for } i = 1, \ N \qquad (2.5)$$

where $\{\phi_i[\rho_o]\}$ are canonic Kohn-Sham orbitals corresponding to $v_s[\rho_o](\mathbf{r})$.

The above equation holds also for density and potential if approximated density functional is used for the exchange-correlation potential ($\tilde{v}_{xc}[\rho](\mathbf{r})$ in the limit of complete basis set [38]. The admissible densities, for which such correspondence exists, will be referred to in this work as *pure-state non-interacting v-representable* (PSNIVR). For pairs of PSNIVR densities, such that $\rho_{tot}(\mathbf{r}) \geq \rho_A(\mathbf{r})$, the functional $v_t^{\text{NAD}}[\rho_A, \rho_{tot}](\mathbf{r})$ can be expressed by means of the functional $v_s[\rho](\mathbf{r})$ [217]. Up to a constant, the non-additive kinetic potential is just the difference between the potentials:

$$v_t^{\text{NAD}}[\rho_A, \rho_{tot}](\mathbf{r}) = v_s[\rho_A](\mathbf{r}) - v_s[\rho_{tot}](\mathbf{r}) + const \qquad (2.6)$$

This relation cannot be used to obtain general analytic expression for the functional $v_t^{\text{NAD}}[\rho_A, \rho_{tot}](\mathbf{r})$. For a given pair $\rho_A(\mathbf{r})$ and $\rho_{tot}(\mathbf{r})$, $v_t^{\text{NAD}}[\rho_A, \rho_{tot}](\mathbf{r})$ can be obtained as *implicit* functional. This requires solving the *inverted Kohn-Sham problem*. Kohn-Sham equation is solved for a given $v_{ext}(\mathbf{r})$ and a given functional $\tilde{v}_{xc}[\rho](\mathbf{r})$. To get $v_s[\rho_{target}](\mathbf{r})$ for a target $\rho_{target}(\mathbf{r})$, one needs to solve the inverted problem - to get a potential for a given density. In a particular case, where one of the densities considered in Eq. 2.6 is obtained from Kohn-Sham calculations, the inversion procedure can be - in principle - avoided for this density. The inversion is, however, for this density in the pair which is not obtained from the Kohn-Sham calculations. Only in a trivial cases of one-electron or spin-compensated two-electron densities, the inversion can be made analytically. This brings us to the key issue of the present review, "the necessity to perform the numerical inversion in order to construct the non-additive kinetic potential numerically for a given input pair of electron densities".

The numerical inversion procedures were introduced for other purposes - to construct the exact exchange-correlation potentials. Reference exchange-correlation potentials were constructed for various chemical species to understand better the flaws of known approximations (see for Refs. [204, 198, 228, 74, 194, 222, 99]). In such calculations, $\rho_{target}(\mathbf{r})$ is obtained from high quality wave-function based calculations. To obtain the reference exchange-correlation

potential, the numerical inversion procedure is performed only once and yields the Kohn-Sham orbitals as well as the exact Kohn-Sham potential. Subtracting from the inverted Kohn-Sham potential ($v_s[\rho_{target}](\mathbf{r})$) the known components (external potential and Coulomb potential) yields the exact exchange-correlation potential for the target density.

The situation is not the same in the case of non-additive kinetic potentials. Inverted potentials are used not only as a reference guiding the development of improved explicit approximations but they can be generated inexpensively (subject to additional approximations) and used in practical simulations. In general case of an arbitrarily chosen pair of densities, two inversion procedures are needed, one for each target density. The orbitals $\{\phi_i[\rho_o]\}$ obtained in the inversion procedure and the corresponding eigenvalues can be also used to express the potential $\frac{\delta T_s[\rho]}{\delta\rho(\mathbf{r})}$ [110]. Up to a constant:

$$\frac{\delta T_s[\rho]}{\delta\rho}\bigg|_{\rho(\mathbf{r})=\rho_o(\mathbf{r})} = \frac{\sum_i(-\frac{1}{2}\phi_i[\rho_o]\Delta\phi_i[\rho_o] - \epsilon_i[\rho_o]\phi_i^2[\rho_o])}{\rho_o} + const \qquad (2.7)$$

Once a robust inversion procedure is at hand, the non-additive kinetic potential can be obtained using either Eqs. 2.2 and 2.7 or Eq. 2.6.

Concerning the domain of the admissible densities, for which the functional $v_t^{\text{NAD}}[\rho_A, \rho_{tot}](\mathbf{r})$ is defined, I notice that the necessary condition for Eq. 2.6 to hold is that the corresponding energy functional $T_s^{\text{NAD}}[\rho_A, \rho_{tot}]$ exists (see the derivation of Eq. 2.6 in Refs. [217, 213]). In practical calculations $\rho_A(\mathbf{r})$, is constructed from the embedded wavefunction. Its N-representability is built-in in its construction. If $\rho_{tot}(\mathbf{r})$ is, however, an independent variable, the quantity $\rho_B(\mathbf{r}) = \rho_{tot}(\mathbf{r}) - \rho_A(\mathbf{r})$ cannot be always interpreted as electron density. The functional $T_s^{\text{NAD}}[\rho_A, \rho_{tot}]$ does not exist if $\rho_B(\mathbf{r}) = \rho_{tot}(\mathbf{r}) - \rho_A(\mathbf{r}) < 0$. If $\rho_A(\mathbf{r})$ and $\rho_{tot}(\mathbf{r})$ are chosen as independent variables, assuring N-representability of $\rho_B(\mathbf{r}) = \rho_{tot}(\mathbf{r}) - \rho_A(\mathbf{r})$ is not straightforward. A safer choice is to use $\rho_A(\mathbf{r})$ and $\rho_B(\mathbf{r})$ as independent variables which yield $\rho_{tot}(\mathbf{r}) = \rho_A(\mathbf{r}) + \rho_B(\mathbf{r})$. The quantity $\rho_{tot}(\mathbf{r}) = \rho_A(\mathbf{r}) + \rho_B(\mathbf{r})$ can *a priori* be made N-representable for any trial N-representable $\rho_A(\mathbf{r})$. To satisfy the conditions of N-representability given by Gilbert [57], it is sufficient that $\rho_B(\mathbf{r}) \geq 0$, $\int_V \rho_B(\mathbf{r})d\mathbf{r}$ is integral, and the function is sufficiently smooth. If $v_t^{\text{NAD}}[\rho_A, \rho_{tot}](\mathbf{r})$ is evaluated, $\rho_A(\mathbf{r})$ is always the electron density represented by means of some quantum mechanical descriptor

(embedded wavefunction) and it is the quantity which is not known *a priori*. It is the result of the calculations. $\rho_{tot}(\mathbf{r})$, on the other hand, can be either the density obtained from independent calculations or it can be constructed as a sum of $\rho_{tot}(\mathbf{r}) = \rho_A(\mathbf{r}) + \rho_B(\mathbf{r})$ for some $\rho_B(\mathbf{r})$ treated as the independent variable. For such a choice of independent variables, the it is convenient to introduce the non-additive kinetic energy functional which admits a larger class of pairs of electron densities:

$$T_s^{\text{nad'}}[\rho_A, \rho_B] = T_s[\rho_A + \rho_B] - T_s[\rho_A] - T_s[\rho_B] \tag{2.8}$$

and express the non-additive kinetic potential as a functional of other variables:

$$v_t^{\text{nad'}}[\rho_A, \rho_B](\mathbf{r}) = \left. \frac{\delta T_s[\rho]}{\delta \rho(\mathbf{r})} \right|_{\rho = \rho_A + \rho_B} - \left. \frac{\delta T_s[\rho]}{\delta \rho(\mathbf{r}} \right|_{\rho = \rho_A} \tag{2.9}$$

The functional given in Eq. 2.8 is more general than that in Eq. 2.1. It admits all N representable electron densities without any additional constraints. For densities admissible in the Eq. 2.8,

$$
\begin{aligned}
T_s^{\text{nad'}}[\rho_A, \rho_B] &= T_s^{\text{NAD}}[\rho_A, \rho_A + \rho_B] \\
v_t^{\text{nad'}}[\rho_A, \rho_B] &= v_t^{\text{NAD}}[\rho_A, \rho_A + \rho_B]
\end{aligned} \tag{2.10}
$$

In methods based on Frozen-Density Embedding Theory (FDET), $\rho_A(\mathbf{r})$ and $\rho_B(\mathbf{r})$ are considered as independent variables. FDET provides self-consistent expressions for the embedding potential and the total energy for various quantum mechanical descriptors of the embedded system such as: non-interacting reference system [217], interacting wavefunction [213], one-particle reduced density matrix [166], or linear response of non-interacting reference system [210]. In each case, the optimal embedded quantum mechanical descriptor such as the embedded wavefunction Ψ_A, is obtained from Euler-Lagrange equations leading to the upper bound of the energy of the total system:

$$E_{AB}^{FDET}[\Psi_A^{opt}, \rho_B] = E_{AB}^{\text{HK}}[\rho_A^{opt} + \rho_B] \geq E_o, \tag{2.11}$$

where E_o is the ground-state energy of the total system, $\rho_A^{opt}(\mathbf{r})$ is the embedded density corresponding to Ψ_A^{opt}, and $E_{AB}^{\text{HK}}[\rho]$ is the universal Hohenberg-Kohn energy functional [94].

If $\rho_A(\mathbf{r})$ and $\rho_B(\mathbf{r})$ are used as independent variables, the functionals $T_s^{\text{nad'}}[\rho_A, \rho_B]$ and $v_t^{\text{nad'}}[\rho_A, \rho_B](\mathbf{r})$ can be approximated directly (without a "parent" $\tilde{T}_s[\rho]$) [56] to the bi-functional for the non-additive kinetic energy:

$$\tilde{T}_s^{\text{nad'}}[\rho_A, \rho_B] \approx T_s^{\text{NAD}}[\rho_A, \rho_B] = T_s[\rho_A + \rho_B] - T_s[\rho_A] - T_s[\rho_B] \qquad (2.12)$$

$$v_t^{\text{nad'}}[\rho_A, \rho_B](\mathbf{r}) \approx \tilde{v}_t^{\text{NAD}}[\rho_A, \rho_B](\mathbf{r}) = \left. \frac{\delta \tilde{T}_s^{\text{NAD}}[\rho, \rho_B]}{\delta \rho} \right|_{\rho(\mathbf{r}) = \rho_A(\mathbf{r})} \qquad (2.13)$$

Methods introduced by Carter and collaborators [69, 70] represent another choice of independent and hinges on the error compensation Ansatz:

$$E_{AB} \approx E_{AB}[\Psi_{AB}^{method_I}] + E_A[\Psi_A^{method_{II}}] - E_A[\Psi_A^{method_I}], \qquad (2.14)$$

where the method of the lower quality ($method_I$) can be applied to the whole system and that of the higher quality ($method_{II}$) only to the embedded part.

Minimization of the energy given as a functional of the embedded wave-function given in Eq. 2.11 or Eq. 2.14 proceeds via Euler-Lagrange equations. Regardless, what is the quantum-mechanical descriptor used for $\rho_A(\mathbf{r})$ in FDET or $method_I$ in methods based on Eq. 2.14, the embeding potential comprises the $v_t^{\text{NAD}}[\rho_A, \rho_{tot}](\mathbf{r})$ term defined in Eq. 2.2. If the non-interacting reference system is used for $\rho_A(\mathbf{r})$ in FDET, the Euler-Lagrange equations will be referred to in this work as Kohn-Sham Equation with Constrained Electron Density (KSCED).

It is worthwhile to notice that these two type of multi-level simulations methods share the need of approximation to $v_t^{\text{NAD}}(\mathbf{r})$ but differ as far as their scope is concerned. Without additional constraints, which to our knowledge where not considered within the context of methods based on Eq. 2.14, the quantity $\rho_B(\mathbf{r}) = \rho_{tot}(\mathbf{r}) - \rho_B(\mathbf{r})$ cannot be interpreted as the electron density. On the other hand, using $\rho_A(\mathbf{r})$, $\rho_B(\mathbf{r})$ as independent variables results in the possibility to use any physical model (even classical) yielding $\rho_B(\mathbf{r})$, which is a physical observable at any scale. For such applications of FDET in multi-scale simulations see Refs. [106, 123], in which $\rho_B(\mathbf{r})$ was obtained from classical statistical-mechanical model.

In practical terms, neither strategy that based on Eq. 2.11 nor 2.14 can yield exact solutions of the quantum-many body problem for the whole system. These two types of multi-level simulation methods target the effect of environment on

properties of embedded species. Eq. 2.14 strategy relies of the choice of the low-level quantum mechanical method used to obtain $\rho_{tot}(\mathbf{r})$ wheres the FDET strategy on the choice of $\rho_B(\mathbf{r})$. Subsystem formulations of DFT, on the other hand, such as that by Cortona [35] or various formalisms enforcing a common embedding potential for all subsystem such as: Partition DFT (PDFT) [46, 48] and the method introduced by Huang and Carter [96], are in principle capable to yield exact solution of quantum many body problem. In such approaches *a priori* assumption is made for neither $\rho_{tot}(\mathbf{r})$ nor $\rho_B(\mathbf{r})$, because also $\rho_B(\mathbf{r})$ (or $\rho_{tot}(\mathbf{r})$) is optimised to minimize the total energy in the presence of the local potential , which is common for all subsystems.

2.2.2 Failures of explicit semi-local approximations to the functional $v_t^{\mathbf{NAD}}[\rho_A, \rho_{tot}](\mathbf{r})$ in numerical simulations

In practical calculations, $v_t^{\text{NAD}}[\rho_A, \rho_{tot}](\mathbf{r})$ is usually not constructed by means of the inversion procedure. It is approximated using some explicit density functional. For any differentiable explicit approximated density functional for the kinetic energy, $\tilde{T}_s[\rho]$, each of the functionals:

$$\tilde{T}_s^{\text{nad'}}[\rho_A, \rho_B] \approx \tilde{T}_s[\rho_A + \rho_B] - \tilde{T}_s[\rho_A] - \tilde{T}_s[\rho_B] \tag{2.15}$$

$$v_t^{\text{NAD}}[\rho_A, \rho_{tot}](\mathbf{r}) \approx \tilde{v}_t^{\text{NAD}}[\rho_A, \rho_{tot}](\mathbf{r}) = \left.\frac{\delta \tilde{T}_s[\rho]}{\delta \rho(\mathbf{r})}\right|_{\rho=\rho_{tot}} - \left.\frac{\delta \tilde{T}_s[\rho]}{\delta \rho(\mathbf{r})}\right|_{\rho=\rho_A} \tag{2.16}$$

can be evaluated as an explicit functional.

Several specialized reviews cover applications of methods in which explicit density functionals are used (see Refs. [101, 221, 102, 208, 152, 59, 13] for instance). This section, I focuses rather on the numerical results indicating the need of the alternative strategies such as the ones based in the inversion procedures.

The errors of any approximated functional $v_t^{\text{NAD}}[\rho_A, \rho_{tot}](\mathbf{r})$ accumulate, if not only $\rho_A(\mathbf{r})$ is optimised but also $\rho_B(\mathbf{r})$ in FDET. Such optimization can be performed in practice by an iterative procedure *freeze-and-thaw*, in which FDET equations are solved iteratively. In subsequent iterations, $\rho_A(\mathbf{r})$ and $\rho_B(\mathbf{r})$ exchange their roles till self-consistency [218]. Such calculations represent the numerical implementation of Cortona formulation of DFT [35], which leads

to the exact solution of quantum-many-body problem at the hypothetical limit of exact functionals. Note that it is not the case of FDET which leads to the upper bound of the total energy at this limit. In the case of error compensation based strategies this limit is reached only if $method_I$ and $method_{II}$ in Eq. 2.14 denote the exact solution of the quantum-many body problem.

The undesired feature of the Cortona formulation is the fact that the pair of optimised densities yielding the exact total density is not unique. Subsystem DFT admits multiple solutions, i.e., pairs of PSNIVR densities $\rho_A(\mathbf{r})$ and $\rho_B(\mathbf{r})$ which add up to the same total energy. In practical applications of the Cortona formulation of DFT, $v_t^{\text{nad'}}[\rho_A, \rho_B](\mathbf{r})$ is approximated as in Eq. 2.16 unique solution is usually obtained. The unique solution of the *freeze-and-thaw* optimization is an artifact due to the error in $\tilde{v}_t^{\text{NAD}}[\rho_A, \rho_{tot}](\mathbf{r})$ (see the relevant discussion in Refs. [97, 221]). Nevertheless, the Cortona formulation of subsystem DFT, introduced to molecular complexes by Wesolowski and Weber [218], was shown to yield surprisingly good description of weak intermolecular complexes near equilibrium geometry [195, 216, 109, 45, 44]. It is probably the combined results of errors in the embedding potential which penalizes the overlap between the subsystem densities. As a result, the approximated components to the total energy such as that due to the non-additive kinetic energy are small. For larger overlaps between $\rho_A(\mathbf{r})$ and $\rho_B(\mathbf{r})$, semi-local approximations to $v_t^{\text{nad'}}[\rho_A, \rho_B](\mathbf{r})$ systematically fail as shown for model systems [15, 176, 215], realistically chemical systems such as intermolecular complexes at small intermolecular separations[218, 219, 220, 209] or covalently bounded subsystems [54, 16, 77].

Another systematic failure of semi-local approximations concerns large separation. Semi-local functionals $\tilde{v}_t^{\text{NAD}}[\rho_A, \rho_{tot}](\mathbf{r})$ were reported to lead to artificial charge distribution between subsystems. Jacob *et al.* [103], analyzed this case in detail and proposed a correction to this problem by enforcing that the total embedding potential in FDET reaches zero at large separations. Lastra *et al.* [56], addressed this problem in a different way, by enforcing exact properties on the functional $v_t^{\text{nad'}}[\rho_A, \rho_B](\mathbf{r})$ at small overlaps between $\rho_A(\mathbf{r})$ and $\rho_B(\mathbf{r})$ and constructing explicit functional $\tilde{v}_t^{\text{nad'}}[\rho_A, \rho_B](\mathbf{r})$ reflecting these properties.

These reported failures of semi-local approximations to $v_t^{\text{NAD}}[\rho_A, \rho_{tot}](\mathbf{r})$,

which are explicit density functionals, motivated the recent interests in the implicit functionals obtained using inversion procedures.

2.2.3 Numerical inversion of the Kohn-Sham Equation with finite atomic basis set

In this section, the universally applicable methods for inverting the Kohn–Sham equation are overviewed. Such methods were developed originally for generating reference exchange-correlation potentials for a given density. I focus on methods, which were used to construct non-additive kinetic potentials. The scheme in Fig.[2.1-a], illustrates the key elements in such procedures.

Step I in the upper panel represents a solver of the Kohn–Sham equation, which uses a given approximation to the exchange-correlation potential. The ground-state density is the density corresponding to the total effective potential at the end of self-consistent calculations. I refer to the problem shown in the lower panel as *inverting Kohn–Sham equation*. The potential corresponding to a given target density $\rho_{in}(\mathbf{r})$ is to be found.

Step I is the key element consisting of the search for the orbitals which yield $\rho_{in}(\mathbf{r})$. In the trivial case of $\rho_{in}(\mathbf{r})$ being an one-electron- or a two-electron spin-compensated density, the orbitals can be obtained analytically and used subsequently in step II to generate the potential $v[\rho_{in}](\mathbf{r})$. In all other cases, inverting the Kohn–Sham equations relies on a numerical procedure. In practice, the numerical inversion uses the Levy's constraint search[127] for the potential $v(\mathbf{r})$ such that:

$$\left(-\frac{1}{2}\nabla^2 + v(\mathbf{r}) \right)\phi_i(\mathbf{r}) = \epsilon_i\phi_i(\mathbf{r}) \rightarrow \rho(\mathbf{r}) = \sum_{i=1}^{N}|\phi_i(\mathbf{r})|^2 = \rho_{in}(\mathbf{r}) \qquad (2.17)$$

In the numerical inversion procedures, the search can be performed either directly (among potentials) or indirectly (among orbitals). Unfortunately, numerical inversion of Kohn–Sham equation is an ill-defined problem if the finite basis sets are used. It results in numerical instabilities or multiple solutions. It is very likely that the numerical problems aggravate if the numerical inversion is performed *twice* for the sake of obtaining $v_t^{\mathrm{NAD}}[\rho_A, \rho_{tot}]$ (the subject of the present review). The problem of nonuniqueness of local potentials, if represented using finite basis sets, is not only relevant for inverting the Kohn–Sham equation, but for other one-electron equations using local potentials. For a comprehensive analysis of this issue, see the work by Staroverov, Scuseria, and Davidson[182]. For other methods to circumvent the numerical
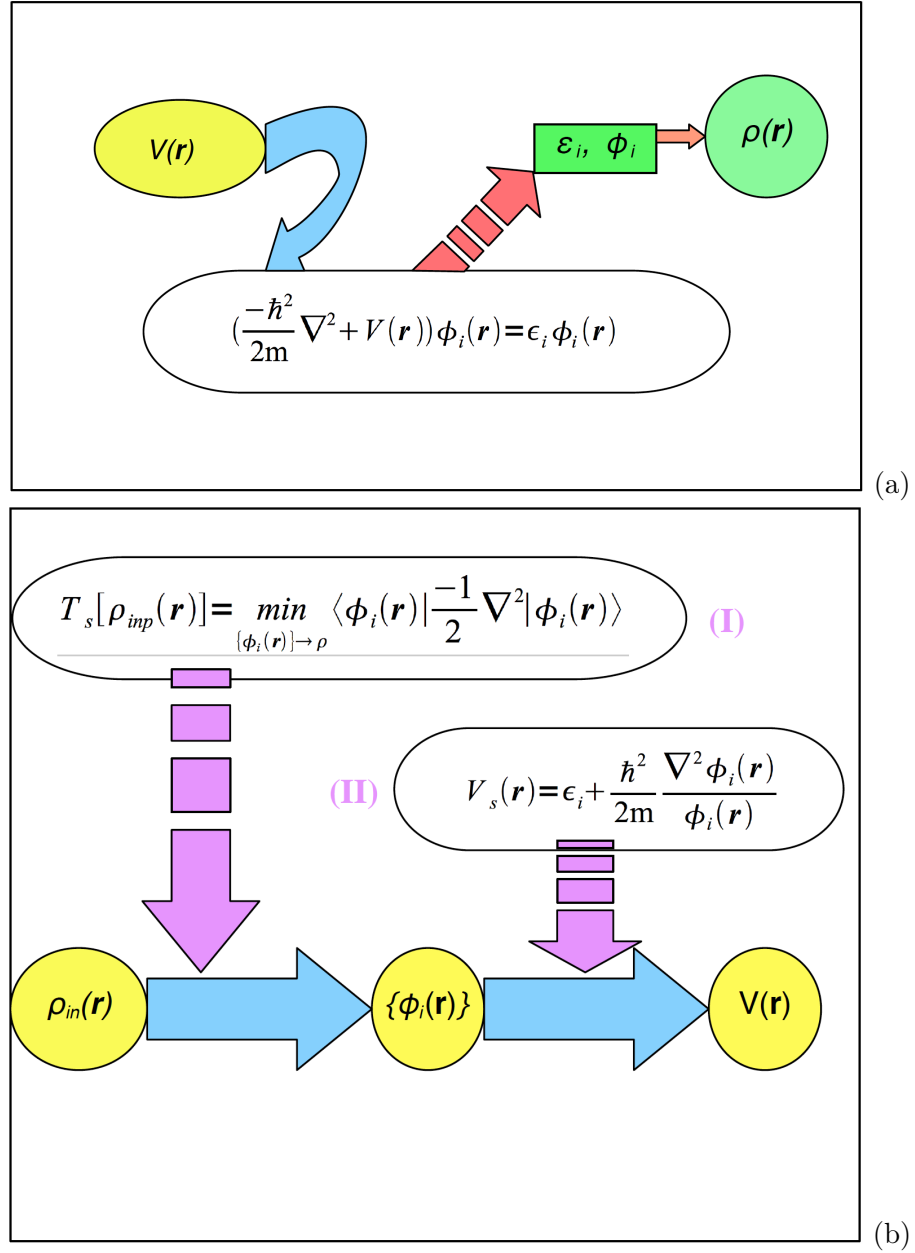
Figure 2.1: KS equation solving procedures. a) Shows a normal Kohn-Sham equation which is solved once there is a good approximation and knowledge to all terms of KS potential. b) Shows the inverted procedure in which from a given electron density of system, the potential is constructed as a functional of electron density. The corresponding orbitals to this latest are found based on Levy CS (step(I)). From the obtained orbitals, inverted potential is calculated (step II) . ϵ_i is a constant in b) equivalent to corresponding eigenvalue.

difficulties due to the nonuniqueness of the optimized effective potential, see Refs.[39, 67, 86, 117, 19, 87] for instance. The second step in the inversion (Step II in the lower panel in Fig.[2.1-a]) consists of using a seemingly trivial analytic formula. Up to a constant, it yields the inverted potential anywhere except nodal planes of the used orbital. This step, however, contributes to nonuniqueness of the inverted potential if a finite basis set is used. As shown numerically by De Silva and Wesolowski[36], each orbital yields qualitatively different inverted potential. A pragmatic solution proposed by King and Handy is to take as inverted potential the density weighted average[110]. Up to a constant (Eq.[2.7]).

Inversion procedure of KS equation contains construction of potential from a given electron density (target) or orbitals as input (Fig.[2.1-b]). From this procedure KS equation will be resolved using the recently constructed inverted potential to yield an electron density equal to target density. The corresponding orbitals to input density could be obtained from numerical application of levy constraint (Step (I) of Fig.[2.1-b]). The inverted potential is used in calculation of non-additive kinetic potential. Eq. 2.6 can be used as the basis for constructing the non-additive kinetic potential implicitly for a given pair of electron densities ρ_A and ρ_{tot}. To this end, the numerical inversion of the Kohn-Sham equation must be performed twice. Once to obtain $v_s[\rho_A](r)$ and once to obtain $v_s[\rho_{tot}](r)$. Several authors proposed generally applicable methods to invert the Kohn-Sham equations for an arbitrarily chosen target density (denoted as ρ_{in} in this section). Some of these methods based on iterative procedures use linear responses [207, 64, 66, 177] and some used more complicated procedures such as ones solving series of coupling equations eventuating to inversion methods more limited to small systems of few electrons [2, 7, 149, 150, 28, 29, 95]. Such procedures were developed to obtain reference exchange-correlation potentials for a given density. The inversion procedure could results potential $V_s(\mathbf{r})$ directly from corresponding orbitals to density, up to a constant (Step (II) of Fig.[2.1-b]). de Silva and Wesolowski [38], showed this constant is equivalent to eigenvalue corresponded to the orbitals. Then King and Handy inversion procedure [194], in which the potential was obtained as the density-weighted average of the potentials obtained from each single occupied KS-Orbitals.

Inverting the Kohn-Sham equations is an ill-defined problem (see also latter in the present work) if the finite basis sets are used for solving Kohn-Sham equation. This leads to numerical instabilities or multiple solutions. In the latest case, one solution to KS equation could be obtained from different used potentials. This raises up the lack of uniqueness problem. I can only expect that performing the numerical inversion *twice* for the sake of obtaining $v_t^{\text{NAD}}[\rho_A, \rho_{tot}](r)$ can only aggravate the numerical problems. The nature of lack of uniqueness could be explained through Eq.2.18 followed form Eq.11 of Jacob [100].

$$\Delta\rho(\mathbf{r}) = cnst. \sum_{i,a}^{N} \frac{\langle \varphi_i \, |\Delta V(\mathbf{r})| \, \varphi_a \rangle}{\epsilon_i - \epsilon_a} \varphi_i(\mathbf{r})\varphi_a(\mathbf{r}) \qquad (2.18)$$

For $\langle \varphi_i \, |\Delta V(\mathbf{r})| \, \varphi_a \rangle = 0$, any changing in $\Delta V(\mathbf{r})$ will not change $\Delta\rho(\mathbf{r})$. Some researchers [222, 22, 81, 80] optimised potential by suggesting a linear combination of potential basis functions that can tune density variation, $V(\mathbf{r}) = \sum_t b_t g_t(\mathbf{r})$, where b_t is expansion coefficient. Some others then tried to fix uniqueness problem differently. For example Jacob [100], proposed an additional constraint to the variation of density by introducing a threshold e_{thresh} Eq. 2.19.

$$e_{densi} = \int |\Delta\rho(\mathbf{r})d\mathbf{r}| \leq const. \sum_t \sigma_t \Big|\Delta\tilde{b}_t\Big| d_t, \qquad (2.19)$$

Where $d_t = \int |\varphi_t(\mathbf{r})|d\mathbf{r}$ and σ_t are the Singular value decomposition of basis-set transformation matrix (look for Eq.(13) in ref. [100] for more details). Hirata et a. [87] for the finite number of orbitals for an ill-defined Optimised Effective Potential (OEP) [71] integral equation suggested to project the equation and $v_x(\mathbf{r})$ upon the function space accessible by kernel and thereby making the exchange potential unique.

Staroverov and scuseria [183], made a procedure to construct local $v_x(\mathbf{r})$ for any number of electrons for any basis set to obtain exact unique HF energy and density. Some other attempts were done to optimise the potential differently to get rid out of ill-defined inverting procedure of KS equation by [58, 67, 86, 117, 19].

Before reviewing the works, in which the non-additive kinetic potentials were obtained by means of TWO numerical inversions, I provide the brief overview of the key methods used in the literature for inverting the Kohn-Sham equations. Due to the fact that the present review concerns $v_t^{\mathrm{NAD}}[\rho_A, \rho_{tot}](r)$, I focus only on the key features of methods for inverting the Kohn-Sham equation. For a more complete overview, of this issue see the dedicated section in the review by Neugebauer and Jacob [102] and the reference therein.

In the researches using DFT procedures, different methods were suggested to calculate or approximate kinetic energy functional and potential from a given density. Some based on iterative procedures use linear responses [207, 64, 66, 177] and some used more complicated procedures such as ones solving series of coupling equations eventuating to inversion methods more limited to small systems of few electrons [2, 7, 149, 150, 28, 29, 95].

Levy showed that one could consider all N-representable densities in such a search, instead of searching in the smaller (and nearly impossible to define) space of v-representable densities. Ground state can always be found by applying the variational principle[157] to Levy's formulation of DFT. From Levy constrained-search for a given density ρ_{in}, the appropriate orbitals of ρ_{Levy}, found from Eq. 2.20, minimise kinetic energy function of form of Eq.2.3 and satisfy equality of $\rho_{in} = \rho_{Levy}$.

$$\rho(\mathbf{r}) = \sum_{i=1}^{N} |\varphi_i(\mathbf{r})|^2, \tag{2.20}$$

Such wave functions are solutions to KS equation in which effective potential is a local Lagrange multiplier function. The set of orbitals φ_i attempting to minimise Eq.2.3 needs to contain normalised orbitals. This latest condition necessitates a set of eigenvalues as Lagrange multipliers. The stationary condition of Eq. 2.21 must also be satisfied by φ_i.

$$W_s[\Psi_s, v_{eff}(\mathbf{r})] = \sum_{i}^{N} \left\langle \varphi_i(\mathbf{r}) \left| \hat{T} \right| \varphi_i(\mathbf{r}) \right\rangle + \int v_{eff}(\mathbf{r})[\rho(\mathbf{r}) - \rho_{in}(\mathbf{r})]d\mathbf{r}, \tag{2.21}$$

Among methods based on Levy CR, one could call Wang et Parr [204] who provided a numerical inversion method in which through a known electron density $\rho_{in}(\mathbf{r})$, they could obtain corresponding called "exact" KS potential plus

non-interacting KS orbitals from self consistent KS solver. They replaced three potential terms of Eq. 2.4 by called effecting potential:

$$\left(-\frac{1}{2}\nabla^2 + v_{eff}^p(\mathbf{r})\right)\varphi_i(\mathbf{r}) = \epsilon_i\varphi_i(\mathbf{r}), \tag{2.22}$$

Then multiply it by $\varphi_i^*(\mathbf{r})$ and divided by ϵ_i, :

$$\sum_i^N \varphi_i^*(\mathbf{r})\varphi_i(\mathbf{r}) = v_{eff}^{(WP)}(\mathbf{r})\sum_i^N \frac{1}{\epsilon_i}\varphi_i^*(\mathbf{r})\varphi_i(\mathbf{r}) + \sum_i^N \frac{1}{\epsilon_i}\varphi_i^*(\mathbf{r})(-\frac{1}{2}\nabla^2)\varphi_i(\mathbf{r}) = \rho_{in}(\mathbf{r}) \tag{2.23}$$

From that known electron density they construct an effective potential in one-to-one correspondence with effective potential. Begining from a first estimation of effective potential, Eq. 2.22 is solved for N lowest orbital energy and their corresponding orbitals. From the initially known electron density and the latest found orbitals, the first effective potential is constructed through Eq. 2.24.

$$v_{eff}^{p(WP)}(\mathbf{r}) = \frac{\rho_{in}(\mathbf{r}) - \sum_i^N \frac{1}{\varepsilon_i}\varphi_i^{p*}(\mathbf{r})(-\frac{1}{2}\nabla^2)\varphi_i^p(\mathbf{r})}{\sum_i^N \frac{1}{\varepsilon_i}\varphi_i^{p*}(\mathbf{r})\varphi_i^p(\mathbf{r})}, \tag{2.24}$$

This procedure is repeated iteratively till the self-consistency be satisfied($v_{eff}^p(\mathbf{r}) = v_{eff}^{p-1}(\mathbf{r})$). Their model has the advantage of being free form Lagrange multiplier which needs supplementary calculations in numerical methods. The fact of being independent on boundary conditions makes this inversion method more general and easy to apply.

Seeking for approximate potentials over all space, van Leeuwen and Baerends [198] suggested a procedure that takes account of the asymptotic behaviour of potential at $r \to \infty$ and $r \to 0$. They made their method similarly to WP as an iterative solver to KS equation and from Eq. 2.22, only from multiplication by $\varphi_i^*(\mathbf{r})$, they constructed:

$$\sum_i^N \epsilon_i\varphi_i^*(\mathbf{r})\varphi_i(\mathbf{r}) = v_{eff}^{(LB)}(\mathbf{r})\sum_i^N \varphi_i^*(\mathbf{r})\varphi_i(\mathbf{r}) + \sum_i^N \varphi_i^*(\mathbf{r})(-\frac{1}{2}\nabla^2)\varphi_i(\mathbf{r}), \tag{2.25}$$

Where iteratively they construct potential as following:

$$v_{eff}^{p(LB)}(\mathbf{r}) = \frac{1}{\rho_{in}(\mathbf{r})}\sum_i^N \varphi_i^{p'*}(\mathbf{r})(-\frac{1}{2}\nabla^2)\varphi_i^{p'}(\mathbf{r}) + \sum_i^N \left|\varphi_i^{p'}(\mathbf{r})\right|^2, \tag{2.26}$$

Till they achieve convergence once following constraint is satisfied for a given threshold ϵ:

$$\max_i \left| 1 - \frac{\rho^{p'}(\mathbf{r})}{\rho_{in}(\mathbf{r})} \right| < \epsilon, \qquad (2.27)$$

Asymptotic behaviour of potential is omitted in their procedure by setting it to zero for $r \rightarrow \infty$. Another advantage of this procedure is that convergence limit is unique due to application of Hohenberg-Kohn theorem-Kohn energy functional on non interacting electron system. What could be considered as risk of this wildly used method is the fact that convergence is not highly guaranteed because while proceeding, some densities are not non-interacting v-representable.

In contrast with LB procedure which updates potential in each iteration and find out corresponding density, Kadantsev et al [105] for each iteration use the difference between iteratively obtained density and ρ_{in} Eq.2.28.

$$v_{eff}^{p+1}(\mathbf{r}) = v_{eff}^p(\mathbf{r}) + \alpha^p \left[\rho^p(\mathbf{r}) - \rho_0(\mathbf{r}) \right], \qquad (2.28)$$

Where $\rho_0(\mathbf{r})$ is fixed grand state density obtained as input density (target density) and α^p is minimisation parameter.

Colonna and Savin [32], used different technique to update potential based on the Lieb Legendre transform definition of density functional.

Zhao, Morrison and Parr (ZMP) [228], supposed an inversion method departing from grand state electron densities. From known grand state electron density $(\rho_{in}(\mathbf{r}))$ and via self-consistence calculation of KS equation, they obtain $v_{eff}(\mathbf{r})$ which is sum over external potential $v_0(\mathbf{r})$ and an additional potential $v_c(\mathbf{r})$, forcing ρ to be equal to $\rho_{in}(\mathbf{r})$. While looking for an effective potential resulting densities (corresponding to the solutions of KS equation) equal to grand state density, they introduced a global Lagrange multiplier λ, Eq. 2.29. This latest form of KS equation tends to Eq. 2.4 for $\lambda \rightarrow \infty$.

$$[-\frac{1}{2}\Delta + v_0(\mathbf{r}) + v_c^\lambda(\mathbf{r})]\varphi_i^\lambda(\mathbf{r}) = \varepsilon_i^\lambda \varphi_i^\lambda(\mathbf{r}), \qquad (2.29)$$

where $v_c^\lambda(\mathbf{r})$ is defined as:

$$v_c^\lambda(\mathbf{r}) = \lambda \int \frac{\rho(\mathbf{r}') - \rho_{in}(\mathbf{r}')}{|\mathbf{r}' - \mathbf{r}|} d\mathbf{r}', \qquad (2.30)$$

Out of this limit, the solution of newly constructed KS equation differs from the one raised up from KS equation without Lagrange multiplier. To satisfy

this expectation, they solve Eq.2.29 self-consistently for a series of specific λ which is extrapolated to $\lambda = \infty$.

Goodpaster *et al.* [62], accomplished ZMP procedure for six large finite vales of λ. Some other authors like Miller *et al.* improved the inversion procedures of non-additive potential construction's algorithm by mixing ZMP.

Wu and Yang [226, 222] applied numerically Levy CS and defined a functional $W_s[\Psi_s[v_{eff}^{(WY)}(\mathbf{r})], v_{eff}^{(WY)}(\mathbf{r})]$ of any N-electron single-determinant trial wavefunction Ψ_s whose orbitals $\{\varphi_i\}$ are eigenstates of its Lagrange multiplier function $v_{eff}^{(WY)}(\mathbf{r})$. For W_s to be stationary with respect to any variation of $v_{eff}^{(WY)}(\mathbf{r})$ they made following constraint condition on electron density:

$$\frac{\delta W_s[\Psi_s[v_{eff}^{(WY)}(\mathbf{r})], v_{eff}^{(WY)}(\mathbf{r})]}{\delta v_{eff}^{(WY)}(\mathbf{r})} = \rho(\mathbf{r}) - \rho_{in}(\mathbf{r}) = 0, \qquad (2.31)$$

They constructed $T_s[\rho_{in}]$ Eq. 2.33, from variational principle in terms of one-electron potential. Their effective potential respects an additional constraint (Eq.2.32).

The procedure is robust owing to the concavity of the functional $W_s[v_{eff}^{(WY)}] = W_s[\Psi_s[v_{eff}^{(WY)}], v_{eff}^{(WY)}]$:

$$\delta^2 W_s[\Psi_s[v_{eff}^{(WY)}(\mathbf{r})], v_{eff}^{(WY)}(\mathbf{r})] =$$
$$2\sum_i^{occ} \sum_a^{unocc} \frac{\left\langle \varphi_i \left| \delta v_{eff}^{(\hat{W}Y)} \right| \varphi_a \right\rangle \left\langle \varphi_a \left| \delta v_{eff}^{(\hat{W}Y)} \right| \varphi_i \right\rangle}{\epsilon_i - \epsilon_a} + const \leq 0, \qquad (2.32)$$

and the fact that the kinetic energy expressed as the functional of $v_{eff}^{(WY)}$ is maximal at the exact inverted potential:

$$T_s[\rho_{in}] = \max_{v_{eff}^{(WY)}(\mathbf{r})} W_s[\Psi_s[v_{eff}^{(WY)}(\mathbf{r})], v_{eff}^{(WY)}(\mathbf{r})], \qquad (2.33)$$

This latest constraint assures that the stationary point is maximum due to concavity of W_s.

The procedure introduced recently by Nafziger *et al.*[148] uses numerical solution of Kohn–Sham equations on a prolate-spheroidal real-space grid applicable for diatomic systems. In each grid point (j) and each orbital (i), the Kohn–Sham orbitals are constrained to satisfy (to some arbitrarily chosen tolerance) the constraint given in Eq.[2.34] associated with the Kohn–Sham equation, and the constraints imposing that orbitals are orthonormal and that the

sum of orbital densities yields $\rho_{in}(\mathbf{r})$. The target orbitals are obtained through direct minimization of the residuals representing each constraint.

$$residual_{i,j}^{KS} = (-\frac{1}{2}\nabla^2\phi_i)_j + v_{s,j}\phi_{i,j} - \epsilon_i\phi_{i,j} \qquad (2.34)$$

The above five procedures were (directly or on some modifications) used by several authors to construct the non-additive kinetic potential over-viewed in section 2.2.

2.3   Non-additive kinetic potential from inversion procedures

In this section, I overview literature reports concerning the construction of non-additive kinetic potential for a given arbitrary choice of a pair of densities (either $\rho_A(\mathbf{r})$ and ρ_B or $\rho_A(\mathbf{r})$ and $\rho_{tot}(\mathbf{r})$). Reports concerning the non-additive kinetic potentials obtained using inversion procedures keep appearing in the literature. The current situation traces its origin to five key publications. As early as in 2004, Zhou, Wang, and Carter, used the numerical inversion procedure to construct local pseudo-potentials [229]. The pairs $\rho_A(\mathbf{r})$ and $\rho_B(\mathbf{r})$ correspond to valence and core electrons. Shortly afterward, Roncero *et al.* [171] introduced an universal inversion procedure to construct $v_t^{\mathrm{NAD}}[\rho_A, \rho_{tot}](\mathbf{r})$ if $\rho_A(\mathbf{r})$ is mainly localized in a pre-defined part of space such as that occupied by one molecule. In 2009, Savin and Wesolowski used a model, for which both Kohn-Sham and KSCED equations can be solved analytically, and proposed an analytical construction of non-additive kinetic potential applicable for some particular choices of $\rho_A(\mathbf{r})$ and $\rho_{tot}(\mathbf{r})$: $\rho_{tot}(\mathbf{r})$ obtained from any exact or approximated Kohn-Sham equation and $\rho_A(\mathbf{r})$ being any one- or spin-compensated two electron density such that $\rho_{tot}(\mathbf{r}) \geq \rho_{tot}(\mathbf{r})$ [176]. In two publications, which appeared in 2010, one by Goodpaster *et al.* [61] and one by Fux *et al.* [55], two universally applicable methods based on numerically inverted potential were proposed. The methods introduced in these two papers were validated in variational calculations using the inverted potentials. Further developments are expected.

In the general case, two inversion procedures are needed to in order to het

non-additive kinetic potential from Eq. 2.6. Only for some model systems, both potentials in the right-hand-side of Eq. 2.6 can be expressed analytically. It is possible to reduce the burden of numerical inversion by generating one of the densities considered in Eq. 2.6 (ρ_{target}) using Kohn-Sham or KSCED calculations (even the ones which use approximated density functionals). The exact potential $v_s[\rho_{target}](\mathbf{r})$ is equal to the sum of the last three components of the operator given in the left-hand-side of Eq. 2.4). In practice, due to the use of finite basis sets such correspondence between the density and Kohn-Sham potentials not unique as demonstrated comprehensively in Ref. [38]. This problem can be circumvented by using the orbital density of the smoothest orbital (see latter in the present work). Concerning the admissible densities, it is worthwhile to underline the fundamental difference between implicit constructions of potentials approximating the exact $v_t^{\mathrm{NAD}}[\rho_A, \rho_{tot}](\mathbf{r})$ and explicit density functionals which affects the numerics of the inversion procedure. The former is defined only for admissible densities (the necessary condition is that $\rho_{tot}(\mathbf{r}) \geq \rho_A(\mathbf{r})$) whereas for the latter approximations might accept pairs of densities violating this condition. For the same reason of admissibility, using $\rho_A(\mathbf{r})$ and $\rho_{tot}(\mathbf{r})$ as independent variables in methods using inverted potentials might lead to additional numerical difficulties and/or additional approximations compared to the independent variables used in FDET ($\rho_A(\mathbf{r})$ and $\rho_B(\mathbf{r})$).

Inverted potential using analytical and numerical inversion procedures are discussed in separate sections below.

2.3.1 $v_t^{\mathrm{NAD}}[\rho_A, \rho_{tot}](\mathbf{r})$ from analytical inversion

Savin and Wesolowski [176, 215] used a simple model system, in which the key quantities defined in FDET: $v_t^{\mathrm{nad'}}[\rho_A, \rho_B](\mathbf{r})$, $T_s^{\mathrm{nad'}}[\rho_A, \rho_B]$, $v_s[\rho_A](\mathbf{r})$ and $v_s[\rho_A + \rho_B](\mathbf{r})$ could be constructed analytically for various $\rho_B(\mathbf{r})$ and a given $\rho_{tot}(\mathbf{r})$. The system consists of four spin-unpolarized non-interacting electrons in external potential $-Z/r$ (in atomic units). The two lowest energy solutions of the corresponding Kohn-Sham equation are the hydrogenic $1s$ and $2s$ functions. The ground-state density for such system is just:

$$\rho_o(\mathbf{r}) = 2|1s(\mathbf{r})|^2 + 2|2s(\mathbf{r})|^2 \tag{2.35}$$

This $\rho_o(\mathbf{r})$ was used as $\rho_{tot}(\mathbf{r})$ in the construction of the non-additive kinetic potential. The second term in Eq. 2.6 is just:

$$v_s[\rho_{tot}](\mathbf{r}) = v_s[\rho_o](\mathbf{r}) = -\frac{Z}{r} \qquad (2.36)$$

As far as $v_s[\rho_A](\mathbf{r})$ is concerned, it is just:

$$v_s[\rho_A](\mathbf{r}) = \frac{1}{2}\frac{\Delta\sqrt{\rho_A(\mathbf{r})}}{\sqrt{\rho_A(\mathbf{r})}} = \frac{1}{2}\frac{\Delta\sqrt{\rho_{tot}(\mathbf{r}) - \rho_B(\mathbf{r})}}{\sqrt{\rho_{tot}(\mathbf{r}) - \rho_B(\mathbf{r})}} + const \qquad (2.37)$$

for any pair of non-negative functions $\rho_A(\mathbf{r})$ and $\rho_B(\mathbf{r})$, such that:

$$\int_V \rho_A(\mathbf{r})d\mathbf{r} = 2 \qquad (2.38)$$

$$\rho_A(\mathbf{r}) + \rho_B(\mathbf{r}) = \rho_{tot}(\mathbf{r}). \qquad (2.39)$$

Eq. 2.6 leads to an analytical expression for the non-additive kinetic potential for any $\rho_{tot}(\mathbf{r})$ (which can be modified by changing Z) and $\rho_A(\mathbf{r})$ chosen arbitrarily to satisfy the conditions given in Eqs. 2.38 and 2.39. This potential reads:

$$v_t^{\text{NAD}}[\rho_A, \rho_{tot}](\mathbf{r}) = v_t^{\text{NAD}}[\rho_{tot} - \rho_B, \rho_{tot}](\mathbf{r}) = \frac{1}{2}\frac{\Delta\sqrt{\rho_{tot}(\mathbf{r}) - \rho_B(\mathbf{r})}}{\sqrt{\rho_{tot}(\mathbf{r}) - \rho_B(\mathbf{r})}} - \frac{Z}{r} + const \qquad (2.40)$$

This example was used to discuss the relation between the pseudopotential theory [168] and FDET. To this end, a series of densities $\rho_B(\mathbf{r})$ satisfying conditions given in Eq. 2.38 and approaching $2|1s(r)|^2$, i.e., the density of the electrons in the core shell, was used. The $v_t^{\text{nad'}}[\rho_A, \rho_B](\mathbf{r})$ was obtained from Eq. 2.6. By construction, addition of this potential to the Kohn-Sham potential results in the lowest energy orbital such that it yields the exact target density $\rho_o(\mathbf{r}) - \rho_B(\mathbf{r}$. At the limit of $\rho_B = 2|1s(r)|^2$, the exact total density can be obtained in two alternative ways. Either using the exact $v_t^{\text{nad'}}[\rho_A, \rho_B](\mathbf{r})$ in FDET or following the pseudopotential strategy. The latter consists of adding a non-local operator which projects out the $1s$ solution. This modification results in $2s$ being the lowest solution of such modified Kohn-Sham equation. In FDET, a local (multiplicative) potential is added to the Kohn-Sham potential and the lowest energy solution yields the same density as $2|2s|^2$. For $\rho_B(\mathbf{r})$ approaching $2|1s(r)|^2$, the embedded orbital obtained from FDET does not approach $2s$ but $|2s|$. FDET leads thus to the same correct total electron density without using on-local operators in a modified Kohn-Sham equation (see Figure 9.2.4 in Ref.

[215]). Concerning the relation between $v_t^{\mathrm{nad'}}[\rho_A, \rho_B](\mathbf{r})$ and pseudopotentials of the pseudopotential theory [168], I noticed that this issue, still is an object of current discussions in the literature. Recent work by Unsleber *et al.* [197], addresses this issue comprehensively in real chemical systems. The potential $v_t^{\mathrm{nad'}}[\rho_A, \rho_B](\mathbf{r})$ obtained from the numerical inversion is used for this purpose. In practical applications, using some semi-local functional $\tilde{v}_t^{\mathrm{nad'}}[\rho_A, \rho_B](\mathbf{r})$, addition of projection operators to the embedding potential might help to reduce the errors due to the used functional (see Refs. [184, 30, 188]). For exact $v_t^{\mathrm{nad'}}[\rho_A, \rho_B](\mathbf{r})$, such addition would result in counting twice the kinetic energy contributions to the total energy and to the potential. Neither the exact energy nor density can be obtained if both exact $v_t^{\mathrm{NAD}}[\rho_A, \rho_{tot}](\mathbf{r})$ and the projector are used.

The analytically solvable case of FDET used in Ref. [176], was also used to discuss the performance of various gradient-dependent approximations to $v_t^{\mathrm{nad'}}[\rho_A, \rho_B](\mathbf{r})$ [215]. The two canonic choices for a semi-local approximation for $T_s[\rho]$ to approximate $v_t^{\mathrm{nad'}}[\rho_A, \rho_B](\mathbf{r})$ as in Eq. 2.16 are:

$$T_s^{\mathrm{vW}}[\rho] = \int_V \frac{1}{8} \frac{|\nabla \rho|^2}{\rho^2} d\mathbf{r} \tag{2.41}$$

the von Weizsäcker functional [201], which is the exact functional for spin-compensated 2-electron systems. Or

$$T_s^{\mathrm{TF}}[\rho] = \int_V C^{\mathrm{TF}} \rho^{5/3} d\mathbf{r} \tag{2.42}$$

the Thomas-Fermi functional [192, 51] which is the exact functional in the case of homogeneous electron gas.

In either cases, the analytical form of the functional derivative is known and can be used in Eq. 2.16 to approximate $v_t^{\mathrm{nad'}}[\rho_A, \rho_B](\mathbf{r})$. Although $v_t^{\mathrm{nad'}}[\rho_A, \rho_B](\mathbf{r})$ obtained from the von Weizsäcker functional reflects some features of the exact functional, such as the large barrier if $\rho_A(\mathbf{r})$ approaches zero, it fails to yield reasonable target density. The density $\tilde{\rho}_A^{opt}(\mathbf{r})$ obtained in variational calculations using approximated non-additive kinetic potential differs qualitatively from the target density in each case [215]. As far as the performance of the Thomas-Fermi functional is concerned, the shape of $\tilde{v}_t^{\mathrm{nad'}}[\rho_A, \rho_B](\mathbf{r})$ does not resemble the exact potential at all. Interestingly, the $\tilde{\rho}_A^{opt}(\mathbf{r})$ obtained in variational calculations using this approximation were better than the ones obtained

using the von Weizsäcker approximation. The former leads to $\tilde{\rho}_A^{opt}(\mathbf{r})$, which collapses onto the $1s$ shell. The Thomas-Fermi approximation, on the other hand, leads to too repulsive $\tilde{v}_t^{\mathrm{nad'}}[\rho_A, \rho_B](\mathbf{r})$. In either cases, the accuracy of the non-additive kinetic potential and energy insufficient, making these approximations in practical simulations useless if the spacial overlap between $\rho_A(\mathbf{r})$ and $\rho_B(\mathbf{r})$ is strong. In particular, using semi-local approximations to $v_t^{\mathrm{nad'}}[\rho_A, \rho_B](\mathbf{r})$ instead of the atomic pseudopotentials does not seem to be a promising strategy if $\rho_A(\mathbf{r})$ and $\rho_B(\mathbf{r})$ correspond to core and valence electron densities. Other semi-local approximations to $v_t^{\mathrm{nad'}}[\rho_A, \rho_B](\mathbf{r})$ considered in Ref. [215] performed not much better than the Thomas-Fermi functional. These analyzes revealed also that the accuracy of the parent approximation to $T_s[\rho]$ does not correlate with that of the corresponding $v_t^{\mathrm{nad'}}[\rho_A, \rho_B](\mathbf{r})$. These results are in line with the results reported by Bernard *et al.* in Ref. [15].

The analytical inversion procedure used in these model studies is obviously not designed for practical applications because it can be made only for particular pairs of densities for $\rho_A(\mathbf{r})$ is a spin-compensated electrons two-electron density and if $v_s[\rho_{tot}](\mathbf{r})$ is known. A more general approach applicable for larger systems uses the fact that Kohn-Sham calculations for any external potential and for any approximate density functional for the exchange-correlation energy, yield the total effective potential in Kohn-Sham equation ($v^{KS}(\mathbf{r})$) and the ground-state electron density $\rho_o(\mathbf{r})$. In principle, therefore, partitioning $\rho_o(\mathbf{r})$ into two non-negative components, such that one of them $\rho_A(\mathbf{r})$ is a spin-compensated two-electron density, makes it possible to obtain $v_t^{\mathrm{nad'}}[\rho_A, \rho_B](\mathbf{r})$ without relying on the numerical inversion procedure - which as a numerical challenge for densities comprising more than two electrons. The exact (at the limit of complete basis set) $v_s[\rho_o](\mathbf{r})$ is nothing else as the Kohn-Sham potential, obtained at the end of the self-consistent procedure to solve Kohn-Sham equation. It is, therefore, available and can be used in Eq. 2.6.

$v_s[\rho_A](\mathbf{r})$, on the other hand, can be obtained analytically form Eq. 2.37. De Silva and Wesolowski explored this possibility and constructed $v_t^{\mathrm{nad'}}[\rho_A, \rho_B](\mathbf{r})$ for various partitioning of the ground-state electron densities for beryllium atom, He-Li$^+$ diatomic, and Be-H$_2$ and B$^+$-H$_2$ complexes [37]. In the construction of the potential, instead of the numerically available Kohn-Sham potential

needed for the second term in Eq. 2.6, it was obtained (up to a constant) from the lowest Kohn-Sham orbital density ($\rho_1(\mathbf{r}) = 2|\phi_1(\mathbf{r})|^2$) using analytic inversion always applicable for spin-compensated two-electron densities.

$$v_s[\rho_{tot}](\mathbf{r}) = v_s[\rho_1](\mathbf{r}) + const = \frac{1}{2}\frac{\Delta\sqrt{\rho_1(\mathbf{r})}}{\sqrt{\rho_1(\mathbf{r})}} + const' \qquad (2.43)$$

For such a case, the non-additive kinetic potential can be obtained for any N-electron system and any $\rho_B(\mathbf{r})$ such that:

$$\rho_{tot}(\mathbf{r}) \geq \rho_B(\mathbf{r}) \qquad \geq 0, \qquad (2.44)$$

and

$$\int_V \rho_B(\mathbf{r})d\mathbf{r} \;=\; N - 2 \qquad (2.45)$$

Eq. 2.6 leads to the following expression for the non-additive kinetic potential:

$$\begin{aligned}
v_t^{\text{NAD}}[\rho_A, \rho_{tot}](\mathbf{r}) &= v_t^{\text{NAD}}[\rho_{tot} - \rho_B, \rho_{tot}](\mathbf{r}) \\
&= \frac{1}{2}\frac{\Delta\sqrt{\rho_{tot}(\mathbf{r}) - \rho_B(\mathbf{r})}}{\sqrt{\rho_{tot}(\mathbf{r}) - \rho_B(\mathbf{r})}} - \frac{1}{2}\frac{\Delta\sqrt{\rho_1(\mathbf{r})}}{\sqrt{\rho_1(\mathbf{r})}} + const
\end{aligned} \qquad (2.46)$$

where $\rho_{tot}(\mathbf{r})$ and $\rho_1(\mathbf{r})$ are available numerically in any Kohn-Sham calculation.

The use of analytically inverted potential corresponding to the orbital density of the lowest energy Kohn-Sham orbital, instead of the explicit Kohn-Sham potential results in elimination of the numerical instability due to the effect of the use of the finite basis sets. The origin of this instability is the difference between the effective potential in Kohn-Sham equations at the end of the self-consistent procedure and the inverted potential corresponding to the ground-state density:

$$v_s[\rho_o^{opt(LCAO)}](\mathbf{r}) \neq v^{KS}(\mathbf{r}) \qquad (2.47)$$

discussed in detail in Ref. [38].

The inverted potential obtained from any of the orbital densities ($|\phi_1|^2$ in particular) using Eq. 2.43, is equal (up to a constant) to the potential in the left-hand-side of the above equation. This inequality is most relevant near the nuclei where the Kohn-Sham potential is singular. The character of the singularity, which might appear in the left-hand-side of Eq. 2.47, depends on the used atomic basis sets, whereas it behaves as $-1/r$ in the right-hand-side

for any basis set used. Far form the molecule, on the other hand, a similar mismatch can be expected in the asymptotic region far from the molecule. In the left-hand-side of Eq. 2.47 it is determined by the basis set whereas the behavior of the right-hand-side is determined by the ionisation energy.

The densities $\rho_B(\mathbf{r})$ for which the non-additive kinetic potential was constructed in Ref. [37] correspond to various linear combinations of Kohn-Sham orbital densities for diatomics and in small intermolecular complexes with four spin-compensated electrons using the following choices for $\rho_B(\mathbf{r})$:

$$\rho_B(\mathbf{r}) = 2\alpha|\phi_1|^2 + 2(1-\alpha)|\phi_2|^2 \tag{2.48}$$

Such choices of $\rho_B(\mathbf{r})$ guarantee the N-representability of $\rho_A(\mathbf{r})$ (but also its pure-state non-interacting v-representability) but result in non-negligible overlap between $\rho_A(\mathbf{r})$ and $\rho_B(\mathbf{r})$ due to the delocalisation of the Kohn-Sham orbitals. The approximate potential $v_t^{\mathrm{NAD}}[\rho_{tot} - \rho_B, \rho_{tot}](\mathbf{r})$ obtained from the von Weizsäcker functional and such choices for $\rho_B(\mathbf{r})$ reproduced some features of the exact $v_t^{\mathrm{nad'}}[\rho_A, \rho_B](\mathbf{r})$ better than other approximations. It remained rather unsatisfactory in other regions of space.

2.3.2 $v_t^{\mathbf{NAD}}[\rho_A, \rho_{tot}](\mathbf{r})$ from numerical inversion

Reports concerning the non-additive kinetic potentials obtained using numerical inversion procedures keep appearing in the literature. The current situation traces its origin to four publications. As early as Zhou, Wang, and Carter, used the numerical inversion procedure to construct local pseudo-potentials [229]. The pairs $\rho_A(\mathbf{r})$ and $\rho_B(\mathbf{r})$ correspond to valence and core electrons. Shortly afterward, Roncero *et al.*[9] introduced an universal inversion procedure to construct $v_t^{\mathrm{NAD}}[\rho_A, \rho_{tot}](\mathbf{r})$ if $\rho_A(\mathbf{r})$ is mainly localized in a predefined part of space such as that occupied by one molecule. In two publications, which appeared i, one by Goodpaster *et al.*[61] and one by Fux *et al.*[55],two universally applicable methods based on numerically

Methods reviewed in this section, concern $v_t^{\mathrm{NAD}}[\rho_A, \rho_{tot}](\mathbf{r})$ obtained for more general choices of the densities $\rho_A(\mathbf{r})$ and $\rho_{tot}(\mathbf{r})$, then the ones discussed in the previous section. They were developed mainly for practical simulations, in which $\rho_A(\mathbf{r})$ and $\rho_{tot}(\mathbf{r})$ are unknown. Compared to the analytically inverted

potentials, for which the unique correspondence between densities and potentials us built-in by construction, the numerically inverted potentials always involve additional approximations. In all procedures reviewed in this section, finite basis sets are used implying the inequality given in Eq. 2.47. The exact relations between $v_s[\rho]((\mathbf{r})$, $v_t^{\mathrm{NAD}}[\rho_A, \rho_{tot}](\mathbf{r})$, $\{[\phi_i[\rho_B]\}$ discussed in the previous sections do not hold for the Kohn-Sham potential, orbital energies, and orbitals. Regularization techniques are used to assure unique correspondence between potential and density. In some methods, additional constrains impose the N-representability of the density for which the inverted potential is constructed. Last but not least, pure-state non-interacting v-representability of the considered densities is always assumed. For these reasons, enforcing that the exact relations hold also for the considered densities in such procedures cannot be made in a controllable manner. The quality of the inverted potentials is validated based on errors in the density (and frequently also other observables such as energy) obtained using them in variational calculations. To this end, the considered quantities are compared to the corresponding targets such as the the total density obtained using the same method as the one used for isolated embedded species but applied to the whole system (see Ref. [61] for instance). Some of the reviewed methods were tested in this way showing their impressive accuracy. The obtained non-additive kinetic potentials provide valuable references for comparisons with potentials derived from explicit functionals.

Turning back to practical applications of numerically inverted potentials, an additional approximation is frequently made:

$$v_t^{\mathrm{NAD}}[\rho_A, \rho_{tot}](\mathbf{r}) \approx v_t^{\mathrm{NAD}}[\rho_A', \rho_{tot}'](\mathbf{r}) \qquad (2.49)$$

if the densities $\rho_A(\mathbf{r})$ and $\rho_{tot}(\mathbf{r})$ for which $v_t^{\mathrm{NAD}}[\rho_A, \rho_{tot}](\mathbf{r})$ is evaluated is different than the final density obtained from the optimised embedded wavefunction. (This approximation is also made in some methods using explicit functionals.) Solving the quantum-many body problem for the embedded wavefunction yielding $\rho_A(\mathbf{r})$, proceeds usually through an iterative procedure. Repeating the inversion (or evaluation of the explicit functionals) at each iteration would not be practical. If the potential and density are not fully consistent, the above approximation might lead to some residual error. Compared to the errors in potentials obtained from explicit approximations it is probably a minor effect.

Goodpaster *et al.* [61], constructed $v_t^{\mathrm{NAD}}[\rho_A, \rho_{tot}](\mathbf{r})$ using the Zhao-Morrison-Parr inversion procedure [228] for $\rho_{tot}(\mathbf{r})$ being the sum of two electron densities $\rho_A(\mathbf{r})$ and $\rho_B(\mathbf{r})$, each obtained from coupled KSCED equations. Such choice of the independent variables assures that all considered densities are N-representable. The first term in Eq. 2.16 was evaluated from Eq. 2.7 using the orbitals obtained in the inversion procedure. The second term could be obtained without involving the numerical inversion because the Kohn-Sham orbitals corresponding to $\rho_B(\mathbf{r})$ ($\{[\phi_i[\rho_B]\}$) are available if $\rho_B(\mathbf{r})$ are obtained in KSCED. The densities $\rho_A(\mathbf{r})$ and $\rho_B(\mathbf{r})$ were optimised using either inverted non-additive kinetic potential or semi-local explicit approximations to it. The soundness of the numerical inversion procedure was verified by comparing of the total density obtained from the coupled KSCEDs with the reference density of the whole system obtained from Kohn-Sham calculations. The results obtained for several three and four electron atomic systems demonstrated qualitative superiority of the inverted potential over the potentials derived from semi-local approximations. These results are in line with the ones demonstrated for model system used by Savin and Wesolowski discussed in the previous section. Inverted potentials led to significantly better ionisation energies than the ones obtained using semi-local approximations. In the subsequent work [62], the authors used the inverted potentials for Li^+-Be, $\mathrm{CH_3}$-$\mathrm{CH_3}$, and water dimer, i.e., for cases featuring both large and small overlaps between large and small $\rho_A(\mathbf{r})$-$\rho_B(\mathbf{r})$ overlaps. Excellent agreement between the Kohn-Sham densities and the ones obtained using inverted potential in coupled KSCED calculations was reported. For the water dimer, the total energies using semi-local approximations to $v_t^{\mathrm{NAD}}[\rho_A, \rho_{tot}](\mathbf{r})$ were slightly worse than the ones obtained using the inverted non-additive kinetic potential but their performance worsened systematically with the increase of the overlap. The authors refined the method targeting the whole embedding potential and not its non-additive kinetic potential only [63]. It was used in calculations based on Eq. 2.14 where $method_I$ used the interacting wavefunction (such approach was called "WFT-in-DFT embedding"). Wu-Yang inversion procedure [222] was used. The very good performance of the method was demonstrated for the total energies in the ethylene-propylene dimer and in the hexaaquaion(II) complex, as well as for low-high spin splitting

energy in open shel systems. Direct direct comparisons with the approximated density functionals were not made.

The method introduced by Fux *et al.* [55] provided also a strong numerical evidence that the inverted potentials overcome the flaws of semi-local explicit approximations for $v_t^{\mathrm{NAD}}[\rho_A, \rho_{tot}](\mathbf{r})$. Instead of building up the total density from subsystem components, as it is made in Ref. [61], the authors partitioned the Kohn-Sham density of the whole system as:

$$\rho_B(\mathbf{r}) = \sum_{i \in frozen-subsystemB} |\varphi_i^{LMO}(\mathbf{r})|^2 \qquad (2.50)$$

where $\varphi_i^{LMO}(\mathbf{r}$ are localized molecular orbitals. The Wu-Yang [222] inversion procedure was used to obtain $v_s[\rho_A](\mathbf{r})$.

The procedure was shown to be numerically robust. It leads to the total density closely resembling $\rho_{tot}(\mathbf{r})$ regardless the magnitude of the overlap between the densities in the subsystems: from small overlaps in the hydrogen-bonded complexes to large ones in covalently bonded subsystem such as C_2H_6. The latter molecule was represented as a sum of two species CH_3^+ and CH_3^- associated formally with $\rho_A(\mathbf{r})$ and $\rho_B(\mathbf{r})$. The corresponding optimised densities obtained using semi-local explicit approximations lead to qualitatively worse total density. Localisation of orbitals involved also a special treatment of locally negative spurious components of the total densities resulting from the localisation procedures in finite basis sets. Compared to the conventional calculations applying explicit semi-local approximations, the deviations from the target density was significantly smaller.

An improved inversion procedure of Fux *et al.* [55] was used by Unsleber *et al.*, [197] to demonstrate performance of the inverted potentials in an extremal case of partitioning the density of argon atom into core and valence components. Without non-local operators, the authors reached the target densities with impressive precision. The integrated module of the density difference was in the range of 10^{-6} electrons. The same method applied for ammonia dimer led to very good agreement between the sum of optimised subsystem densities and the target density from Kohn-Sham calculations for the whole system (the integrated density difference in the range of 10^{-3} electrons). Interestingly, the semi-local approximation to $v_t^{\mathrm{NAD}}[\rho_A, \rho_{tot}](\mathbf{r})$ introduced in Ref. [219] per-

formed not much worse leading tho the integrated density error in the range of 10^{-2} electrons.

Artiukhin et al [6] applied the inversion procedure by Fux *et al.* [55] in calculations of excitation energies obtained from the method combining FDET and LR-TDDFT [211] for several organic chromophores such as *cis*-hydroxyquinoline, 2-aminopyridine, acetophenone, in complex with small hydrogen bonded such as water or methanol. For numerical inversion, the improved procedure introduced by Jacob [99] was used. Excitation energies obtained using the inverted potential were systematically closer to the reference data obtained from conventional LR-TDDFT calculations for the whole complex, than the results using the tested semi-local approximations. It is worthwhile to notice that such uses of the inverted potential do not allow for incorporating the kinetic energy component to the response kernel in a straightforward manner because the inverted potential is not an explicit density functional. Such approximation corresponds to Eq. 2.49 because the potential in the right-hand-side of this equation is $\rho_A(\mathbf{r})$-independent and as such does not contribute to the response kernel.

In the literature discussed so far, the case where $\rho_A(\mathbf{r})$ and $\rho_B(\mathbf{r})$ were associated with core and valence electrons, were used as ultimate test cases for validations of numerical algorithm. A side product of such studies was a comprehensive demonstration that none of the considered semi-local approximations is applicable for such a case. A proper description of the embedding potential for such a case was the main target in the earlier work by Zhou *et al.* [229], who used numerical inversion to get local pseudopotential to be used for simulations of solids. The Wang-Parr procedure was used for numerical inversion [204]. Various properties of bulk Si and defects in Si (structure, electron density, total energy, transition pressure) obtained using the constructed local embedding potentials compared very well with their counterparts derived using conventional non-local pseudopotentials. The same construction of the embedding potential was subsequently used in simulations of CO on Cu(111) surface, in a method based in Eq. 2.14 where CO was considered as emebdded species and with the embedded wavefunction of the Configuration Interaction type [179]. Such calculations also invoke approximation given in Ref. 2.49.

Roncero et al, [171] proposed an inversion precedure based computational

method also using the approximation given in Eq. 2.49. As far of the densities at which the inverted potential is concerned, $\rho_{tot}(\mathbf{r})$ was obtained from conventional Kohn-Sham calculations whereas $\rho_A(\mathbf{r})$ was "carved out" from $\rho_A(\mathbf{r})$ in a way assuring that $\int_V \rho_A(\mathbf{r})$ is a desired integer number of electrons. Zhao-Morrison-Parr procedure [228] was used for numerical inversion. The inverted potential was used as the one-electron operator in MCSCF and MRCI calculations of embedded species. The method was tested on a model system of consisting of a chain of hydrogen atoms of which a subgroup was earmarked as "embedded part". The same technique was used to for a complex of H_2 interacting with a H_{10} chain, to demonstrate the adequacy of the method for description of van der Waals interactions. Compared to reference CI results for the whole systems, the used embedding method led to the indistinguishable interaction energy curves (or underestimated by less than 10% if a simple variant of the method was used) [172]. Further applications of the proposed method include a case of Br_2 in water clusters. This model system was used to investigate the performance of the proposed method if the electronic excitation in embedded species lead to a significant amount of charge transfer [173].

In summary, the numerical inversion methods were shown by many authors to overcome the flaws of simple semi-local approximations which are inadequate at large overlaps between $\rho_A(\mathbf{r})$ and $\rho_B(\mathbf{r})$. To our knowledge, the inverted potential at the small overlap limit was not investigated so far in detail. The next section attempts to fill this gap.

2.4 Supplementary results:Analytically inverted $v_t^{\mathbf{NAD}}[\rho_A, \rho_{tot}](\mathbf{r})$ at small $\rho_A(\mathbf{r}) - \rho_B(\mathbf{r})$ overlaps
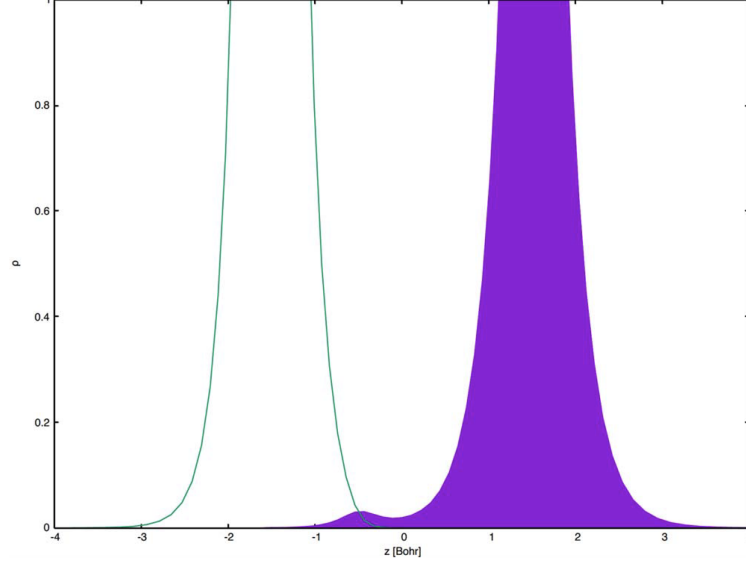
Figure 2.2: Kohn–Sham (PBE) electron density for LiHe$^+$ ($\rho_{tot}(\mathbf{r})$ shown in green) and $\rho_B(\mathbf{r})$ from Eq.[2.51] (shown as shaded area) in the overlap region. Li is situated at -1.5 Bohr and He at 1.5 Bohr. $\int_V \rho_A(\mathbf{r})\rho_B(\mathbf{r})d\mathbf{r} = 0.0292499$

The potentials constructed in this section were obtained following the procedure used previously in Ref. [37] for which Eqs. 2.43-2.46 apply. Two significant modifications of the procedure were made to adopt the calculations for small overlaps: a) $\rho_A(\mathbf{r})$ was generated using the Kohn-Sham equation with Perdew-Burke-Ernzerhof (PBE) exchange-correlation functional [165] was solved numerically for diatomic systems using the code DARSEC [135], $\rho_{tot}(\mathbf{r})$ was partitioned into $\rho_A(\mathbf{r})$ and $\rho_B(\mathbf{r})$ in such a way that the overlap was small. Numerical solver of Kohn-Sham equation assures that the exact relations given in Eqs. 2.43-2.46 are satisfied with arbitrary accuracy. The artificial numerical instabilities as the ones reported in Ref. [37] due to the use of finite basis sets are, therefore, avoided.

As far as the smallness of the overlap is concerned, the following $\rho_B(\mathbf{r})$ was used:

$$\rho_B(z) = f(z).\rho_{tot}(\mathbf{r}) \tag{2.51}$$

where

$$f(z) = \frac{1}{e^{\alpha z - \alpha' \kappa} + 1} \qquad (2.52)$$

the parameters α and α' were constrained to satisfy conditions given in Eqs. 2.44 and 2.45. All results shown in this section were obtained for densities $\rho_B(\mathbf{r})$ satisfying the condition given in Eq. 2.45 within $\pm 1 \times 10^{-5}$.

In contrast to the partitioning used in Ref. [37], the densities $\rho_A(\mathbf{r})$ and $\rho_B(\mathbf{r})$ are localized in different regions of space with a minimal overlap region between atoms. The amount of the overlap can be varied by varying the interatomic distance and/or varying the parameters α and α' constrained to satisfy Eq. 2.45 with arbitrary accuracy.

The numerical solver of Kohn-Sham equation assures that the considered potentials are not affected by the used basis set (compare the asymptotic behavior of the inverted potentials for the same system shown in Figure 2 of Ref. [37]. The symmetric grid comprises 2107 points and the the boundary sphere radius is set at 14 bohr.

Figure 2.3 shows the analytically inverted potentials obtained from Eq. 2.46 together with the corresponding density differences $\rho_A(\mathbf{r}) - \rho_1(\mathbf{r})$ for three interatomic distances. We note that the exact potential $v_t^{\text{nad'}}[\rho_A, \rho_B](\mathbf{r})$ is relatively smooth in the overlap region compared to a sharp spike near Li and a narrow well near He. $\rho_A(\mathbf{r}) - \rho_1(\mathbf{r})$, which is the change of the density due to $v_t^{\text{NAD}}[\rho_A, \rho_B](\mathbf{r})$, behaves corresponding to this potential. Without $v_t^{\text{nad'}}[\rho_A, \rho_B](\mathbf{r})$ the lowest energy solution of the Kohn-Sham equation is ϕ_1 which is localized mainly near Li. $v_t^{\text{nad'}}[\rho_A, \rho_B](\mathbf{r})$ is repulsive near Li. As a result, the lowest energy solution of KSCED in which the effective potential contains the exact $v_t^{\text{nad'}}[\rho_A, \rho_B](\mathbf{r})$, does not collapse on Li. The attractive well near He adds up to this effect. These behavior does not change with increased interatomic distance.

A striking feature of $v_t^{\text{nad'}}[\rho_A, \rho_B](\mathbf{r})$ is that it is almost flat in the overlap region. It varies the most where $\rho_A(\mathbf{r})$ and $\rho_B(\mathbf{r})$ is negligible! We underline this feature of $v_t^{\text{nad'}}[\rho_A, \rho_B](\mathbf{r})$ in view of attempts to approximate $v_t^{\text{nad'}}[\rho_A, \rho_B](\mathbf{r})$ by means of explicit density functionals. Only the overlap region contributes to $T_s^{\text{nad'}}[\rho_A, \rho_B]$ if this functional is approximated by means of a semi-local density functional. At zero overlap such contributions disappear. The errors

in total energy due $\tilde{T}_s^{nad(semi-local)'}[\rho_A, \rho_B]$ and in density obtained using the corresponding $\tilde{v}_t^{nad(semi-local)'}[\rho_A, \rho_B](\mathbf{r})$ cannot be expected to be related. The contributions to these functionals comes from different regions. We note also that semi-local approximations to $v_t^{\mathrm{nad'}}[\rho_A, \rho_B](\mathbf{r})$ are doomed to fail in reproducing the exact functionals if $\rho_A(\mathbf{r})$ disappears (near Li in our case). This probably is not very important flaw of semi-local approximations in practice because it is relatively easy to force $\rho_A(\mathbf{r})$ to avoid certain regions in space it is known *a priory*. This is commonly made in multi-level simulations simulations, by localizing the basis sets in a predefined region in space (such as the embedded molecule - see the analyses in Ref. [208]). Alternatively, it can be achieved by forcing the embedding potential to disappear in certain regions of space (see the correction to the embedding potential proposed in Ref. [103]) or adding an *ad hoc* fixed repulsive component to the embedding potential where it is needed (see Ref. [122]). The attractive well in $v_t^{\mathrm{nad'}}[\rho_A, \rho_B](\mathbf{r})$ near He reflected also in $\tilde{v}_t^{nad(weiz)'}[\rho_A, \rho_B](\mathbf{r})$ (see Figure 2.4) is a less general feature and reflects the fact that $\rho_A(\mathbf{r})$ is a two-electron density in this example.
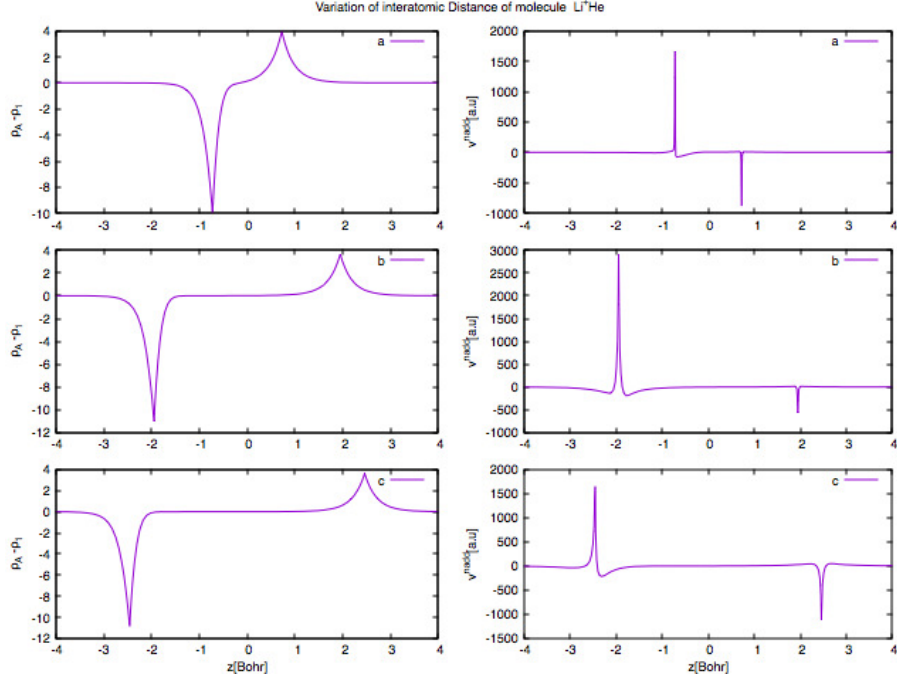
Figure 2.3: The analytically inverted potentials $v_t^{\text{nad'}}[\rho_A, \rho_B](\mathbf{r})$ obtained from Eq. 2.46 at various Li-He distances (right column) and the corresponding density difference $\rho_A(\mathbf{r}) - \rho_1(\mathbf{r})$ (left column): a) top: d(Li-He)=0.944863 bohr $\int_V \rho_A(\mathbf{r})\rho_B(\mathbf{r}d\mathbf{r} = 0.357595$, b) middle: d(Li-He)=3.897687 bohr $\int_V \rho_A(\mathbf{r})\rho_B(\mathbf{r}d\mathbf{r} = 0.0000311497$, c) bottom: d(Li-He)=4.917687 bohr $\int_V \rho_A(\mathbf{r})\rho_B(\mathbf{r}d\mathbf{r} = 4.8 \times 10^{-7}$.

Approximated potentials derived from von Weizsäcker or Thomas-Fermi density functionals for $T_s[\rho]$: $\tilde{v}_t^{nad(weiz)'}[\rho_A, \rho_B](\mathbf{r})$ and $\tilde{v}_t^{nad(TF)'}[\rho_A, \rho_B](\mathbf{r})$ only partially reflect the features of the corresponding $v_t^{\text{nad'}}[\rho_A, \rho_B](\mathbf{r})$ (see Figure 2.4).
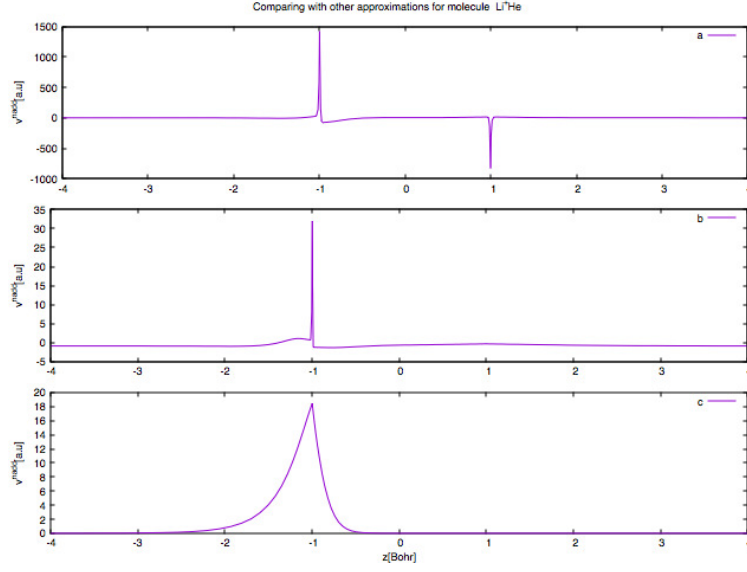
Figure 2.4: Analytically inverted potential $v_t^{\text{nad'}}[\rho_A, \rho_B](\mathbf{r})$ (top) and the approximated potentials $\tilde{v}_t^{nad(weiz)'}[\rho_A, \rho_B](\mathbf{r})$ (middle) $\tilde{v}_t^{nad(TF)'}[\rho_A, \rho_B](\mathbf{r})$ (bottom). All functionals are evaluated for the same pair of densities. Li is situated at -1 bohr and He at 1 bohr.

Figure 2.5 shows the same tendencies concerning the exact potential and its approximated counterparts in other four-electron systems.
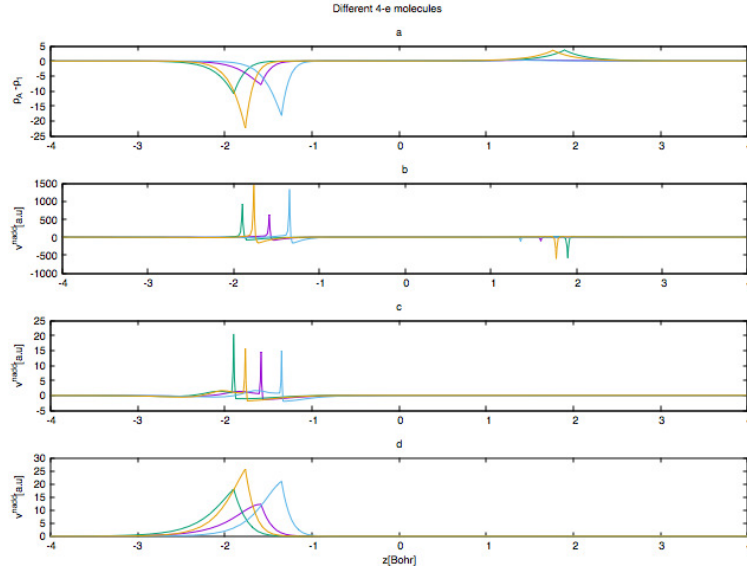
Figure 2.5: (a) Density difference $\rho_A(\mathbf{r}) - \rho_1(\mathbf{r})$, (b) analytically inverted potential $v_t^{\text{nad'}}[\rho_A, \rho_B](\mathbf{r})$, (c) $\tilde{v}_t^{nad(weiz)'}[\rho_A, \rho_B](\mathbf{r})$, (d) $\tilde{v}_t^{nad(TF)'}[\rho_A, \rho_B](\mathbf{r})$, in several four-electron diatomic molecules: LiHe (green), BeHe (orange), LiH (violet), and BeH (blue).

2.5   Conclusions and Outlook

The non-additive kinetic potential is a functional of a pair of electron densities $\rho_A(\mathbf{r})$ and $\rho_{tot}(\mathbf{r})$, i.e., up to constant it is uniquely determined by this pair. In numerical simulations, this functional is usually approximated by means of explicit semi-local density functionals. An alternative strategy uses implicit functionals which involve solving the "inverted Kohn-Sham problem" has been recently explored in several research groups. The construction of implicit potentials is based on the constrained search as formulated by Levy in his seminal paper *Electron densities in search of their Hamiltonians* [127]. The potentials used from this strategy were shown comprehensively to perform qualitatively better than explicit approximations in the case where subsystem associated with $\rho_A(\mathbf{r})$ is covalently bounded to its environment or if $\rho_A(\mathbf{r})$ represents core electrons. In such cases, the overlap between $\rho_A(\mathbf{r})$ and $\rho_{tot}(\mathbf{r}) - \rho_A(\mathbf{r})$ is large. To our knowledge, no semi-local approximation to the non-additive kinetic potential exists which could be applied for such cases. The results reported by various authors show comprehensively that the numerical inversion is the method of choice at small overlaps even if the inversion involves additional approximations. Moreover, even for small overlaps, the numerically inverted potentials perform usually slightly better than the explicit approximations.

Several authors constructed very accurate inverted potentials using either analytical inversion techniques such as the analytical inversion for some model choice of $\rho_A(\mathbf{r})$ and $\rho_{tot}(\mathbf{r})$ or inversion techniques especially designed for this purpose. Potentials obtained in this way might serve as guidelines in construction of explicit approximations. They were used to identify the origin of failures of existing semi-local approximations in the strongly overlapping case.

The overview of these developments made in the present work is supplemented by examples of analytically inverted non-additive kinetic potentials and their semi-local counterparts at small overlaps. Inverted potentials have not been constructed so far for such cases. Cases, where the overlap is small (molecules non-covalently bound to their environment), belong to the domain of most successful applications of explicit functionals. The analytically inverted potentials were obtained using especially designed procedure, which involves numerical solver of Kohn-Sham equation to assure that the densities and or-

bitals satisfy the exact relations with arbitrary accuracy. The procedure can be used to generate the reference potentials for a controllable amount of the overlap. Comparisons with reference potentials indicate that there is still a room of improvement for semi-local functionals at small overlaps.

2.6 Re-production of the Fig. 3 in the publication IJQC (erratum)

I have been suspicious about the previous results of the $v^{\mathrm{NAD}}[\rho_A, \rho_{tot}](\mathbf{r})$ representing the cusp-like singularities at the position of the nuclei. The properties of the input partitioned density, together with the fact that the analytically inverted potential from an orbital density or the density that integrates to one or two made me to expect a cusp-less $v^{\mathrm{NAD}}[\rho_A, \rho_{tot}](\mathbf{r})$ at the end. I kept investigating more in the numerical implementations also developed more theoretical and analytical arguments to clarify the correct shape of the potential. Those approaches are provided in chapter 3.

In the publication I reported the results in $[a.u]$ however DARSEC produces the realisable outputs in Ry. The analytically inverted $v^{\mathrm{NAD}}[\rho_A, \rho_{tot}](\mathbf{r})$ reported in section.2.4 are provided from:

$$v^{\mathrm{NAD}}[\rho_A, \rho_{tot}](\mathbf{r}) = v_s[\rho_A](\mathbf{r}) - v_s[\rho_1](\mathbf{r}) \qquad (2.53)$$

where $v_s[\rho_i](\mathbf{r})$ for $i = 1, A$ are calculated from Eq.[2.37]. As the results are in Ry, I had to divide the values by 2 to obtain the energy in the atomic unit. In the code I added a factor $1/2$ to the terms of the $v^{\mathrm{NAD}}[\rho_A, \rho_{tot}](\mathbf{r})$ and surprisingly one of the terms in the equation were missing this factor and remained hidden from our eyes at the time of the publication. Later on, I fixed the numerical problem in the code and re-calculated the systems with the same properties as it was reported in our publication and inserted the correct results here (Fig.[2.6]).

The new results will be sent to the journal for the erratum purpose.

The caption of the Fig.[2.6] is the same as the one in Fig.3 of the published review.
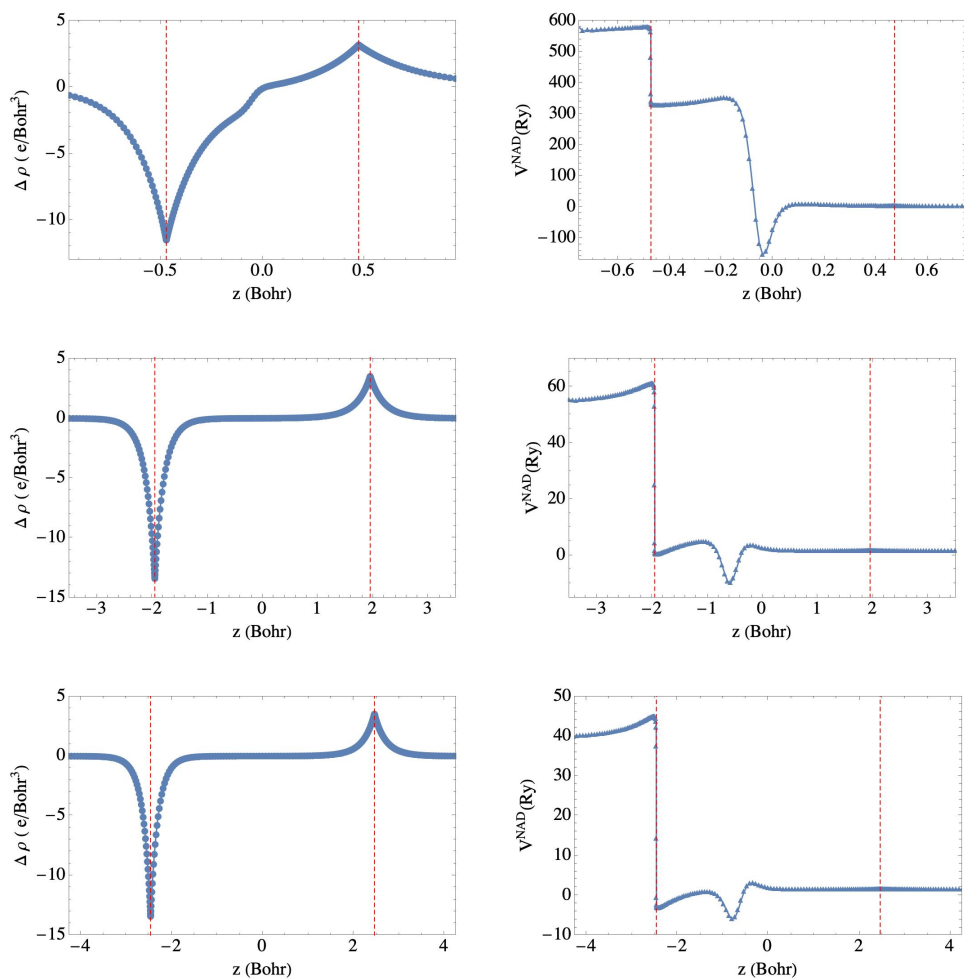
Figure 2.6: ..., (left column): **top**: d(Li-He)=0.944863 Bohr $\int_v \rho_A(\mathbf{r})\rho_B(\mathbf{r})d\mathbf{r} = 2.17 \times 10^{-2}$, : **middle**: d(Li-He)=3.897687 Bohr $\int_v \rho_A(\mathbf{r})\rho_B(\mathbf{r})d\mathbf{r} = 6.74 \times 10^{-5}$, : **Bottom**: d(Li-He)=4.917687 Bohr $\int_v \rho_A(\mathbf{r})\rho_B(\mathbf{r})d\mathbf{r} = 1.58 \times 10^{-5}$.

The published plot is repeated here (Fig.[2.7]) for easier comparison.
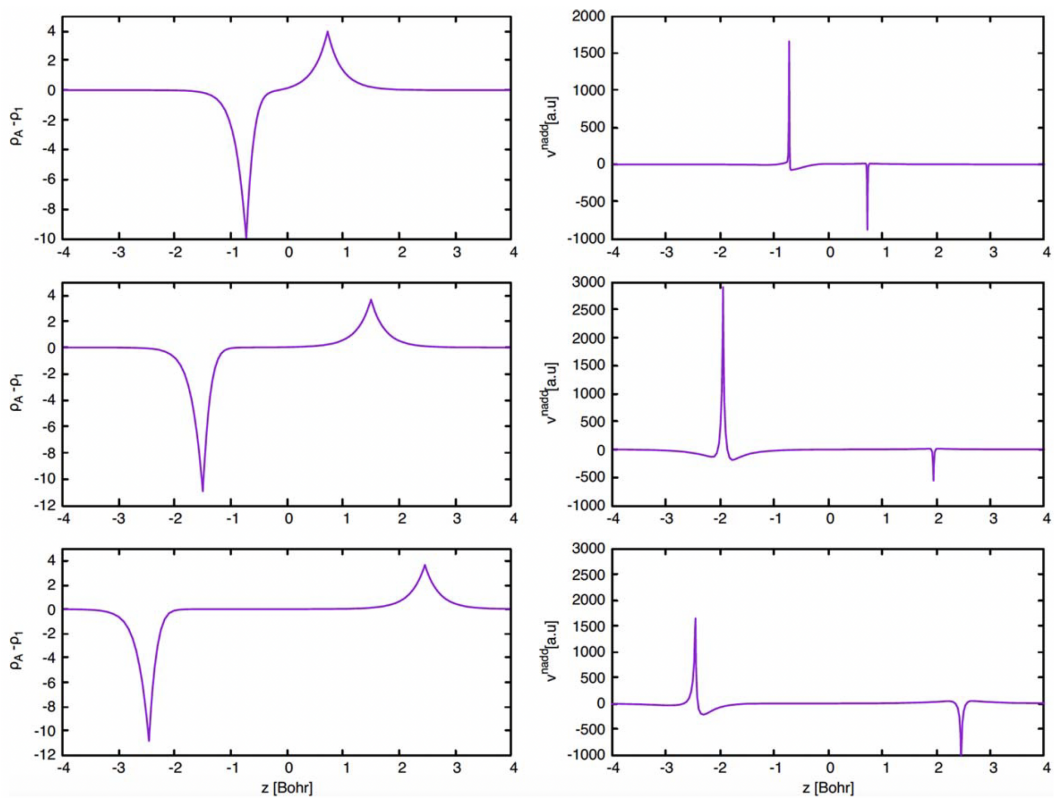
Figure 2.7: Fig.3 in IJQC

The Figure 3 of *M. Banafsheh, T. A. Wesolowski, Int. J. Quant. Chem. 118 (2018): e25410* is reproduced with the debugged numerical implementation.

Chapter 3

Nuclear Cusp and singularities in Non-Additive Kinetic Potential bi-Functional from Analytical Inversion

3.1   Abstract

Non-additive kinetic potential bi-functional that is the key issue of embedding DFT theory, Partition DFT and almost all ab-initio Non-additive kinetic potential functional remained unknown due to available computational tools so it has been approximated. The cusps that appeared in the results from both numerical and analytical inversion of the potential remained suspicious. Some accepted them as numerical artifacts, and others tried to find an appropriate physical interpretation. In this work, I prove the non-existence of the cusps mathematically in non-additive kinetic potential bi-functional for a class of density partitioning and prove our argument with results of analytically inverted non-additive kinetic potential bi-functional from a pair of densities for some model systems in real space from a given ground state density. I explain the partitioning class for which the inverted potential is expected to include singularity at the vicinity of the nuclei.

3.2 Introduction

When the precise descriptions of large and complex systems are not affordable computationally, I often partition them into smaller subsystems. The investigation procedure of main quantities of interest frequently takes place in a localised region of the whole system. Such a region can be solved separately, with a higher level of theories that usually are computationally costly. In contrast, the rest of the system can be solved with computationally cheaper methods.

Frozen-density embedding theory (FDET) method [217, 213, 166, 178, 35] and Partitioning DFT (PDFT) methods [146] are appealing methods for calculating the electronic structure of complex molecular systems. They allow in a formally exact framework, the total electronic density to be divided into subsystem densities that can be separately calculated.

In calculations based on system-fragmenting methods within the Kohn-Sham DFT framework, the relation between the potential of two subsystems is investigated by so-called non-additive kinetic potential functional v^{NAD}.

This quantity plays a critical role in calculating correct ground state density. In the overlap regions between partitioned densities, v^{NAD} is the quantity that ensures that the solution of the entire system is orthonormal. Also, the exact v^{NAD} is supposed to predict the discontinuity at integer particle numbers. The latter makes v^{NAD} applicable in search for delocalised electronic charge-density. Delocalised charge density is the critical issue of intermolecular charge transfer, a ground-state phenomenon. The fact that the charge transfer itself was also suggested for excitation studies [144] makes non-additive potential widely demanded for different purposes.

Non-additive kinetic potential functional has been approximated until now for real systems. The approximations within DFT are evaluated by their capacity in providing the well-known properties of the ground-sate with high accuracy. The cusps relations (known as Kato Theorem) [185, 108, 151, 155] as an important property of accurately calculated ground-state density. The importance of the cusps of the density, initially revealed by Wilson [17], is that it can determine the nuclei's location and atomic number. Despite interesting results of v^{NAD} from both numerical and analytical inversion, works have not

been published arguing the existence of nuclear cusps . The following questions have remained unanswered in the past: " Does v^{NAD} contain the singularities at the vicinity of the nuclei? ", " Does v^{NAD} represent any other discontinuities? If yes, how are they related to the ground-state charge density?" In this work, I theoretically prove the nonexistence of singularity on analytically inverted v^{NAD} at the vicinity of the nuclei from a class of pair of densities and I show the related numerical results for a few model systems. I discuss the cases with the nuclear singularity expected to appear on the potential to ensure the cusp condition of the ground state density.

In the coming section, I recall the analytical inversion of Kohn-Sham potential followed by the construction of non-additive potential bi-functional from analytical inversion. The setup for a specific class of densities for which the inverted potential is free of singularities will be explained in the same section, and we'll conclude the cases for which the singularities at the vicinity of the nuclei are expected. In the following section to this latter, I provide the numerical preparations, and in the result section, for some model systems, I justify the theories and compare our results with ones from von Weizsäcker kinetic potential functional [200].

The complementary calculations are given in the appendices.

3.3   Theory

The non-additive kinetic bi-functional is defined by the pair of densities provided by total ground state density $\rho_{tot}(\mathbf{r})$, and is denoted by $v^{\mathrm{NAD}}[\rho_A, \rho_{tot}](\mathbf{r})$ where $\rho_A(\mathbf{r})$ is one of the possible partitions of the total density. v^{NAD} in fact is given by the functional derivative of the non-additive kinetic-energy bi-functional:

$$
\begin{aligned}
v_t^{\mathrm{NAD}}[\rho_B, \rho_{tot}](\mathbf{r}) &= \left.\frac{\delta T_s^{\mathrm{NAD}}[\rho, \rho_{tot}](\mathbf{r})}{\delta \rho(\mathbf{r})}\right|_{\rho=\rho_B} \\
&= \frac{\delta T_s[\rho_{tot}](\mathbf{r})}{\delta \rho_{tot}(\mathbf{r})} - \frac{\delta T_s[\rho_B](\mathbf{r})}{\delta \rho_B(\mathbf{r})}
\end{aligned}
\tag{3.1}
$$

where ρ_B and $\rho_A = \rho_{tot} - \rho_B$ have different qualities, depending on how they are partitioned. In numerical approaches $T_s^{\mathrm{NAD}}[\rho, \rho_{tot}]$ is defined in the

constrained search procedure [127]. The exact form of $\frac{\delta T_s[\rho_i]}{\delta \rho_i}$ is not known , so it requires to be approximated. Within the Kohn-Sham formulation of Density Functional Theory (KS-DFT), the explicit semi-local approximations to the functional v^{NAD} in numerical simulations are doomed to fail [9]. Such failures prompted the interest in the implicit functionals for the non-additive kinetic potential constructed by means of numerical inversion (of Kohn-Sham equation) procedures. Unfortunately, numerical inversion of Kohn-Sham equation is an ill-defined problem if finite basis sets are used. It results in numerical instabilities for multiple solutions. A more recent analysis of the non-uniqueness of the numerical inversion, and an approach to deal with it, can be found in the work by Jacob [103]. Banafsheh and Wesolowski published a complete review of the construction of v^{NAD} within approximations and inversion procedures [9].

Only for some model systems, v^{NAD} can be expressed analytically [214]. The systems have to satisfy the constraints of analytical inversion:

3.3.1 One-Orbital Formula

A Kohn-Sham system is described by a set of orbitals, ϕ_i, that obey the Kohn-Sham equations,

$$\left[-\frac{1}{2} \nabla^2 + v_{KS}(\mathbf{r}) \right] \phi_i(\mathbf{r}) = \epsilon_i \phi_i(\mathbf{r}) \tag{3.2}$$

where v_{KS} is the Kohn-Sham potential. The density is then,

$$\rho(\mathbf{r}) := \sum_i f_i |\phi_i(\mathbf{r})|^2 \tag{3.3}$$

where f_i is the occupation factor of orbital, ϕ_i. In order to apply one-orbital formula, I shall restrict $0 \leq f_i \leq 2$ but not require it to be integer.

For one electron or two spin-compensated electrons where the solution is real and positive (means $\phi_i(\mathbf{r}) = \sqrt{\rho_i(\mathbf{r})}$), Eq. (3.2) could be rearranged as:

$$v_{KS}(\mathbf{r}) = \frac{\nabla^2 \phi_i(\mathbf{r})}{2\phi_i(\mathbf{r})} + \epsilon_i \tag{3.4}$$

Thus the Kohn-Sham potential reads:

$$v_{KS}(\mathbf{r}) = \frac{\nabla^2 \sqrt{\rho_i(\mathbf{r})}}{2\sqrt{\rho_i(\mathbf{r})}} + \epsilon_i \qquad (3.5)$$

where i defines is the orbital index. We define analytical inversion of the density as:

$$v_s[\rho_i](\mathbf{r}) := \frac{\nabla^2 \sqrt{\rho_i(\mathbf{r})}}{2\sqrt{\rho_i(\mathbf{r})}} \qquad (3.6)$$

So that in one orbital formula case:

$$v_s[\rho_i](\mathbf{r}) = v_{KS}(\mathbf{r}) + \epsilon_i \qquad (3.7)$$

In the context of Eq.[2.46] for finite molecular systems, it reads:

$$v_t[\rho](\mathbf{r}) := \frac{\delta T_s[\rho]}{\delta \rho(\mathbf{r})} = -v_{KS}[\rho](\mathbf{r}) = -v_s[\rho](\mathbf{r}) \qquad (3.8)$$

If the exact $T_s[\rho](\mathbf{r})$ is known (in Eq.[2.46]), then $v_s[\rho](\mathbf{r}) = \frac{\partial T_s}{\partial \rho}$. in terms of the Kohn-Sham potential,

$$v_{KS}[\rho](\mathbf{r}) := v_{ext}(\mathbf{r}) + v_{Hxc}[\rho](\mathbf{r}), \qquad (3.9)$$

where $v_{Hxc}[\rho](\mathbf{r}) := \frac{\delta E_{Hxc}}{\delta \rho}$ is the Hartree, exchange and correlation (Hxc) potential obtained exactly or via an approximation.

3.3.2 Cusps, Singularities and the non-additive potential

Let us consider very generally the relationship between cusps in densities, and singularities in potentials – I shall define both below. Before beginning, we will impose two restrictions on densities and potentials that will be assumed in the remainder of this work: 1) densities will be obtained from and yield singularity-free Hxc potentials; 2) the states considered will always have at least one $1s$ orbital at each nucleus, which dominates the density near each nucleus. Both restrictions apply to the exact ground state density and potentials. They ensure (see conclusions of [137]) that cusp conditions [108, 18, 155, 151, 137] hold for cusps in densities, and singularities in both external and approximated Kohn-Sham potentials.

Our goal in this section will be to explore how cusps in densities manifest as singularities in non-additive potentials. Since this varies depending on the nature of densities, I will first derive a general rule; and then apply it to examples from the literature and the work done here.

A nuclear cusp means that the angularly averaged density obeys, $\lim_{\mathbf{r}\to\mathbf{R}_N} |\nabla\rho| = 2Z_N\rho$; while a nuclear singularity means that the potential obeys, $\lim_{\mathbf{r}\to\mathbf{R}_N} r_N v \to Z$, where $\mathbf{r}_N = \mathbf{r} - \mathbf{R}_N$. We will use a short-hand notation to describe cusps via $e^{-2Z_N|\mathbf{r}-\mathbf{R}_N|}$ and singularities via $\frac{-Z_N}{|\mathbf{r}-\mathbf{R}_N|}$. Each cusp and singularity is uniquely described by $(\mathbf{R}_N, Z_N)$ for some set of nuclei, $N \in \mathcal{N}$. Sums over N without extra clarification imply $N \in \mathcal{N}$.

Note, the notation covers behaviour near each nucleus, but does not describe every aspect of the system. The true density and potentials may be written as,

$$\rho(\mathbf{r}) := \sum_N \rho_{0,N} e^{-2Z_N|\mathbf{r}-\mathbf{R}_N|} + \rho_{\text{smooth}}(\mathbf{r}) \;, \tag{3.10}$$

$$v(\mathbf{r}) := \sum N \frac{-Z_N}{|\mathbf{r}-\mathbf{R}_N|} + v_{\text{non-sing}}(\mathbf{r}) \;. \tag{3.11}$$

Here, $\rho_{\text{smooth}}(\mathbf{r})$ has no cusps and is zero at each nucleus. $v_{\text{non-sing}}(\mathbf{r})$ has no singularities, but few other restrictions. Both functions are discussed in a little more depth in Appendix A.

All subsequent results follow from three theorems:

Theorem 1: The density of any electronic system has a cusp of form $\rho(\mathbf{r}) \approx \rho_{0,N} e^{-2Z_N|\mathbf{r}-\mathbf{R}_N|}$ near every singularity in the external or KS potential, $v_{\text{ext}}(\mathbf{r}) \approx v_s(\mathbf{r}) \approx \frac{-Z_N}{|\mathbf{r}-\mathbf{R}_N|}$.

Proof: A more general case is a long-known result. [108, 137] Here, I used that $\rho_{0,N}$ is non-zero, consistent with our second restriction of having a $1s$ orbital, to narrow it down to systems of relevance. Our first restriction extends it to approximate Kohn-Sham systems.

Theorem 2: If the density of an electronic system has a cusp of form $\rho(\mathbf{r}) \approx \rho_{0,N} e^{-|\mathbf{r}-\mathbf{R}_N|}$, then the external and Kohn-Sham potentials have singularities, $v_{\text{ext}}(\mathbf{r}) \approx v_s(\mathbf{r}) \approx \frac{Z_N}{-|\mathbf{r}-\mathbf{R}_N|}$.

Proof: The result for interacting systems follows from Theorem 1 and the Hohenberg-Kohn theorem. [93, 113] The KS result is easily shown for up to two

electrons, by using the von Weizsäcker potential,

$$v^{vW}[\rho](\mathbf{r}) := \frac{\nabla^2\sqrt{\rho(\mathbf{r})}}{2\sqrt{\rho(\mathbf{r})}} = \frac{\nabla^2\rho(\mathbf{r})}{4\rho(\mathbf{r})} - \frac{|\nabla\rho(\mathbf{r})|^2}{8\rho^2(\mathbf{r})} \ , \tag{3.12}$$

and properties of the Laplacian and Gradient. Since, $v_s = v_{vW} + C$, for some constant, C, the singularities are inherited by v_s. For more than two electrons one may use the results of (Appendix C). This extends the known result for exact potentials [137] to well-behaved approximations consistent with our restrictions.

Theorem 3: There are thus one-to-one mapping between cusps in the density and singularities in the potential. That is,

$$\rho(\mathbf{r}) \approx \sum_N \rho_{0,N} e^{-|\mathbf{r}-\mathbf{R}_N|} \longleftrightarrow \sum_N \frac{-Z_N}{|\mathbf{r}-\mathbf{R}_N|} \approx v \tag{3.13}$$

up to smooth terms. This includes the important special case of no singularities leading to no cusps, which relies on restriction 1 for approximations to DFT.

Proof: This follows directly from the previous two theorems and a recognition that singularities and cusps near a nucleus at $\mathbf{R}_N$ are smooth functions near a different nucleus at $\mathbf{R}_M \neq \mathbf{R}_N$.

These theorems let us understand how the non-additive potential in Eq.[2.46] behaves in the vicinity of a nucleus. The most general result is that the set of singularities in

$$v_t^{\text{NAD}}[\rho_A, \rho_B] = v_s[\rho_A] - v_s[\rho_A + \rho_B]$$

(from Eq. (2.46) and $v_s = -\frac{\delta T_s}{\delta \rho}$) is equal to the set of singularities from ρ_A minus the set of singularities from $\rho = \rho_A + \rho_B$, which follows from Theorem 3.

More precisely, if ρ_A has a set of cusps $\mathcal{C}^A := \{(\mathbf{R}_N^A, Z_N^A)\}_{N\in\mathcal{N}^A}$, ρ_B has a set of cusps $\mathcal{C}^B := \{(\mathbf{R}_N^B, Z_N^B)\}_{N\in\mathcal{N}^B}$, and $\rho = \rho_A + \rho_B$ has a set of cusps $\mathcal{C} := \{(\mathbf{R}_N, Z_N)\}_{N\in\mathcal{N}}$ then the singular part of the non-additive potential is,

$$v_{\text{sing}}^{\text{NAD}}(\mathbf{r}) = \sum_{N\in\mathcal{N}^A} \frac{-Z_N^A}{|\mathbf{r}-\mathbf{R}_N^A|} + \sum_{N\in\mathcal{N}} \frac{Z_N}{|\mathbf{r}-\mathbf{R}_N|} \ , \tag{3.14}$$

Although I treated it as independent above, it follows from $\rho = \rho_A + \rho_B$ that $\mathcal{C}$ can be obtained from $\mathcal{C}^A$ and $\mathcal{C}^B$ by the following rules: i) if $\mathbf{R} = \mathbf{R}_N^A = \mathbf{R}_M^B$ for some $N \in \mathcal{N}^A$ and $M \in \mathcal{N}^B$ then $\mathcal{C}$ has a combined cusp $(\mathbf{R}, \frac{\rho^A(\mathbf{R})Z_N^A + \rho^B(\mathbf{R})Z_M^B}{\rho(\mathbf{R})})$;

ii) other cusps in A and B are included unmodified. Either set can be empty (although this would be very strange for $\mathcal{C}$), leading to zero for the corresponding sum.

Applying these rules depends on precise details of the embedding or partitioning scheme. The next sections therefore applies Eq. (3.14) to the case of smooth partitioning of densities studied here, as well as some cases from the literature.

Smooth partitioning of densities

The remainder of the manuscript deals with densities that are partitioned according to, $\rho_A(\mathbf{r}) = w(\mathbf{r})\rho(\mathbf{r})$ and $\rho_B = (1 - w(\mathbf{r}))\rho$ where $0 < w(\mathbf{r}) < 1$ is a smooth, cusp-free and positive function. $1 - w$ therefore has the same qualities as w. In this case, the non-additive potential has no cusps.

To show this, I recognise that ρ_A, ρ_B and ρ *all* have the same cusps, which follows from the definition of the density, and w and $1 - w$ being smooth and finite, so that they only contribute to smooth terms. Therefore, $\mathcal{C}^A = \mathcal{C}^B = \mathcal{C}$ and I obtain,

$$v_{\text{sing}}^{\text{NAD,part}}(\mathbf{r}) = 0 \tag{3.15}$$

In section [3.4], I numerically apply a smooth cusp-less function to partition the ground-state density of some model diatomic systems of two and four electrons and I show that the corresponding non-additive potential has no singularities at the nuclei, consistent with theory.

Embedding with a cusp-free density

In some cases, such as that considered in Appendix A of García-Lastra *et al.* [56] where it is an implicit assumption, one obtains a density ρ_A that is cusp free in some region of interest, but otherwise has the same cusps as ρ. These problems appear in (e.g.) embedding calculations where some molecules (with cusps at nuclei) are treated at one level of theory and an additional molecule (with existing cusps and new cusps at the additional nuclei) is embedded in the pre-computed set.

As a result, all cusps of ρ_A appear in ρ_B and ρ, but not vice versa. All cusps appear with the same value and at the same nuclear positions, when they are present, giving $\mathcal{C}^B = \mathcal{C}$. I use, $\mathcal{N}_{B \notin A}$ to denote nuclei yielding cusps in B and $A + B$ that are not in A. It follows that,

$$v_{\text{sing}}^{\text{NAD,emb}}(\mathbf{r}) = \sum_{N \in \mathcal{N}_{B \notin A}} \frac{Z_N}{|\mathbf{r} - \mathbf{R}_N|} \; . \tag{3.16}$$

Use of a finite basis to represent densities

Another interesting case is where densities are obtained using a finite basis set. I first consider a Slater-type orbital (STO) basis set, which is able to reproduce cusps, but where the resulting cusps are imperfect. [37] In a finite STO base one obtains, $\rho(\mathbf{r} \to \mathbf{R}_N) \approx \rho(\mathbf{R}_N)e^{-\tilde{Z}_N|\mathbf{r}-\mathbf{R}_N|}$ where $\tilde{Z}_N$ is the finite basis approximation for Z_N. $\tilde{Z}_N \approx Z_N$ varies with choice of basis, choice of density functional approximation, and other details of the calculation.

For convenience I shall assume that all densities contain all cusps, like in Sec. 3.3.2. This leads to ρ_A, ρ_B and ρ defined by cusp sets $\mathcal{C}_A = \{(\tilde{Z}_N^A, \mathbf{R}_N)\}$, $\mathcal{C}_B = \{(\tilde{Z}_N^B, \mathbf{R}_N)\}$ and $\mathcal{C} = \{(\tilde{Z}_N, \mathbf{R}_N)\}$, respectively. Importantly, $\mathbf{R}_N$ is the same in all cases but $\tilde{Z}_N^A \approx \tilde{Z}_N^B \approx \tilde{Z}_N$ are not the same (but are similar) because of errors introduced by the finite basis. The singular part of the non-additive potential is therefore,

$$v_{\text{sing}}^{\text{NAD,STO}} = \sum_{N \in \mathcal{N}} \frac{\tilde{Z} - \tilde{Z}_A}{|\mathbf{r} - \mathbf{R}_N|} \tag{3.17}$$

where the terms $\tilde{Z} - \tilde{Z}_A$ in the numerator are effectively random artefacts, defined by the basis set and other computational and methodological choices. These artefacts also apply to embedding, per Sec. 3.3.2. Eq. (3.17) then acts in addition to the "exact" cusps from Eq. (3.16).

Gaussian-type orbitals (GTOs) cannot reproduce cusps at all, unlike STOs, as they are analytic near nuclei. Nevertheless, they have an effective analogue to Eq. 3.17 for small but finite r_N in the vicinity of a nucleus.

Of greatest relevance to the present work is that calculations on a finite grid can eliminate these errors entirely. This involves effective use of numerical methods, chosen such that derived potentials are as consistent as possible with the routines used to solve effective Hamiltonians. Especially, one should use

$\frac{\nabla^2 \sqrt{\rho}}{\sqrt{\rho}}$ rather than the mathematically equivalent $\frac{\nabla^2 \rho}{2\rho} - \frac{|\nabla \rho|^2}{4\rho^2}$ when computing potentials.

3.4   Numerical Calculation

The calculations are obtained on accurate numerical grids using the all-electron program package DARSEC [135]. Consequently, I are restricted to computations of molecules with two atomic centres with spherical symmetry. In DARSEC, the Kohn-Sham equations are solved self-consistently using the high-order finite difference approach [52, 11]. In this work, the stencil was set to 12 for the finite difference. A real-space grid based on prolate-spherical coordinates is used to describe a system with two atomic centres. The grid is very dense near two centres and increasingly sparse farther from the centres. Due to the cylindrical symmetry of diatomic molecules, the problem is reduced to a two–dimensional one. In the calculations for this work, the systems are defined within 15 *Bohr* of radius and number of 115×121 grid points. The $\rho_{tot}(\mathbf{r})$ is the ground-state density of the systems performed with the LDA [24, 162].

Based on Eq.[3.4] I implemented Eq.(3.18)

$$v^{\text{NAD}}[\rho_A, \rho_{tot}](\mathbf{r}) = v_s[\rho_A](\mathbf{r}) - v_s[\rho_1](\mathbf{r}) \tag{3.18}$$

where $\rho_1(\boldsymbol{r}) = 2 \mid \psi_1(\boldsymbol{r}) \mid^2$. The $\rho_{tot}(\mathbf{r})$ is obtained by a common DFT theory. Such analytical inversion is correct under specific constraints. The density used as an independent variable of analytically inverted potential functional has to integrate to integers 1 or 2 in whole space for one-electron or two spin-compensated electrons, respectively. Knowing that v^{NAD} obtained from von Weizsäcker theory is equal to Eq.[3.18] up to a constant, I implemented numerically

$$v^{\text{NAD/vW}}[\rho_B, \rho_{tot}](\mathbf{r}) = v_s^{vW}[\rho_B](\mathbf{r}) - v_s^{vW}[\rho_1](\mathbf{r}) \tag{3.19}$$

where $v_s^{vW}[\rho(\mathbf{r})]$ is given by Eq.[3.20].

$$v_s^{\text{vW}}[\rho](\mathbf{r}) = \frac{1}{4}\left(\frac{\nabla^2\rho(\mathbf{r})}{\rho(\mathbf{r})}\right) - \frac{1}{8}\frac{|\nabla\rho(\mathbf{r})|^2}{\rho^2(\mathbf{r})} \tag{3.20}$$

In section 3.5, I introduce the *cst* that ensures the equality $v^{\text{NAD/vW}}[\rho_A, \rho_{tot}](\mathbf{r}) = v^{\text{NAD}}[\rho_A, \rho_{tot}](\mathbf{r}) + cst$ for different systems for the cases in which $\int \rho_{tot}(\mathbf{r}) > 2$. In section 3.5.3 I show for $\int \rho_{tot}(\mathbf{r}) \leq 2$ $v^{\text{NAD/vW}}[\rho_A, \rho_{tot}](\mathbf{r}) = v^{\text{NAD}}[\rho_A, \rho_{tot}](\mathbf{r})$. The derivation of the latter equality is given in Appendix D .

Localisation of one or two electrons

For partitioning the ground state density numerically, I use a smooth distribution function $0 \leq F(z) \leq 1$ that has no cusps and respects the smoothness of the function explained in Section[3.3.2]. The choice for such a function used for the reported result is Fermi-Dirac distribution function that changes smoothly from value one to zero (Eq.[3.21]). This latter was realised within binary-search algorithm to localised the density around one nucleus.

$$F(z) = \frac{1}{e^{\alpha(z - z_0)} + 1} \tag{3.21}$$

By partitioning the whole density to two sub densities I obtain: $\rho_B(\mathbf{r}) = F(z).\rho_{tot}(\mathbf{r})$ and $\rho_A(\mathbf{r}) = \rho_{tot}(\mathbf{r}) - \rho_B(\mathbf{r})$.

In a diatomic system of $N = 2 + 2M$ electrons where two spin-compensated electrons can be localised around one nucleus, the following construction is applied:

$$\rho_A(\mathbf{r}) = \int_v F(z)\rho_{tot}(\mathbf{r})d\mathbf{r} = 2 \tag{3.22}$$

For the case of one-electron-localisation, $F(z)$ can be chosen to equal the integration of Eq.(3.22) to 1. By definition, the second fragment of the system is:

$$\rho_B(\mathbf{r}) = \rho_{tot}(\mathbf{r}) - \rho_A(\mathbf{r}) \tag{3.23}$$

In the present calculations $\alpha = 20$ was chosen.

3.5 Results and Discussion

Two classes of diatomic model systems were chosen to study. One class contains two electrons in the whole system in which one electron is localised around one nucleus. In the other one, four electrons are distributed in the system among which two electrons are localised around one nucleus. The latter includes two model systems; one is a homonuclear diatomic system and the other one is a heteronuclear model system. For each system, I compare the analytically inverted potential with v^{NAD} obtained through von Weizäcker (Eqs.[3.19] and [3.20]).

The ground state charge density used as input in all calculations are obtained by LDA theory, consequently the inverted potential (Eq.[3.5]) is compared with $v_{\text{KS}}^{\text{LDA}}$.

To facilitate the density localisation around a nuclei and minimise the overlap charge density between the atoms, the calculations are done for interatomic distance of 6 Bohr. For mononuclear systems the maximum density overlap occurs at half distance between the atoms while for the heteronuclear system the location of maximum overlap occurs closer to the nuclei with smaller atomic number.

3.5.1 Two-electron-localisation

Homonuclear model system: He-He

The potential is inverted analytically from Eq.[3.5] for $\rho_1 = 2|\phi_1(\mathbf{r})|^2$ and the eigenvalue ϵ_1. The exactitude of the analytical inversion of the potential yields to $\Delta V = v_{\text{KS}}^{\text{LDA}} - v_s[\rho_1] = 0$. In Fig.[3.1] although the ΔV doesn't constantly appear zero everywhere in the space but comparing the difference between the orders of magnitude of two curves of about 10^{10}, ΔV satisfies the value 0 numerically. As it is shown in Fig.[3.2] the system represents symmetrically distributed charge density, once two electrons are localised around the left atom, two other electrons are sited around the right nucleus. In Fig.[3.2] the cutoff z_0 from Eq.[3.21] is shown by a vertical gray line at $z = 0$ Bohr.
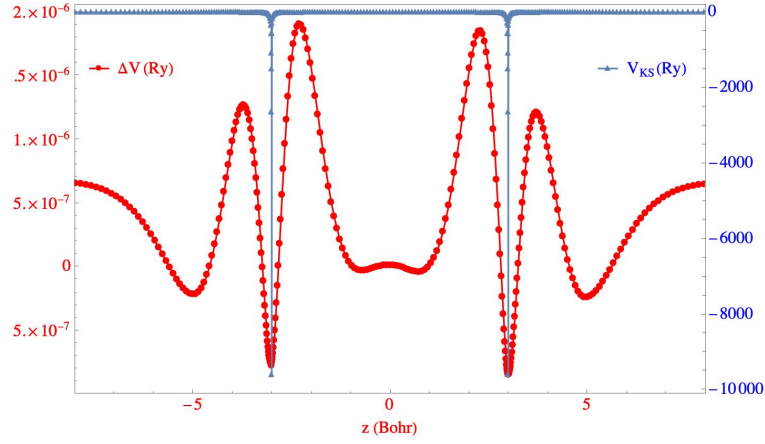
Figure 3.1: Difference between the analytically inverted $v_s[\rho_1](\mathbf{r})$ and $v^{\mathrm{KS}}(\mathbf{r})$. system: He-He, Blue curve: Kohn-Sham Potential from LDA calculations. Red curve: $\Delta v = v^{\mathrm{KS}}(\mathbf{r}) - v_s[\rho_1](\mathbf{r})$.

Consequently, the ρ_A and ρ_B are integrated both to 2 and both are distributed around one nucleus separately as they have close to 0 charge distribution at the vicinity of the opposite nucleus (Fig.[3.3]).

The potential $v^{\mathrm{NAD/vW}}$ from von Weizsäcker is alternative mathematically to $v^{\mathrm{NAD/inverted}}$. In Fig.[3.4] I see this equality as both potentials superpose perfectly and the small orders of magnitude of their difference (showed by red curve representing Δv in the figure) is an additional numerical confirmation to that fact. The 2D representation of $v^{\mathrm{NAD/vW}}$ and $v^{\mathrm{NAD/inverted}}$ shows that the difference between two potential is considered negligible.
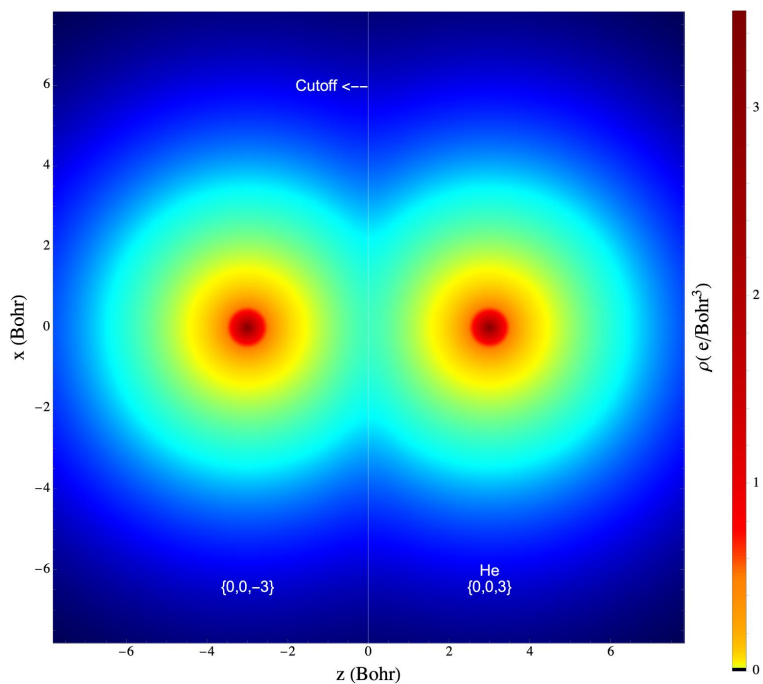
Figure 3.2: system: He-He, Ground-State charge density distribution, calculated from LDA approximation. The cutoff line represent spatial location at which the whole density is partitioned to two sub-densities that each integrates to two electrons. The precision of localisation is: $\int (\rho_A(\mathbf{r}).\rho_B(\mathbf{r}))d\mathbf{r} = 3.8 \times 10^{-6} \; (\frac{e^2}{Bohr^3})$
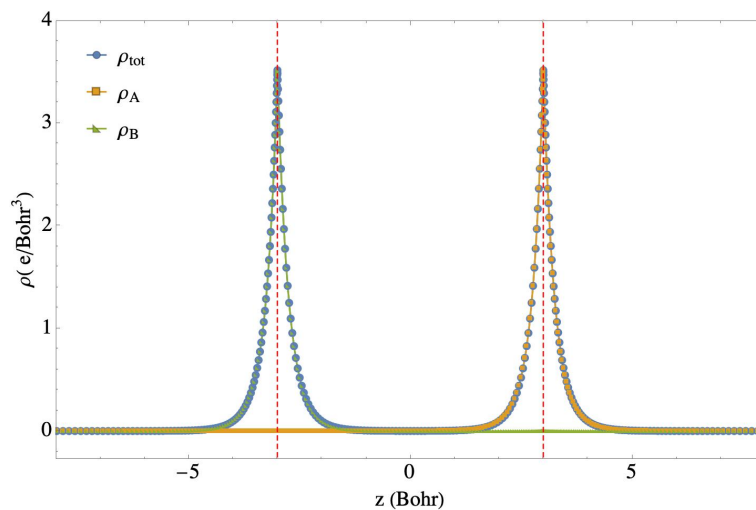
Figure 3.3: Localised densities from ground-state density, provided from LDA calculation. system: He-He, 1D representation of density localisation.
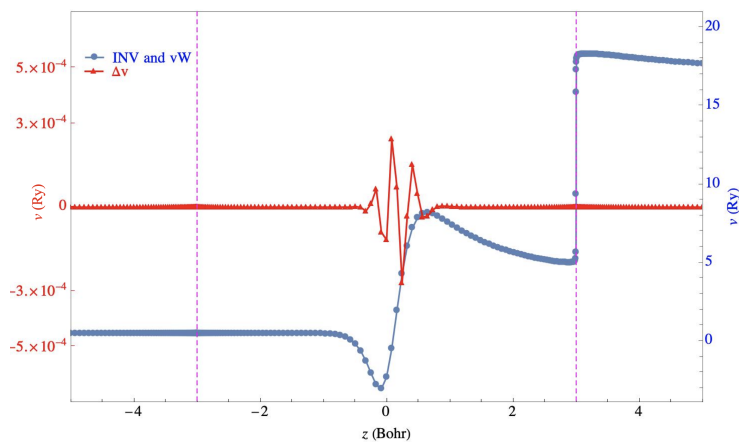
Figure 3.4: Analytically inverted bi-functional potential vs the one from von Weizsäcker theory. system: He-He, **Blue-Mark-Line:** $v^{\mathrm{NAD/inverted}}[\rho_B, \rho_{tot}](\mathbf{r})$; **Orange-Square-Line:** $v^{\mathrm{NAD/vW}}[\rho_B, \rho_{tot}](\mathbf{r})$. **Vertical Dashed Lines:** nuclei.
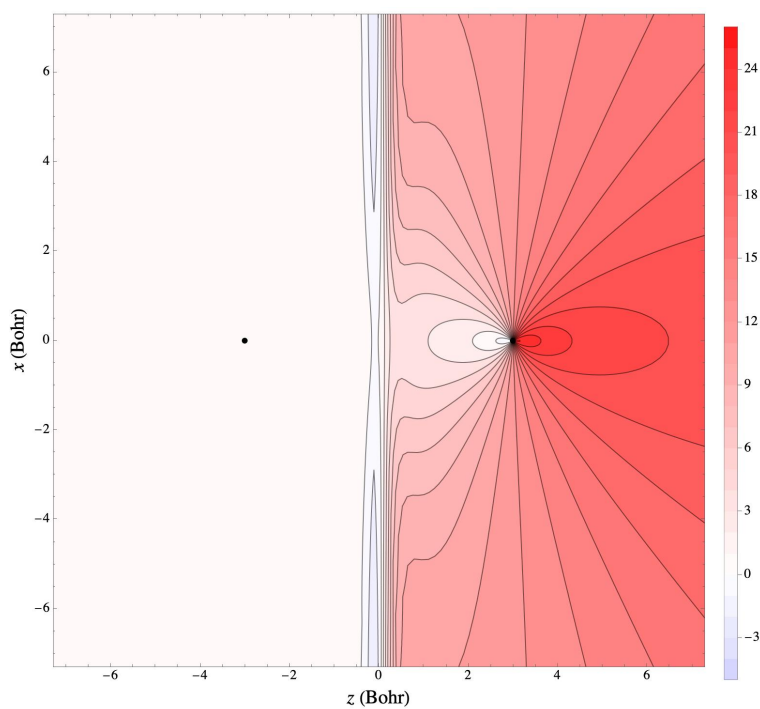
Figure 3.5: Analytically inverted non-additive kinetic potential bi-functional in real space. system: He-He, Two-dimensional representation of $v_s^{\mathrm{NAD/inverted}}[\rho_B, \rho_{tot}](\mathbf{r})$. **Black dots:** nuclei.
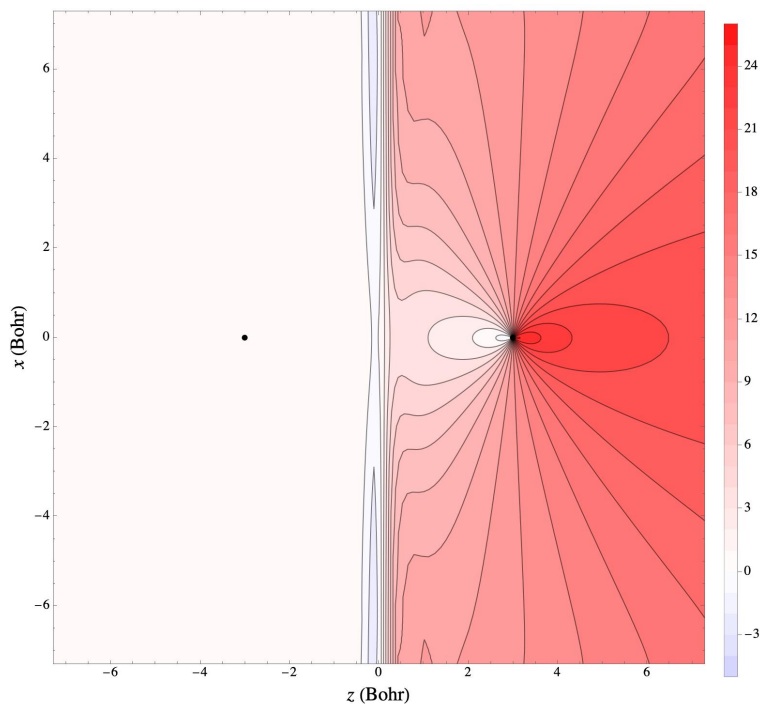
Figure 3.6: von Weizsäcker non-additive kinetic potential bi-functional in real space. system: He-He, Two-dimensional representation of $v_s^{\text{NAD/vW}}[\rho_B, \rho_{tot}](\mathbf{r})$. **Black dots:** nuclei.

Heteronuclear model system: $LiHe^+$

The localisation in $LiHe^+$ (Li at the left side in all figures), occurs at its highest precision integrating to 2, for $z_0 = -0.29$ Bohr which is closer to the nucleus with a smaller atomic number. Similarly the overlapping density integrates to a higher value compared to the homonuclear system.

When ρ_B is localised around the larger nucleus the $v^{\text{NAD/vW}}$ has to be subtracted by ϵ_1 to become comparable with $v^{\text{NAD/inverted}}$ (see Fig.[3.7]). Instead, if I localise the electrons around the smaller nucleus (He in our model system), I must subtract ϵ_2 from $v^{\text{NAD/vW}}$.
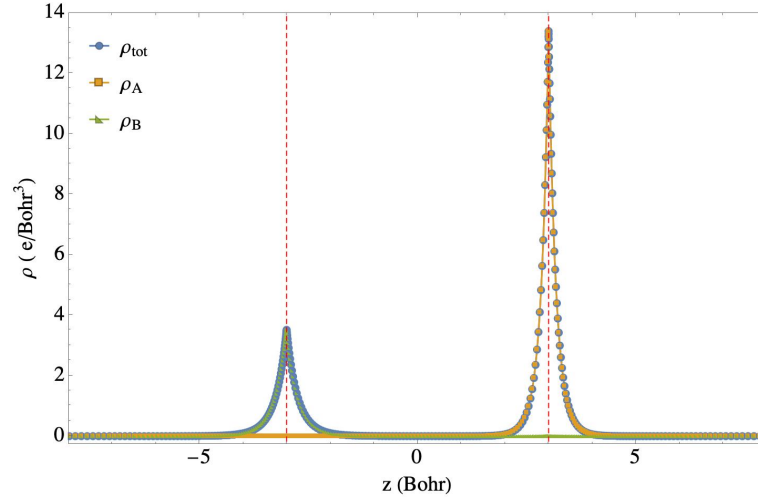
Figure 3.7: Localised densities from ground-state density, provided from LDA calculation. System: LiHe$^+$, 1D representation of density localisation. The precision of localisation is: $\int(\rho_A(\mathbf{r}).\rho_B(\mathbf{r}))d\mathbf{r} = 2.51 \times 10^{-3}$ ($\frac{e^2}{Bohr^3}$). **Vertical Dashed Lines:** nuclei.

For the heteronuclear system, as we see in Fig.[3.7], Δv is zero in the space with some noise at the overlap region. The appeared noise is negligible due to its small order of magnitudes considering the machine precision. This numerical artefact rose up from numerical difference between the Laplacian and the gradient for the very small values.
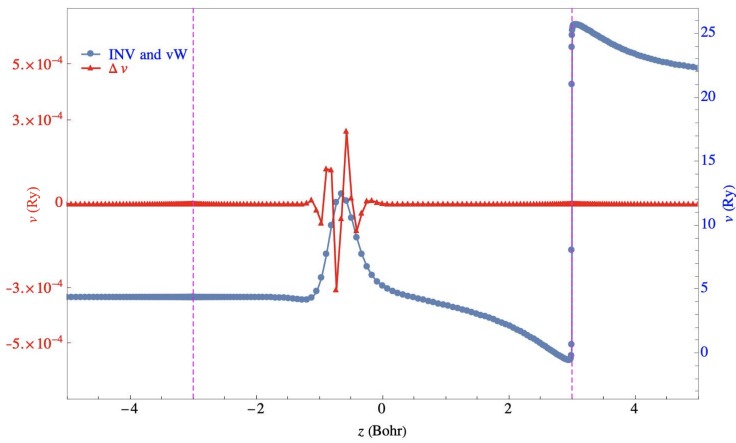
Figure 3.8: Analytically inverted bi-functional potential vs the one from von Weizsäcker theory. System: LiHe$^+$, **Blue-Mark-Line:** $v^{\text{NAD/inverted}}[\rho_B, \rho_{tot}](\mathbf{r})$; **Orange-Square-Line:** $v^{\text{NAD/vW}}[\rho_B, \rho_{tot}](\mathbf{r})$. **Vertical Dashed Lines:** nuclei.
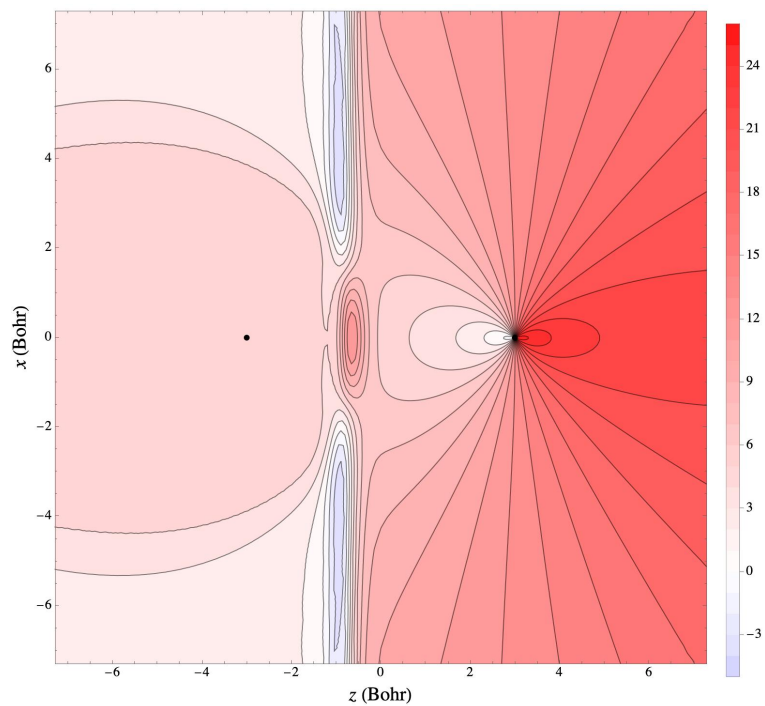
Figure 3.9: Analytically inverted non-additive kinetic potential bi-functional in real space. System: LiHe$^+$, Two-dimensional representation of $v_s^{\text{NAD/inverted}}[\rho_B, \rho_{tot}](\mathbf{r})$. **Black dots:** nuclei.
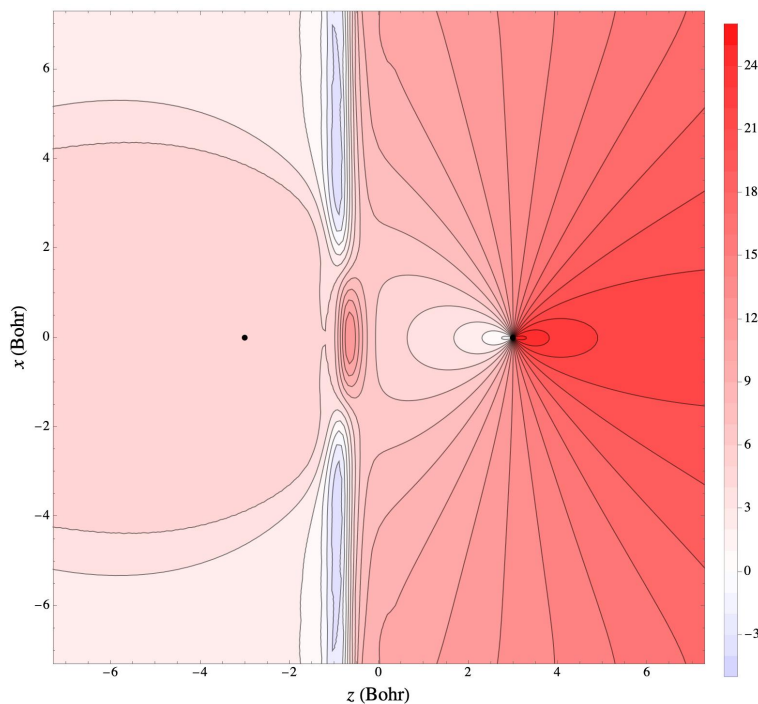
Figure 3.10: von Weizsäcker non-additive kinetic potential bi-functional in real space. System: LiHe$^+$, Two-dimensional representation of $v_s^{\text{NAD/vW}}[\rho_B, \rho_{tot}](\mathbf{r})$. **Black dots:** nuclei.

3.5.2 One-electron-localisation

The expectation of equality between $v^{\text{NAD/inverted}}[\rho_B, \rho_{tot}](\mathbf{r})$ and $v^{\text{NAD/vw}}$ becomes maximal for a two-electron heteroatomic system of two nuclei. I studied stretched H_2 system in which one electron is localised around the left nucleus (Fig.[3.11]). The $z_0 = 0$ Bohr to make the cutoff to provide the localisation of one electron. $v^{\text{NAD/vw}}$ matches perfectly $v^{\text{NAD/inverted}}[\rho_B, \rho_{tot}](\mathbf{r})$ (Fig.[3.12]). The difference between the two potentials is zero in the entire space, and the noise observed on the curve is shown in Fig.[3.12] is interpreted as numerical. The 2D representations of v^{NAD}s are also perfectly matching(Fig.[3.13] and Fig.[3.14]).
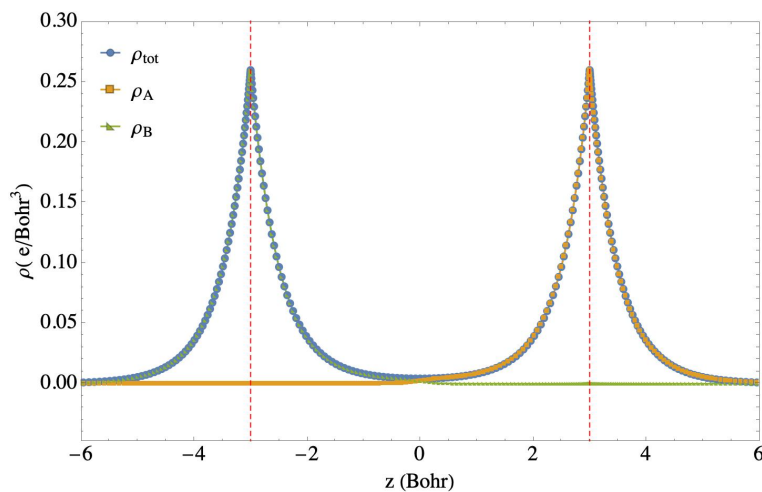
Figure 3.11: Localised densities from ground-state density, provided from LDA calculation. System: H_2, 1D representation of density localisation. $\int (\rho_A(\mathbf{r}).\rho_B(\mathbf{r}))d\mathbf{r} = 1.75 \times 10^{-5}$ $(\frac{e^2}{Bohr^3})$
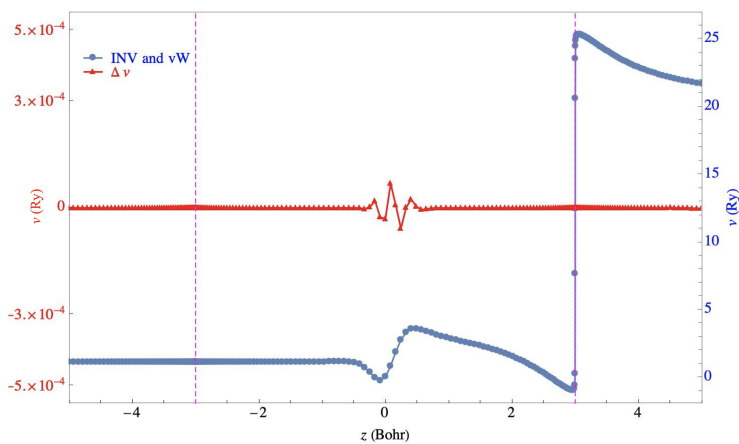
Figure 3.12: Analytically inverted bi-functional potential vs the one from von Weizsäcker theory. System: H_2, Blue-Mark-Line: $v^{\text{NAD/inverted}}[\rho_B, \rho_{tot}](\mathbf{r})$ Orange-Square-Line: $v^{NAD/vW}[\rho_B, \rho_{tot}](\mathbf{r})$. Red dots: nucleii.
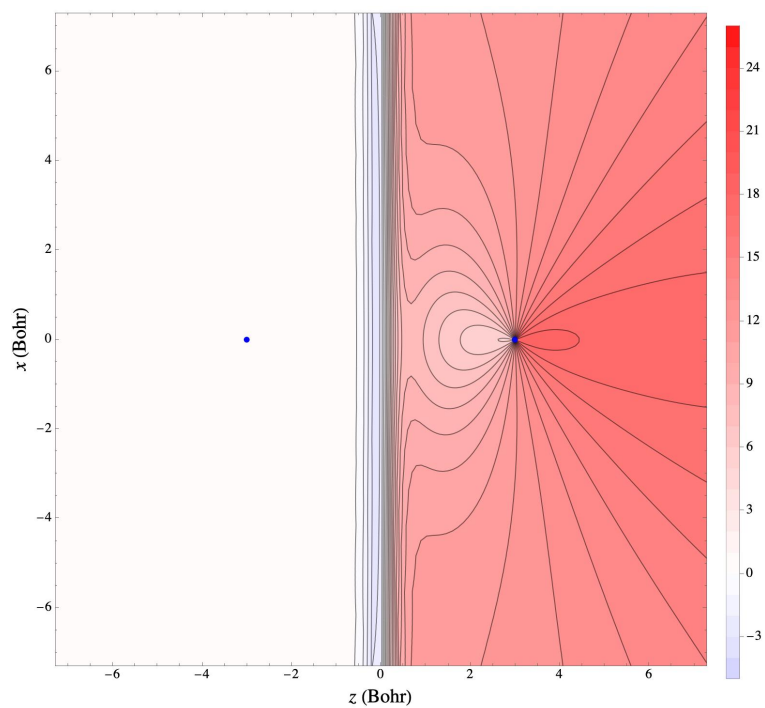
Figure 3.13: Analytically inverted non-additive kinetic potential bi-functional in real space. System: H_2, Two-dimensional representation of $v_s^{\text{NAD/inverted}}[\rho_B, \rho_{tot}](\mathbf{r})$. **Blue dots:** nuclei.
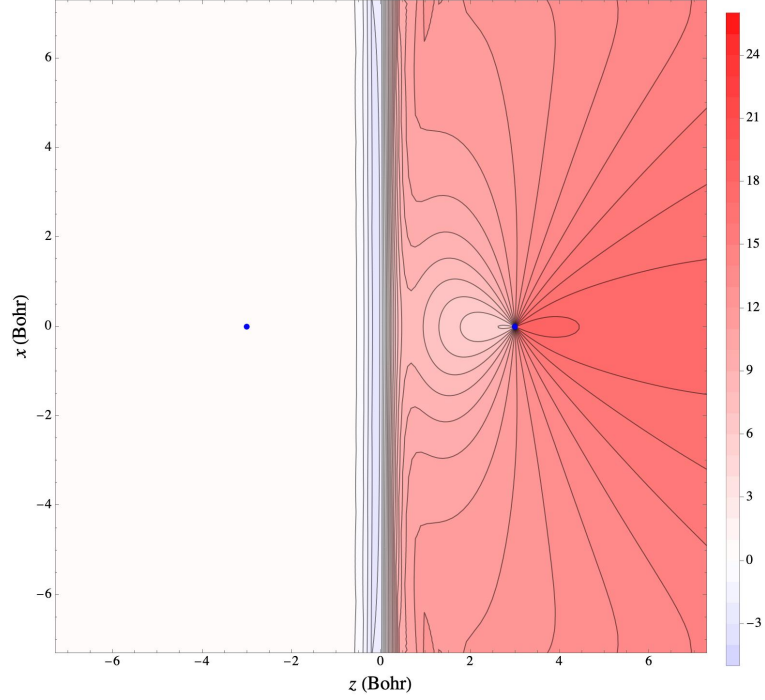
Figure 3.14: von Weizsäcker non-additive kinetic potential bi-functional in real space. System: H_2, Two-dimensional representation of $v_s^{NAD/vW}[\rho_B, \rho_{tot}](\mathbf{r})$. **Blue dots:** nuclei.

3.5.3 Different Approach towards $v^{NAD/vW}[\rho_B, \rho_{tot}]$

$v_s^{vW}[\rho_i]$ is exact if ρ_i integrates to 2 in whole space. $v^{NAD/vW}[\rho_B, \rho_{tot}]$ can be calculated in two ways. Either from:

$$v^{NAD/vw}[\rho_B, \rho_{tot}](\mathbf{r}) = v_s^{vW}[\rho_B](\mathbf{r}) - v_s^{vW}[\rho_{tot}](\mathbf{r}) \tag{3.24}$$

or:

$$\begin{aligned} v^{NAD/vw}[\rho_B, \rho_{tot}](\mathbf{r}) = \\ v_s^{vW}[\rho_B](\mathbf{r}) - (v_s^{vW}[\rho_1](\mathbf{r}) - \epsilon_1) \end{aligned} \tag{3.25}$$

where in each equation $v_s^{vW}[\rho_i]$ for $i = A, B, 1$ or tot is calculated from Eq.[3.20]. If for all i in Eq.[3.24] and Eq.[3.25] the $0 \leq \int_v \rho_i(\mathbf{r}) \leq 2$ both equations are exactly equal otherwise $v_s^{vW}[\rho_i]$ is not exact analytical form of inversion. Below, I calculated $v^{NAD/vW}[\rho_B, \rho_{tot}]$ from Eq.[3.25] for diatomic systems of for electrons. I see that this latter matches exactly the analytical inverted potential (Eq.3.18).

Homonuclear model system HeHe

TEST!!!
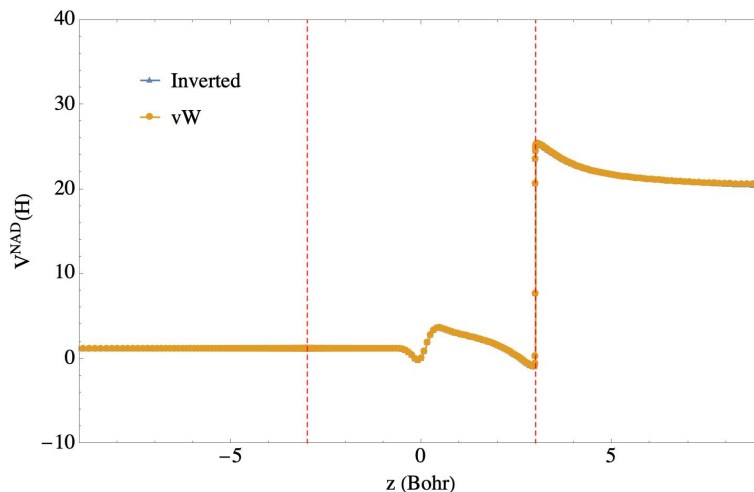
Figure 3.15: Analytically inverted bi-functional potential vs the one from von Weizsäcker theory. System: H_2, Blue-Mark-Line: $v^{\mathrm{NAD/inverted}}[\rho_B, \rho_{tot}](\mathbf{r})$ Orange-Square-Line: $v^{NAD/vW}[\rho_B, \rho_{tot}](\mathbf{r})$ obtained from Eq.[3.25]. **Vertical Dashed Lines:** nuclei.

Heteronuclear model system $LiHe^+$
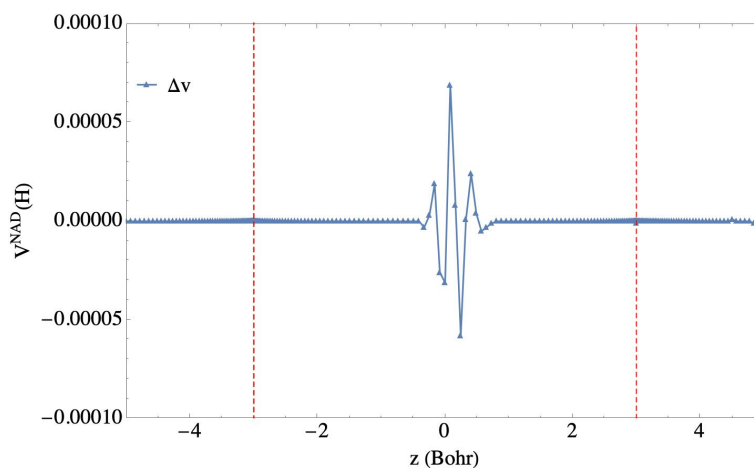
Figure 3.16: Difference between the analytically inverted potential bi-functional and the one from von Weizsäcker approximation. System: LiHe$^+$, **Blue-Mark-Line:** $\Delta v = v_s^{\mathrm{Inverted}}[\rho_B](\mathbf{r}) - v_s^{\mathrm{vW}}[\rho_B](\mathbf{r})$ (from Eq.[3.25]); **Vertical Dashed Lines:** nuclei.
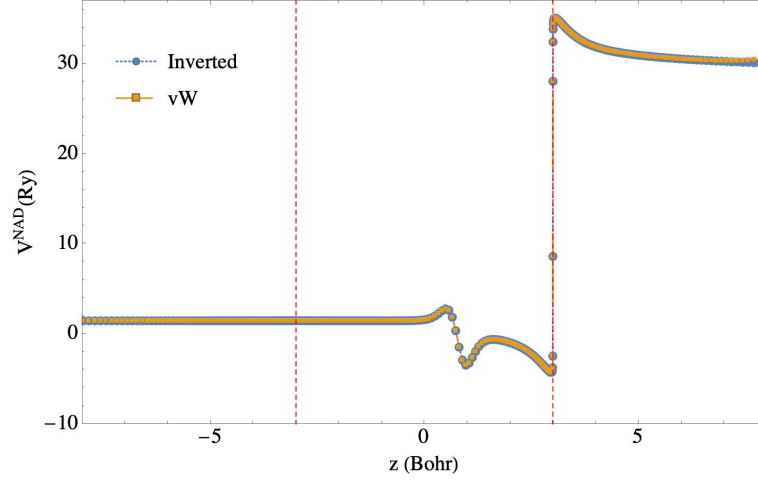
Figure 3.17: Analytically inverted bi-functional potential vs the one from von Weizsäcker theory. System: H_2, Blue-Mark-Line: $v^{\mathrm{NAD/inverted}}[\rho_B, \rho_{tot}](\mathbf{r})$ Orange-Square-Line: $v^{\mathrm{NAD/vW}}[\rho_B, \rho_{tot}](\mathbf{r})$ obtained from Eq.[3.25].**Vertical Dashed Lines:** nuclei.
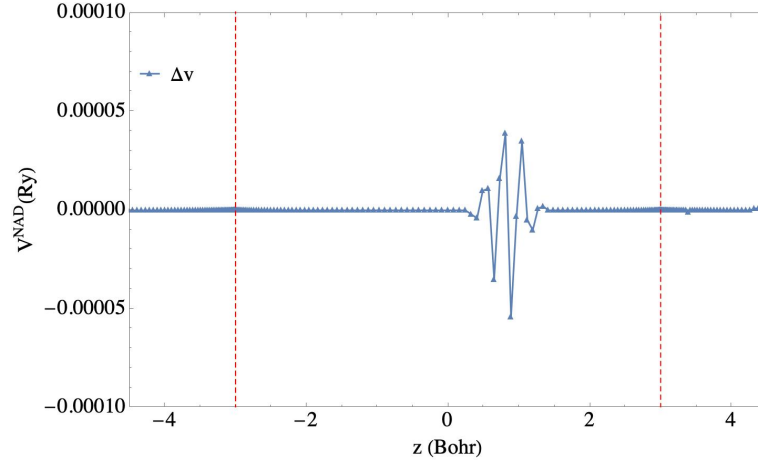
Figure 3.18: Difference between the analytically inverted potential bi-functional and the one from von Weizsäcker approximation. System: LiHe$^+$, **Blue-Mark-Line:** $\Delta v = v_s^{\mathrm{Inverted}}[\rho_B](\mathbf{r}) - v_s^{\mathrm{vW}}[\rho_B](\mathbf{r})$(from Eq.[3.25]); **Vertical Dashed Lines:** nuclei.

3.6   Conclusion

To defend the exactitude of analytically inverted potential three remarks are considered:

1. For the class of two sub-densities that overlap weakly and the inverted potential of each that represent the singularities at the vicinity of the

nuclei, analytically inverted $v^{\text{NAD/inverted}}[\rho_B, \rho_{tot}](\mathbf{r})$ has to appear with no cusp-like singularity at the nuclei. It requires to be smooth everywhere in the space except at the region where two densities overlap.

2. The potentials shown in Figs.[(3.4,3.8,3.12)], feature a step and a barrier between the two nuclei. These are desired and expected features of $v^{\text{NAD}}[\rho_B, \rho_{tot}](\mathbf{r})$ evaluated for such pair $\rho_B(\mathbf{r})$ and $\rho_{tot}(\mathbf{r})$ for which $\rho_{tot} - \rho_B$ disappears near the nucleus B. From the practical perspective, any approximation to $v^{\text{NAD}}[\rho_B, \rho_{tot}](\mathbf{r})$ should reproduce these features. Practical calculations using an approximated $v^{\text{NAD}}[\rho_B, \rho_{tot}](\mathbf{r})$ that does not reproduce these features are prone to an artificial leak of electrons on the nucleus B (for a detailed discussion of this issue see [56]).

3. As it is proven in the theory that $v^{\text{NAD/vw}}$ is exact for a system in which the electron density integrates to a value between 0 and 2, the exactitude of the analytically inverted potential can be evaluated by comparing these two potentials. The equality of these potentials ensures that the exact analytically inverted potential is not suffering by numerical artefacts.

For all the model systems of our study, the three conditions above were respected. I proved that a system that analytically inverted potential from each partition includes the same cusp-shape singularity at the nuclei as the ones in Kohn-Sham potential would provide non-additive potential with no cusps at nuclei. The $v^{\text{NAD/inverted}}[\rho_B, \rho_{tot}](\mathbf{r})$ requires to be exactly zero where the localisation happens. When the localised density is the same as one of the solutions of the system, its inverted potential must be equal to the Kohn-Sham potential up to a constant and this constant as it was shown in this work must be the corresponding eigenvalue to the solution.

3.7 Supplementary Information on Calculations for "Nuclear Cusp and singularities in Non-Additive Kinetic Potential bi-Functional from Analytical Inversion."

In this document the choice of different numerical parameters are explained for the calculations in the current chapter. In addition, $v^{\text{NAD/inverted}}$ is compared with $v^{\text{NAD/vW}}$ for localisation around different nuclei in HeLi$^+$.

Note for readers: The plots all concern the He-He system. If not specified!

3.8 Stencil for Gradient and Laplacian

DARSEC uses the Finite difference method for gradient and Laplacian calculations. The users can choose an even number for stencil (s) of the Finite difference between 2 to 20. In the code $s = 12$ is suggested as an accurate choice for the calculations. In Fig.[3.19], v^{NAD} is showed from different stencils. The $s \leq 10$ do not provide the smooth extrema on the curves so; the final choice has to be one among $s \geq 12$ (Fig.[3.20]). To choose a reliable stencil, I finally compared $s = 12$ with $s = 20$ at the region where the densities overlap. As it showed in Fig.[3.22], the difference between these two choices is negligible except at a distance above 10 Bohr from the system's centre, where it is not the region of our interests. The potentials from $s = 12$ and $s = 20$ at this region are zoomed in in Fig.[3.23]. In this region, the Laplacian is more sensitive to the choice of the stencil (Fig.[3.21]).

Based on the reported calculations in this work, I decided to stay with $s = 12$ for the calculations of the up-coming paper.
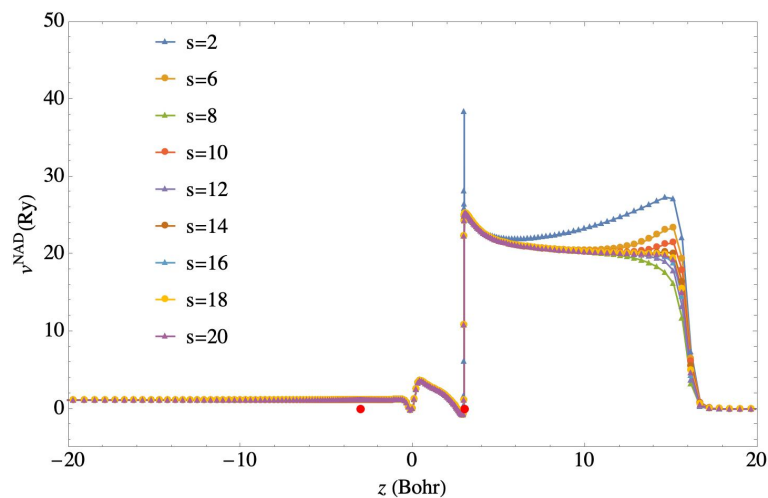
Figure 3.19: For system He-He where the atoms are located at $(0, 0, -3)$ Bohr and $(0, 0, 3)$ Bohr, the $v^{\mathrm{NAD/inverted}}$ is calculated with different choice of stencil number for the higher order calculations within the finite-difference approach. Red Dots: Location of the nuclei.
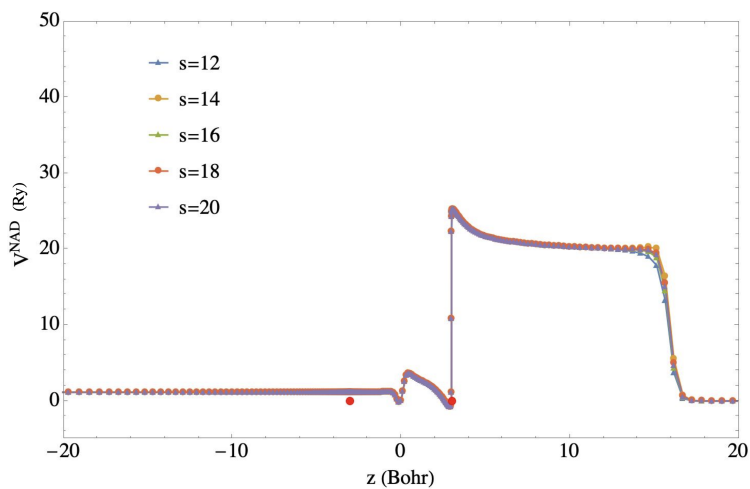
Figure 3.20: $s \geq 12$ provides smoother curves at the extrema of the potential. Red Dots: Location of the nuclei.
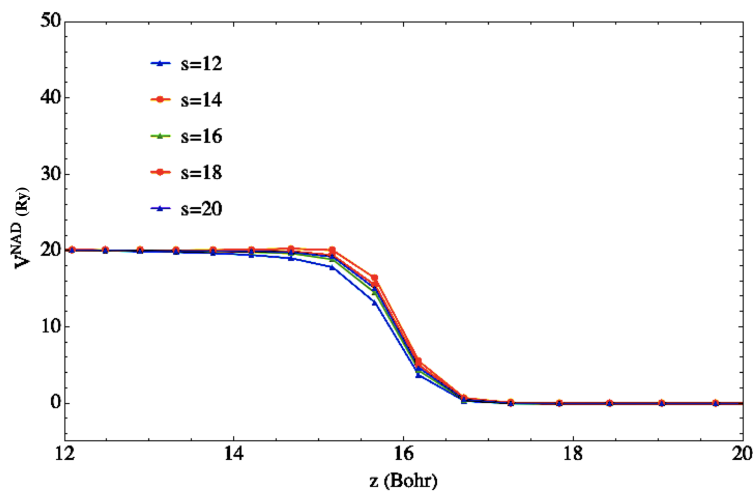
Figure 3.21: With the choice of $s \geq 12$, the curves goes smooth up to the infinity as the radius of the system is defined 15 Bohr. Only beyond 15 Bohr different stencils vary slightly the potential.
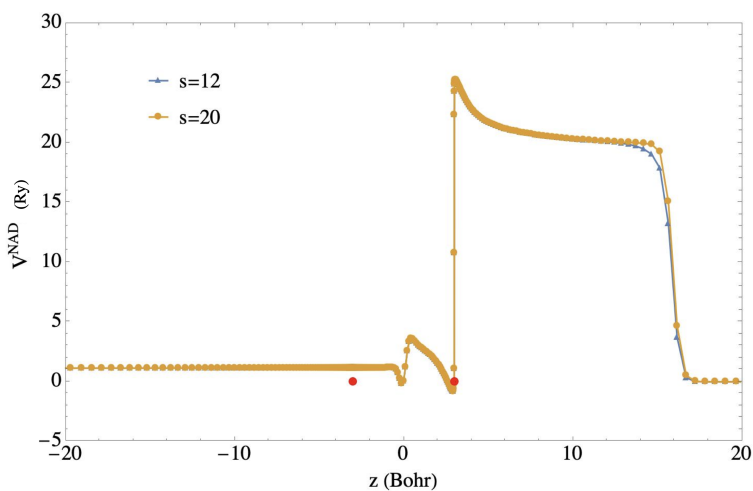
Figure 3.22: Between the suggestion of the authors of DARSEC for $s = 12$ as default and the maximum possible value implemented in DARSEC $s = 20$; the potentials remain the same except where in the space it is considered as out-of-range. Red Dots: Location of the nuclei.
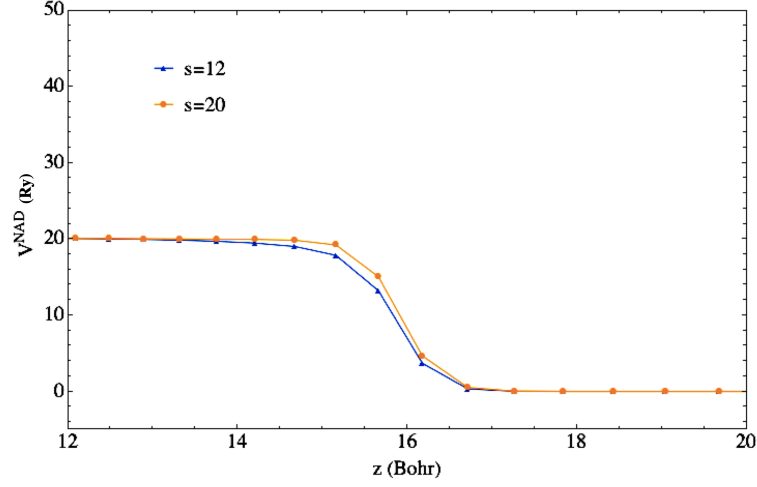
Figure 3.23: Even beyond 15-Bohr from the system's center, the difference between $v_{s=12}^{\text{NAD/inverted}}$ and $v_{s=20}^{\text{NAD/inverted}}$ is negligible.

3.9 Correction to possible division by zero

DARSEC doesn't provide the values on axis $z = 0$. As there is nowhere in the space except at the infinity where the density tends to be zero; I don't need to prepare any correction (δ) to plausible division-b-zero issue in the calculations. Still, I tried to make sure that the results are not affected unwillingly by the lack of the correction to division-by-zero. The corrections are done by adding δ to where in the equation the terms might be question of the division-by-zero issue.

$$v^{\text{NAD}}[\rho_B, \rho_{tot}](\mathbf{r}) = \frac{1}{2}\frac{\nabla^2\sqrt{\rho_B(\mathbf{r})}}{\sqrt{\rho_B(\mathbf{r})}+\delta} - \frac{1}{2}\frac{\nabla^2\sqrt{\rho_1(\mathbf{r})}}{\sqrt{\rho_1(\mathbf{r})}+\delta} \tag{3.26}$$

From Fig.[3.24] to Fig.[3.26] I see that if the correction is a number $\delta \leq 1 \times 10^{-10}$, our calculations are not affected. in Fig.[3.27] I see that with no correction applied to the calculations (case 0 in the graph), the results remain the same.

Based on the presented results for the paper, the calculations are all done with "NO-CORRECTION" to the division-by-zero issue.
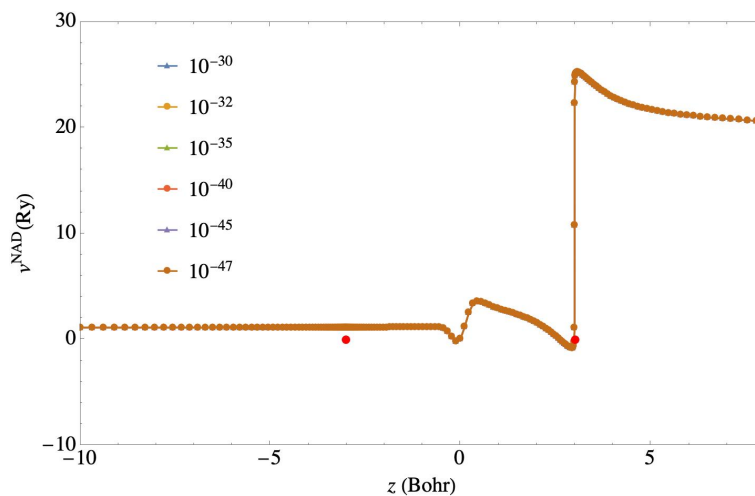
Figure 3.24: $v^{\mathrm{NAD/inverted}}$s for which the calculations include the correction to the division-by-zero issue, overlap in whole space if the correction is chosen to be smaller than $\delta = 1 \times 10^{-10}$. All curves overlap entirely for δ varying from 1×10^{-10} to 1×10^{-47}. Red Dots: Location of the nuclei.
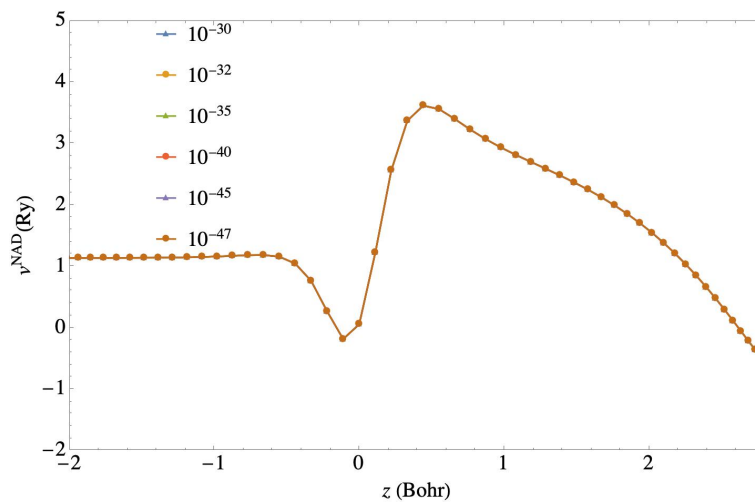
Figure 3.25: Here I zoomed Fig.[3.24] in the region where the overlap of the densities tend to be maximum.
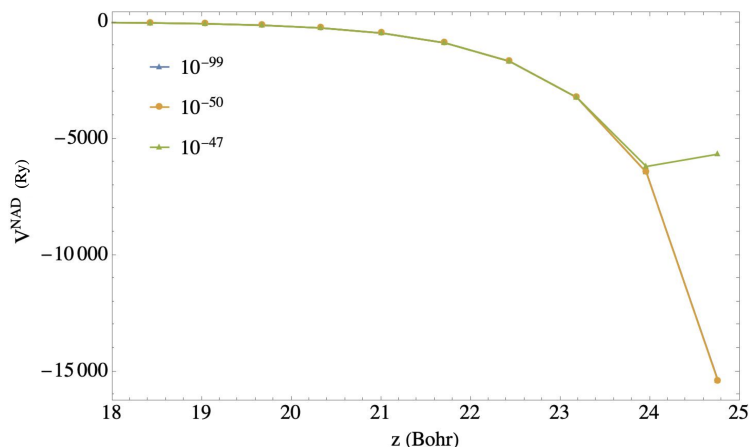
Figure 3.26: With the very small δs, the potential may vary at the infinity, where it is not a region of interest.
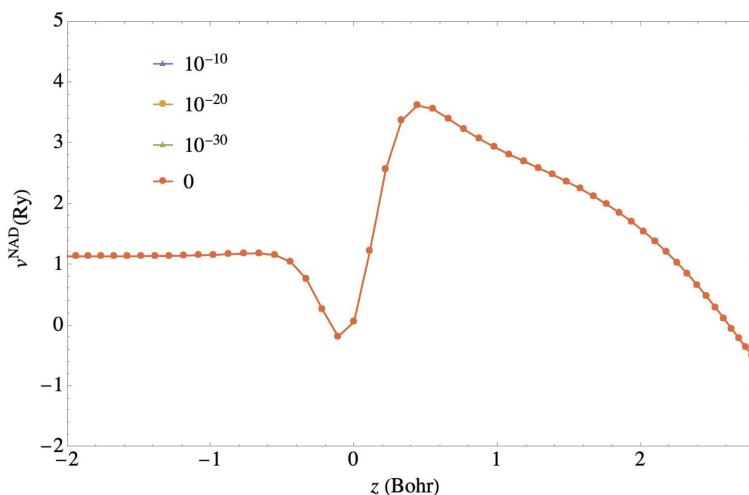
Figure 3.27: No correction to the division-by-zero issue (case of $\delta = 0$) is compared to some other small values of δ. As the overlap region of the densities is our main part of interests, and no changes appear in the potential's curve at this region, I remain with no-correction for the rest of calculations.

3.10 Parameter α in the Fermi-Dirac Distribution Function for Density Localisation

The parameter alpha in the Fermi-Dirac distribution function (Eq.[3.21]) for density localisation from Eq.[3.22] was sought for the most accurate value.

The Fig.[3.28] and Table [3.1] the most appropriate choices for α are shown in the table together with the v^{NAD} from the different choices of α.
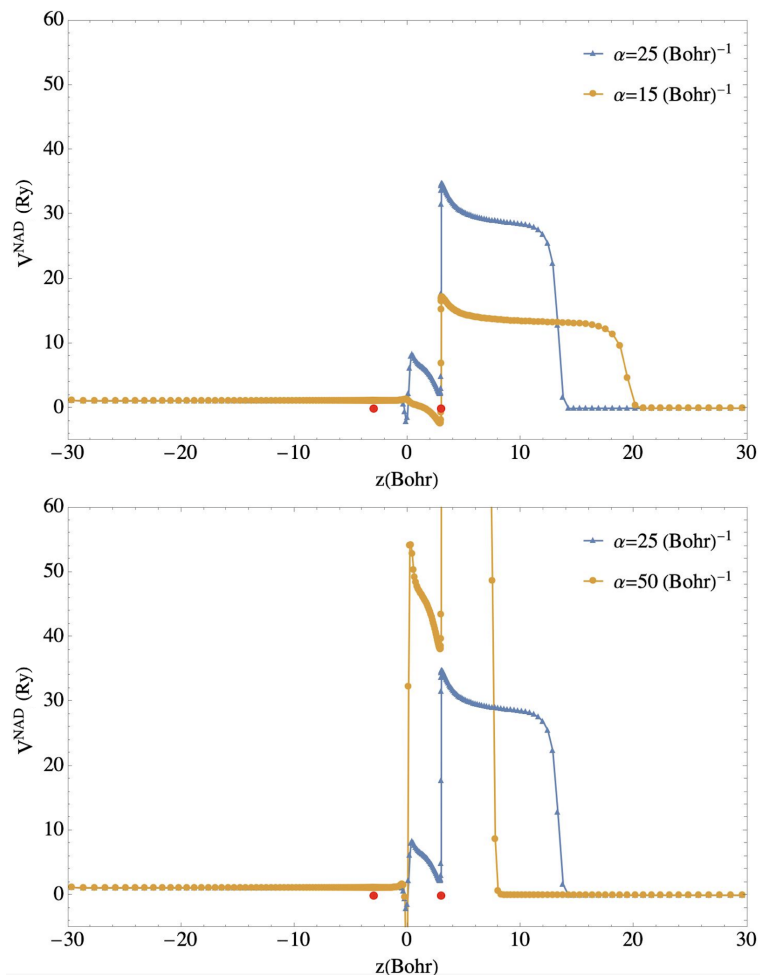
Figure 3.28: Among different choices of α in Fermi-Dirac distributions, I decided to accept $20 \leq \alpha \leq 30$. For the calculations that will be published, $\alpha = 20$ which ensures the density localisation with the highest numerically possible precision. Red Dots: Location of the nuclei.

Choice of α

	$\int \rho_B(\mathbf{r})d\mathbf{r}$	z_0 (Bohr)
$\alpha = 5$ (Bohr)$^{-1}$	2.00000000004284	1.18743628263474E-08
$\alpha = 15$ (Bohr)$^{-1}$	2.00000000002135	1.22934579849243E-07
$\alpha = 25$ (Bohr)$^{-1}$	2.0000000000015	1.564621925354E-07
$\alpha = 35$ (Bohr)$^{-1}$	2.00000000001369	1.67638063430786E-07
$\alpha = 50$ (Bohr)$^{-1}$	1.99999999999667	1.78813934326172E-07
$\alpha = 100$ (Bohr)$^{-1}$	2.00000000008729	2.23517417907715E-07

Table 3.1: The choice of α in Eq.[3.21] and the corresponding $\rho_B(\mathbf{r})$ and obtained cutoff z_0.

In the paper, the calculations will be shown; all done from $\alpha = 20$ for $F(z)$ defined in Eq.[3.21].

3.11 Density Localisation Numerical Algorithm

To localise two electrons around one nucleus, I chose the binary-Search algorithm in which the start-point is the location of the left nuclei, and the end-point is the location of the right nuclei. The precision of the localisation is given as input parameter by user, and the algorithm stops turning when $end - start \leq Precision$.

3.12 Density Localisation Around He vs Density Localisation Around Li in HeLi$^+$

The $v^{\text{NAD/vW}} - \epsilon_1$ becomes comparable with $v^{\text{NAD/inverted}}$ for the homonuclear diatomic systems, . Instead, for the heteronuclear diatomic system, the eigenvalue that must be subtracted from $v^{\text{NAD/vW}}$ is a question of the location of the density localisation. I show that if the density is localised at the vicinity of the nuclei with larger atomic number (in our case Li) the corresponding eigenvalue to be involved in the calculation is ϵ_1, instead if the density is localised around the smaller nuclei (in our case He), I need $v^{\text{NAD/vW}} - \epsilon_2$ to compare it with $v^{\text{NAD/inverted}}$.

In both case $\Delta v = (v^{\text{NAD/vW}} - \epsilon_i) - v^{\text{NAD/inverted}}$ where $i = 1, 2$, shows a step that is related to the difference of the eigenvalues, $\Delta\epsilon$.

See Fig.[3.29] to Fig.[3.31].
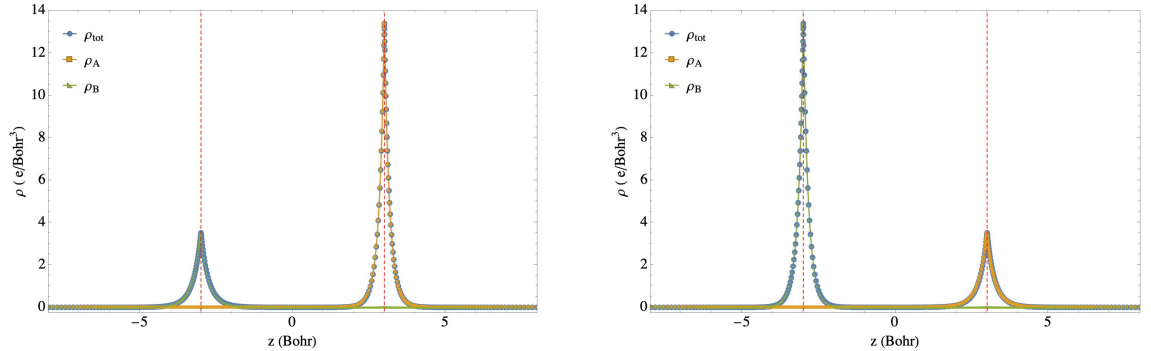
(a) He at the left where the density is localised.

(b) Li at the left where the density is localised.

Figure 3.29: The atoms are at 6 Bohr distance from each other. **(a)** HeLi$^+$, where the density ρ_B is localised around the atom He at the left. **(b)** LiHe$^+$, where the density ρ_B is localised around the atom Li at the left.
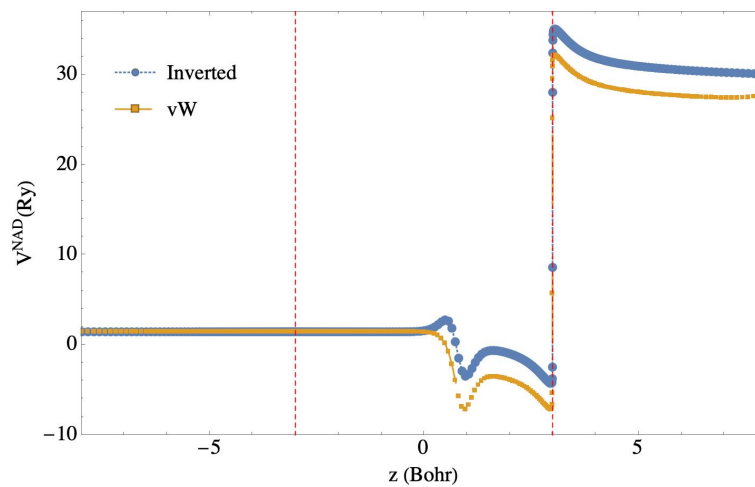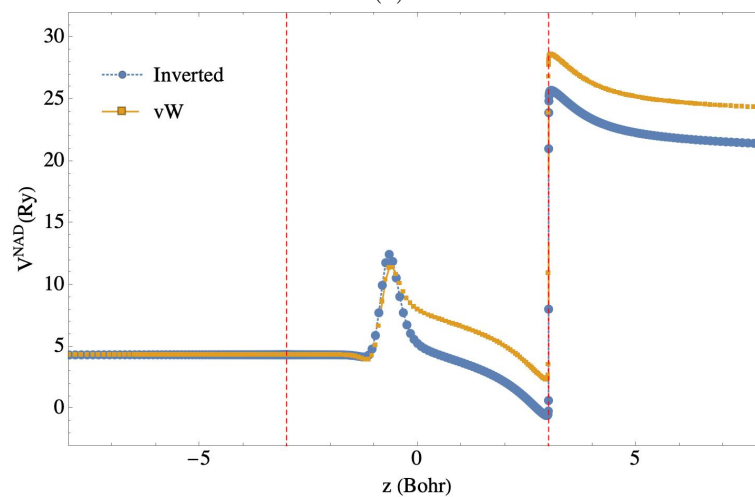
Figure 3.30: Inverted potential from density localisation around different atoms. Vertical dashed lines: nuclei. Interatomic distance: 6 Bohr. **(a)** System: HeLi$^+$, Blue-Mark-Line: $v^{\mathrm{NAD/inverted}}[\rho_B, \rho_{tot}](\mathbf{r})$ Orange-Square-Line: $v^{\mathrm{NAD/vW}}[\rho_B, \rho_{tot}](\mathbf{r}) - \epsilon_2$. **(b)** System: LiHe$^+$, Blue-Mark-Line: $v^{\mathrm{NAD/inverted}}[\rho_B, \rho_{tot}](\mathbf{r})$ Orange-Square-Line: $v^{\mathrm{NAD/vW}}[\rho_B, \rho_{tot}](\mathbf{r}) - \epsilon_1$.

3.13 Spatial Symmetry In homonuclear diatomic system with two or four electrons

In Fig.[3.32], I show that within our density localisation approach when two electrons are localised around one nucleus and two other one around the other nucleus, for the homonuclear diatomic systems $v^{\text{NAD}}[\rho_A, \rho_{tot}](\mathbf{r})$ and $v^{\text{NAD}}[\rho_B, \rho_{tot}](\mathbf{r})$ are spatially symmetric. By spatially symmetry I mean: $v^{\text{NAD}}[\rho_A, \rho_{tot}](\mathbf{r}) = v^{\text{NAD}}[\rho_B, \rho_{tot}](\mathbf{-r})$.

(a)

(b)

(c) .
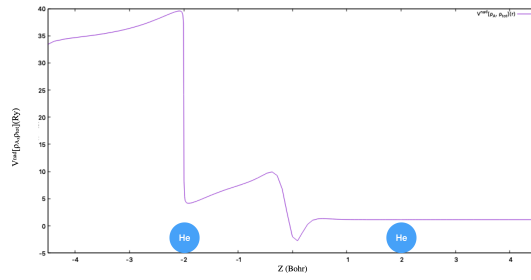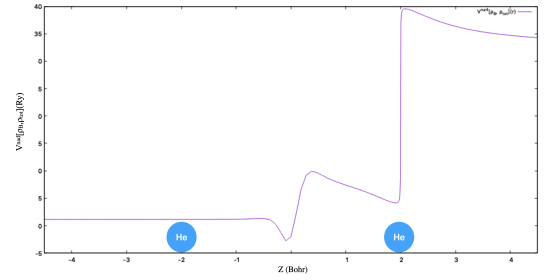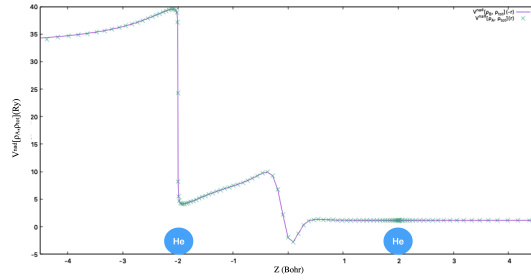
$$v_t^{nad}[\rho_B, \rho_{tot}](-\mathbf{r}) = \frac{1}{2}\frac{\Delta\sqrt{\rho_B(-\mathbf{r})}}{\sqrt{\rho_B(-\mathbf{r})}} - \frac{1}{2}\frac{\Delta\sqrt{\rho_1^\alpha(-\mathbf{r})}}{\sqrt{\rho_1^\alpha(-\mathbf{r})}} + \epsilon_1^\alpha$$

$$= \frac{1}{2}\frac{\Delta\sqrt{\rho_B(-\mathbf{r})}}{\sqrt{\rho_B(-\mathbf{r})}} - \frac{1}{2}\frac{\Delta\sqrt{\rho_1^\alpha(\mathbf{r})}}{\sqrt{\rho_1^\alpha(\mathbf{r})}} + \epsilon_1^\alpha$$

$$= \frac{1}{2}\frac{\Delta\sqrt{\rho_A(\mathbf{r})}}{\sqrt{\rho_A(\mathbf{r})}} - \frac{1}{2}\frac{\Delta\sqrt{\rho_1^\alpha(\mathbf{r})}}{\sqrt{\rho_1^\alpha(\mathbf{r})}} + \epsilon_1^\alpha$$

$$= v_t^{nad}[\rho_A, \rho_{tot}](\mathbf{r})$$

(d)

Figure 3.32: **(a)** $v^{\text{NAD}}[\rho_A, \rho_{tot}](\mathbf{r})$; **(b)** $v^{\text{NAD}}[\rho_B, \rho_{tot}](\mathbf{r})$; **(c)** $v^{\text{NAD}}[\rho_A, \rho_{tot}](\mathbf{r})$ and $v^{\text{NAD}}[\rho_B, \rho_{tot}](\mathbf{-r})$
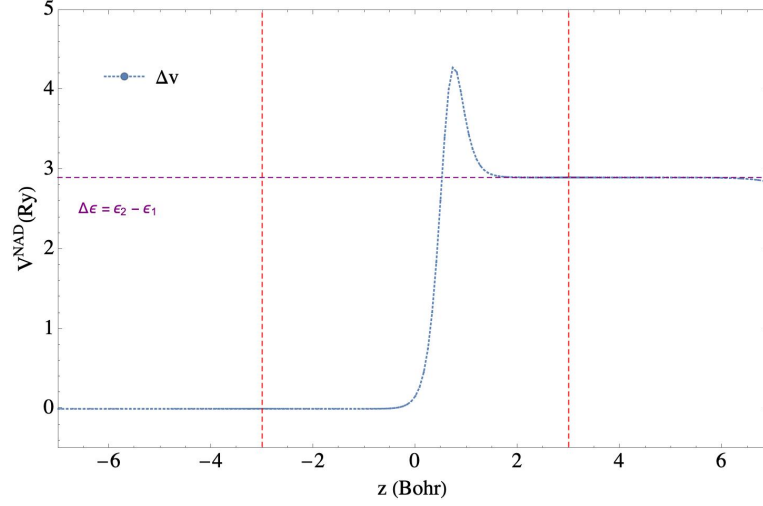
(a)
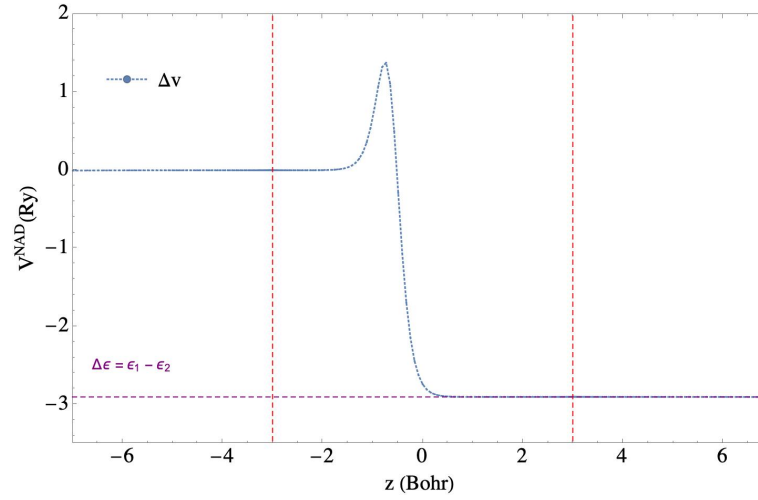
(b)

Figure 3.31: Eigenvalue shift in the von Weizsäcker potential from total density. Vertical dashed lines: nuclei. Interatomic distance: 6 Bohr. **(a)** System: HeLi$^+$, Blue-Mark-Line:$\Delta v = v_s^{Analytic}[\rho_B](\mathbf{r}) - [v_s^{vW}[\rho_B](\mathbf{r}) - \epsilon_2]$; Horizontal dashed line: the difference between the first and second eigenvalues: $\Delta\varepsilon = \varepsilon_2 - \varepsilon_1 = [-1.476393 - (-4.376893)](Ry) = 2.9005(Ry)$. **(b)** System: LiHe$^+$, Blue-Mark-Line:$\Delta v = v_s^{Analytic}[\rho_B](\mathbf{r}) - [v_s^{vW}[\rho_B](\mathbf{r}) - \varepsilon_1]$; Horizontal dashed line: the difference between the first and second eigenvalues: $\Delta\varepsilon = \epsilon_1 - \epsilon_2 = [-4.376893 - (-1.476393)](Ry) = -2.9005(Ry)$.

Chapter 4

Step Structure

4.1 Abstract

The step structure is a direct result and mandatory attribute of the exact potential in the Kohn-Sham formulation of the DFT. The step is a mandatory structure to align the KS energy levels within the ionisation potentials in the two fragments. For the first time, I calculate the gap energy of a partitioned system of two atoms through the analytically inverted potential bi-functional of two sub-densities. The results are compared with the most accurate results obtained from OEP theory with the KLI local approximation.

4.2 Introduction

The strength and quality of the theories in DFT are evaluated by the accuracy of calculations based on the approximation of the unknown exchange correlation energy. While many successful approximations exist, they often lack the derivative discontinuity (DD) [164, 31, 8, 141, 143, 142] of $E_{xc}[\rho](\mathbf{r})$ concerning integer electron number, N. In some theories one of the property of the accuracy of the theory is evaluated with when its $E_{xc}[\rho](\mathbf{r})$ represents at DD that when added to the Kohn-Sham band gap, results in the fundamental band gap of the system. The fundamental gap $E_g = I - A$ describes the difference between I, the ionisation potential (IP), and A, the electron affinity (EA).

The presence of the DD is expected in molecular dissociation when two atoms are stretched far apart[136]. The atoms take on integer numbers of

94

electrons to neutralise their charges, so the total energy of the system, which is additive, tends to show a DD relative to a number change of electrons when one atom transfers its electron to another.

If any potential claims to be exact, the DD has to appear in form of a step on the curve of the potential solving a system of stretched atoms , the open-shell systems or excited time-dependent systems. It is manifested in the xc potential and appears in form of a jump in the level of the potential. The importance of the step structure (SS) is in approaches that look for the tunneling electrons and charge transfer or electron excitation [199, 82, 73].

It is essential to consider the step structure in the approximations to ensure the accuracy of the methods. The step structure provides an accurate ground state electron density. It is a direct result of the necessary alignment of the KS energy levels (the ionisation potentials) in the two fragments [133, 129].

4.3 Origin of Step structure

A stretched heteronuclear diatomic molecule toward the molecular dissociation approaches into neutral atoms A and B. Atoms A and B in form of isolated elements possessing different external potentials so consequently different HOMO energies ϵ_{HOMO}^A and ϵ_{HOMO}^B. In the exact Kohn-Sham formulation HOMO energies must be equal to first ioinosation energy:$\epsilon_{HOMO}^A = -I_A$ and $\epsilon_{HOMO}^B = -I_B$. The variational principle for the total energy implies ensuring $\epsilon_{HOMO}^A = \epsilon_{HOMO}^B$ for when A and B are considered as constituent parts of a dissociated AB molecule. Within the approximate theories of DFT, an artificial transferring a fractional electron charge from A to B is forced to ensure the equalisation of HOMO energies in the dissociated molecules. This leads to incorrect physics. Instead, in the exact formulations of DFT, this equality is obtained by the optimisation of $v_{xc}(\mathbf{r})$ at the vicinity of one of the nuclei (Atom B for when the electronic charge has the potential of being transferred from A t o B) that reads[1]:

$$\epsilon_{HOMO}^A - \epsilon_{HOMO}^B = I_B - I_A \tag{4.1}$$

The physical interpretation of this formula is that $v_{xc}(\mathbf{r})$ represents a well for each atom. Through this equality, the $v_{xc}(\mathbf{r})$ well of the atom with a higher electronegativity will be raised by $I_B - I_A$ accordingly to the $v_{xc}(\mathbf{r})$ well of the other atom. This upshift is what is called "Step Structure", characteristics to the exact $v_{xc}(\mathbf{r})$. In some literatures, it is also known as the "counterionic field"[72]. The name is deduced from the fact that this phenomenon will prevent the electron density from flowing toward the more electronegative atom. In DFT approximations it is often found that atoms carry functional charges in a stretched molecule. The reason is that those approximations of the step structure is absent[174]. Step structure of molecular $v_{xc}(\mathbf{r})$ has been studied by different groups both analytically and numerically [75, 73, 72, 107, 136, 190, 82, 84, 119, 21]. Hodgston *et al.*[89, 90] explained the origin of the step structure from model systems for which the exact electron density is known. They showed that the steps forms at points in the density when the probability of the existence of a charge in the local effective ionisation energy of the electrons is nonzero. They also determined the shape of the step,

its heights and position for ground state density both for time-dependent and time-independent systems.

4.3.1 Height of the step in a stretched diatomic molecule

The step height S for a system of two distant atoms is given by:

$$S = I_R - I_L + \eta_R^{HOMO} - \eta_L^{HOMO} \tag{4.2}$$

where I_L and I_R are the ionisation energy of the left and right atoms respectively and η refers to the HOMO energy of molecular KS orbital localised around an atom. If the stretched molecule compromise two open-shell atoms, $\eta_R^{HOMO} = \eta_L^{HOMO}$ and Eq.[4.2] will simplify to $S = I_R - I_L$ which is the famous Almbladh and von Barth's expression [1]. If the overall ionisation potential (IP) of the molecule be the IP of one the atoms (for example the one of the right atom), then $\eta_R^{HOMO} = -I_R$ so the height of the step becomes $S = \eta_L^{HOMO} - I_L$. This latter can be zero or not essentially.

To interpret more clearly the functionality of the step I may introduce the molecular energy η_L^{HOMO} in terms of the atomic energy ϵ_L^{HOMO}:

$$\eta_L^{HOMO} = \epsilon_L^{HOMO} + S \tag{4.3}$$

Eq.[4.3] means that the molecular energy is elevated by the step height relatively to the atomic energy.

4.3.2 Height of the step in terms of the derivative discontinuity of $E_{xc}[\rho](\mathbf{r})$

The Derivative Discontinuity in the well-known approximations underestimate the gap [162, 12, 125, 165] underestimate the gap energy almost by 50%. The failure of those approximations may appear while calculation of charge transfer in chemical processes. Derivative discontinuity could be manifested as a uniform shift Δ, in the level of exact Kohn-Sham potential in the position in real space when the ground state density integrates to a value that exceeds the integer value infinitesimally. The shift Δ has similar nature to step height explained previously:

$$\Delta = \epsilon^{HOMO}(N_0^+) - \epsilon^{HOMO}(N_0^-) - (\epsilon^{LUMO} - \epsilon^{HOMO}) \tag{4.4}$$

where N_0 is the expected integer value, the ground state density integrates to in absence of the derivative discontinuity ($\int_V \rho_0(\mathbf{r})d\mathbf{r}$), and ϵ^{HOMO} and ϵ^{LUMO} are the highest occupied and lowest unoccupied Kohn-Sham eigenvalues, respectively. The charge N_0 varying infinitesimally by δ from integer is $N_0^{\pm} = N_0 \pm \delta$.

As it was already mentioned the HOMO and LUMO Kohn-Sham eigenvalues are related to the ionisation potential and electron affinity[227, 130, 161, 164, 79].

$$\epsilon^{HOMO}(N_0^+) = -A \tag{4.5a}$$

$$\epsilon^{HOMO}(N_0^-) = -I \tag{4.5b}$$

It is important that Δ explains the correct gap energy in form of Eq.[4.6].

$$E_g = \Delta - (\epsilon^{LUMO} - \epsilon^{HOMO}) \tag{4.6}$$

This is the case for the stretched molecules in which the atoms can not be considered as isolated.

4.3.3 Step Height S vs Step Height Δ

The two preceding phenomena, Δ and S, are generally treated as independent and unrelated properties of the exact KS potential. Their differences mainly are related to the fact that S is a quantity related to two fragments of the system in which the atoms could be approximated to the isolated elements whereas Δ is the quantity that defines the correct gap energy of the entire system as a whole. Additionally, the EA and the LUMO energy, yielding Δ, are absent from S. Convincingly, in a system, S occurs at an integer of electrons in a fixed location in the space while the Δ occurs when a small amount of charge is added to the whole system. However, depending on the range of the system and the interaction between elements the S step could be related to the derivative discontinuity. The relation between the interatomic step, S, and the DD, Δ is published by Hodgson *et al.*[90].

4.3.4   Position of the step

Far from the localised electrons (around the midpoint of interatomic axis) in subsystems the density must decrease with the ionisation energy of the entire system. This is the case of a molecule of separate atoms with weakly overlapping atomic wavefunctions. There exist locally a second charge in the effective ionisation energy away from the system if any subsystem density does not decrease with this energy. This local additional charge in form of the step on $v_{xc}(\mathbf{r})$ was initially observed by Perdew. [157] and then later by Makmal *et al*. [136] in the exact exchange potential for LiF, where they attribute the steps to shifts in the Kohn-Sham eigenvalues.

Thus, the step is expected to appear on the exact $v_{xc}(\mathbf{r})$ to define the decay charge occurring in $\rho_0(\mathbf{r})$ far from the nuclei. More about the position of the step structure could be find in Ref.[190].

For the model systems that can be solved by one-orbital formula (see section 3.3.1), a spatial function in the form of $\tilde{I}(x) = \frac{1}{8\rho^2}(\frac{\partial \rho}{\partial x})^2$ could be defined that is sensitive to the ionisation energy for when the density decays asymptotically. As this asymptotic decay is manifested in form of the step on the exact $v_{xc}(\mathbf{r})$ so, $\tilde{I}(x)$ may predict the location in the space where the step occurs[89]. The detection of the step through $\tilde{I}(x)$ is from the fact that in the vicinity of the nucleus $\tilde{I}(x)$ is equal to the corresponding ionisation energies whereas at the point where a change happens in the local ionisation energy (far from the nuclei), $\tilde{I}(x)$ shows a step. Both the height and the position of the step were previously reported by the one-dimensional (1D) Heitler–London model wave function[190].

4.3.5   Shape of the step

The shift is spatially uniform only for $\delta \to 0^+$. In a finite system, such as an atom or molecule, for any small, but finite δ, $v_{KS}(\mathbf{r})$ forms a "plateau" that elevates the level of the potential in the vicinity of the nuclei. At the edge of the plateau, the level of $v_{KS}(\mathbf{r})$ must drop to 0, forming a sharp spatial step. As δ vanishes, the plateau extends over all space, becoming spatially uniform, and its height approaches the value Δ.

A plateau in the exact $v_{KS}(\mathbf{r})$ is also observed for a different physical sce-

nario: a stretched diatomic molecule with an integer number of electrons, $L \ldots R$, which is one system consisting of Atom L and Atom R with a large separation, d.

The plateau forms around one of the atoms, introducing an interatomic[83, 82, 14], and ensuring the correct distribution of charge throughout the system[91, 159, 175, 129, 136, 53, 68, 190, 147, 116, 118, 131].In the general case, the step height, S, is related to I_R and I_L, the IPs of atoms R and L, respectively, as in Eq.[4.2].

4.4 Step Structure in $v^{\mathbf{NAD}}[\rho_B, \rho_{tot}](\mathbf{r})$

Previously Makmal *et al.*[136] published their work on molecular dissocia-
tion of a diatomic molecule with an all electron Kohn-Sham solver DARSEC.
They used the orbital formulation of OEP [121, 180, 187, 71, 49] locally mod-
ified by KLI[120]. Their main goal was to examine exact-exchange (EXX)
Kohn-Sham potential. The $v_{xc}(\mathbf{r})$ of semi-local functionals in molecules decays
exponentially along with the density. The asymptotic behaviour of the exact
$v_{xc}(\mathbf{r})$ instead, is $-\frac{1}{r}$ [3, 40]. The incorrect asymptotic behaviour of the semi-
local $v_{xc}(\mathbf{r})$ is the consequence of self-interaction error. The self-interaction
problem of semi-local potentials can be compensated by Perdew-Zunger self-
interaction correction [163]. Even with such correction and calculations within
the methods that are exact for all-electron calculations, the correct asymptotic
behaviour of $v_{xc}(\mathbf{r})$ is not guaranteed[202]. It was shown by Makmal *et al.*
that Kohn-Sham EXX plays an important role in curing the problem of frac-
tional molecular dissociation. They used stretched LiF molecule to study the
performing EXX calculation. They achieved correct binding energy in their
calculations while using the lowest-energy electronic configuration for different
interatomic distances. The correct binding energy was reflected by a plateau-
like local Kohn-Sham $v_{xc}(\mathbf{r})$ accompanied by two step structures.

The steps that appeared locally on $v_{xc}(\mathbf{r})$ bring the fact that the exact $v_{xc}(\mathbf{r})$
of a diatomic molecule is not simply given by the sum of corresponding atomic
potentials. This latter is always true even for very large arbitrary interatomic
distances. The reason is that one of the atomic potentials is shifted by a
constant due to the HOMO localised energy while the other atom lacks this
shift.

The density-dependent theories within DFT suffer from the lack of this pre-
cision in their $v_{xc}(\mathbf{r})$ even the successful accurate approximations. Instead, the
orbital-dependent approaches such as KLI can reflect the molecular dissociation
through the derivative discontinuity of the corresponding $E_{xc}(\mathbf{r})$ at the level of
the nonzero atomic shift of the potential.

We expected that the exact non-additive potential bi-functional thanks
to the analytical inversion reflect the step structure spatially where the in-
dividual atomic potential shifts oppose. Within DARSEC, I solved the same

model systems with EXX locally approximated by KLI and also calculated $v^{\mathrm{NAD}}[\rho_B, \rho_{tot}](\mathbf{r})$ with a given ground state density. I examined if the step structure appears spatially at the same position for both calculations. I also verified the relation between the height of the step and the gap energy.

4.5 Numerical Calculation

The calculations are obtained on accurate numerical grids using the all-electron program package DARSEC [135]. Consequently, I are restricted to computations of molecules with two atomic centres with spherical symmetry. In DARSEC, the Kohn-Sham equations are solved self-consistently using the high-order finite difference approach [52, 11]. In this work, the stencil was set to 12 for the finite difference. A real-space grid based on prolate-spherical coordinates (see Eq.[1.20] and Eq.[1.19]) is used to describe a system with two atomic centres. The grid is very dense near two centres and increasingly sparse farther from the centres. Due to the cylindrical symmetry of diatomic molecules, the problem is reduced to a two–dimensional one. In the calculations for this work, the systems are defined within 15 Bohr of radius and number of 115×121 grid points. The $\rho_{tot}(\mathbf{r})$ is the ground-state density of the systems performed with the LDA [24, 162].

The calculations are down for two different sub-densities: 1) for when $\int \rho_B(\mathbf{r})d\mathbf{r} = 2.0$, and for the case in which the charge density is not localised into an integer value at the vicinity of the nuclei, $\int \rho_B(\mathbf{r})d\mathbf{r} = 1.5$.

For partitioning the ground state density numerically, I use a smooth distribution function $0 \leq F(z) \leq 2$ that has no cusps and respects the smoothness of the function explained in Section[3.3.2]. The choice for such a function used for the reported result is the Fermi-Dirac distribution function that changes smoothly from value one to zero (Eq.[3.21]). This latter was realised within binary-search algorithm to localised the density around one nucleus.

All the calculations for the exact and the approximated theories were performed based on the same choice of the parameters explained above.

4.6   Results and Discussion

I seek for the SS in exact $v^{\text{NAD}}[\rho_B, \rho_{tot}](\mathbf{r})$ analytically inverted from a ground state density and a partitioned sub-density integrating to two spin-compensated charge density for two diatomic model systems one heteronuclear and one homonuclear. The $v^{\text{NAD}}[\rho_B, \rho_{tot}](\mathbf{r})$ appears in both cases with the SS in the space, where the overlap between two sub-densities is maximal. In Fig.[4.1] and in Fig.[4.2] I compared the related $v^{\text{NAD}}[\rho_B, \rho_{tot}](\mathbf{r})$ with $v_{xc}^{KLI}(\mathbf{r})$ for a heteronuclear and homonuclear model systems respectively.

The DD in $v^{\text{NAD}}[\rho_B, \rho_{tot}](\mathbf{r})$ appears spatially at the same position in which the SS appears on $v_{xc}^{KLI}(\mathbf{r})$ in both models. In the Figs. [4.3] and [4.4] the DD of potentials are zoomed and obviously, it doesn't appear easy to deduce the height of the SS from the $v_{xc}^{KLI}(\mathbf{r})$. Instead, the $v^{\text{NAD}}[\rho_B, \rho_{tot}](\mathbf{r})$ shows more information about the behaviour of the related ground state density where the charge number varies infinitesimally from the integer where the sub-densities overlap.

The zoomed in plot on the overlap region in Fig.[4.3] and Fig.[4.4]shows that compared to $v_{xc}^{KLI}(\mathbf{r})$, the step appears at the vicinity of the inflection point of the in the $v^{\text{NAD}}[\rho_B, \rho_{tot}](\mathbf{r})$ closer to the first argument of the potential, here, $\rho_B(\mathbf{r})$. This is true for both the heteronuclear and homonuclear model systems. This means the second derivative nor the third order of the $v^{\text{NAD}}[\rho_B, \rho_{tot}](\mathbf{r})$ is zero where the step happens regarding the step position from KLI.
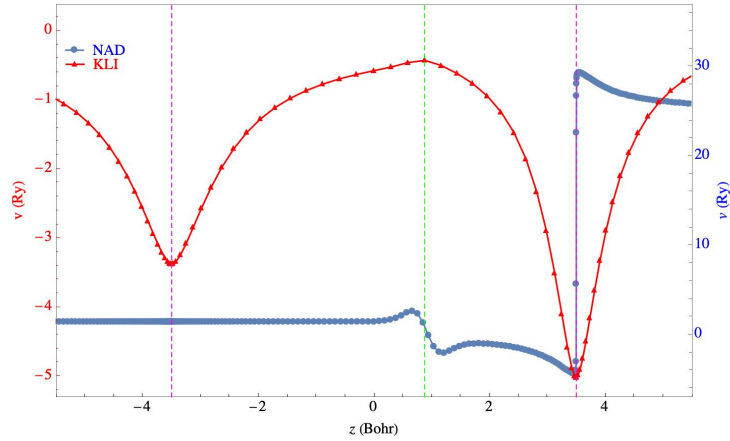
Figure 4.1: In search of the Step Structure on the exact $v^{\text{NAD}}[\rho_B, \rho_{tot}(\mathbf{r})]$ from LDA density input through the comparison of it with the location of the Step Structure on the curve of the $v_{xc}^{\text{OEP-KLI}}(\mathbf{r})$; System: HeLi$^+$ where He is at $(0, 0, -3.5)$ Bohr and Li is at $(0, 0, 3.5)$ Bohr; Blue line: $v^{\text{NAD}}[\rho_B, \rho_{tot}(\mathbf{r})]$; Red Line: $v_{xc}^{\text{OEP-KLI}}(\mathbf{r})$; Vertical brown line: nuclei; Vertical green line: the location of the Step.
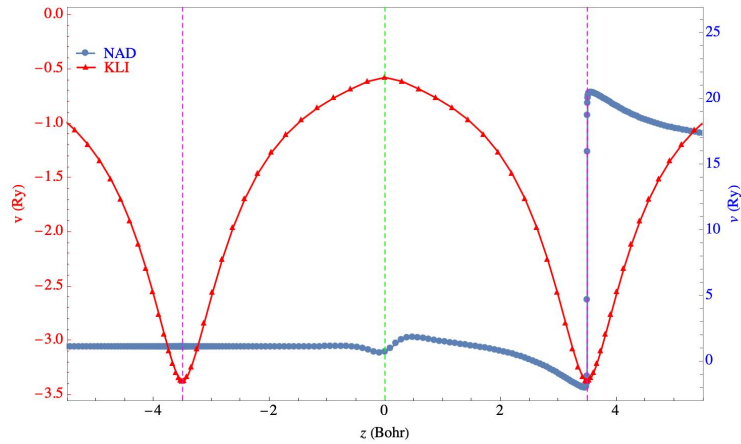
Figure 4.2: Comparing the position Step Structure on the exact $v^{\text{NAD}}[\rho_B, \rho_{tot}(\mathbf{r})]$ from LDA density with the Step Structure on the curve of the $v_{xc}^{\text{OEP-KLI}}(\mathbf{r})$; System: He-He where He is at $(0, 0, -3.5)$ Bohr and He is at $(0, 0, 3.5)$ Bohr; Blue line: $v^{\text{NAD}}[\rho_B, \rho_{tot}(\mathbf{r})]$; Red Line: $v_{xc}^{\text{OEP-KLI}}(\mathbf{r})$; Vertical brown line: nuclei; Vertical green line: the location of the Step.

We need to dig more in the results for the heteronuclear system but the step position at first glance is expected to be exactly at the middle of the interatomic distance for a homonuclear model. In fact, it is not exactly the $v^{\text{NAD}}[\rho_B, \rho_{tot}](\mathbf{r})$ that tells us about the exact position of the step. The difference between

the exact analytically inverted potential (so-noted as $v_s^{\text{EXACT}}[\rho_{A/B}](\mathbf{r})$) of the density of the separated systems ($v_s^{\text{EXACT}}[\rho_B](\mathbf{r})$ or $v_s^{\text{EXACT}}[\rho_A](\mathbf{r})$) can provide the exact position of the SS. In the end what is obvious and the $v^{\text{NAD}}[\rho_B, \rho_{tot}](\mathbf{r})$ or $v^{\text{NAD}}[\rho_A, \rho_{tot}](\mathbf{r})$ have to reflect is that the inflection point of the curve occurs in the vicinity of the SS in the exact potential. In section 4.6.3, the exact position of the SS from analytically inverted potential together with the correct gap energy will be discussed.
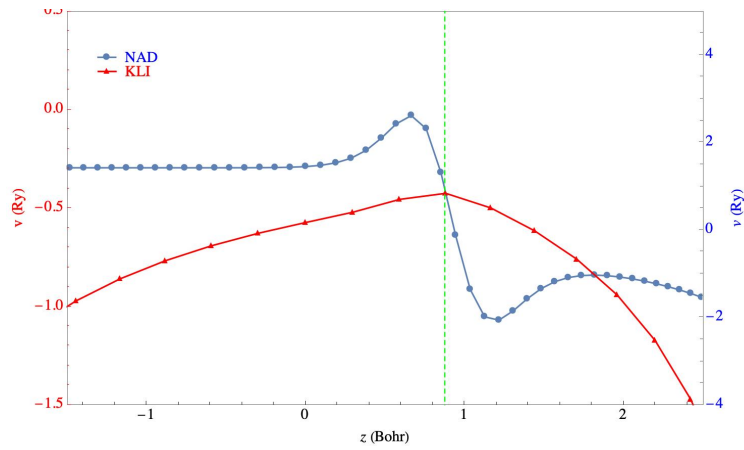
Figure 4.3: Zoom-in representation of the potentials around the overlap region between $\rho_A(\mathbf{r})$ (around Li) and $\rho_B(\mathbf{r})$ (around He) in search of the Step on the exact potential bi-functional (optained from LDA density); System: HeLi$^+$ where He is at $(0, 0, -3.5)$ Bohr and Li is at $(0, 0, 3.5)$ Bohr; Blue line: $v^{\text{NAD}}[\rho_B, \rho_{tot}(\mathbf{r})]$; Red Line: $v_{xc}^{\text{OEP-KLI}}(\mathbf{r})$; Vertical green line: the location of the Step.
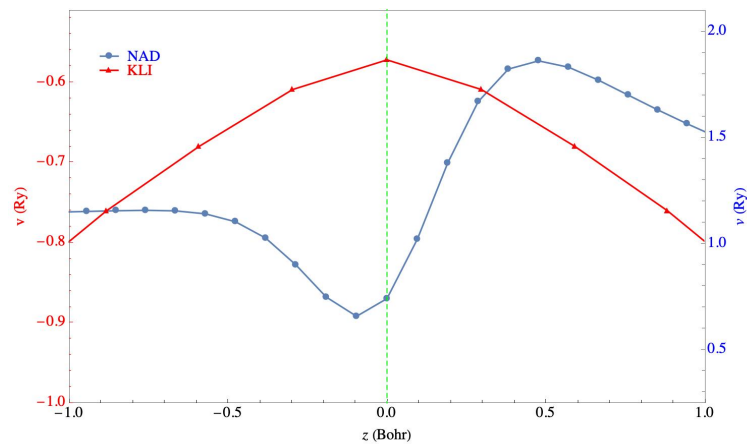
Figure 4.4: Zoom-in representation of the potentials around the overlap region between $\rho_A(\mathbf{r})$ (around He at the right) and $\rho_B(\mathbf{r})$ (around He at the left) in search of the Step on the exact potential bi-functiona; System: He-He where He is at $(0, 0, -3.5)$ Bohr and Li is at $(0, 0, 3.5)$ Bohr; Blue line: $v^{\mathrm{NAD}}[\rho_B, \rho_{tot}(\mathbf{r})]$; Red Line: $v_{xc}^{\mathrm{OEP\text{-}KLI}}(\mathbf{r})$; Vertical green line: the location of the Step.

4.6.1 The Exact Position of the Step

The origin of the exact position of the Step is based on the information carried by the SS is predicted to happened in the curve of the $v^{\text{NAD}}[\rho_B, \rho_{tot}(\mathbf{r})]$ where the overlap between $\rho_B(\mathbf{r})$ and $\rho_A(\mathbf{r})$ occurs to be maximal. The $\rho_A(\mathbf{r}) = \rho_{tot}(\mathbf{r}) - \rho_B(\mathbf{r})$ where for the specific system models used in this work the $\int \rho_A(\mathbf{r})d\mathbf{r} = 2$.

Although the position of the step accurately appeared on the $v^{\text{NAD}}[\rho_B, \rho_{tot}(\mathbf{r})]$ but its exact position remains ambiguous on the curve. If the exact position of the step be directly related to the difference of the sub-densities, then the step has to happen on the local critical point of the curve $\Delta v(\mathbf{r})] = v_s[\rho_A](\mathbf{r}) - v_s[\rho_B](\mathbf{r})$.
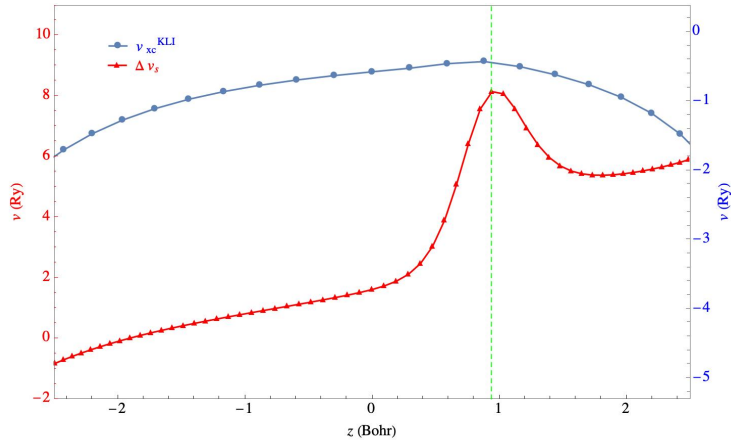
Figure 4.5: Deducing the position of the step from the difference between $v_s[\rho_A]$ and $v_s[\rho_B]$; System: HeLi$^+$ where He is at $(0,0,-3.5)$ Bohr and Li is at $(0,0,3.5)$ Bohr; Red line: $\Delta v(\mathbf{r}) = v_s[\rho_A](\mathbf{r}) - v_s[\rho_B](\mathbf{r})$; Blue Line: $v_{xc}^{\text{OEP-KLI}}(\mathbf{r})$; Vertical green line: the location of the Step.
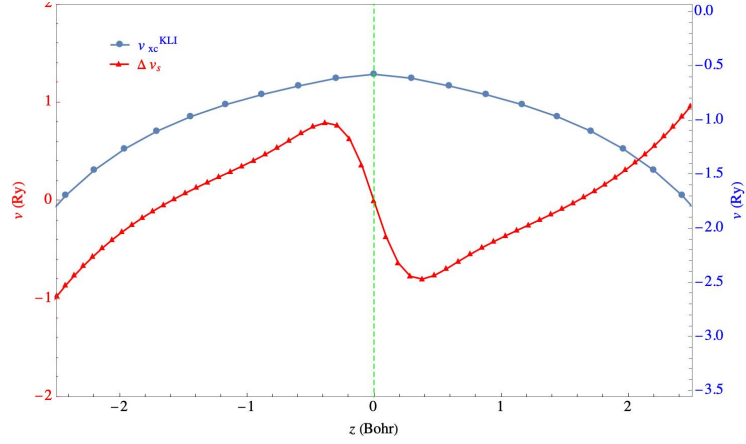
Figure 4.6: Deducing the position of the Step from the difference between $v_s[\rho_A]$ and $v_s[\rho_B]$; System: He-He where He is at $(0, 0, -3.5)$ Bohr and He is at $(0, 0, 3.5)$ Bohr; Red line: $\Delta v(\mathbf{r}) = v_s[\rho_A](\mathbf{r}) - v_s[\rho_B](\mathbf{r})$; Blue Line: $v_{xc}^{\text{OEP-KLI}}(\mathbf{r})$; Vertical green line: the location of the Step.

The difference between charge densities $\Delta v(\mathbf{r})$ is plotted in Fig.[4.5] and compared to the $v_{xc}^{\text{OEP-KLI}}(\mathbf{r})$. Although, OEP being locally approximated by the KLI theory is highly accurate but might vary slightly from the exact $v_{xc}(\mathbf{r})$. After all, the $v_{xc}^{\text{OEP-KLI}}(\mathbf{r})$ is the best available candidate to evaluate the SS of the $v^{\text{NAD}}[\rho_B, \rho_{tot}(\mathbf{r})]$.

The position of the step shown in Fig.[4.5] from two theories although are infinitesimally dis-matched (about 0.04 Bohr) but is a good confirmation of the accuracy of the $v^{\text{NAD}}[\rho_B, \rho_{tot}](\mathbf{r})$. In Fig.[4.6] the results are shown for He-He model system and this time both theory shows exactly the same position for the SS in both curves.

4.6.2   LDA vs KLI and $v^{\mathbf{NAD}}[\rho_B, \rho_{tot}^{\mathbf{LDA}}]$

The SS as it's been already mentioned previously is one of the properties of the exact potential. Now that the $v^{\mathrm{NAD}}[\rho_B, \rho_{tot}(\mathbf{r})]$ provides precisely this information, it could be used as a reference for the evaluation of the other theories.
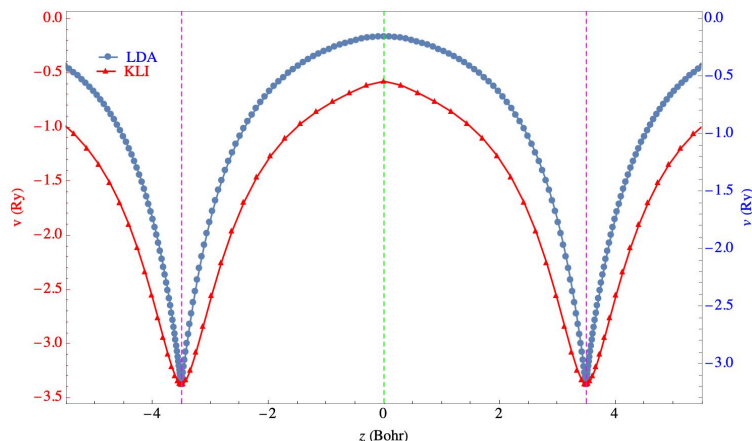
Figure 4.7: Assessment of $v_{xc}^{\mathrm{LDA}}(\mathbf{r})$ from the appearance or nonappearance of the Step on its curve vs the $v_{xc}^{\mathrm{OEP\text{-}KLI}}(\mathbf{r})$; System: He-He where He is at $(0,0,-3.5)$ Bohr and He is at $(0,0,3.5)$ Bohr; Red line: $v_{xc}^{\mathrm{OEP\text{-}KLI}}(\mathbf{r})$; Blue Line: $v_{xc}^{\mathrm{LDA}}(\mathbf{r})$; Vertical green line: the location of the Step.
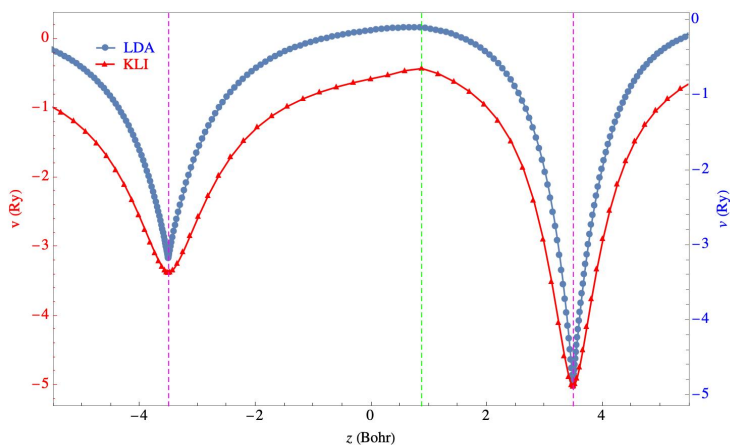
Figure 4.8: Evaluation of $v_{xc}^{\mathrm{LDA}}(\mathbf{r})$ from the appearance or nonappearance of the Step on its curve vs the $v_{xc}^{\mathrm{OEP\text{-}KLI}}(\mathbf{r})$; System: HeLi$^+$ where He is at $(0,0,-3.5)$ Bohr and Li is at $(0,0,3.5)$ Bohr; Red line: $v_{xc}^{\mathrm{OEP\text{-}KLI}}(\mathbf{r})$; Blue Line: $v_{xc}^{\mathrm{LDA}}(\mathbf{r})$; Vertical green line: the location of the Step.

The LDA was already evaluated to be not exact but accurate enough to be used as a low-cost theory within the Kohn-Sham formulation of the DFT. I simply chose this theory to show that it misses the physical information carried by SS on the $v_{xc}(\mathbf{r})$ curve. The $v_{xc}^{\mathrm{LDA}}(\mathbf{r})$ is compared with the $v_{xc}^{\mathrm{OEP\text{-}KLI}}(\mathbf{r})$ and the $v^{\mathrm{NAD}}[\rho_B, \rho_{tot}^{\mathrm{LDA}}]$ for He-He and HeLi$^+$ in Fig.[4.8] and Fig.[4.7], consecutively.

4.6.3 Gap Energy

The Gap Energy is the first physical property to be deduced from the SS. In an section 4.3 I explained that the origin of the step is related to the atomic $\epsilon^{HO/LU}$ or the molecular $\eta_{R/L}^{HO/LU}$ (see Eq.[4.2] and Eq.[4.4]).

Within a heteronuclear diatomic close-shell system, the step height is related to the difference between HOMO and LUMO of the whole system but mathematically can be deduced from both the localised charge densities and the $v^{\mathrm{NAD}}[\rho_B, \rho_{tot}^{\mathrm{LDA}}](\mathbf{r})$.

When it concerns the charge distribution of the sub-densities, the position of the step has to match the local extremum of the charge density that represents the density around the larger nuclei (here $\rho_A(\mathbf{r})$ that is formed around atom Li).

However, when the system concerns a homonuclear diatomic case, the step is expected to occur in the middle of the interatomic distance and the position of the step has to match the intersection of two sub-densities' curves.
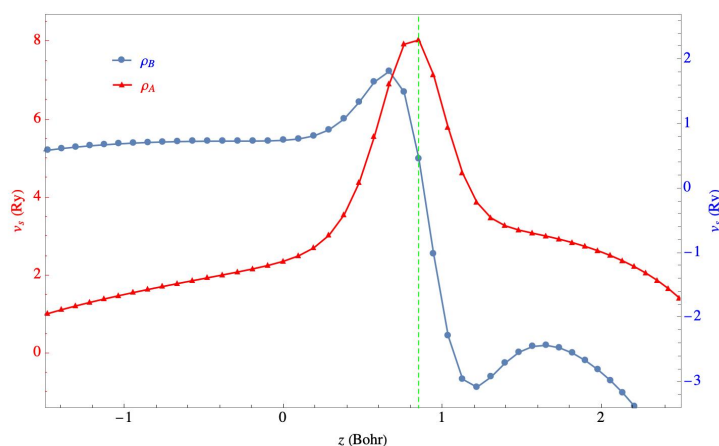
Figure 4.9: Analytical inversion of the potential from $\rho_A(\mathbf{r})$ (localised around Li at the right site of the interatomic axis) and $\rho_B(\mathbf{r})$ (localised around He at the left site of the interatomic axis); System: HeLi$^+$ where He is at $(0, 0, -3.5)$ Bohr and Li is at $(0, 0, 3.5)$ Bohr; Red line: $v_s^{\mathrm{EXACT}}[\rho_A](\mathbf{r})$; Blue line: $v_s^{\mathrm{EXACT}}[\rho_B](\mathbf{r})$; Vertical green line: the location of the Step observed on the $v^{\mathrm{NAD}}[\rho_B, \rho_{tot}(\mathbf{r})]$.

In Fig.[4.9] I plotted the sub-densities for HeLi$^+$ in which the density $\rho_B(\mathbf{r})$ is localised around He atom at the left side. Accurately, the position of the SS occurs at the local critical point of the charged distribution corresponding to

the Li atom at the right side of the interatomic axis.
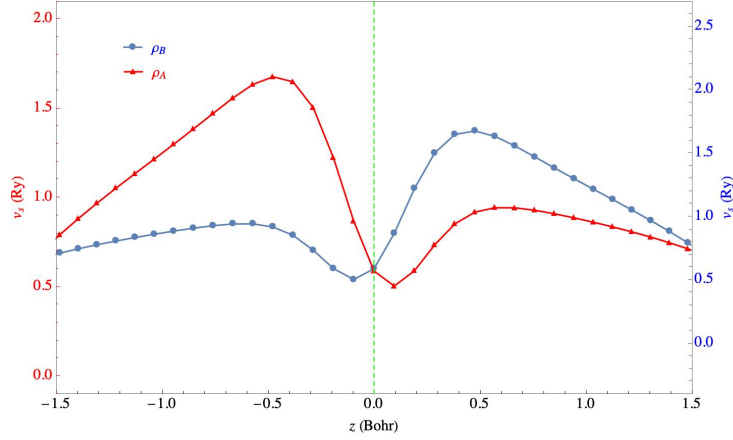
Figure 4.10: Analytical inversion of the potential from $\rho_A(\mathbf{r})$ (localised around He at the right site of the interatomic axis) and $\rho_B(\mathbf{r})$ (localised around He at the left site of the interatomic axis); System: He-He where He is at $(0,0,-3.5)$ Bohr and Li is at $(0,0,3.5)$ Bohr; Red line: $v_s^{\text{EXACT}}[\rho_A](\mathbf{r})$; Blue line: $v_s^{\text{EXACT}}[\rho_B](\mathbf{r})$; Vertical green line: the location of the Step observed on the $v^{\text{NAD}}[\rho_B, \rho_{tot}(\mathbf{r})]$.

Fig.[4.10] shows the position of the step happening accurately at the intersection of the two graphs.

The tangents to the second spatial derivative of the $v^{\text{NAD}}[\rho_B, \rho_{tot}](\mathbf{r})$ (I mean $\frac{d^2 v^{\text{NAD}}[\rho_B, \rho_{tot}](\mathbf{r})}{d\mathbf{r}^2}$) at the vicinity of the step position have been parallel to the interatomic axis. The half of the difference between the energy related to each tangent is the E_g. If that is the correct value, then the exact position of the step must occurs spatially exactly at the mid-distance of two local extrema. If Fig.[4.11] the vertical green line shows where the step happened on $v_{xc}^{\text{OEP-KLI}}(\mathbf{r})$. I see that this line is not happening at the mid-distance of two local extrema of the exact potential. That means the E_g^{EXACT} must be underestimated compared to the E_g^{NAD} for when the localised density is highly comparable with any of the $|\phi_i|^2(\mathbf{r})$. In Table.[4.1] I see clearly this underestimation of the E_g^{EXACT} compared to the E_g^{NAD} by a value about 1.6×10^{-3} Ry. To have a more accurate conclusion from this comparison I also want to see how the energy gap calculated by v^{NAD} varies for non-localised charge density.
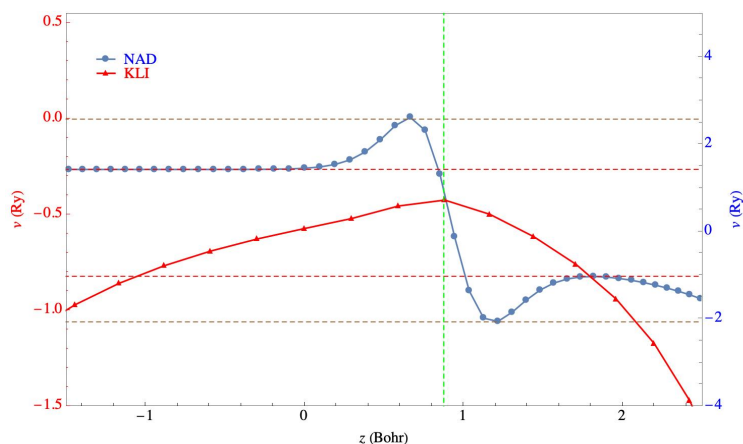
Figure 4.11: Finding the gap energy from the exact $v^{\mathrm{NAD}}[\rho_B, \rho_{tot}](\mathbf{r})$; System: HeLi$^+$ where He is at $(0,0,-3.5)$ Bohr and Li is at $(0,0,3.5)$ Bohr; Vertical green line: location of the step. The E_g is the half value of the difference between the tangent to the inflection points (horizontal brown lines) before the local extremum of the cure at the neighbouring of the step position (horizontal red lines).

4.6.4 Non-localised Electrons

This comparison between the E_g^{EXACT} and the E_g^{NAD} could be not justified if both theories don't share the same density distribution of sub-densities in order to calculate the E_g.

In fact, the $v_{KS}^{\mathrm{OEP\text{-}KLI}}$ was suggested to solve accurately a molecular system in which the molecular orbital densities could partially surpass the integer value while being integrated spatially in the whole space. So, it is more justified if I evaluate the $OEP-KLI$ approach with comparing its E_g^{EXACT} with gap energy obtained from $v^{\mathrm{NAD}}[\rho_{B'}, \rho_{tot}^{\mathrm{LDA}}](\mathbf{r})$ where $\int \rho_{B'}(\mathbf{r})d\mathbf{r} = 2 \pm \delta$.
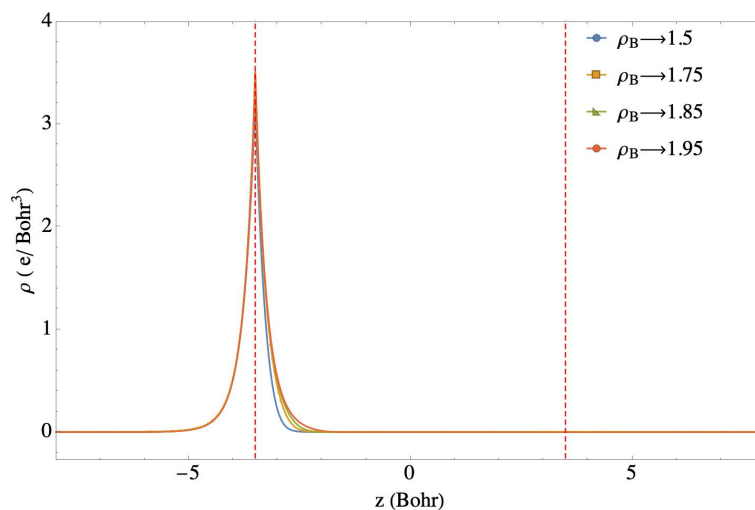
Figure 4.12: Different partial localisation of the charge density around the He nuclei at the left side of the interatomic axis; System: HeLi$^+$ where He is at $(0, 0, -3.5)$ Bohr and Li is at $(0, 0, 3.5)$ Bohr; Vertical brown line: nuclei.

4.6.5   Heteronuclear System

4.6.6   HeLi$^+$

The $v^{\mathrm{NAD}}[\rho_{B'}, \rho_{tot}](\mathbf{r})$ for partially localised charge density shown in Fig.[4.13] compared to inverted potential from the integer localisation of charge density (Fig.[4.1]) shows a significant change on the potential curve. The change of the future of the potential inverted from partial localisation, although appears on the overlap region and close to the nuclei around which the charge density is localised but remain comparable for different partially localised densities.
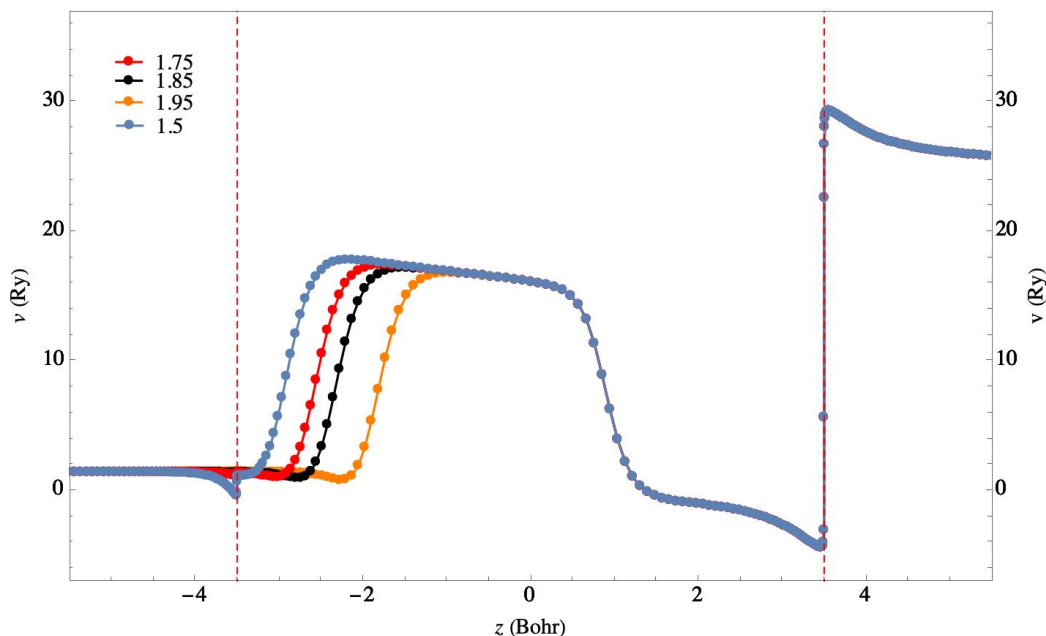
Figure 4.13: The exact $v^{\mathrm{NAD}}[\rho_B, \rho_{tot}](\mathbf{r})$ from analytical inversion for different partial localisation of the charge density around the He nuclei at the left side of the inter-atomic axis plotted in Fig.[4.12]; System: HeLi$^+$ where He is at $(0, 0, -3.5)$ Bohr and Li is at $(0, 0, 3.5)$ Bohr; Vertical brown line: nuclei. The $E_g \simeq 1.44$ (Ry).

The jump of the step in between two atoms happens to have a similar height for different $\rho_B(\mathbf{r})$s. However, the closer the charge localisation is to the integer value, the more the jump (from the left to the right) on the potential is shifted to the right side and the smaller gets the width of the step.

As I asserted previously that the exact position of the Step must occur at the local extremum of the inverted potential from the reminder charge density, it's essential to verify this fact by looking at the $v_s[\rho_i](\mathbf{r})$ for $i = A, B$.

In Fig.[4.14] the position of the step happens exactly at the bump of the $v_s[\rho_A](\mathbf{r})$ and accurately crosses the mid-hight of the change in $v_s[\rho_B](\mathbf{r})$.

The E_g^{NAD} this time is the same as the E_g^{EXACT} (last line in Table.[4.1]).
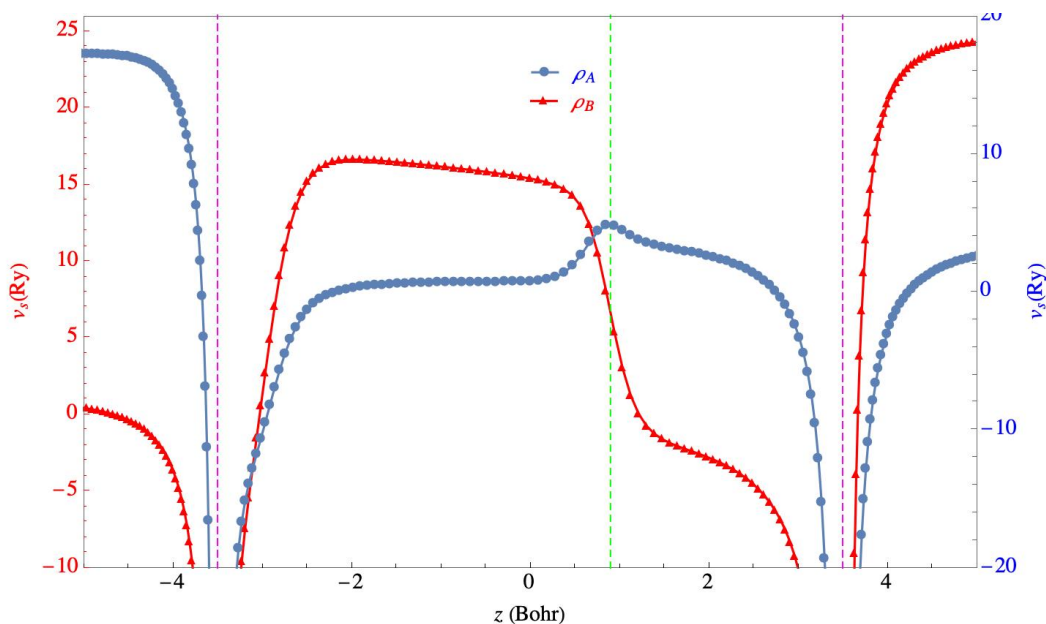
Figure 4.14: Analytical inversion of the potential from $\rho_A(\mathbf{r})$ (localised around Li at the right site of the interatomic axis) and $\rho_B(\mathbf{r})$ (localised around He at the left site of the interatomic axis) for partial localisation($\int \rho_B(\mathbf{r})d\mathbf{r} = 1.5$) of the charge density around the He nuclei at the left side of the interatomic axis plotted in Fig.[4.12]; System: HeLi$^+$ where He is at $(0, 0, -3.5)$ Bohr and Li is at $(0, 0, 3.5)$ Bohr; Vertical brown line: nuclei. The $E_g \simeq 1.44$ (Ry).

Theory	**HOMO** (Ry)	**LUMO** (Ry)	**Gap** (Ry)
LDA	-2.814	-0.415	1.088
KLI	-2.122	-0.683	1.439
NAD	$--$	$--$	1.215
NAD'	$--$	$--$	1.441

Table 4.1: The energy gap from different theories for the model system LiHe$^+$. NAD refers to the potential inverted from the density that integrates to 2 and NAD' corresponds to the potential inverted from a density that integrates to 1.5. All input densities are from LDA.
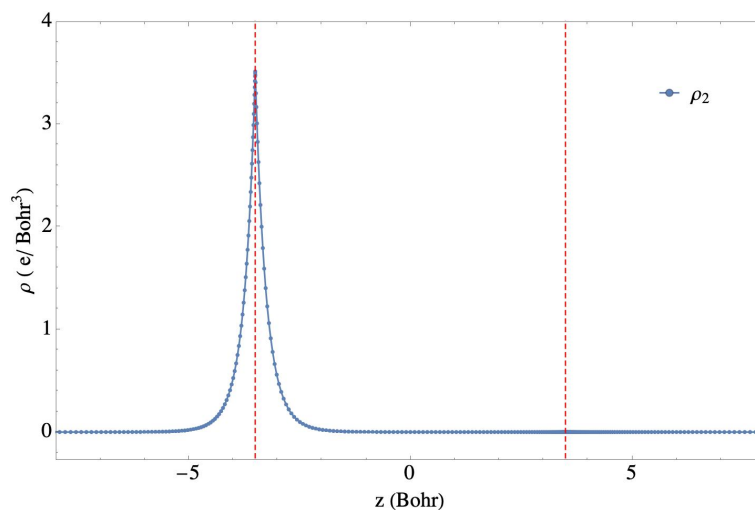
Figure 4.15: 1D representation of the $2s$ orbital $\rho_2(\mathbf{r}) = 2|\phi_2(\mathbf{r})|^2$ for the system HeLi$^+$; He is sited at $(0,0,-3.5)$ Bohr and Li is located at $(0,0,3.5)$ Bohr; Vertical brown line: nuclei.

We plotted the $\rho_2(\mathbf{r}) = 2|\phi_2(\mathbf{r})|^2$ in Fig.[4.15] and showed the $\Delta\rho(\mathbf{r}) = \rho_2(\mathbf{r}) - \rho_B(\mathbf{r}) = \rho_1(\mathbf{r}) - \rho_A(\mathbf{r})$ if Fig.[4.16] for different partially localised charge densities.
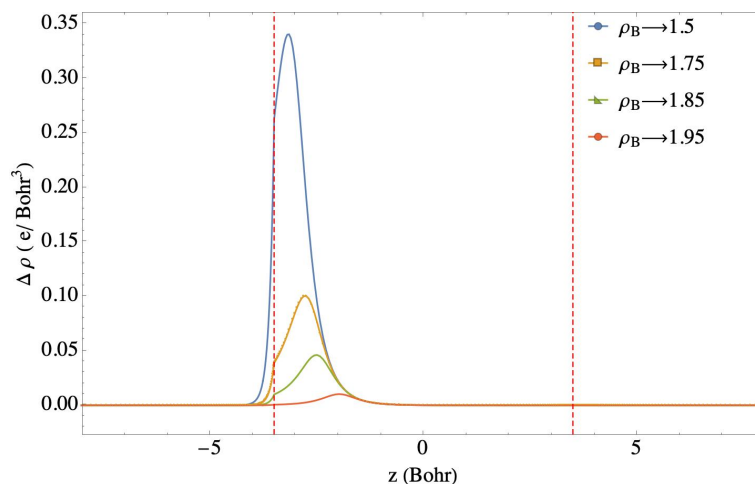
Figure 4.16: Variation of the partially localised $\rho_B(\mathbf{r})$ from the $2s$ orbital-density around the He nuclei; System: HeLi$^+$; He is sited at $(0,0,-3.5)$ Bohr and Li is located at $(0,0,3.5)$ Bohr; Vertical brown line: nuclei; coloured curves: $\Delta\rho(\mathbf{r}) = \rho_2(\mathbf{r}) - \rho_B(\mathbf{r}) = \rho_1(\mathbf{r}) - \rho_A(\mathbf{r})$ for $1.5 \le \int \rho_B(\mathbf{r})d\mathbf{r} \le 1.95$.

The Analytically inverted potential bi-functional needs to predict the missing charge to compensate $\rho_B(\mathbf{r})$ to become a ground state orbital density.

4.6.7   HLi

To verify the $v^{\mathrm{NAD}}[\rho_{B'}, \rho_{tot}](\mathbf{r})$ for more realistic system, the HLi molecule was chosen to be studied. First I take a look at the first orbital density distribution in the space to understand its locality (Fig.[4.17]).
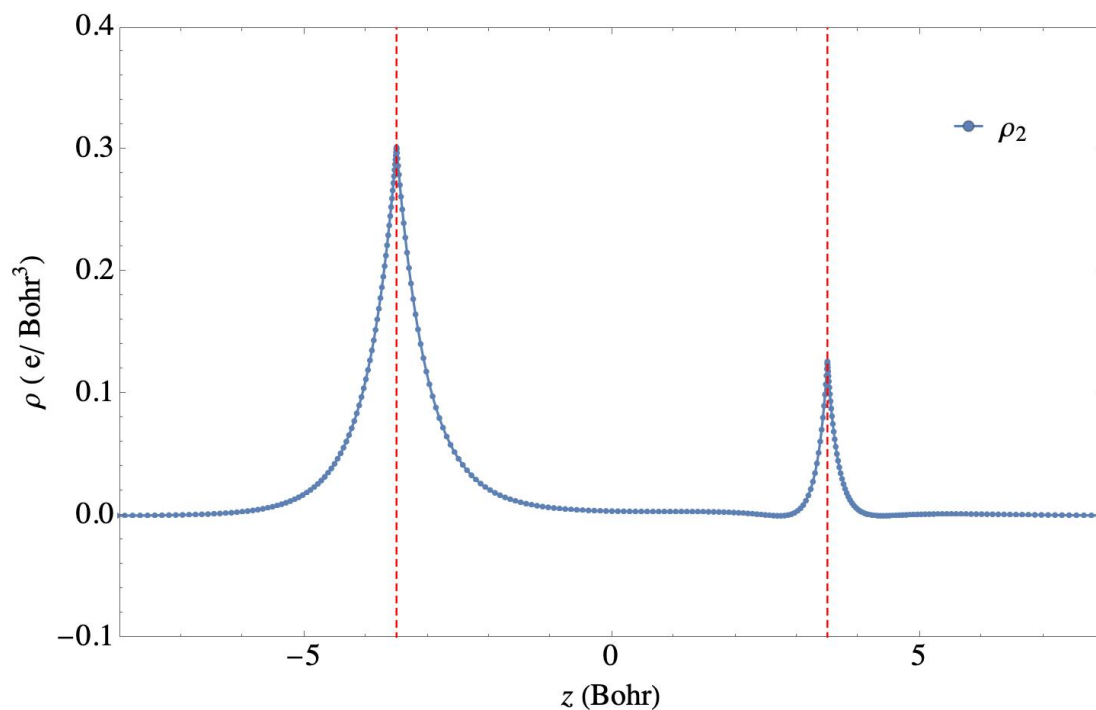
Figure 4.17: 1D representation of the Orbital density; System: HLi; H at $(0, 0, -3.5)$ Bohr and Li at $(0, 0, 3.5)$ Bohr; the density is $\rho_2(\mathbf{r}) = 2|\phi_2(\mathbf{r})|^2$

Obviously for HLi, the $\rho_B(\mathbf{r})$ nor$\rho_A(\mathbf{r} = \rho_{tot}(\mathbf{r} - \rho_B(\mathbf{r})$ for the condition in which $\int_V \rho_B(\mathbf{r})d\mathbf{r} = 2$ cannot be localised at the vicinity of one of the atoms (Fig.[4.18]).
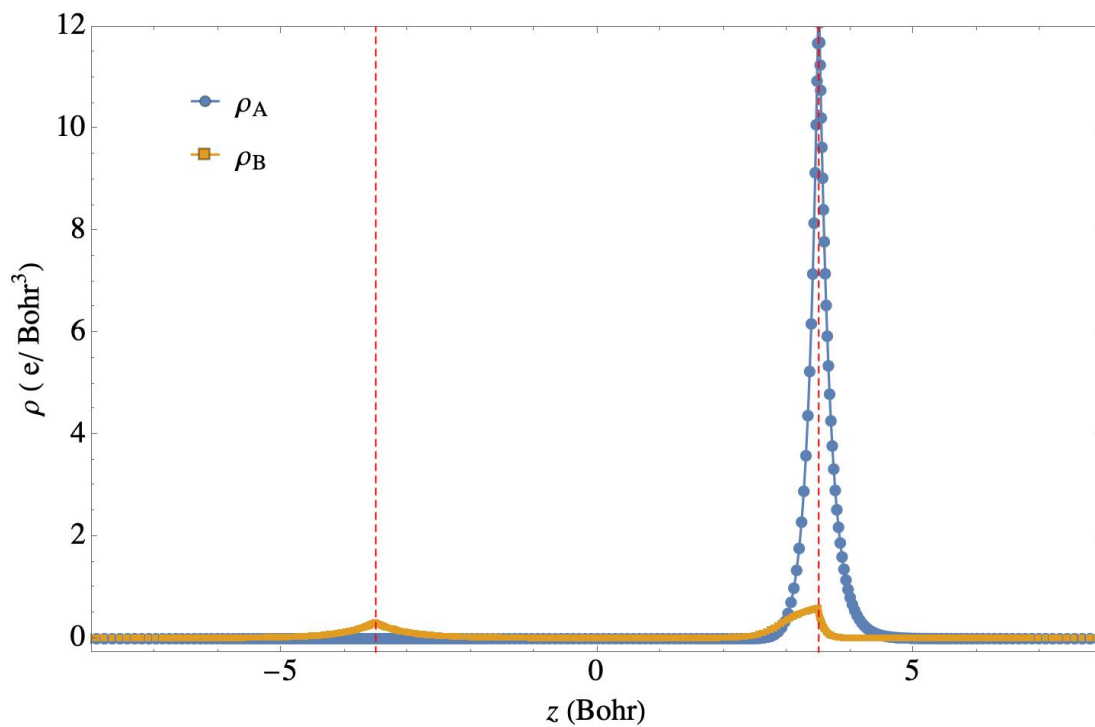
Figure 4.18: 1D representation of the localised density; System: HLi; H at $(0, 0, -3.5)$ Bohr and Li at $(0, 0, 3.5)$ Bohr; Blue mark-line: $\rho_B(\mathbf{r})$ as $\int_V \rho_B(\mathbf{r}) d\mathbf{r} = 2$; Orange mark-line: $\rho_A(\mathbf{r}) = \rho_{tot}(\mathbf{r}) - \rho_B(\mathbf{r})$

Instead the $\rho_B(\mathbf{r})$ become more localised around the H atom at the left side of the interatomic axis if $\int_V \rho_B(\mathbf{r}) d\mathbf{r} = 1.5$ (Fif.[4.19]).
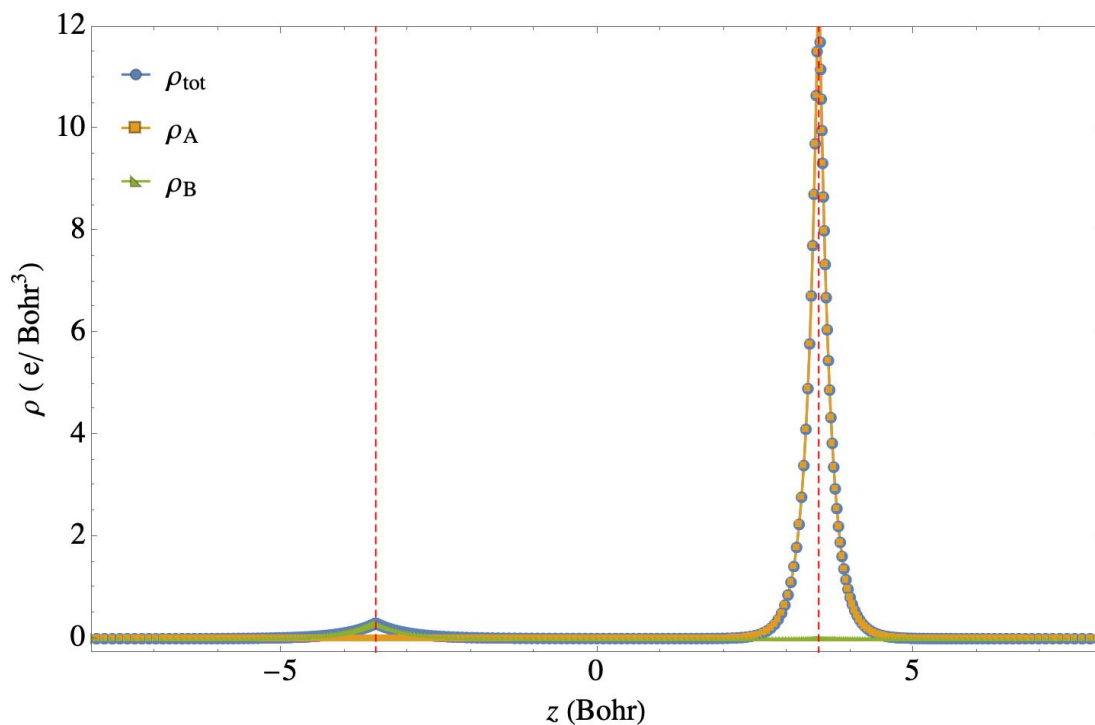
Figure 4.19: 1D representation of the densities; System: HLi; H at $(0, 0, -3.5)$ Bohr and Li at $(0, 0, 3.5)$ Bohr; Blue mark-line: $\rho_{tot}(\mathbf{r})$; Green mark-line: $\rho_B(\mathbf{r})$ as $\int_V \rho_B(\mathbf{r})d\mathbf{r} = 1.5$; Orange mark-line: $\rho_A(\mathbf{r}) = \rho_{tot}(\mathbf{r}) - \rho_B(\mathbf{r})$; Vertical dashed lines: nuclei.

We choose the latter localisation of the $\rho_B(\mathbf{r})$ and I provide the $v_s[\rho_A](\mathbf{r})$ and $v_s[\rho_A](\mathbf{r})$ (Fif.[4.20]) from which I can obtained more information about the gap energy.
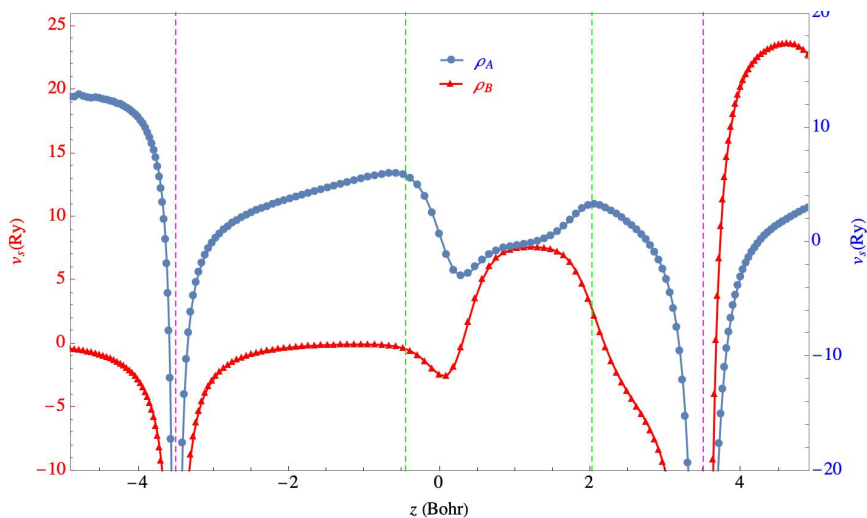
Figure 4.20: Analytical inversion of the potential from $\rho_A(\mathbf{r})$ (localised around Li at the right site of the interatomic axis) and $\rho_B(\mathbf{r})$ (localised around H at the left site of the interatomic axis) for partial localisation($\int \rho_B(\mathbf{r})d\mathbf{r} = 1.5$) of the charge density around the He nuclei at the left side of the interatomic axis plotted in Fig.[4.12]; System: HLi where H is at $(0,0,-3.5)$ Bohr and Li is at $(0,0,3.5)$ Bohr; Vertical brown line: nuclei.

As the $v^{\text{NAD}}[\rho_{B'}, \rho_{tot}](\mathbf{r})$ must carry the information about the difference between $\rho_B(\mathbf{r})$ and $\rho_i\mathbf{r})$ (for $i = 1, 2, 3, ...$), it's essential to know the feature of the $\Delta\rho(\mathbf{r}) = \rho_2(\mathbf{r}) - \rho_B(\mathbf{r}) = \rho_1(\mathbf{r}) - \rho_A(\mathbf{r})$. For different density localisation around the H atom this difference is plotted in Fig.[4.21].
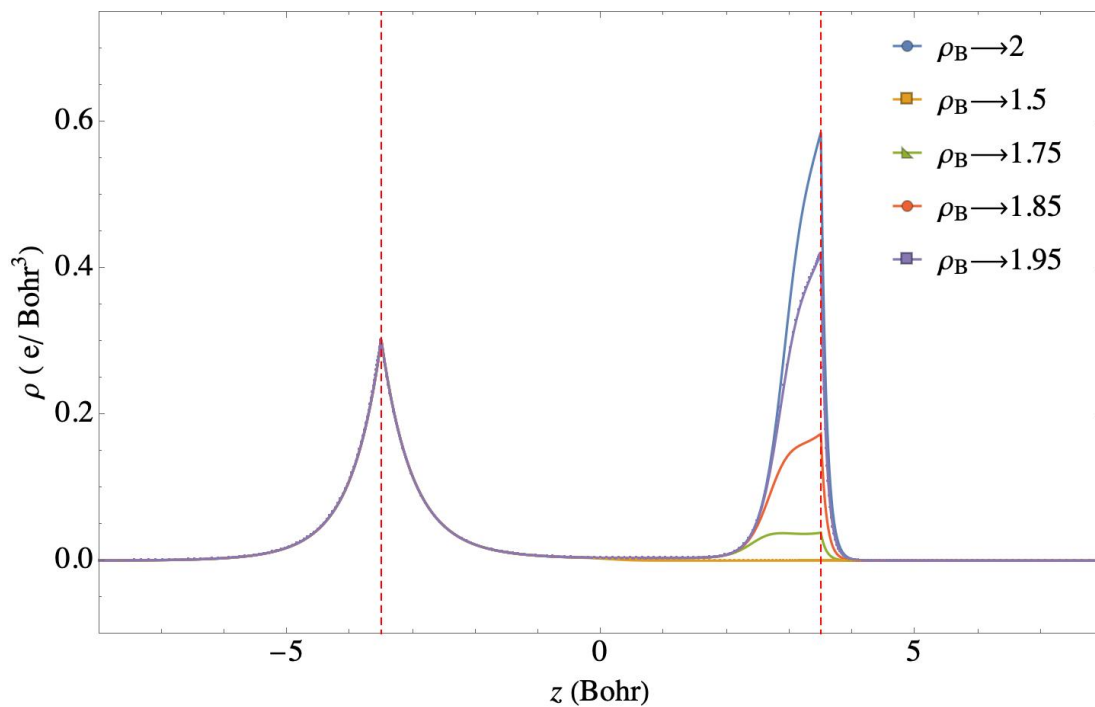
Figure 4.21: Variation of the partially localised $\rho_B(\mathbf{r})$ from the $2s$ orbital-density around the He nuclei; System: HLi; H is sited at $(0,0,-3.5)$ Bohr and Li is located at $(0,0,3.5)$ Bohr; Vertical brown line: nuclei; coloured curves: $\Delta\rho(\mathbf{r}) = \rho_2(\mathbf{r}) - \rho_B(\mathbf{r}) = \rho_1(\mathbf{r}) - \rho_A(\mathbf{r})$ for $1.5 \leq \int \rho_B(\mathbf{r})d\mathbf{r} \leq 2$.

The corresponding $v^{\mathrm{NAD}}[\rho_{B'}, \rho_{tot}](\mathbf{r})$ for different $\rho_B(\mathbf{r})$ is demonstrated in 1D representation in Fig.[4.22].
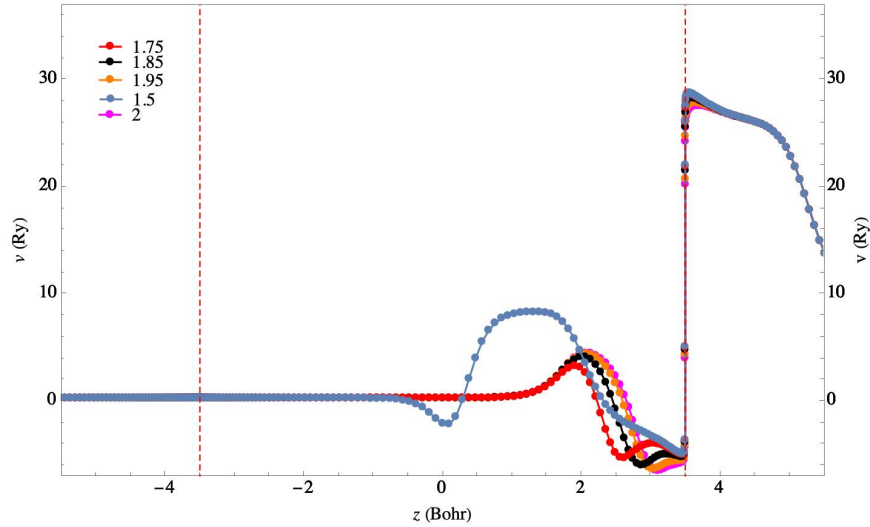
Figure 4.22: The exact $v^{\mathrm{NAD}}[\rho_B, \rho_{tot}](\mathbf{r})$ from analytical inversion for different partial localisation of the charge density around the He nuclei at the left side of the inter-atomic axis plotted in Fig.[4.12]; System: HLi where H is at $(0, 0, -3.5)$ Bohr and Li is at $(0, 0, 3.5)$ Bohr; Vertical brown line: nuclei.

Theory	**HOMO** (Ry)	**LUMO** (Ry)	**Gap** (Ry)
LDA	-0.283	-0.111	0.172
NAD'	$--$	$--$	0.334

Table 4.2: The energy gap from different theories for the model system HLi. NAD' corresponds to the potential inverted from a density that integrates to 1.5.

For the system in which any atom carry a density distribution at its vicinity that integrate into an integer value, the step structure forms very close to the larger atom where the overlap between the density cannot be minimised ultimately. What is obvious is the fact that, even the localised density integrating close to 2 is not localised in the space, but its difference with the orbital density happens to be localised. That's why in Fig.[4.22] I see that the inverted potential from all different $\rho_B(\mathbf{r})$ provide a smooth curve around the H atom and in between the atoms except the potential obtained by $\int_V \rho_B(\mathbf{r})d\mathbf{r} = 1.5$. This latter could be a good candidate from which one can extract the most accurate gap energy from.

It is important to know that the $v^{\mathrm{NAD}}[\rho_B, \rho_{tot}](\mathbf{r})$ obtained form the $\rho_B(\mathbf{r})$ in which $\int_V \rho_B(\mathbf{r})d\mathbf{r} > 1.5$ does not calculate very accurately the gap energy

for a system in which the atoms are forming strong bounding.

4.6.8 Homonuclear System
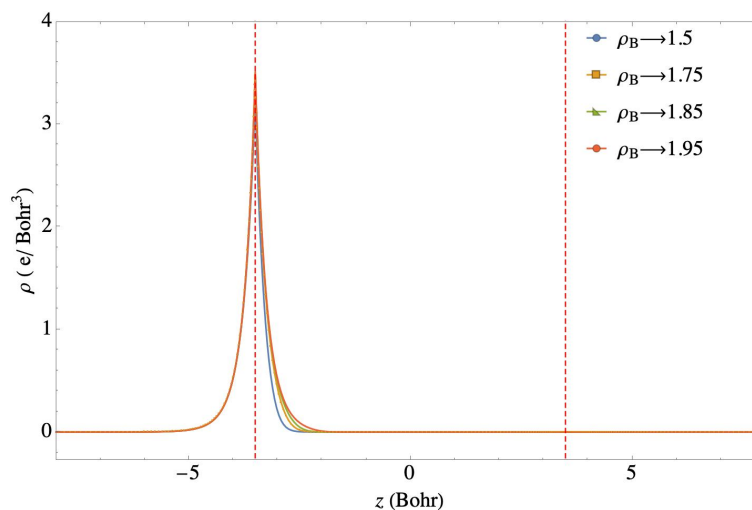
Figure 4.23: Different partial localisation of the charge density around the He nuclei at the left side of the interatomic axis; System: He-He where He is at $(0, 0, -3.5)$ Bohr and other He is at $(0, 0, 3.5)$ Bohr; Vertical brown line: nuclei.
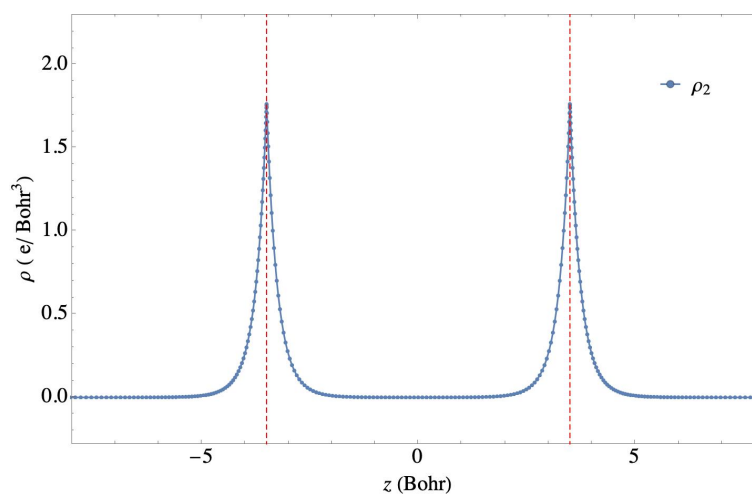
Figure 4.24: 1D representation of the $2s$ orbital $\rho_2(\mathbf{r}) = 2|\phi_2(\mathbf{r})|^2$ for the system He-He; He is sited at $(0, 0, -3.5)$ Bohr and other He is located at $(0, 0, 3.5)$ Bohr; Vertical brown line: nuclei.

Choosing rhoB15:
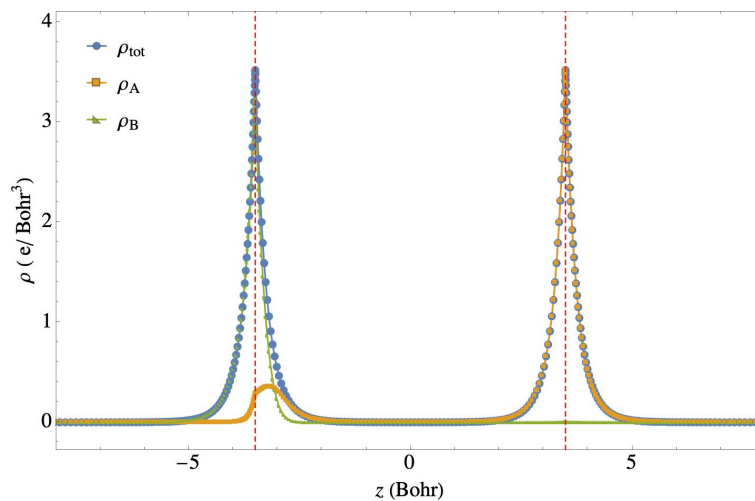
Figure 4.25: 1D representation of the $\rho_B(\mathbf{r})$, $\rho_A(\mathbf{r})$and $\rho_{tot}(\mathbf{r})$for the system He-He; He is sited at $(0,0,-3.5)$ Bohr and other He is located at $(0,0,3.5)$ Bohr; Vertical red line: nuclei.

Theory	HOMO (Ry)	LUMO (Ry)	Gap (Ry)
LDA	-1.14	0.07	1.206
KLI	-1.835	-0.280	1.555
NAD	$--$	$--$	1.4727
NAD'	$--$	$--$	1.555

Table 4.3: The energy gap from different theories for the model system He-He. NAD refers to the potential inverted from the density that integrates to 2 and NAD' corresponds to the potential inverted from a density that integrates to 1.5.
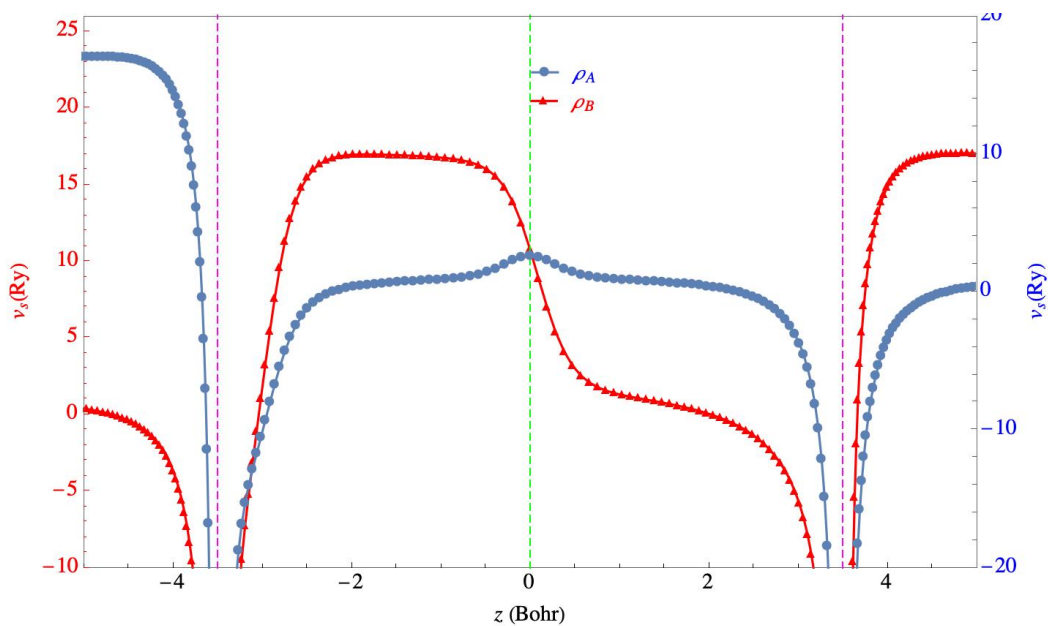
Figure 4.26: Analytical inversion of the potential from $\rho_A(\mathbf{r})$ (localised around He at the right site of the interatomic axis) and $\rho_B(\mathbf{r})$ (localised around He at the left site of the interatomic axis) for partial localisation($\int \rho_B(\mathbf{r})d\mathbf{r} = 1.5$) of the charge density around the He nuclei at the left side of the interatomic axis plotted in Fig.[4.12]; System: He-He where one He is at $(0, 0, -3.5)$ Bohr and another one is at $(0, 0, 3.5)$ Bohr; Vertical brown line: nuclei. The $E_g \simeq 1.555$ (Ry).
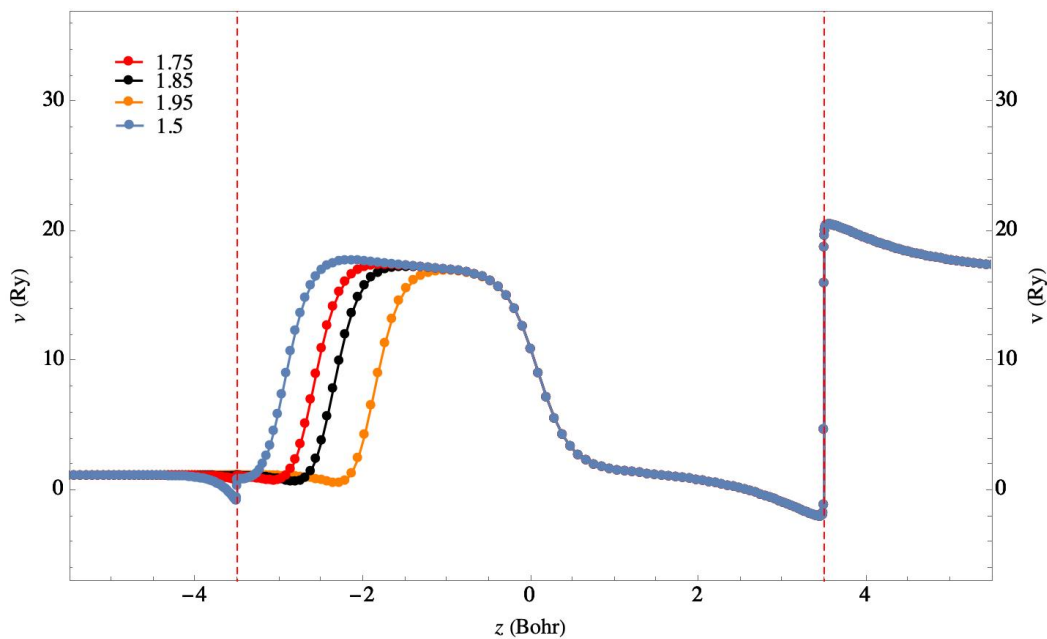
Figure 4.27: The exact $v^{\text{NAD}}[\rho_B, \rho_{tot}](\mathbf{r})$ from analytical inversion for different partial localisation of the charge density around the He nuclei at the left side of the inter-atomic axis plotted in Fig.[4.12]; System: He-He where one He is at $(0, 0, -3.5)$ Bohr and another one sits at $(0, 0, 3.5)$ Bohr; Vertical brown line: nuclei. The $E_g \simeq 1.44$ (Ry).

4.7 Conclusion and Outlook

The exact analytically inverted non-additive potential bi-functional is accurately predicts the position of the step structure. This latter is correct for both cases of integer-localisation of the charge density around nuclei and partially localised density.

The energy gap obtained from the analytically inverted potential is strongly comparable with the one obtained from orbital related DFT model, the OEP-KLI. The difference between two energies becomes negligible when the bi-functional potential is inverted analytically from partially localised charge density. The case related to the partially localised charge density is more realistic case that immitates the partially occupied orbitals. The partially occupied orbitals are the source of the gap energy that must be manifested on the potential curve. This proves that the height of the SS appeared on the curve of the potential is also accurate.

The finding in this work confirms that the low-cost exact $v^{\mathrm{NAD}}[\rho_{B'}, \rho_{tot}](\mathbf{r})$ is a very reliable and accurate candidate to help the common approximations for more relevant calculations of the band gap. It has the advantage of being applicable to the other methods in order to improve them. Such application could be done both numerically within the modification of the potential with the help of the $v^{\mathrm{NAD}}[\rho_{B'}, \rho_{tot}](\mathbf{r})$ in the iterative procedures or analytically modifying the $v_{\mathrm{xc}}(\mathbf{r})$.

The $v^{\mathrm{NAD}}[\rho_B, \rho_{tot}](\mathbf{r})$, provides the exact position of the SS, its height and the correct E_g. I may suggest that this work be repeated by other ground state densities (for example the experimental GS densities or more exact theories such as full CI). The very first guess is that the $v^{\mathrm{NAD}}[\rho_B, \rho_{tot}](\mathbf{r})$ will provide very accurate energy gap if one use one of the suggested inputs.

The least but not the last point to bring up is that the width of the step appearing on the $v^{\mathrm{NAD}}[\rho_B, \rho_{tot}](\mathbf{r})$ inverted from the charge density integrating to a non-integer value must not be neglected. It is possible that some physical interpretation could be deduced from it. The first guess is the spatial probability where the system starts to attract or repulse the electron. This latter is related to the binding energy so it is essential to investigate more in this direction.

Chapter 5

Non-additive Potential bi-functional from Analytical Inversion for Diatomic Systems with $2 + N$ Electrons

5.1 Introduction

In reality the physical systems include more than two atoms with larger number of the electrons. Now that the enough information is accessible about the $v_s^{\text{NAD/inverted}}[\rho_B, \rho_{tot}](\mathbf{r})$ for diatomic model systems of two or four electrons, it is indispensable to understand the behaviour of the potential for larger systems.

In this chapter I study couple of diatomic model systems including more than four electrons but have the capacity based on which, two electrons can be localised around one of the atoms with high precision.

The inversion is analytic for when we invert the potential from a charge density integrating to 0 to 2, however I used the same formula to invert the potential from a charge density integrating to > 2 using the analytical inversion formula. In that case we are not anymore in the regime of exact potential. We use the ground state density calculated from LDA for diatomic atoms stretched about 7 Bohr from each other. The $v_s^{\text{NAD/inverted}}[\rho_B, \rho_{tot}](\mathbf{r})$ is calculated from

Eq.[5.1] for which I localised charge density $\rho_B(\mathbf{r})$ from Eq.[5.1].

$$v_s^{\text{NAD/inverted}}[\rho_B, \rho_{tot}](\mathbf{r}) = v_s[\rho_B](\mathbf{r}) - v_s[\rho_1](\mathbf{r}) \tag{5.1}$$

where $\rho_{tot}(\mathbf{r})$ is an input ground sate density.

$$\rho_B(\mathbf{r}) = \int_v F(z)\rho_{tot}(\mathbf{r})d\mathbf{r} = 2 \tag{5.2}$$

The $F(z)$ is defined in Eq.[3.21]. We also want to understand how the $v_s^{\text{NAD/inverted}}[\rho_A, \rho_{tot}](\mathbf{r})$ (Eq.[5.3]) behaves as the $\int_V \rho_A(\mathbf{r})d\mathbf{r} > 2$.

$$v_s^{\text{NAD/inverted}}[\rho_A, \rho_{tot}](\mathbf{r}) = v_s[\rho_A](\mathbf{r}) - v_{KS}^{\text{LDA}}(\mathbf{r}) \tag{5.3}$$

where

$$\rho_A(\mathbf{r}) = \rho_{tot}(\mathbf{r}) - \rho_B(\mathbf{r}) \tag{5.4}$$

and $\int_v \rho_B(\mathbf{r})d\mathbf{r} = 2$

As the first attempt I decided to pick the atoms from the noble gas group. The fact that those atoms are unwilling to attract an additional electron, the corresponding inverted potentials from both $\rho_B(\mathbf{r})$ and $\rho_A(\mathbf{r})$ will be more forced to a constant value around the atom where the charge density is localised. This will allow us to study the potential's behaviour more accurately elsewhere in the space.

Similarly, the analytical inversion of the non-additive kinetic potential bi-functional is known to be exact if the inversion is done from the density that integrates in the space between 0 and 2. The feature of the analytically inverted $v_s^{\text{NAD/inverted}}[\rho_{A/B}, \rho_{tot}](\mathbf{r})$ remained unknown for the cases in which the $\int_V \rho_{A/B}(\mathbf{r})d\mathbf{r} > 2$. This was because of the available numerical tools that where mainly basis-set dependent, also because the theory were studied previously for strongly overlapping densities.

Also, when the number of the electrons in a system surpass four, the higher orbitals start to form. Those orbitals include nodes at various locations in the space. It is very interesting to see how the $v_s^{\text{NAD/inverted}}[\rho_{A/B}, \rho_{tot}](\mathbf{r})$ is affected by those singularities existing in the charge density. The inverted potential for all calculations was compared to its mathematically alternative formulation $v_s^{\text{NAD/vW}}[\rho_{A/B}, \rho_{tot}](\mathbf{r})$ (see Eq.[3.19]).

Once the results were obtained for the model system of the noble gas, I tried a more realistic diatomic system with 10 electrons. In the next section the results are presented for both case in 1D and 2D representation. The visual interpretation of the 1D plots is given in section 1.2.5.

5.2   Results and Discussion

5.2.1   HeNe

We start first the He-Ne model system with 12 electrons. The ground state density calculated from LDA is shown in Fig.[5.1] known as $\rho_B(\mathbf{r})$. The model system provides the condition that $\rho_B(\mathbf{r})$ can be easily localised around the He atom at the left side of the interatomic axis. The reminder density $\rho_A(\mathbf{r})$ is located around the Ne atom at the right side. Those sub-densities are overlapping very weakly in between the atoms close to Ne.
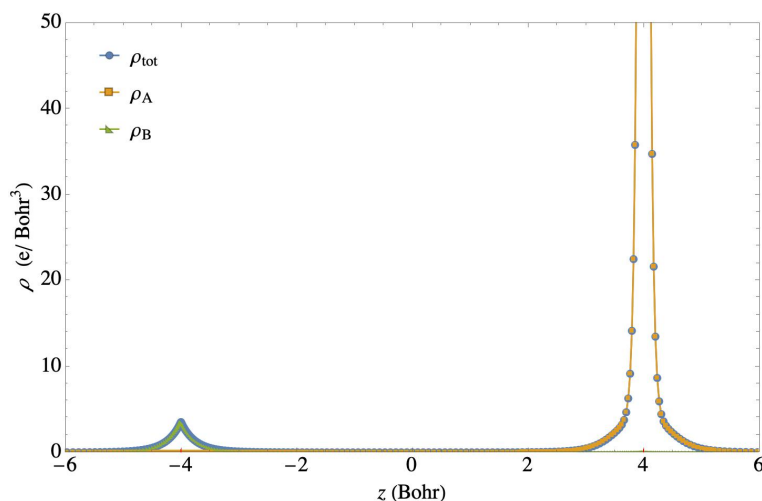
Figure 5.1: System: He-Ne; 1D representation of the $\rho_B(\mathbf{r})$, $\rho_A(\mathbf{r})$ and $\rho_{tot}(\mathbf{r})$; He is sited at $(0, 0, -4)$ and other Ne is located at $(0, 0, 4)$

We first showed interest in understanding the $v_s^{\text{NAD/inverted}}[\rho_A, \rho_{tot}](\mathbf{r})$. Our expectation based on the theory was that the potential shows a harsh wall at the location of the atom He. That is the prove to the fact that the He is saturated by electrons and does not desire to receive an additional electron. However, the behaviour of the potential around the other atom and at the overlap region of the sub-densities was unknown known to us.
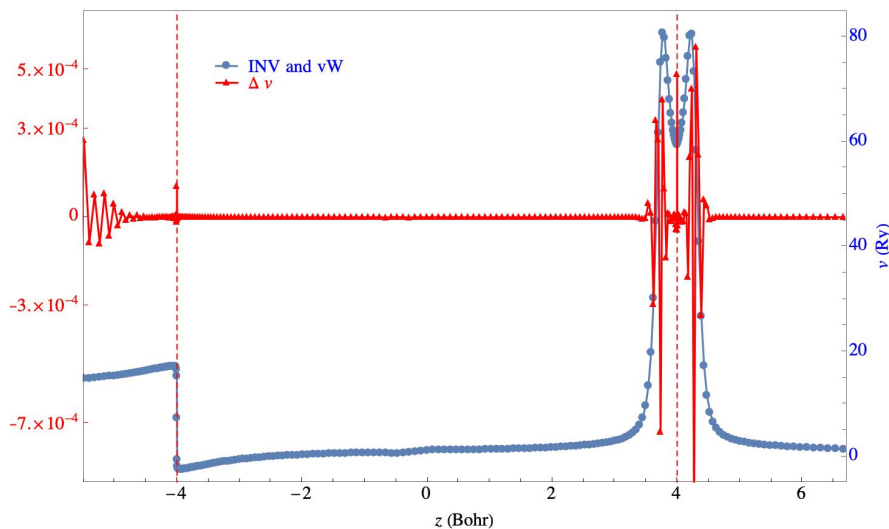
Figure 5.2: Analytically inverted bi-functional potential vs the one from von Weizsäcker theory; System He-Ne; Blue-Mark-Line: $v^{\mathrm{NAD/inverted}}[\rho_A, \rho_{tot}](\mathbf{r})$ superposing $v^{\mathrm{NAD/vW}}[\rho_B, \rho_{tot}](\mathbf{r})$; Red mark-Line: $\Delta v = v^{\mathrm{NAD/inverted}}[\rho_A, \rho_{tot}](\mathbf{r}) - v^{\mathrm{NAD/vW}}[\rho_A, \rho_{tot}](\mathbf{r})$. Vertical Brown line: nuclei.

In Fig.[5.2] it is shown that our expectation about the wall-form of the potential at the He position is confirmed. The potential remains smooth between the nuclei with small bump where the sub-densities' overlap is maximal. The difference between the inverted potential and the von Weizsäcker potential ($\Delta v = v^{\mathrm{NAD/inverted}}[\rho_A, \rho_{tot}](\mathbf{r}) - v^{\mathrm{NAD/vW}}[\rho_A, \rho_{tot}](\mathbf{r})$) appears to be zero in whole space, of course with some numerical so-called noises.

The shape of the $v^{\mathrm{NAD/inverted}}[\rho_A, \rho_{tot}](\mathbf{r})$ at the vicinity of the atom Ne is new to us compared to the potential calculated for all the other model systems with equal and less than four electrons.

We then verified if it is also the case for the $v^{\mathrm{NAD/inverted}}[\rho_B, \rho_{tot}](\mathbf{r})$. In Fig.[5.3] this latter is shown to be confirmed. The good news is that the potential appears to be constant where the charge density os localised.
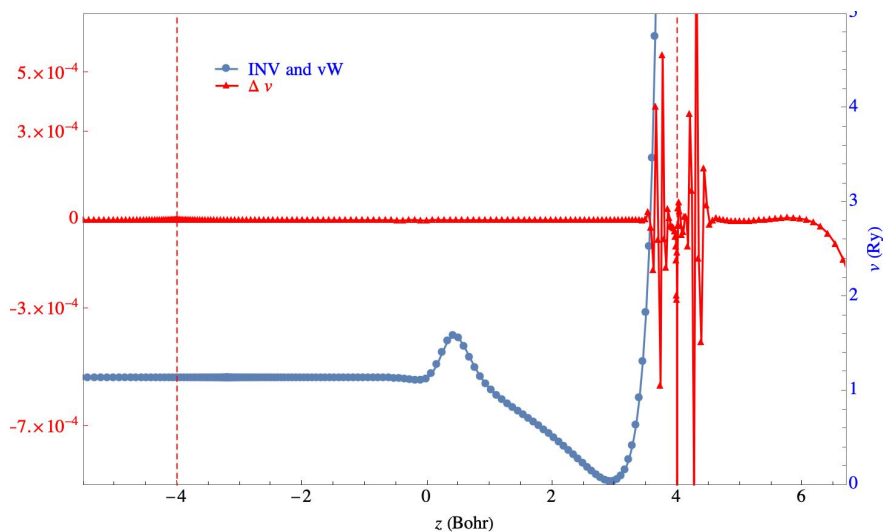
Figure 5.3: Analytically inverted bi-functional potential vs the one from von Weizsäcker theory; System He-Ne; Blue-Mark-Line: $v^{\mathrm{NAD/inverted}}[\rho_B, \rho_{tot}](\mathbf{r})$ superposing $v^{\mathrm{NAD/vW}}[\rho_B, \rho_{tot}](\mathbf{r})$; Red mark-Line: $\Delta v = v^{\mathrm{NAD/inverted}}[\rho_B, \rho_{tot}](\mathbf{r}) - v^{\mathrm{NAD/vW}}[\rho_B, \rho_{tot}](\mathbf{r})$. Vertical Brown line: nuclei.
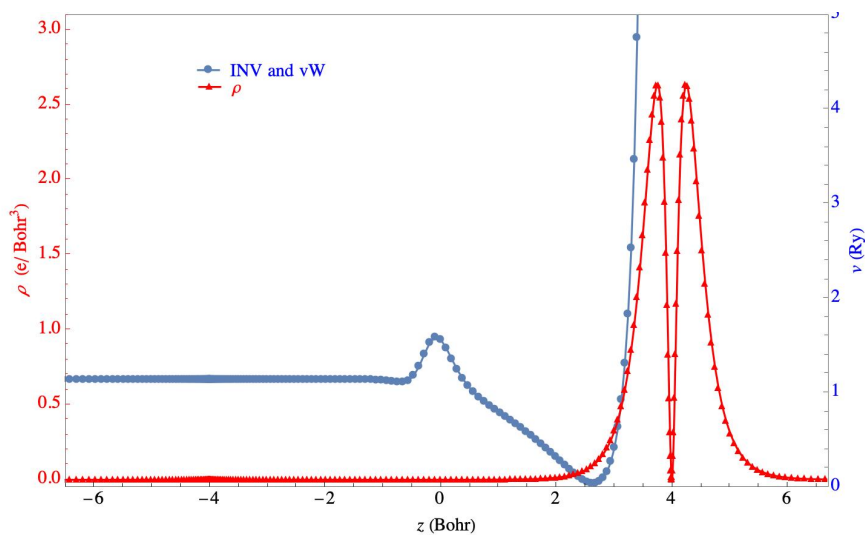
Figure 5.4: Analytically inverted bi-functional potential vs the one from von Weizsäcker theory; System He-Ne; Blue-Mark-Line: $v^{\mathrm{NAD/inverted}}[\rho_B, \rho_{tot}](\mathbf{r})$ superposing $v^{\mathrm{NAD/vW}}[\rho_B, \rho_{tot}](\mathbf{r})$; Red mark-Line: $\rho_4(\mathbf{r}) = 2|\phi_4(\mathbf{r})|^2$. Vertical Brown line: nuclei.

We guessed that the change in the curve of the potential around the atom Ne must be related to the nodes existing in higher level orbitals. To verify that this

change of the potential happens exactly at the same position of the node in an orbital happening, I chose to plot the orbital density $\rho_4(\mathbf{r}) = 2|\phi_4(\mathbf{r})|^2$ together with $v^{\text{NAD/inverted}}[\rho_B, \rho_{tot}](\mathbf{r})$. From the illustration in Fig.[5.4] I can deduce that the potential is clearly affected by the nodes existing in the higher orbitals. That means the $v^{\text{NAD/inverted}}[\rho_B, \rho_{tot}](\mathbf{r})$ provides much more information that what I explained previously in the other chapters.
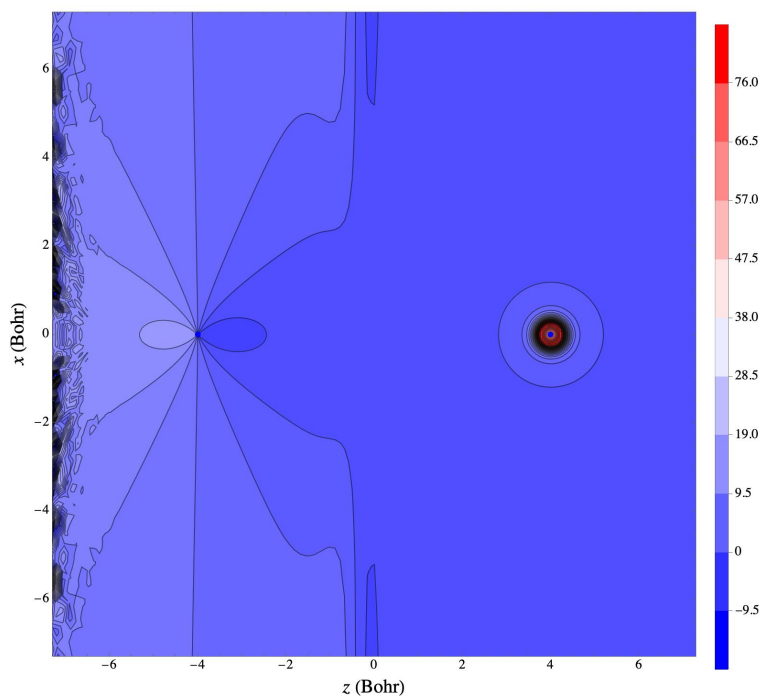
Figure 5.5: 2D representation of the non-additive kinetic potential bi-functional from Eq.[5.1]; System: He-Ne; Two-dimensional representation of $v_s^{\text{NAD/inverted}}[\rho_A, \rho_{tot}](\mathbf{r})$ Ry. Black dots: nuclei.
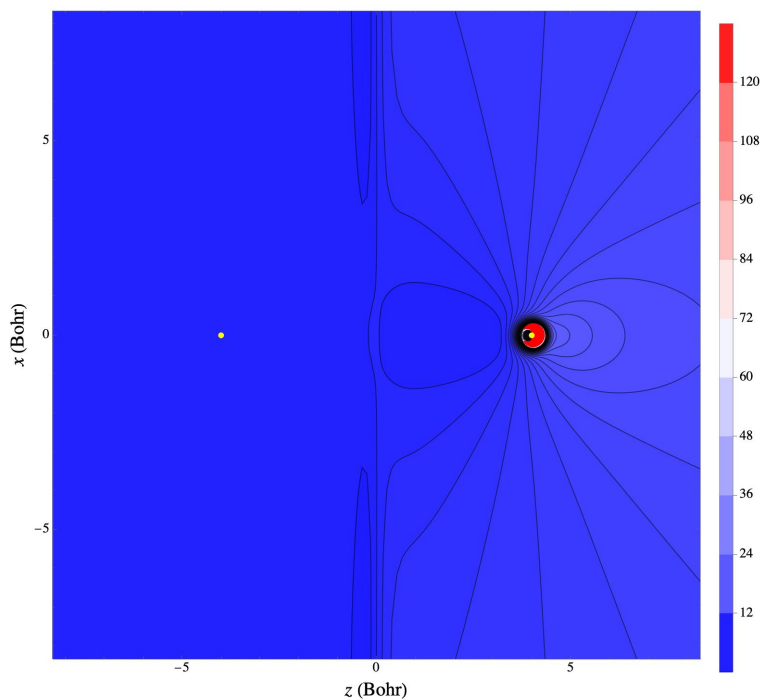
Figure 5.6: 2D representation of the non-additive kinetic potential bi-functional from Eq.[8.17]; System: He-Ne; Two-dimensional representation of $v_s^{\text{NAD/inverted}}[\rho_B, \rho_{tot}](\mathbf{r})$ Ry. Black dots: nuclei.

To see how the analytically inverted potentials behave in whole space, I plotted $v_s^{\text{NAD/inverted}}[\rho_B, \rho_{tot}](\mathbf{r})$ and $v_s^{\text{NAD/inverted}}[\rho_A, \rho_{tot}](\mathbf{r})$ in 2D (Fig.[5.5] and Fig.[5.5]).

Where I interpreted the potentials to be smooth in the space form the 1D representations previously are also confirmed by the last two figures.

5.2.2 LiF^{2+}

In this section I show the results for a more realistic system LiF^{2+}. The motivation of starting the calculation for LiF with ten electrons instead of 12 was to avoid numerical possible artifacts while localising two electrons around the left atom, Li.

Also, the investigation can be generated to further understating of the step structure and related gap energy for when we decide to remove one electron from each atom of LiF.
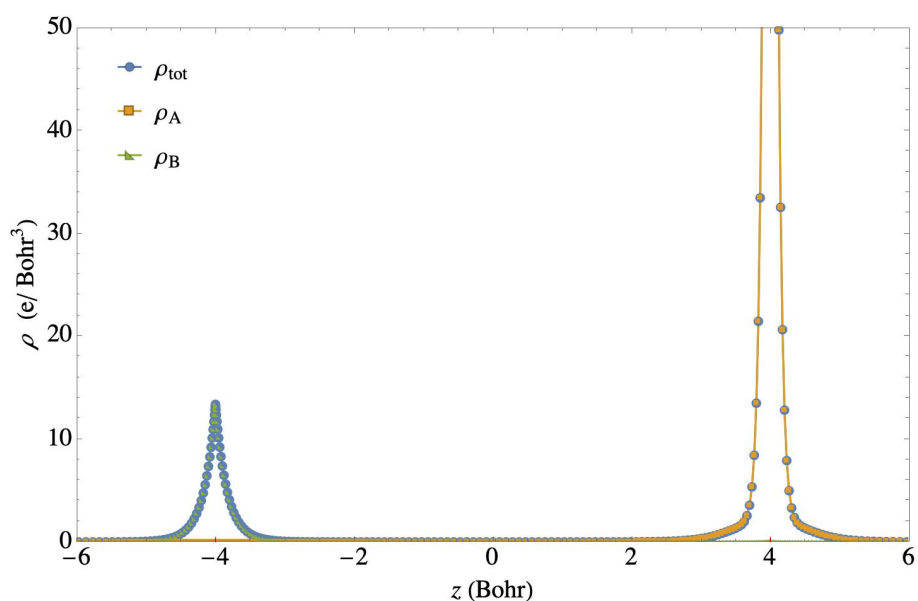
Figure 5.7: System: LiF^{2+}; 1D representation of the $\rho_B(\mathbf{r})$, $\rho_A(\mathbf{r})$and $\rho_{tot}(\mathbf{r})$; Li is sited at $(0, 0, -4)$ and other F is located at $(0, 0, 4)$
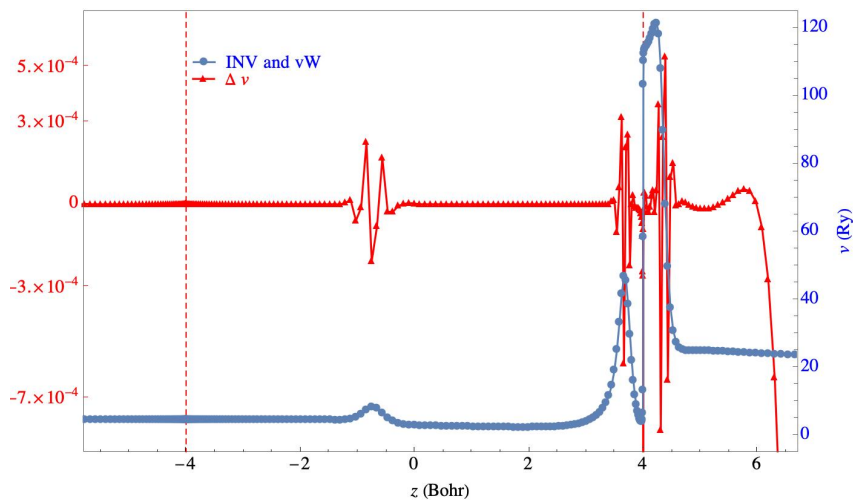
Figure 5.8: Analytically inverted bi-functional potential vs the one from von Weizsäcker theory; System LiF^{2+}; Blue-Mark-Line: $v^{\text{NAD/inverted}}[\rho_B, \rho_{tot}](\mathbf{r})$ superposing $v^{\text{NAD/vW}}[\rho_B, \rho_{tot}](\mathbf{r})$; Red mark-Line: $\Delta v = v^{\text{NAD/inverted}}[\rho_B, \rho_{tot}](\mathbf{r}) - v^{\text{NAD/vW}}[\rho_B, \rho_{tot}](\mathbf{r})$. Vertical Brown line: nuclei.
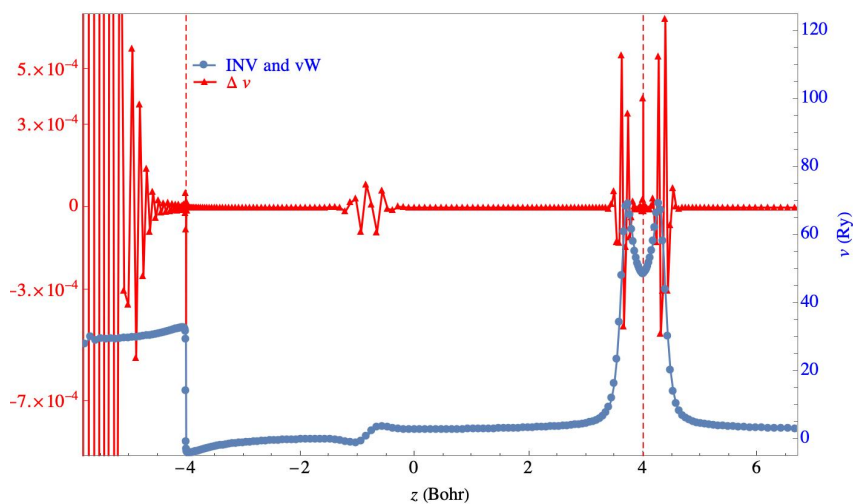
Figure 5.9: Analytically inverted bi-functional potential vs the one from von Weizsäcker theory; System LiF^{2+}; Blue-Mark-Line: $v^{\text{NAD/inverted}}[\rho_A, \rho_{tot}](\mathbf{r})$ superposing $v^{\text{NAD/vW}}[\rho_B, \rho_{tot}](\mathbf{r})$; Red mark-Line: $\Delta v = v^{\text{NAD/inverted}}[\rho_A, \rho_{tot}](\mathbf{r}) - v^{\text{NAD/vW}}[\rho_A, \rho_{tot}](\mathbf{r})$. Vertical Brown line: nuclei.
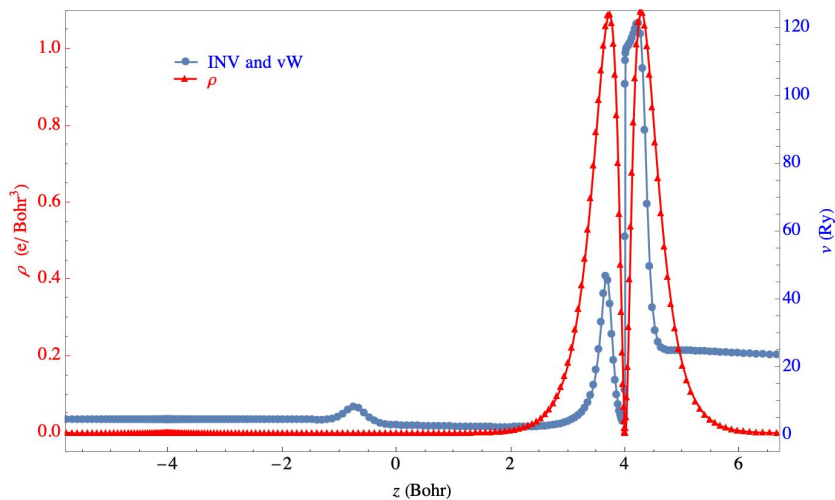
Figure 5.10: Effect of orbital nodes on the inverted potential. Analytically inverted bi-functional potential vs the one from von Weizsäcker theory; System: LiF^{2+}; Blue-Mark-Line: $v^{\text{NAD/inverted}}[\rho_B, \rho_{tot}](\mathbf{r})$ superposing $v^{\text{NAD/vW}}[\rho_B, \rho_{tot}](\mathbf{r})$; Red mark-Line: $\rho_4(\mathbf{r}) = 2|\phi_4(\mathbf{r})|^2$. Vertical Brown line: nuclei.
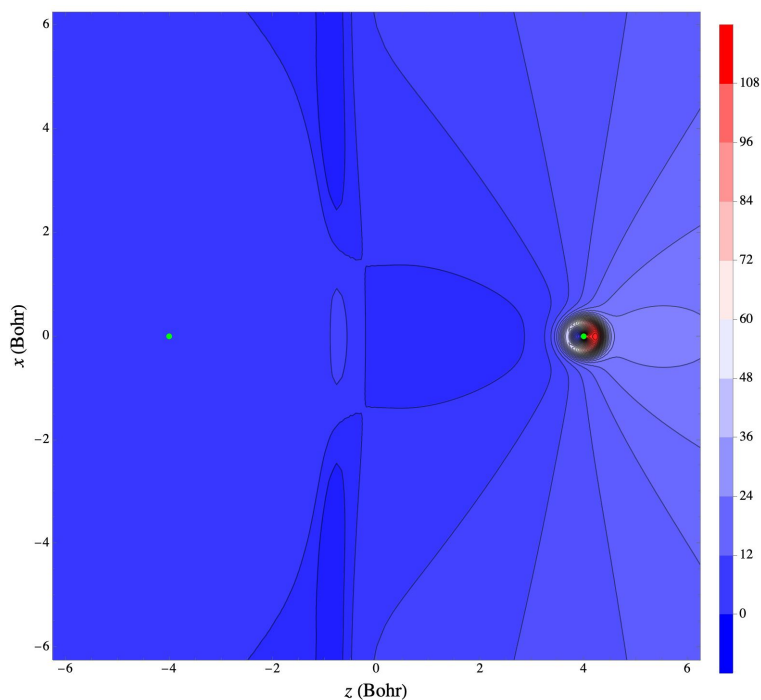
Figure 5.11: 2D representation of the non-additive kinetic potential bi-functional from Eq.[8.17]; System: LiF^{2+}; Two-dimensional representation of $v_s^{\text{NAD/inverted}}[\rho_B, \rho_{tot}](\mathbf{r})$ Ry. Black dots: nuclei.
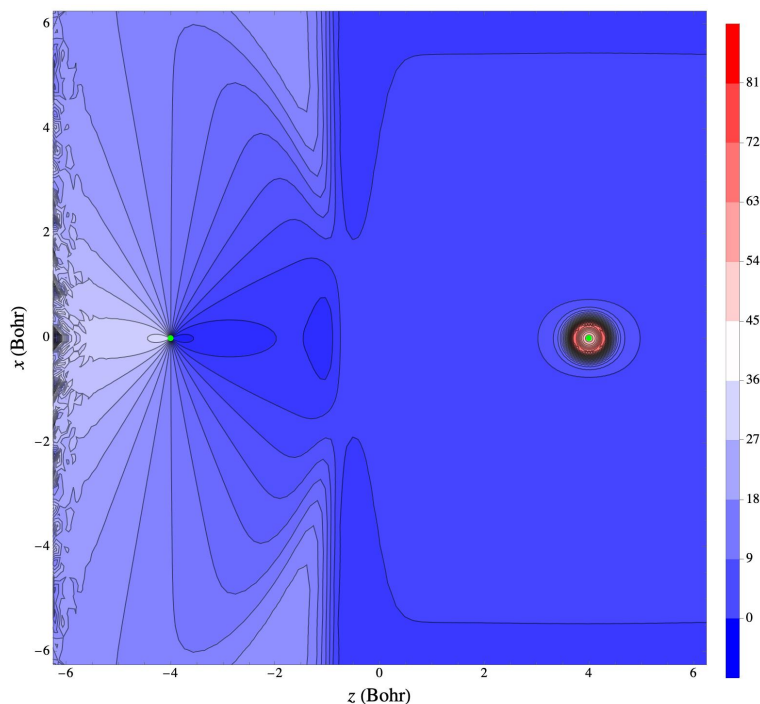
Figure 5.12: 2D representation of the non-additive kinetic potential bi-functional from Eq.[5.1]; System: LiF^{2+}; Two-dimensional representation of $v_s^{\mathrm{NAD/inverted}}[\rho_A, \rho_{tot}](\mathbf{r})$ Ry. Black dots: nuclei.

The explanation of the results for LiF^{2+} is the same as the one given for the system HeNe. Non of the deductions taken for HeNe is violated for LiF^{2+}.

5.3 Conclusion and Outlook

The fact that the results shown in this chapter were accurately according our physical expectation of the potential is very promising step for further investigations. Previously I showed in chapter 3 that the analytically inverted potential is exact if and only if it is inverted from the density related to one or two spin compensated electrons. However, the results of this chapter shows similar behaviour of the non-additive potential functional from the inversion of a charge density corresponding to more than two electrons. This progression must be absolutely evolved and spread to further investigations to know more about the inverted potential. The fact that the inverted potential shows the specific feature where in the space the orbitals involve the nodes is not a hazard. This means that the potential carries important information of the solution of

the system in those regions. Plausibly, it can tell about the spatial probability of the different lobes of the higher orbitals. One of the suggestions is remaining with LiF system and understanding the $v_s^{\mathrm{NAD/inverted}}[\rho_{A/B}, \rho_{tot}](\mathbf{r})$ for different number of the electrons, different interatimic distances, etc. Finding the gap energy form the $v_s^{\mathrm{NAD/inverted}}[\rho_{A/B}, \rho_{tot}](\mathbf{r})$ is necessary step to be done as well.

Chapter 6

Analytically inverted Non-additive Potential bi-Functional from All-electron calculations vs Pseudopotential calculations

6.1 Introduction

To evaluate the existence of the cusp-like singularity on the v^{NAD}, one is to compare the potential obtained from all-electron calculation to one from the pseudopotential calculation. I know that in pseusopotential approach the total potential of a system is smooth at the vicinity of the nuclei and does not represent such singularity. If the feature of the v^{NAD} happens to be comparable from both Pseudopotential and all-electron calculations, one can deduce that the exact analytically inverted v^{NAD} must lack the cusp-like singularities even within an all-electron calculation. In this work, for a simple diatomic heteronuclear model system of four electrons, I compared $v^{\mathrm{NAD}}[\rho_B, \rho_{tot}](\mathbf{r})$ obtained from pseudopotential and all-electron approaches. The same approach as was done in the all-electron calculation is taken to localise two electrons in the vicinity of one atom in a diatomic model system with four-electron with pseudopotential method. The implementation was simpler within Octopus code[189], as the Kohn-Sham analytical inversion was already implemented. In Octopus there

143

exists the choice of ground-state electron density for input from different approximations. In the result section I show our finding for He-He system while using the input density calculated by the LDA approximation. The closure of the chapter includes some ideas for further application of the non-additive kinetic potential bi-functional for pseudopotential-related calculations.

6.2   Theory

In all-electron calculations in real space are subject to the divergence of the wavefunctions at $-\frac{Z}{r}|_{r=0}$ where r signifies the distance between electron and nuclei. This issue is known as Cusp-condition in mechanical quantum simulations. It concerns the singularity problem of the potential which causes non-differentiable wavefunction, for which the pseudopotential introduces a smoother at this point in the space. Among various numerical tricks to deal with this problem, pseudopotential method is the most accurate and frequently used approach as it is the exact reformulation of the atomic calculation. For the cases in which the quantities of interest are mainly related to the chemically active valence electrons, pseudopotential calculation is a great candidate. It focuses on valence electrons by replacing the strong all-electron atomic potential with a weakly interacting pseudopotential. This successfully reproduces the effects of the core electrons on the valence states. Valence electrons occupy the outermost shell or highest energy level of an atom while core electrons are those occupying the innermost shell or lowest energy levels. The advantage of such approximation is substantial for complex and large systems, especially for heavier elements since it significantly reduces the number of eigenpairs to be handled. The pseudopotential which corresponds to the sum of true potential v of the whole system and repulsive potential related to $E_c - E_v$ (core energy and valence energy respectively) reads:

$$v^{ps}(E) = v + \sum_c (E - E_v)|\psi_c\rangle\langle\psi_c|. \tag{6.1}$$

where ψ_c is core wavefunction. The valence and core wavefunctions are related through Eq.[6.2] in which the valence states, ϕ_v are found from with time-independent Schrödinger equation.

$$|\phi_v\rangle = |\psi_v\rangle + \sum_c |\psi_c\rangle\alpha_{cv} \qquad (6.2)$$

where $\alpha_{cv} = \langle\psi_c|\phi_v\rangle$.

Considering the computing time and effort involved, pseudopotential method gives significantly accurate results. It is a good approximation of potential for the cases in which the core electrons of neighbouring atoms interact weakly and for a single atom pseudopotential is exact.

The schematic representation of the pseudopotential versus the all-electron potential is shown in Fig.[6.1][156]. From the region of r smaller than the critical distance r_c from the nuclei, pseudopotential is significantly different from the potential in the all-electron scheme consequently the wavefunctios in that region are not the same for those different approaches. The real and the pseudo wavefunction and potentials match outside a certain cutoff radius r_c.

The solutions are the same for both methods. Since pseudopotential smooths the curve on the cusp position, the solution varies significantly from the one of all-electron calculation. The pseudopotential method is frequently used also to deal with the cusp issue. This latter is briefly explained in the next section.
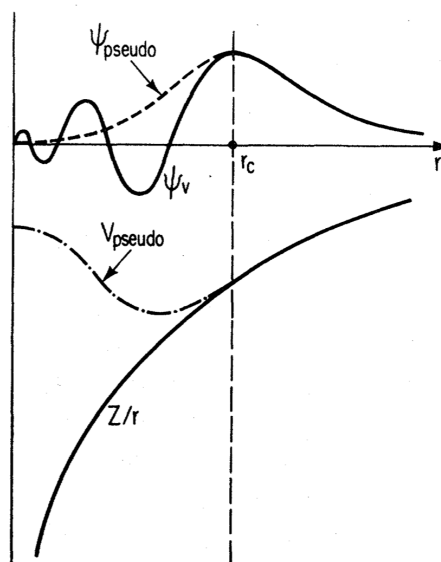
Figure 6.1: Schematic illustration of all-electron (solid lines) and pseudoelectron (dashed lines) potentials and their corresponding wave functions. The radius at which all-electron and pseudoelectron values match is designated r_c[156].

6.3 Numerical Calculations

For the calculations within the pseudopotential approach, Octopus code[5, 4, 138] has been used and developed. Octopus was initially created to solve the time-dependent DFT equations. It uses the Kohn-Sham formulation of DFT and couples a set of single-particle equations to yield many-body ground-state density. For "xc" functional of Kohn-Sham equations, Octopus contains a rich library of approximations that include local, semilocal (implemented as a separate component, known as Libxc library [139]) and even orbital-dependent functionals notably, Optimal Effective Potential (OEP) and hybrid approaches. All data represented within a real-Space grid (Fig.[6.2]), Octopus sums the quantities over the grid for integration and approximates differential operators with high-order finite-difference methods [27].

It is possible to model both finite and periodic systems as the real-space grid is not limited by any particular form of boundary conditions. Octopus has the computational cost advantage with parallel calculation. It is possible to provide the data with different formats for post-analysing the data. The problems are solved in 3D and the possibility of theoretical modelling up to 5D is available within the code. The results could be extracted in 1D, 2D, and 3D. In Fig.[6.2] a 2D ($y = 0$) grids is shown for two atoms sited at $[-2, 0, 0], [2, 0, 0]$. For the purpose of this work the analytical inversion, was implemented in octopus initially for the purpose of "Exact Kohn-Sham potential of correlated finite systems" [82] is used for the sake of Non-Additive Potential Functional.
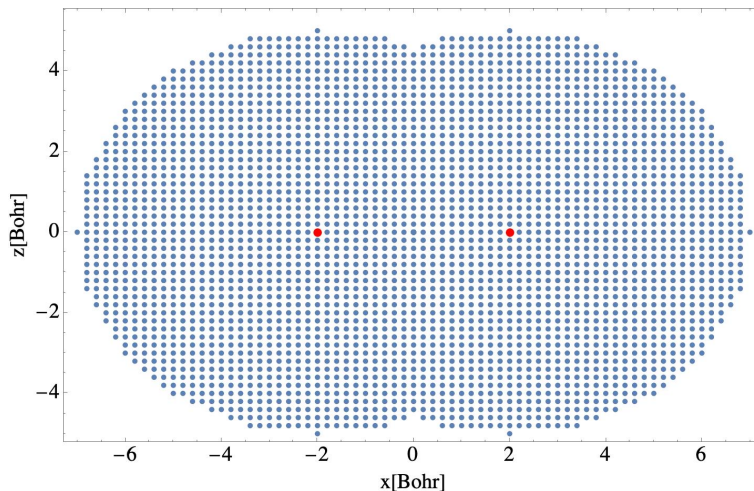
Figure 6.2: Octopus visualization of the real space grid. The blue dots represent position atom centres, with red dots denoting the grid of the coordinate system. Octopus employs the use of a real-space Cartesian grid.

6.4   Results and Discussion

The $v^{\mathrm{NAD}}[\rho_B, \rho_{tot}]$ obtained from the all-electron calculation turned out to have pronounced singularity at the other nuclei (He at the right side) compared to the one from the pseudopotential calculation. Such singularity has physical interpretation and doesn't affect our expectation of the non-additive potential bi-functional. The fact that this singularity does not have a cusp shape is aligned with our understanding in chapter 3. Actually if the nature of the pseudopotential approach was not smoothing the potential around the nuclei, I would obtain similar potential from both calculations. Also the pit form of the $v^{nad/pseudopotential}[\rho_B, \rho_{tot}]$ at the position of the left atom comes from the fact that part of the localised density is trapped in core-electrons in pseudopotential approach. So the potential shows the capacity of the nuclei to absorb slightly the electron at this position. This must not be the case for the potential obtained withing the all-electron calculation and the Fig.[6.3] shows perfectly 0 Ry around the He at the left side.

148
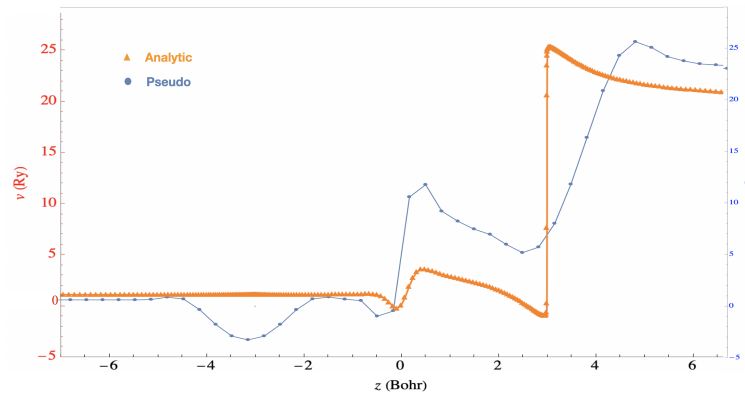
Figure 6.3: For He-He placed at -2 and +2 Bohr, $v^{\text{NAD}}[\rho_B, \rho_{tot}]$ was calculated within pseudopotential approach (grey doted line) and all-electron calculation (orange dotted line).

6.5 Conclusion and Outlook

It is very important to verify such systems in both all-electron and pseudopotential approaches as the physical interpretations of them might change based on the choice of the calculations. For example, studying v^{NAD} a system such as $LiLi^+$ in all-electron calculation, while two electrons are localised around one atom will yield the energy required for the valence electron of the other atom to wander from one atom to the others. In the end the obtained energy from v^{NAD} won't give any exact information for either of the atoms separately. The v^{NAD} for the same system studied in pseudopotential instead will result in exact information about the valence electron in the system as the electron related to $2s$ orbital will be a one-electron system which can be solved exactly within the analytical approach of v^{NAD}.

One of the further and interesting research is to study the behaviour of v^{NAD} within the pseudopotential calculation for H-Rb system as this system contains the atom with particular pseudopotential. For example in the pseudopotential approach, the atom H or He contains no core electrons but only the valence electrons. Now that I have a clear understanding of the exact analytical inversion of v^{NAD} I can use it to evaluate the gap energy of the systems calculated within the pseudopotential theory[169] and FDET. The best models could be the system that contains one or two valance electrons.

Chapter 7

Analytically inverted Non-additive Potential bi-Functional from the Ground-State Density calculated by different Theories

7.1 Introduction

The non-additive potential bi-functional is entirely an orbital-free approach. Its only input is a ground-state charge density. It is important to know how sensitive the $v^{\text{NAD/inverted}}[\rho_B, \rho_{tot}](\mathbf{r})$ is to the input density. In all chapters of this work, I showed the potential obtained from ρ_{in} calculated from LDA. Here I re-evaluate some properties of the potential obtained from different inputs. In this chapter I compare the calculations from the input of the local approximation with the potential obtained from PBE[165] (in GGA family of the DFT framework) and also with the $v^{\text{NAD/inverted}}[\rho_B, \rho_{tot}](\mathbf{r})$ obtained by using the ground-state density calculated by the orbital-dependent theory OEP[180, 187, 71] approximated locally by KLI[98]. In practice I used the EXX[65] functional for the OEP approach.

From the properties of the $v^{\text{NAD/inverted}}[\rho_B, \rho_{tot}](\mathbf{r})$, I mainly compare the height, the position, and width of the step structure at the overlapped-density region between two sub-densities. I also evaluate the level of the analytically in-

verted potential from one admissible density $(v_s[\rho_i](\mathbf{r})$ where $i = 1, 2, A, B, etc)$ around the nuclei.

The width of the step can be interpreted as the exact position in the space where the step structure has to happen. If the feature of the localised density varies from one input density to another, the position of the SS has to be different. However, the width of the SS on the potential curve must not vary significantly from different theories. The width varies only if in one theory the potential is forced to be smooth in the region where the atomic orbitals are overlapping. More the theory is exact more precisely the density at the overlap region is calculated, consequently the width of the SS has to be smaller.

At the end, if the potentials calculated from different input densities happen to be different the exactitude of the analytically inverted potential will be concluded as more reliable. This is true because one of the attribute of a reliable calculation is its uniqueness. That means that even slightly different inputs have to provide different potentials.

The arguments above are tested for the heteronuclear and homonuclear diatomic model systems of four electrons. The results are shown in next section, graphically represented in 1D along the interatomic axis. All calculations are done in the real-space all-electron diatomic system solver DARSEC. Some more calculations and applications are suggested in section 7.3.

7.2   Results and Discussion

Within DARSEC I examined the $v^{\text{NAD/inverted}}[\rho_B, \rho_{tot}](\mathbf{r})$ for two diatomic model systems, one heteronuclear and one mononuclear system. Both include four electrons. I compared the potential for three different inputs. The results for the heteronuclear system are provided by the calculation of the potential from the ground-state density obtained from LDA and OEP-KLI (we shorten the notation to KLI here) methods.

In addition, for the homonuclear model system, I also evaluated the potential using the ground-state density obtained from the PBE calculation.

7.2.1 HeLi$^+$

In Fig.[7.1], the $\rho_{tot}^{\text{LDA}}(\mathbf{r})$ appears to superpose entirely the $\rho_{tot}^{\text{KLI}}(\mathbf{r})$. As the KLI and the LDA theories has totally different approaches to solve the system, it is obvious that their GS densities cannot be the same.
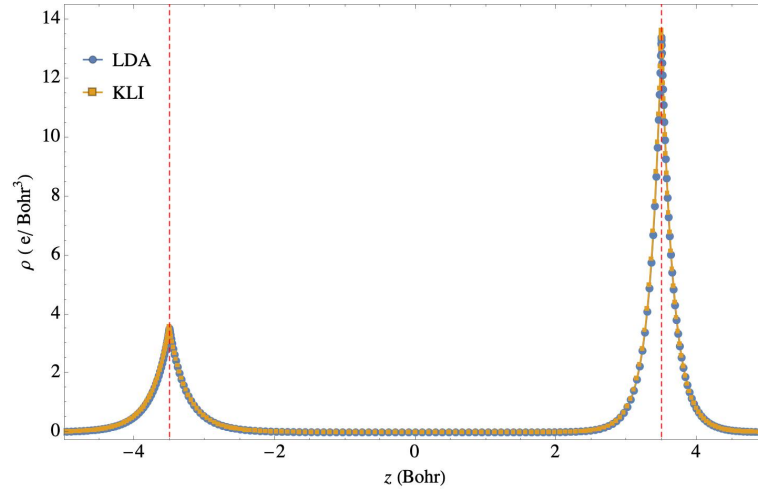
Figure 7.1: 1D representation of the ground-state density $\rho_{tot}^{\alpha}(\mathbf{r})$ where α =LDA, KLI; System: [HeLi]$^+$ with 7 Bohr of interatomic distance; Blue Mark-line: GS from LDA; Orange Mark-line: GS from KLI; Vertical dashed-lines: position of the nuclei.

To have the better vision of the difference between the results of these two theories, the $\Delta\rho(\mathbf{r}) = \rho_1^{\text{LDA}}(\mathbf{r}) - \rho_1^{\text{KLI}}(\mathbf{r})$ is shown in Fig.[7.1] is shown, where $\rho_1^{LDA/KLI}(\mathbf{r}) = 2|\phi_1^{LDA/KLI}(\mathbf{r})|^2$.
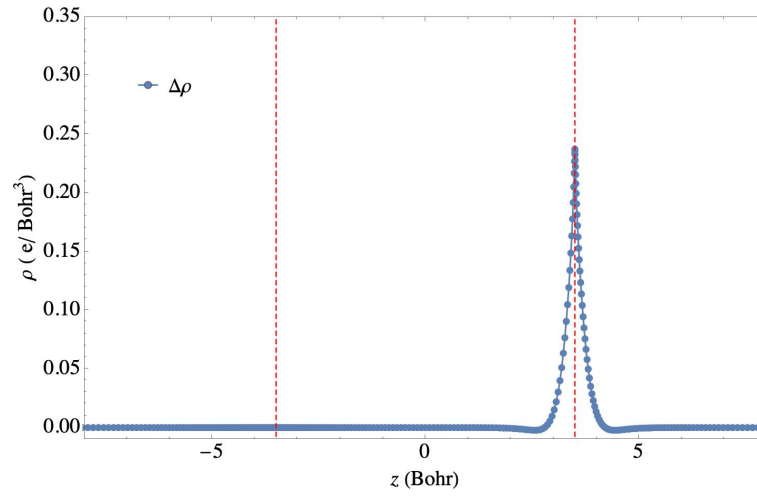
Figure 7.2: Difference between orbital density calculated with LDA vs the one from OEP-KLI; System: $[\mathrm{HeLi}]^+$; where He locates at $(0,0,-3.5)$ Bohr and Li locates at $(0,0,3.5)$ Bohr; Blue mark-line: $\Delta\rho(\mathbf{r}) = \rho_1^{\mathrm{LDA}}(\mathbf{r}) - \rho_1^{\mathrm{KLI}}(\mathbf{r})$; Vertical dashed lines: nuclei.

Clearly I see that $\Delta\rho(\mathbf{r}) \neq 0$. That means the $\rho_B^{\mathrm{LDA}}(\mathbf{r})$ must be also different than $\rho_B^{\mathrm{KLI}}(\mathbf{r})$. I recall again that $\rho_B(\mathbf{r})$ used in the calculation of this chapter is obtained from Eq.[3.23].

Based on analytical inversion from one-orbital formula, I want to see how $\Delta v(\mathbf{r}) = v_{KS}(\mathbf{r}) - v_s[\rho_1](\mathbf{r})$ between LDA and KLI. In Fig.[7.3] I see that $\Delta v(\mathbf{r})$ is smaller for KLI. That means, more exact is the input solution, better information will be available about the analytically inverted potential functional.
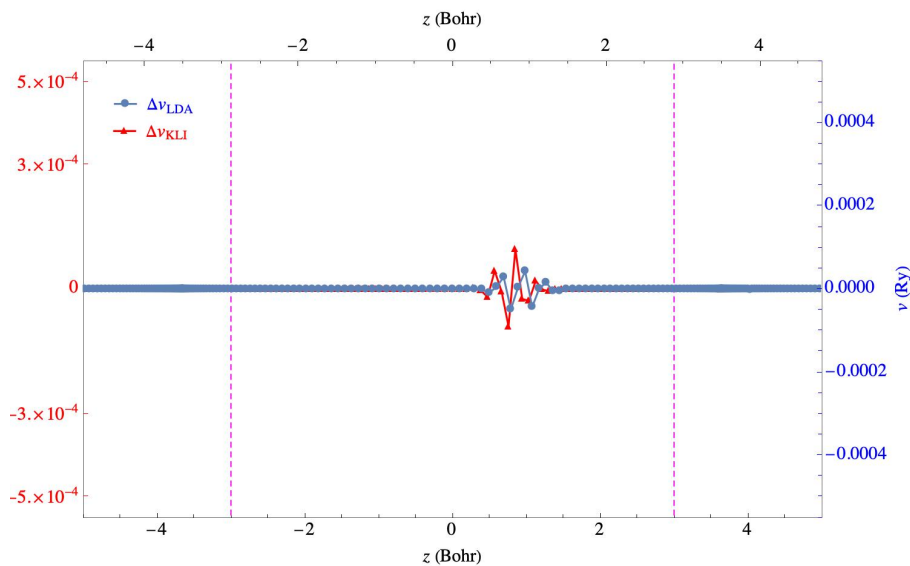
Figure 7.3: Difference between the $v_{KS}(\mathbf{r})$ and the $v_s[\rho_1](\mathbf{r})$; System: [HeLi]$^+$ where He is ate the left and Li is sited at the right on the z-axis; Blue mark-line: the results calculated from LDA; Red mark-line: the results calculated from OEP-KLI; Vertical dashed lines: nuclei.
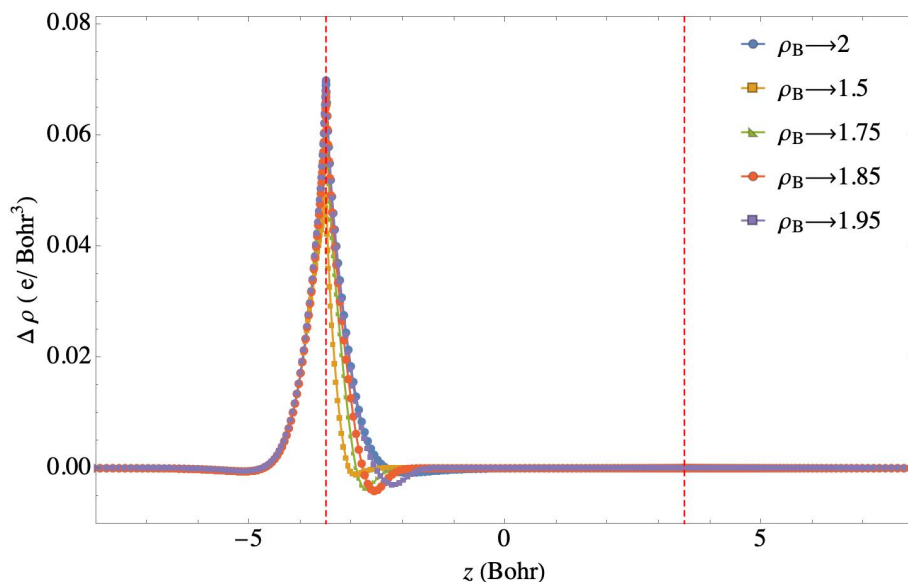
Figure 7.4: $\Delta\rho_B(\mathbf{r}) = \rho_B^{\text{LDA}}(\mathbf{r}) - \rho_B^{\text{KLI}}(\mathbf{r})$ for $1.5 \leq \int \rho_B(\mathbf{r})d\mathbf{r} \leq 2$;System: [HeLi]$^+$ where He locates at $(0,0,-3.5)$ Bohr and Li locates at $(0,0,3.5)$ Bohr; Vertical dashed lines: nuclei.

To see the variation of the $\rho_B(\mathbf{r})$ obtained from different theories and also for different electron localisations, I calculated $\Delta\rho_B(\mathbf{r}) = \rho_B^{\text{LDA}}(\mathbf{r}) - \rho_B^{\text{KLI}}(\mathbf{r})$ for

$1.5 \leq \int \rho_B(\mathbf{r})d\mathbf{r} \leq 2$. As I see in Fig.[7.4], the height if the $\Delta\rho_B(\mathbf{r})$ doesn't change for different $\rho_B(\mathbf{r})$ but closer the $\rho_B(\mathbf{r})$ is to the molecular orbital more the two theories behave differently.

This consequence must reflect in the analytical exact inversion of the $v_s[\rho_B](\mathbf{r})$. As I explained in Chapter.4, the height of the $v_s[\rho_i](\mathbf{r})$ for $i = A, B$ is related to the gap energy. I also know that LDA underestimate the gap compared to OEP-KLI. This latter requires that the level of the $v_s^{LDA}[\rho_B](\mathbf{r})$ be slightly in lower-level than the $v_s^{KLI}[\rho_B](\mathbf{r})$ in the space (Fig.[7.5]-Fig.[7.9]). In contract, the level (height of the step when it is in the overlap region) of the $v_s^{LDA}[\rho_A](\mathbf{r})$ be slightly higher than the $v_s^{KLI}[\rho_A](\mathbf{r})$ in the space (see Fig.[7.13]).
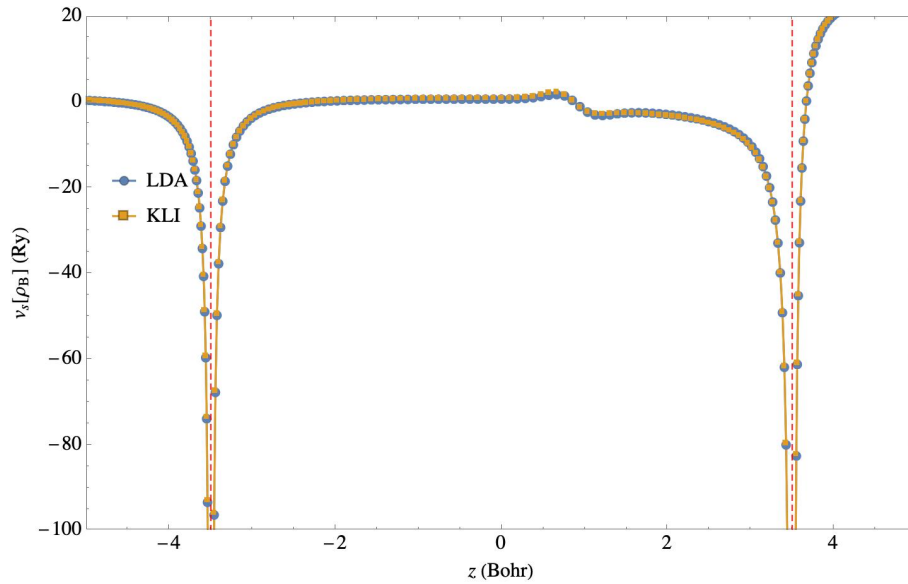
Figure 7.5: Analytical inversion of the potential from localised charge density around the atom He. System: [HeLi]$^+$; Orange mark-line: $v_s^{KLI}[\rho_B](\mathbf{r})$; Blue mark-line: $v_s^{KLI}[\rho_B](\mathbf{r})$; Both for $\int \rho_B(\mathbf{r})d\mathbf{r} = 2$;System: [HeLi]$^+$ where He locates at $(0, 0, -3.5)$ Bohr and Li locates at $(0, 0, 3.5)$ Bohr; Vertical dashed lines: nuclei.
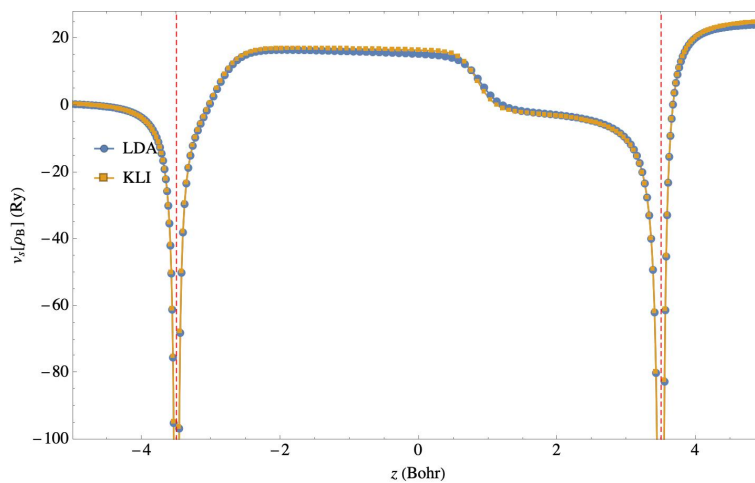
Figure 7.6: Potential from partial localisation of the charge density around the atom He. System: $[\text{HeLi}]^+$; Orange mark-line: $v_s^{\text{KLI}}[\rho_B](\mathbf{r})$; Blue mark-line: $v_s^{\text{KLI}}[\rho_B](\mathbf{r})$; Both for $\int \rho_B(\mathbf{r})d\mathbf{r} = 1.5$;System: $[\text{HeLi}]^+$ where He locates at $(0, 0, -3.5)$ Bohr and Li locates at $(0, 0, 3.5)$ Bohr; Vertical dashed lines: nuclei.
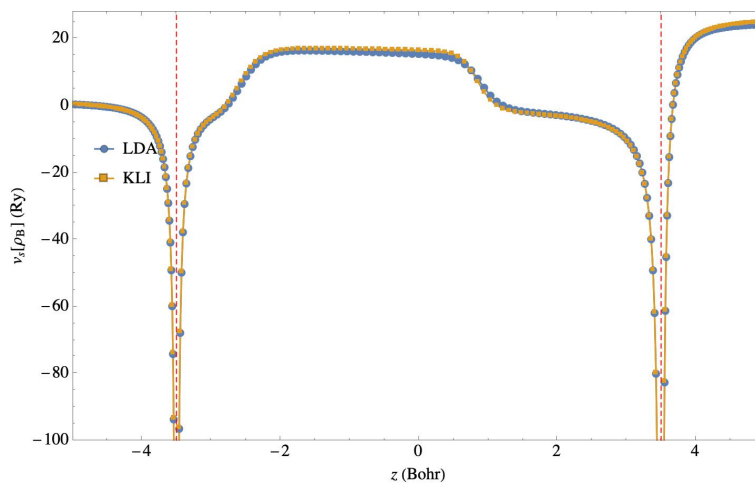
Figure 7.7: Potential from partial localisation of the charge density around the atom He. System: $[\text{HeLi}]^+$; Orange mark-line: $v_s^{\text{KLI}}[\rho_B](\mathbf{r})$; Blue mark-line: $v_s^{\text{KLI}}[\rho_B](\mathbf{r})$; Both for $\int \rho_B(\mathbf{r})d\mathbf{r} = 1.75$;System: $[\text{HeLi}]^+$ where He locates at $(0, 0, -3.5)$ Bohr and Li locates at $(0, 0, 3.5)$ Bohr; Vertical dashed lines: nuclei.
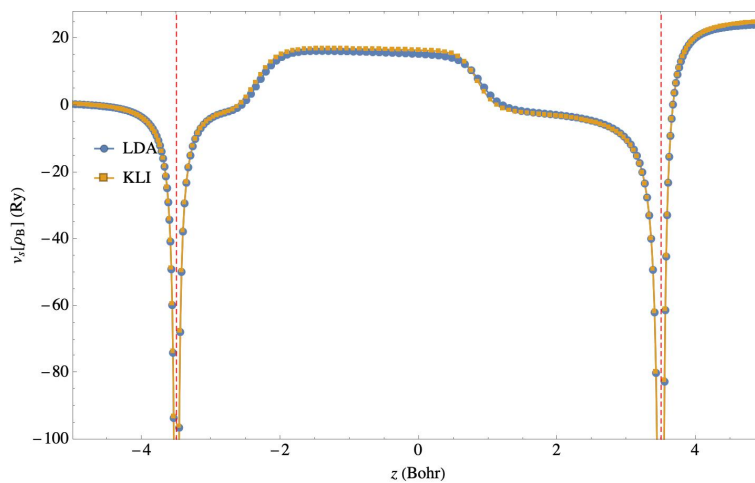
Figure 7.8: Potential from partial localisation of the charge density around the atom He. System: [HeLi]$^{+}$; Orange mark-line: $v_s^{\mathrm{KLI}}[\rho_B](\mathbf{r})$; Blue mark-line: $v_s^{\mathrm{KLI}}[\rho_B](\mathbf{r})$; Both for $\int \rho_B(\mathbf{r})d\mathbf{r} = 1.85$;System: [HeLi]$^{+}$ where He locates at $(0,0,-3.5)$ Bohr and Li locates at $(0,0,3.5)$ Bohr; Vertical dashed lines: nuclei.
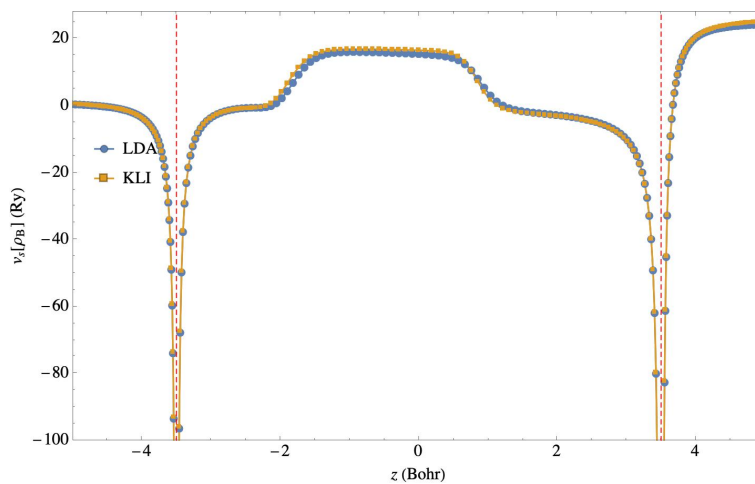
Figure 7.9: Potential from partial localisation of the charge density around the atom He. System: [HeLi]$^{+}$; Orange mark-line: $v_s^{\mathrm{KLI}}[\rho_B](\mathbf{r})$; Blue mark-line: $v_s^{\mathrm{KLI}}[\rho_B](\mathbf{r})$; Both for $\int \rho_B(\mathbf{r})d\mathbf{r} = 1.95$;System: [HeLi]$^{+}$ where He locates at $(0,0,-3.5)$ Bohr and Li locates at $(0,0,3.5)$ Bohr; Vertical dashed lines: nuclei.
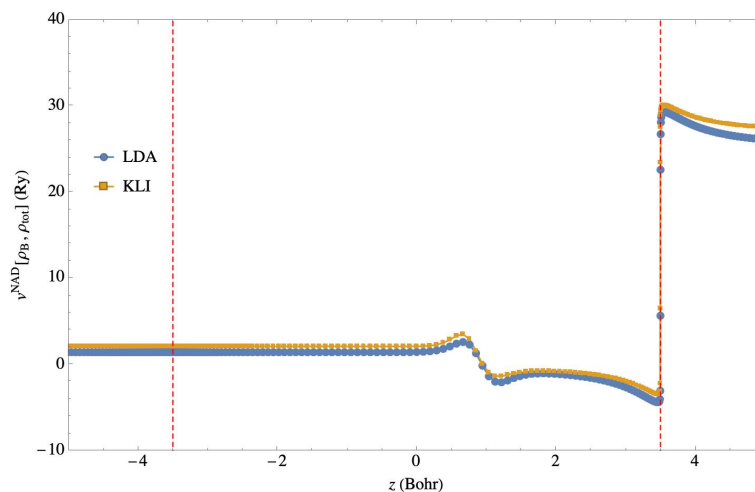
Figure 7.10: Analytically inverted Potential bi-functional based on one-orbital formula for the localisation of the charge density around the atom He. System: $[HeLi]^+$; Orange mark-line: $v^{NAD/KLI}[\rho_B, \rho_{tot}](\mathbf{r})$; Blue mark-line: $v^{NAD/LDA}[\rho_B, \rho_{tot}](\mathbf{r})$; Both for $\int \rho_B(\mathbf{r})d\mathbf{r} = 2$;System: $[HeLi]^+$ where He locates at $(0,0,-3.5)$ Bohr and Li locates at $(0,0,3.5)$ Bohr; Vertical dashed lines: nuclei.
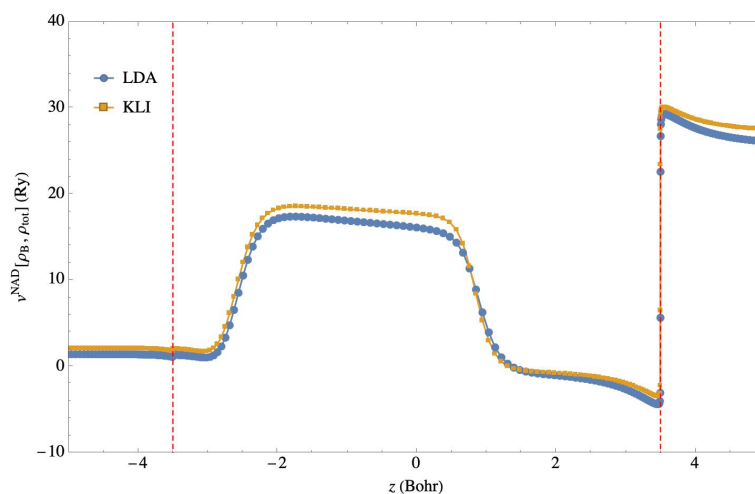
Figure 7.11: Analytically inverted Potential bi-functional based on one-orbital formula for the partial localisation of the charge density around the atom He. System: $[HeLi]^+$; Orange mark-line: $v^{NAD/KLI}[\rho_B, \rho_{tot}](\mathbf{r})$; Blue mark-line: $v^{NAD/LDA}[\rho_B, \rho_{tot}](\mathbf{r})$; Both for $\int \rho_B(\mathbf{r})d\mathbf{r} = 1.75$;System: $[HeLi]^+$ where He locates at $(0,0,-3.5)$ Bohr and Li locates at $(0,0,3.5)$ Bohr; Vertical dashed lines: nuclei.
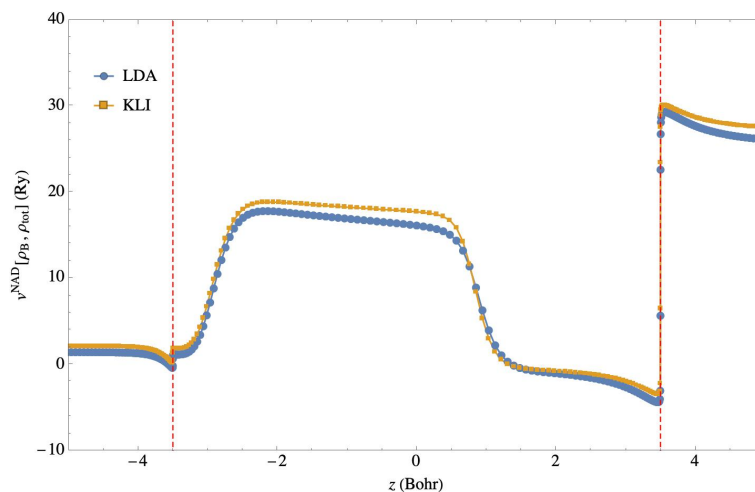
Figure 7.12: Analytically inverted Potential bi-functional based on one-orbital formula for the partial localisation of the charge density around the atom He. System: [HeLi]$^+$; Orange mark-line: $v^{\mathrm{NAD/KLI}}[\rho_B, \rho_{tot}](\mathbf{r})$; Blue mark-line: $v^{NAD/LDA}[\rho_B, \rho_{tot}](\mathbf{r})$; Both for $\int \rho_B(\mathbf{r})d\mathbf{r} = 1.5$;System: [HeLi]$^+$ where He locates at $(0, 0, -3.5)$ Bohr and Li locates at $(0, 0, 3.5)$ Bohr; Vertical dashed lines: nuclei.

Knowing the system includes four electrons, while localising two electrons in the space $(\rho_B(\mathbf{r}))$ the reminder of the total charge density $(\rho_A(\mathbf{r}))$ will also integrate to 2. For the heteronuclear system such as HeLi$^+$ that provides localised orbitals standing at the vicinity of the nuclei, both $\rho_B(\mathbf{r})$ and $\rho_A(\mathbf{r})$ become comparable to the molecular orbital densities. It is totally fare to compare the analytically inverted potential bi-functionals from different ground-state densities (input) for the inversion from the $\rho_A(\mathbf{r})$.

For that purpose, I reported $v_s[\rho_A](\mathbf{r})$ for two theories for the case $\int \rho_A(\mathbf{r})d\mathbf{r} = 2$ (Fig.[7.13]) and the related $v^{\mathrm{NAD}}[\rho_A, \rho_{tot}](\mathbf{r})$ (Fig.[7.14]).

159
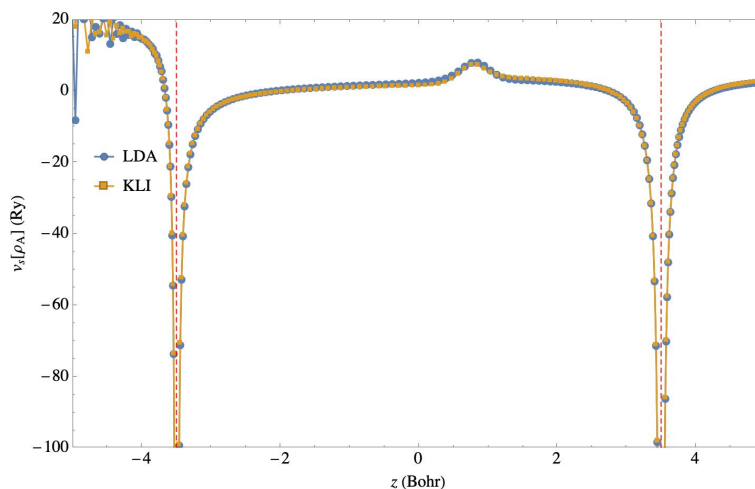
Figure 7.13: Analytical inversion of the potential from localised charge density around the atom He. System: [HeLi]$^+$; Orange mark-line: $v_s^{\text{KLI}}[\rho_A](\mathbf{r})$; Blue mark-line: $v_s^{\text{KLI}}[\rho_A](\mathbf{r})$; Both for $\rho_A(\mathbf{r}) = \rho_{tot}(\mathbf{r}) - \rho_B(\mathbf{r})$ where $\int \rho_B(\mathbf{r})d\mathbf{r} = 2$;System: [HeLi]$^+$ where He locates at $(0,0,-3.5)$ Bohr and Li locates at $(0,0,3.5)$ Bohr; Vertical dashed lines: nuclei.
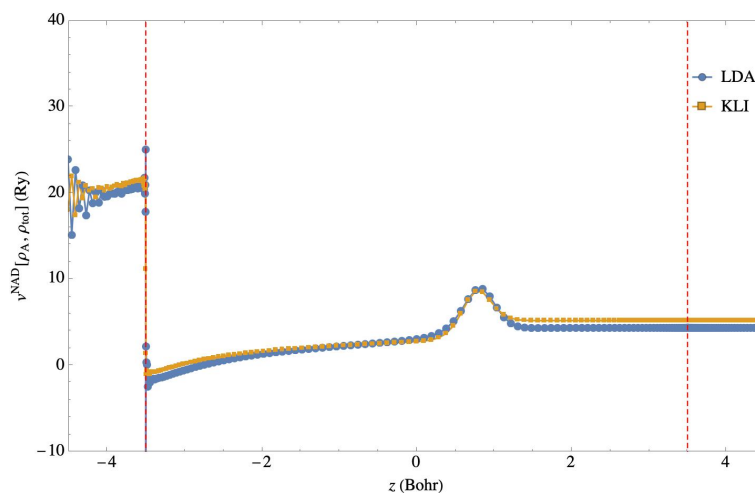
Figure 7.14: Analytically inverted Potential bi-functional based on one-orbital formula for the localisation of the charge density around the atom He. System: [HeLi]$^+$; Orange mark-line: $v^{\text{NAD/KLI}}[\rho_A, \rho_{tot}](\mathbf{r})$; Blue mark-line: $v^{NAD/LDA}[\rho_A, \rho_{tot}](\mathbf{r})$; Both for $\rho_A(\mathbf{r}) = \rho_{tot}(\mathbf{r}) - \rho_B(\mathbf{r})$ where $\int \rho_B(\mathbf{r})d\mathbf{r} = 2$;System: [HeLi]$^+$ where He locates at $(0,0,-3.5)$ Bohr and Li locates at $(0,0,3.5)$ Bohr; Vertical dashed lines: nuclei.

As I see the potentials shown in Fig.[7.13] and Fig.[7.14] confirm our argument about the fact that LDA underestimate the gap energy compared to OEP-KLI theory.

7.2.2   He-He

In this part of the work I try to see if the difference between the $v^{\text{NAD/inverted}}[\rho_A, \rho_{tot}](\mathbf{r})$ is less or more pronounced for the case of entirely symmetric diatomic system, He-He as our choice. When it concern the mononuclear system, I expect to see the $v^{\text{NAD/inverted}}[\rho_A, \rho_{tot}](\mathbf{r})$ shows larger difference between the different input densities. This is because of the fact that the orbitals in such system are not localised. That means the difference between two theory will be reflected in whole space instead of appearing locally as it was the case for the heteronuclear system (see Fig.[7.16]).
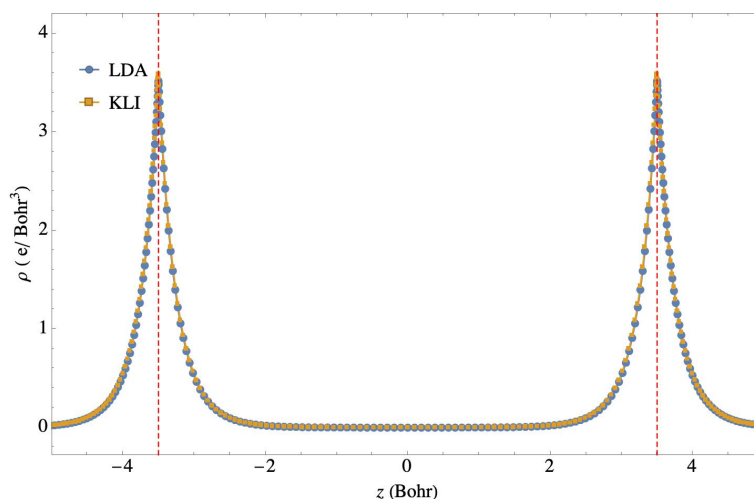
Figure 7.15: 1D representation of the ground-state density $\rho_{tot}^{\alpha}(\mathbf{r})$ where α =LDA, KLI; System: He-He with 7 Bohr of interatomic distance; Blue Mark-line: GS from LDA; Orange Mark-line: GS from KLI; Vertical dashed-lines: position of the nuclei.

We repeated the same approaches numerically as it was explained in previous subsection for He-He. The Fig.[7.15] shows the ground state density calculated from LDA vs the one obtained by OEP-LKT.

The difference between $\rho_1\mathbf{r}$ from both theory is plotted in Fig.[7.16].
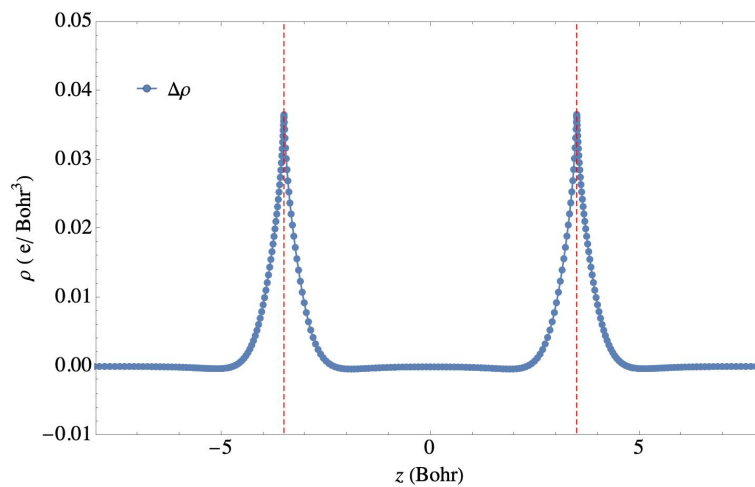
Figure 7.16: Difference between orbital density calculated with LDA vs the one from OEP-KLI; System: He-He; where one He locates at $(0, 0, -3.5)$ Bohr and another one locates at $(0, 0, 3.5)$ Bohr; Blue mark-line: $\Delta\rho(\mathbf{r}) = \rho_1^{\mathrm{LDA}}(\mathbf{r}) - \rho_1^{\mathrm{KLI}}(\mathbf{r})$; Vertical dashed lines: nuclei.
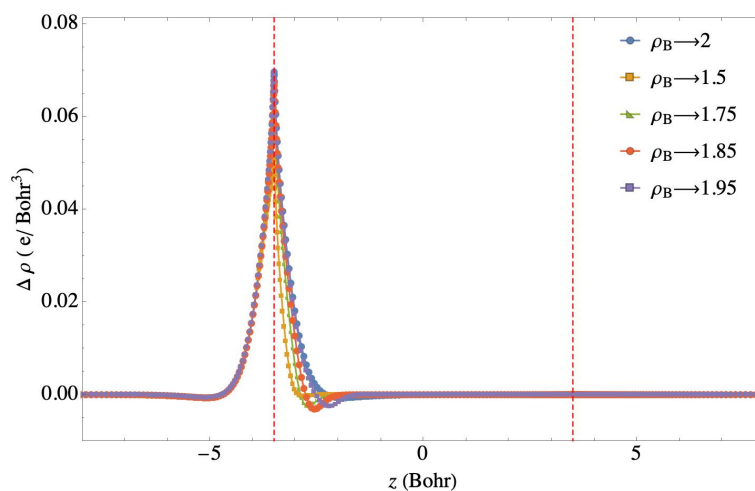

Figure 7.17: $\Delta\rho_B(\mathbf{r}) = \rho_B^{\mathrm{LDA}}(\mathbf{r}) - \rho_B^{\mathrm{KLI}}(\mathbf{r})$ for $1.5 \leq \int \rho_B(\mathbf{r})d\mathbf{r} \leq 2$; System: He-He where one He locates at $(0, 0, -3.5)$ Bohr and another He locates at $(0, 0, 3.5)$ Bohr; Vertical dashed lines: nuclei.
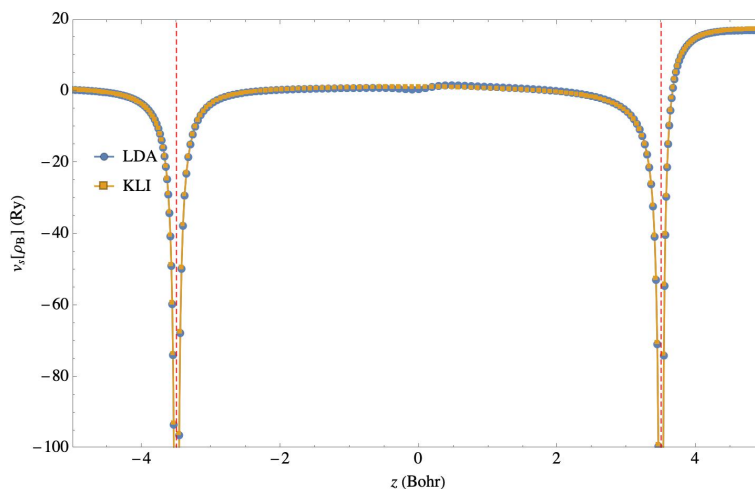
Figure 7.18: Analytical inversion of the potential from localised charge density around the atom He. System: He-He; Orange mark-line: $v_s^{\text{KLI}}[\rho_B](\mathbf{r})$; Blue mark-line: $v_s^{\text{KLI}}[\rho_B](\mathbf{r})$; Both for $\int \rho_B(\mathbf{r})d\mathbf{r} = 2$; System: He-He where one He locates at $(0,0,-3.5)$ Bohr Bohr and another one locates at $(0,0,3.5)$ Bohr; Vertical dashed lines: nuclei.

The difference between localised density $\Delta\rho_B(\mathbf{r})$ around the left atom of both theory for various localisations are shown in Fig.[7.17] and the related $v_s[\rho_B](\mathbf{r})$ are represented in figures [7.18] to [7.21].
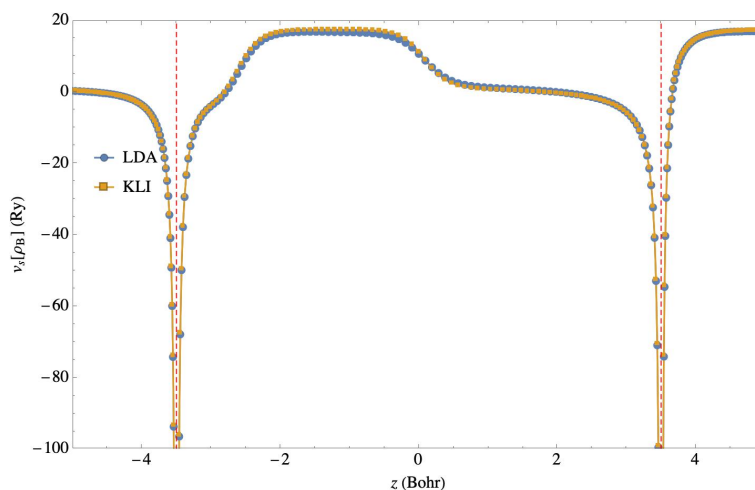
Figure 7.19: Potential from partial localisation of the charge density around the atom He at the left. System: He-He; Orange mark-line: $v_s^{\text{KLI}}[\rho_B](\mathbf{r})$; Blue mark-line: $v_s^{\text{KLI}}[\rho_B](\mathbf{r})$; Both for $\int \rho_B(\mathbf{r})d\mathbf{r} = 1.75$;System: He-He where one He locates at $(0,0,-3.5)$ Bohr and another one locates at $(0,0,3.5)$ Bohr; Vertical dashed lines: nuclei.
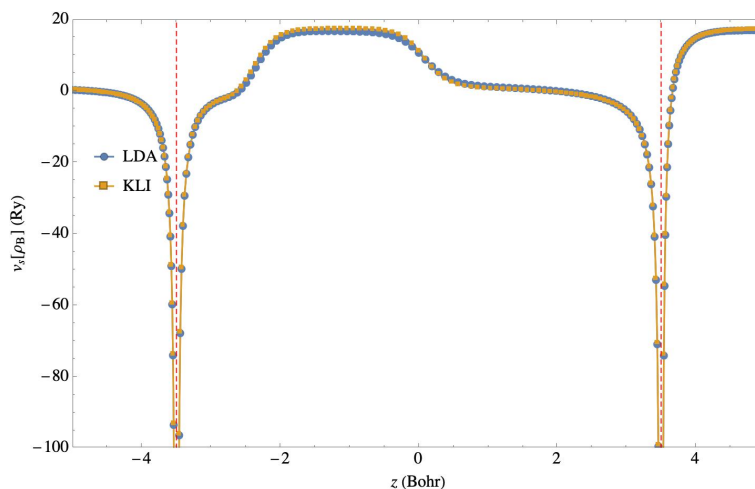
Figure 7.20: Potential from partial localisation of the charge density around the atom He at the left side of the z-axis. System: He-He; Orange mark-line: $v_s^{\text{KLI}}[\rho_B](\mathbf{r})$; Blue mark-line: $v_s^{\text{KLI}}[\rho_B](\mathbf{r})$; Both for $\int \rho_B(\mathbf{r})d\mathbf{r} = 1.85$;System: He-He where one He locates at $(0, 0, -3.5)$ Bohr and another one locates at $(0, 0, 3.5)$ Bohr; Vertical dashed lines: nuclei.
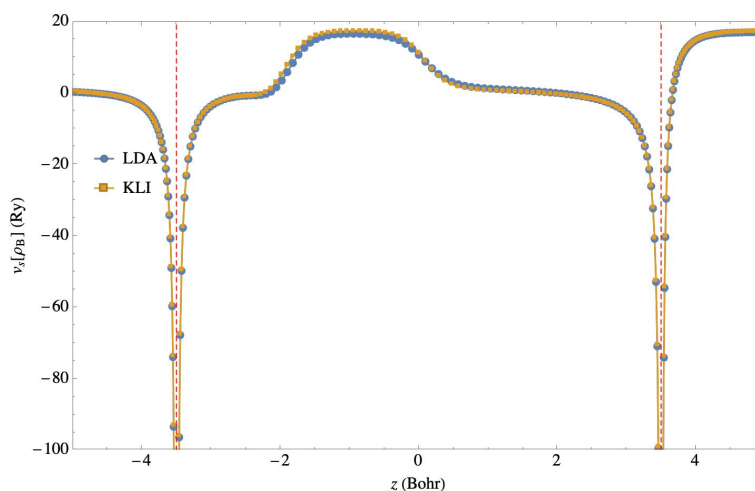

Figure 7.21: Potential from partial localisation of the charge density around the left atom He. System: He-He; Orange mark-line: $v_s^{\text{KLI}}[\rho_B](\mathbf{r})$; Blue mark-line: $v_s^{\text{KLI}}[\rho_B](\mathbf{r})$; Both for $\int \rho_B(\mathbf{r})d\mathbf{r} = 1.95$;System: He-He where one He locates at $(0, 0, -3.5)$ Bohr and another one locates at $(0, 0, 3.5)$ Bohr; Vertical dashed lines: nuclei.
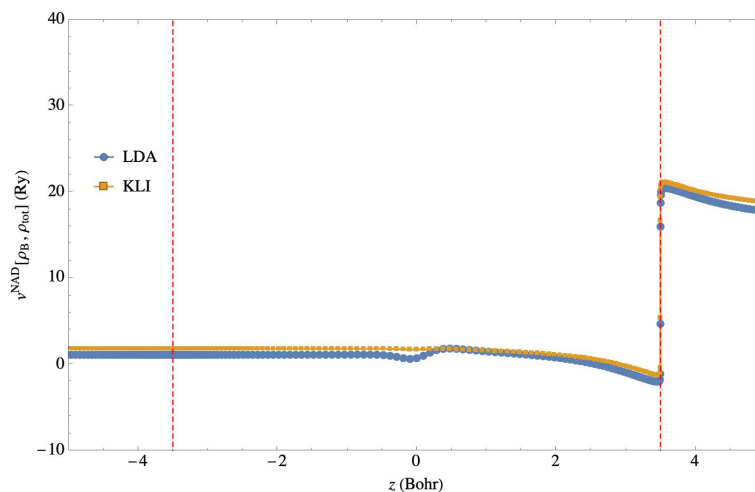
Figure 7.22: Analytically inverted Potential bi-functional based on one-orbital formula for the localisation of the charge density around the left atom; System: He-He; Orange mark-line: $v^{\mathrm{NAD/KLI}}[\rho_B, \rho_{tot}](\mathbf{r})$; Blue mark-line: $v^{NAD/LDA}[\rho_B, \rho_{tot}](\mathbf{r})$; Both for $\int \rho_B(\mathbf{r})d\mathbf{r} = 2$;System: He-He where one He locates at $(0, 0, -3.5)$ Bohr and another He locates at $(0, 0, 3.5)$ Bohr; Vertical dashed lines: nuclei.

In Fig.[7.22] I see that the $v^{\mathrm{NAD/KLI}}[\rho_B, \rho_{tot}](\mathbf{r})$ shows very smooth behaviour of the potential at the overlap region between two sub-densities compared to $v^{NAD/LDA}[\rho_B, \rho_{tot}](\mathbf{r})$. This is very probably because the orbital dependency approach involved in OEP-KLI calculate more precisely the molecular orbital that locally integrates to a very small value.

To see if the $v^{\mathrm{NAD/KLI}}[\rho_B, \rho_{tot}](\mathbf{r})$ curve provides also information about the weakly overlapping partitioned densities, I zoomed in the curve in that specific region. This latter is represented in Fig.[7.23]. It appears that the $v^{\mathrm{NAD/inverted}}[\rho_B, \rho_{tot}](\mathbf{r})$ from both theory contains the information about the region where the partitioned densities overlap. Taking into account of our understanding from the step structure, the width of the step happens to be comparable in both cases, however, the energy level of the curves at the point of changing sign (second spatial derivative of the potential as it was explained in section.4.6.3 to calculate the gap energy) varies significantly between two theories.

This is the source of obvious difference between the gap energy in OEP-KLI methods vs LDA one.
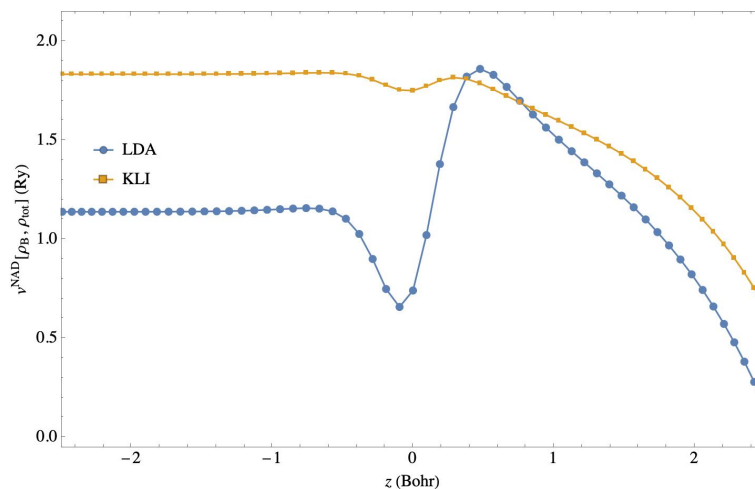
Figure 7.23: Zoomed in potentials showed in Fig.[7.22] at the overlap region of the sub-densities.

From figures [7.24] to [7.26] I see that the feature of the $v^{\mathrm{NAD/KLI}}[\rho_B, \rho_{tot}](\mathbf{r})$ become more similar to the $v^{\mathrm{NAD/KLI}}[\rho_B, \rho_{tot}](\mathbf{r})$ in whole space. We may understand from that observation that the theories differs more when it is the exact solution of a system is sought rather than a decided solution is imposed.
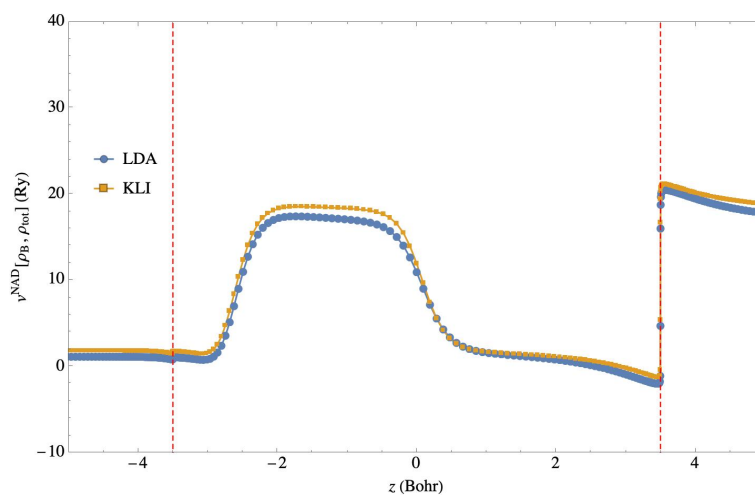

Figure 7.24: Analytically inverted Potential bi-functional based on one-orbital formula for the partial localisation of the charge density around the left atom ; System: He-He; Orange mark-line: $v^{\mathrm{NAD/KLI}}[\rho_B, \rho_{tot}](\mathbf{r})$; Blue mark-line: $v^{NAD/LDA}[\rho_B, \rho_{tot}](\mathbf{r})$; Both for $\int \rho_B(\mathbf{r})d\mathbf{r} = 1.75$;Vertical dashed lines: nuclei.
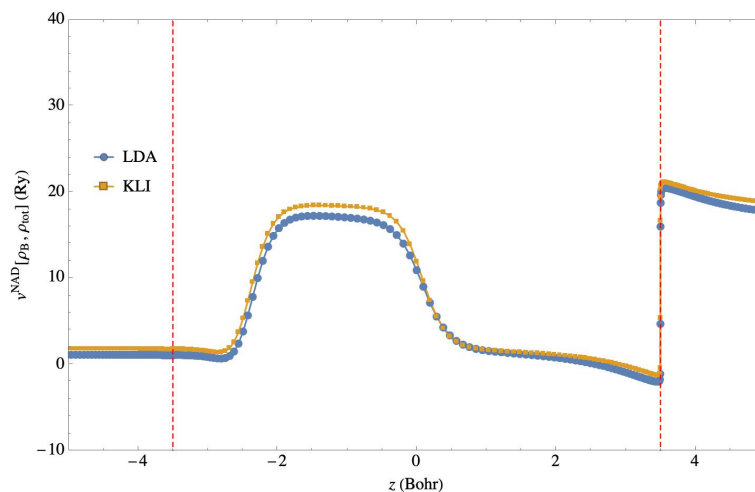
Figure 7.25: Analytically inverted Potential bi-functional based on one-orbital formula for the partial localisation of the charge density around the left atom He; Orange mark-line: $v^{\text{NAD/KLI}}[\rho_B, \rho_{tot}](\mathbf{r})$; Blue mark-line: $v^{NAD/LDA}[\rho_B, \rho_{tot}](\mathbf{r})$; Both for $\int \rho_B(\mathbf{r})d\mathbf{r} = 1.85$; system: He-He with 7 Bohr of the distance between the atoms; Vertical dashed lines: nuclei.
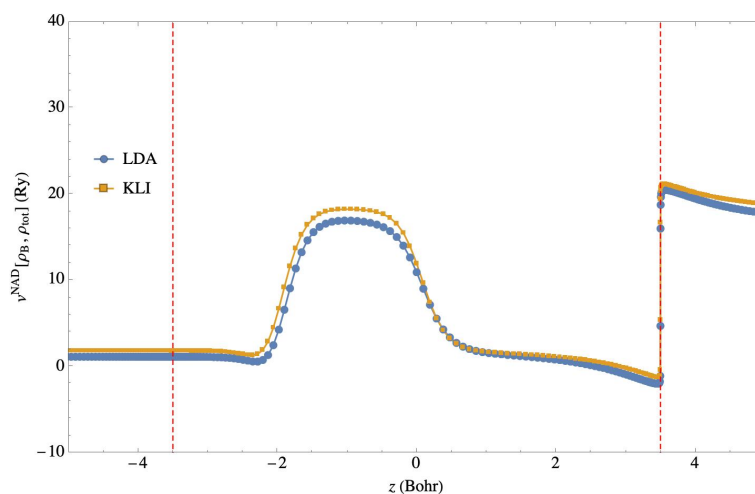
Figure 7.26: Analytically inverted Potential bi-functional based on one-orbital formula for the partial localisation of the charge density around the left atom ; Orange mark-line: $v^{\text{NAD/KLI}}[\rho_B, \rho_{tot}](\mathbf{r})$; Blue mark-line: $v^{NAD/LDA}[\rho_B, \rho_{tot}](\mathbf{r})$; Both for $\int \rho_B(\mathbf{r})d\mathbf{r} = 1.95$; system: He-He; Vertical dashed lines: nuclei.

Similarly to HeLi$^+$, I calculated the $v^{\text{NAD/inverted}}[\rho_A, \rho_{tot}](\mathbf{r})$; for He-He from both theories. I show the $v_s[\rho_A](\mathbf{r})$ in Fig.[7.27] and the corresponding $v^{\text{NAD/inverted}}[\rho_A, \rho_{tot}](\mathbf{r})$s in Fig.[7.28].
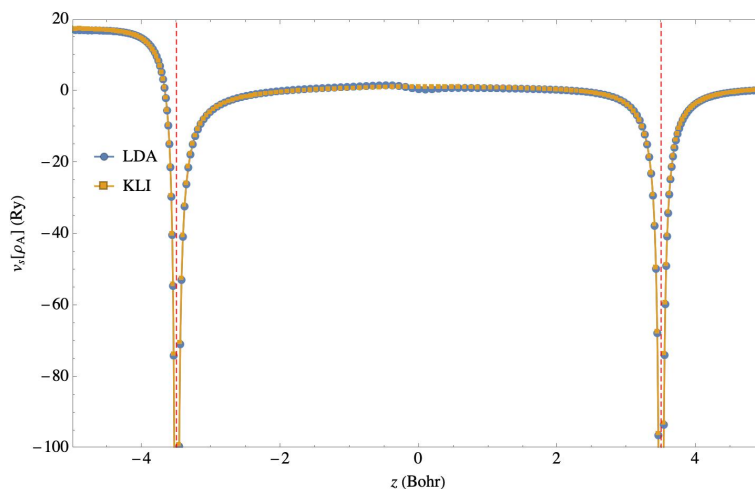
Figure 7.27: Analytical inversion of the potential from localised charge density around the left atom; Orange mark-line: $v_s^{\text{KLI}}[\rho_A](\mathbf{r})$; Blue mark-line: $v_s^{\text{KLI}}[\rho_A](\mathbf{r})$; Both for $\rho_A(\mathbf{r}) = \rho_{tot}(\mathbf{r}) - \rho_B(\mathbf{r})$ where $\int \rho_B(\mathbf{r})d\mathbf{r} = 2$; System: He-He where one He locates at $(0, 0, -3.5)$ Bohr and another He locates at $(0, 0, 3.5)$ Bohr; Vertical dashed lines: nuclei.
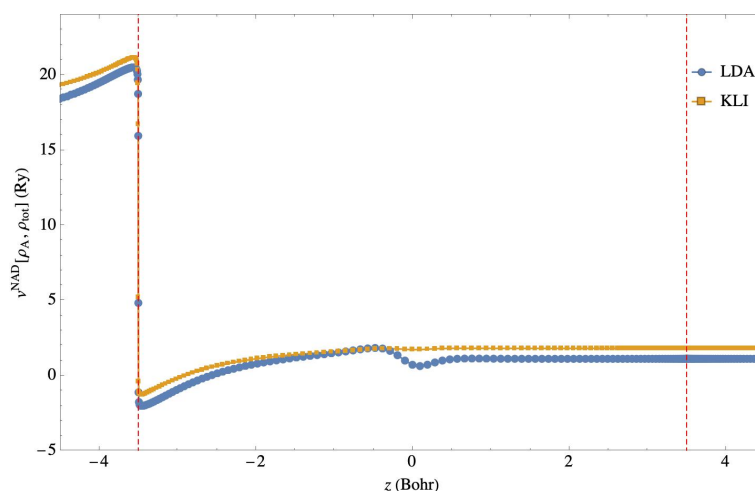

Figure 7.28: Analytically inverted Potential bi-functional based on one-orbital formula for the localisation of the charge density around the left atom; Orange mark-line: $v^{\text{NAD/KLI}}[\rho_A, \rho_{tot}](\mathbf{r})$; Blue mark-line: $v^{NAD/LDA}[\rho_A, \rho_{tot}](\mathbf{r})$; Both for $\rho_A(\mathbf{r}) = \rho_{tot}(\mathbf{r}) - \rho_B(\mathbf{r})$ where $\int \rho_B(\mathbf{r})d\mathbf{r} = 2$;System: He-He where one He locates at $(0, 0, -3.5)$ Bohr and another He locates at $(0, 0, 3.5)$ Bohr; Vertical dashed lines: nuclei.

Zooming in the $v^{\text{NAD/inverted}}[\rho_A, \rho_{tot}](\mathbf{r})$s as it is ilustrated in Fig.[7.29] confirms our arguments about the $v^{\text{NAD/inverted}}[\rho_B, \rho_{tot}](\mathbf{r})$ previously.
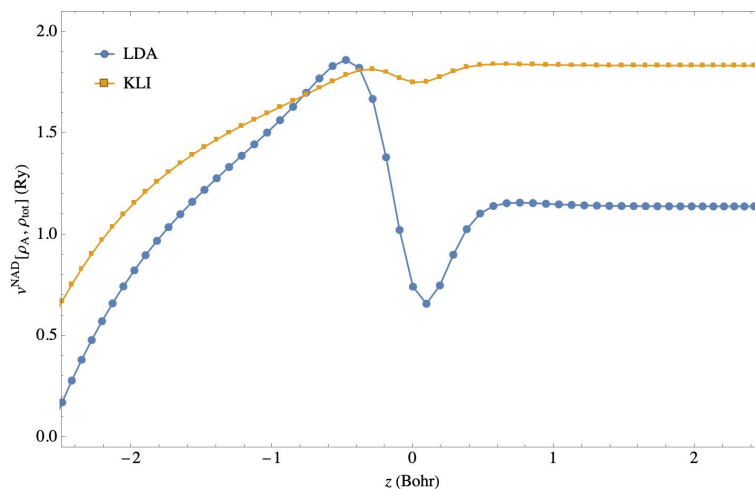
Figure 7.29: Zoomed in potentials showed in Fig.[7.28] at the overlap region of the sub-densities.

Test

7.2.3 PBE input for the calcuation of the system He-HE

The PBE mainly varries from the LDA based on the fact that it is locally dependent to the gradient of the density. That means the potential inverted from density might vary slightly and locally between PBE and LDA. That variety must appear mostly in from of the smoothness of the potential at the position the density changes not continuously.

We compare in Fig.[7.30] the $v_s[\rho_B](\mathbf{r})$ between LDA, PBE and LKT calculations for the case $\int_V \rho_B(\mathbf{r})d\mathbf{r} = 2$. Together, with the corresponding $v^{\text{NAD/inverted}}[\rho_B, \rho_{tot}](\mathbf{r})$ shown in Fig.[7.32] with the help of the zoomed in graphs at the region of weakly overlapping densities, I conclude that the difference between the results coming from LDA and PBE is neglectable. However, the results related to the input density provided by OEP-KLI required to be discussed.
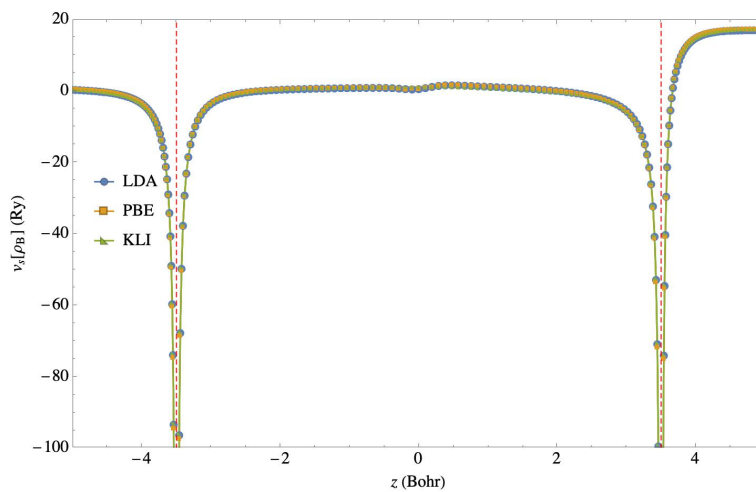
Figure 7.30: Analytical inversion of the potential from localised charge density around the atom He at the left; Blue mark-line: $v_s^{LDA}[\rho_B](\mathbf{r})$; Orange mark-line: $v_s^{\mathrm{PBE}}[\rho_B](\mathbf{r})$; Green mark-line: $v_s^{\mathrm{KLI}}[\rho_B](\mathbf{r})$; Both for $\int \rho_B(\mathbf{r})d\mathbf{r} = 2$; System: He-He where one He locates at $(0,0,-3.5)$ Bohr and another one locates at $(0,0,3.5)$; Vertical dashed lines: nuclei.
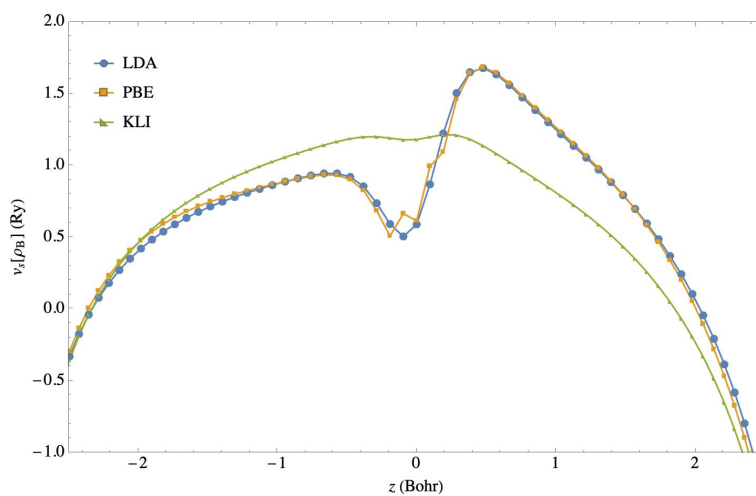
Figure 7.31: Zoomed in potentials of Fig.[7.30].
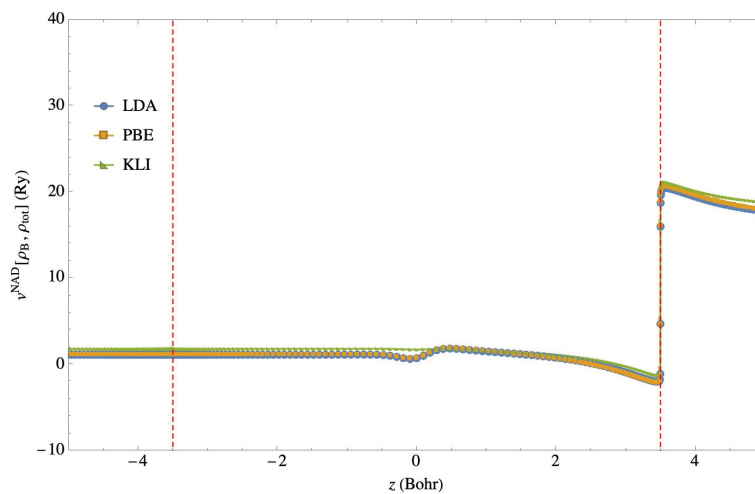
Figure 7.32: Analytically inverted Potential bi-functional based on one-orbital formula for the localisation of the charge density around the left atom; Blue mark-line: $v^{NAD/LDA}[\rho_A, \rho_{tot}](\mathbf{r})$; Orange mark-line: $v^{NAD/PBE}[\rho_A, \rho_{tot}](\mathbf{r})$; Green mark-line: $v^{\mathrm{NAD/KLI}}[\rho_A, \rho_{tot}](\mathbf{r})$; all calculated for $\int \rho_B(\mathbf{r})d\mathbf{r} = 2$; System: He-He where one He locates at $(0,0,-3.5)$ Bohr and another He locates at $(0,0,3.5)$ Bohr; Vertical dashed lines: nuclei.

Both the $v_s[\rho_A](\mathbf{r})$ and the $v^{\mathrm{NAD/inverted}}[\rho_A, \rho_{tot}](\mathbf{r})$ follows the same arguments reported for the inversion of the potential from the $\rho_B(\mathbf{r})$ (Fig.[7.34] to Fig.[7.37]).
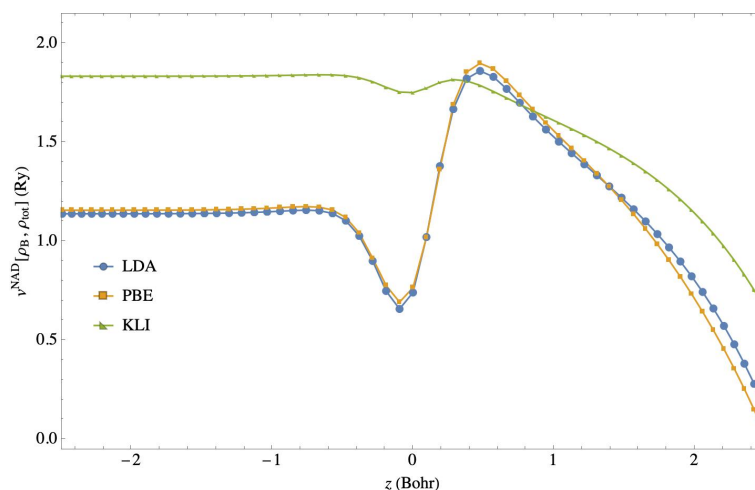
Figure 7.33: Zoomed in potentials of Fig.[7.32].
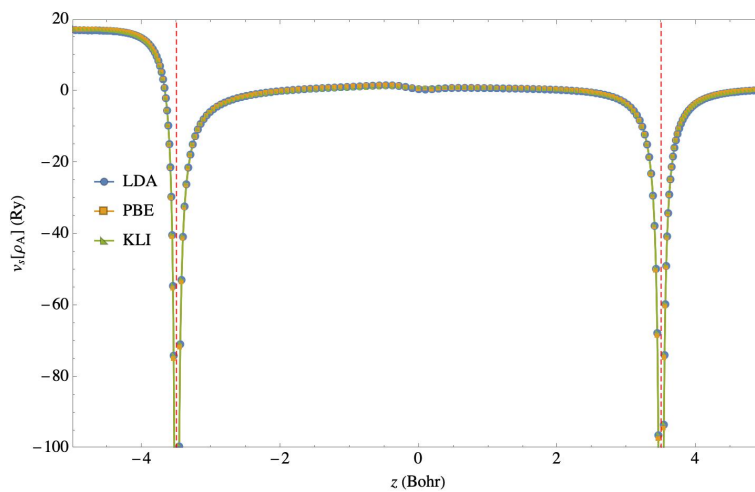
Figure 7.34: Analytical inversion of the potential from localised charge density around the left atom; Orange mark-line: $v_s^{\text{KLI}}[\rho_A](\mathbf{r})$;Blue mark-line: $v_s^{LDA}[\rho_B](\mathbf{r})$; Orange mark-line: $v_s^{\text{PBE}}[\rho_B](\mathbf{r})$; Green mark-line: $v_s^{\text{KLI}}[\rho_B](\mathbf{r})$; all calculated for $\rho_A(\mathbf{r}) = \rho_{tot}(\mathbf{r}) - \rho_B(\mathbf{r})$ where $\int \rho_B(\mathbf{r})d\mathbf{r} = 2$; System: He-He where one He locates at $(0,0,-3.5)$ Bohr and another He locates at $(0,0,3.5)$ Bohr; Vertical dashed lines: nuclei.
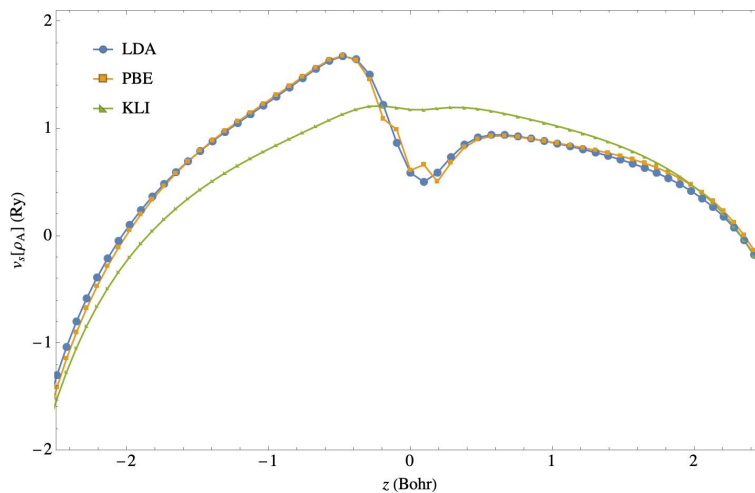
Figure 7.35: Zoomed in potentials of Fig.[7.34].
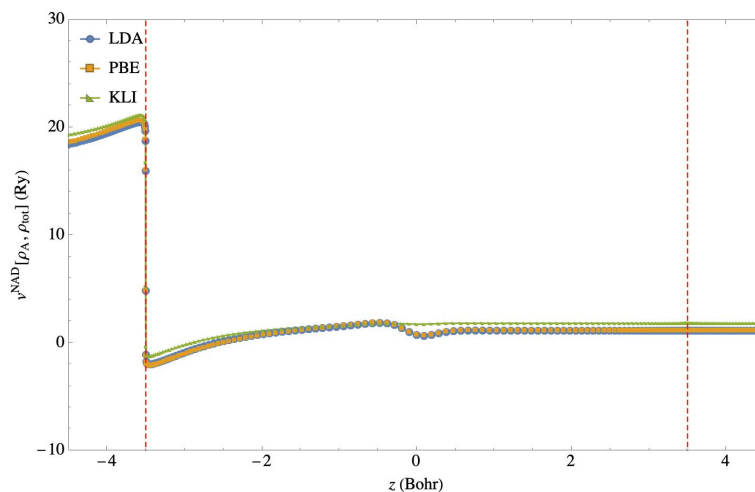
Figure 7.36: Analytically inverted Potential bi-functional from one-orbital formula; Orange mark-line: $v^{\mathrm{NAD/KLI}}[\rho_A, \rho_{tot}](\mathbf{r})$; Blue mark-line: $v_s^{LDA}[\rho_B](\mathbf{r})$; Orange mark-line: $v_s^{\mathrm{PBE}}[\rho_B](\mathbf{r})$; Green mark-line: $v_s^{\mathrm{KLI}}[\rho_B](\mathbf{r})$; all calculated for $\rho_A(\mathbf{r}) = \rho_{tot}(\mathbf{r}) - \rho_B(\mathbf{r})$ where $\int \rho_B(\mathbf{r})d\mathbf{r} = 2$; System: He-He where one He locates at $(0, 0, -3.5)$ Bohr and another He locates at $(0, 0, 3.5)$ Bohr; Vertical dashed lines: nuclei.
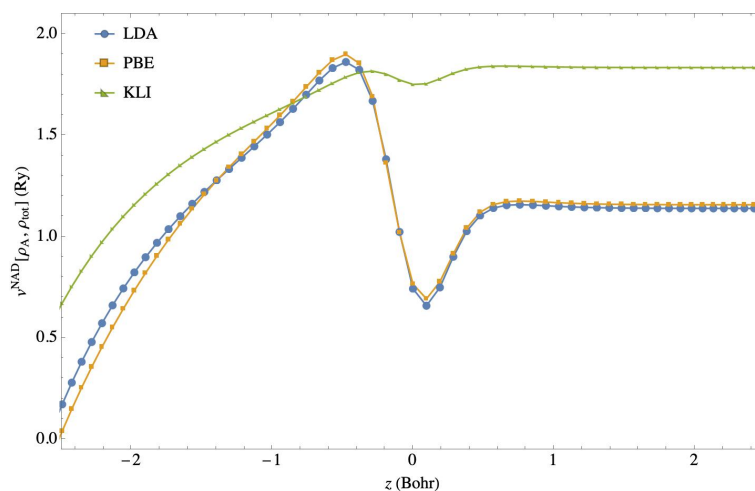

Figure 7.37: Zoomed in potentials of Fig.[7.36].

7.3   Conclusion and Outlook

The exact non-additive potential bi-functional behaves sensitively into the change of the input ground state charge density. The attempts to this part of the investigation of correct $v^{\mathrm{NAD/inverted}}[\rho_{A/B}, \rho_{tot}](\mathbf{r})$ confirms one of the properties of an exact density functional potential, the "Uniqueness". The one-to-one

relation between a potential functional of density and a given density has to be unique in order to have a reliable correct potential. The fact that the results showed $v^{NAD/PBE}[\rho_A, \rho_{tot}](\mathbf{r}) \neq v^{NAD/LDA}[\rho_A, \rho_{tot}](\mathbf{r}) \neq v^{\mathrm{NAD/KLI}}[\rho_A, \rho_{tot}](\mathbf{r})$ for infinitesimally differentiating $\rho_{GS}^{NAD/PBE}(\mathbf{r})$ from $\rho_{GS}^{NAD/LDA}(\mathbf{r})$ and from $\rho_{GS}^{\mathrm{NAD/KLI}}(\mathbf{r})$ is a strong confirmation toward the accuracy of the analytically inverted $v^{\mathrm{NAD/inverted}}$.

Above that conclusion, the difference between the $v^{\mathrm{NAD/KLI}}[\rho_A, \rho_{tot}](\mathbf{r})$ and the $v^{NAD/LDA}[\rho_A, \rho_{tot}](\mathbf{r})$ explains the origin of the difference between the gap energy calculated in both theory(see table.[4.1] and table.[4.3]).

Another important conclusion is about the shape, height and position of the step. In all three theories those properties of the step structure were present and acceptably accurate based on the theoretical expectations explained in chapter 4.

Now that I know enough about the feature of the correct $v^{\mathrm{NAD/inverted}}[\rho_{A/B}, \rho_{tot}](\mathbf{r})$ I need to find out the exact value of the potential. In order to provide the exact potential bi-functional, I need to use an exact ground state density as the input. This latter can be prepared whether experimentally or from more accurate theories although they might be computationally more expensive.

For such small model systems, full CI can be a good candidate for a better input for the potential. This can be a small but very fruitful project in close future.

Chapter 8

Evaluation and Improvement of Common Theories

8.1 Abstract

From the GGA family of DFT theories, I evaluated the accuracy of an unconventional, constraint-based and unconventional orbital free kinetic energy density functional approximation, proposed by Luo *et al*. from the functional derivative of the latter and compare it with exact analytically inverted potential.

8.2 Introduction

The advantage of the explicit KEF compared to the implicit KEF is that they correspond to OF-DFT and computationally are less expensive as it concerns linear computational scaling (approximately). OF-DFT in its place is a promising approach in large-scale molecular calculations. When it is the question of isolated or balk systems, a practical KEDF become challenging in development.

Three generations have been developed in the construction of KEDFs. 1) the local approach started by TF functional[192, 50], that is exact for when the density is exact in any region of the space and for homogeneous gas; 2) the semi-local approaches match the terms based on electron density gradient to the TF functionals like vW functional[200]. 3) the non-local approaches use two-point functionals with the information of the density for two positions

and are performed by the relationship between the KE and density response [25, 76, 85].

The functionals of GGA category depend on the local density and the local density gradient. The GGA functionals expanded to so-called meta-GGA functionals by taking into account of the local gradient expansion to second derivative or higher-order dependencies of the density. For longtime, semi-local approximations were known to be not accurate enough for OF-DFT calculations[224]. Recently, those functionals improved significantly to calculate the ground-state properties of semiconductors and balk metals [34, 41, 196, 205, 206, 167, 124, 181, 26, 223]. Among those attempts, the one from Luo *et al.*, known as LKT approximation provided highly accurate results. It is important to mention that LKT is a meta-GGA approximation that is known also as a reduced-cost version of SCAN[186] semi-local density functional.

Considering the advantages of semi-local OF-DFT approximations and their wide application, some deserve to be improved locally by modifying the xc potential with the help of exact non-additive potential bi-functional. Even if the idea sounds ambitious, at least comparing the functional derivative of the semi-local OF-DFT KE with the exact analytically inverted potential will help understand where and at what point those approximations doom to fail.

In the next section, a brief explanation of semi-local functionals is given. The section is included an introduction to LKT functional and will be followed by the recipe of the functional derivative applied to KEDF of LKT T_s^{LKT} to calculate the inverted kinetic potential functional v_s^{LKT}.

The numerical calculations are explained in section.8.4 and the results of the calculations for some diatomic model systems are presented graphically in section.8.5.

In the discussion section, some potential ideas for future works are suggested.

8.3   Theory

The semi-local KE functionals in their general form are made by a sum over the von Weizsäcker KE functional and a TF-KE form functional:

$$T_s^{\text{semi-local}}[\rho](\mathbf{r}) = T_s^{\text{vW}}[\rho](\mathbf{r}) + T_s^{\Theta}[\rho](\mathbf{r}) \tag{8.1}$$

where $T_s^{\Theta}[\rho](\mathbf{r})$ is the Pauli KE functional [128, 92] and is defined in form of:

$$T_s^{\Theta}[\rho](\mathbf{r}) = \int \tau^{\text{TF}}(\mathbf{r}) F_s^{\theta}(s, q) d\mathbf{r} \tag{8.2}$$

where $\tau^{\text{TF}} = \frac{3}{10}(3\pi^2)^{2/3}\rho^{5/3}(\mathbf{r})$, and:

$$s = \frac{|\nabla \rho(\mathbf{r})|}{2(3\pi^2)^{1/3}\rho^{4/3}(\mathbf{r})} \tag{8.3}$$

s is the inhomogeneity wave vector, and

$$q = \frac{\nabla^2 \rho(\mathbf{r})}{4(3\pi^2)^{2/3}\rho^{5/3}(\mathbf{r})} \tag{8.4}$$

In this formulation of the semi-local KE functionals the vW-KE functional can be written as:

$$T_s^{\text{vW}}[\rho](\mathbf{r}) = \int \tau^{\text{TF}}(\mathbf{r}) \frac{5}{3} s^2 d\mathbf{r} \tag{8.5}$$

The exact constraint condition [128] requires that $F_s^{\theta}(s, q) \geq 0$.

The GGA approximations are recognised by their definition of the $T_s^{\theta}[\rho](\mathbf{r})$. It might be essential to understand the reasons behind the development of the various approximations to $T_s^{\theta}[\rho](\mathbf{r})$. A short historical review is provided in section.8.3.1.

8.3.1   Toward approximations of the $T_s^{\theta}[\rho](\mathbf{r})$

The majority of the approximations started by considering slowly varying electron density. The corresponding KE functionals could be represented by a gradient expansion[111, 88] as following:

$$T_s^{\theta}[\rho](\mathbf{r}) = \int \left\{ k_0 + k_2 + k_4 + ... \right\} d\mathbf{r} \tag{8.6}$$

where

$$k_0 = \frac{\pi^{\frac{4}{3}} 3^{\frac{5}{3}}}{10} \rho^{\frac{5}{3}}(\mathbf{r}) = C_{\text{TF}} \rho^{\frac{5}{3}}(\mathbf{r}),$$

$$k_2 = \frac{1}{72} \frac{|\nabla \rho(\mathbf{r})|^2}{\rho(\mathbf{r})},$$

$$k_4 = \frac{(3\pi^2)^{\frac{-2}{3}}}{540} \rho^{\frac{1}{3}} \left\{ \left(\frac{\nabla^2 \rho(\mathbf{r})}{\rho(\mathbf{r})} \right)^2 - \frac{9}{8} \frac{\nabla^2 \rho(\mathbf{r})}{\rho(\mathbf{r})} \left[\frac{|\nabla \rho(\mathbf{r})|}{\rho(\mathbf{r})} \right]^2 \right.$$

$$\left. + \frac{1}{3} \left[\frac{|\nabla \rho(\mathbf{r})|}{\rho(\mathbf{r})} \right]^4 \right\},$$

(8.7)

etc.

Those series are asymptotic expansions in which each term depends on local values of the scale-density-gradients (we mean s). Clearly, I find out that $k_0 = T_s^{\text{TF}}[\rho](\mathbf{r})$. If the system is one of the uniform electronic density, this latter yields an accurate value of the KE. However it is not a correct assumption for molecular systems. The $k_2 = T_s^{\text{vW}}[\rho](\mathbf{r})$. In some approximations k_2 is the dominant term in the series. $T_s^{\text{vW}}[\rho](\mathbf{r})$ yields to very accurate KE and provides the correct asymptotic behaviour far from the vicinity of the nuclei. As it is already mentioned, $T_s^{\text{vW}}[\rho](\mathbf{r})$ is exact of the cases of the single orbital systems. The disadvantage of the $T_s^{\text{vW}}[\rho](\mathbf{r})$ is that it does not satisfy[10] the inhomogeneity condition (see section.8.7 for more information). The k_4 yields the divergent functional derivative of $T_s[\rho](\mathbf{r})$ and the terms of the higher orders are divergent for both molecules and atoms[145]. The main challenge of the gradient expansion-based strategy towards the approximations is they are not adapted to the approaches based on the Euler–Lagrange equations. To that end, other strategies were proposed. One was developed by Ou-Yang *et al.*[154] to modify the series in Eq.[8.7]. They replaced the k_i terms with analytical terms functional of $[\rho, \nabla \rho]$ while taking into account the scaling properties. They came out with two approximations knowm as $T_s^{OL1}[\rho](\mathbf{r})$ and $T_s^{OL2}[\rho](\mathbf{r})$[220].

There exist approximations in family of TFλvW functionals are defined by Pauli enhancement factor. Their $F_s^{\theta}(s)$ functions have the following form:

$$F_s^{TF\lambda vW}(s) = \frac{5}{3}(\lambda vW - 1) + 1$$

(8.8)

where λ is a parameter[34].

Another family of these approximations is Pauli-Gaussian KE functionals (PGS-KE) in which the $F_s^\theta(s)$ is related to the scale-density-gradients exponentially:

$$F_s^{PG\mu}(s) = \exp\{-\mu s^2\} \tag{8.9}$$

where λ is a parameter[111, 34].

The PGS functionals upgraded to so-called PGSLβ family of approximations [34] in which a Laplacian-level correction was added to the $F_s^{PGS}(s)$.

$$F_s^{PGSL\beta}(s) = F_s^{PGS}(s) + \beta q^2 \tag{8.10}$$

where β is a parameter and q is given in Eq.[8.4].

Finally The PGSL family of approximations was developed by a complementary strategy, known as PGSLr functionals. In this new family, the $F_s^\theta(s)$ is expressed in Taylor expansion of higher orders of both s and q[88, 20, 225, 33].

Some other researchers replaced the local s-dependency of the KE by several analytical values to smooth the KE functionals [42, 170].

Analytical form of the KE functional form the ex energy was another approach to improve the GGA approximations . This idea was suggested first by Lee et al.[126] who suggested the new $T_s^{approximate}[\rho](\mathbf{r})$ in form of the Eq.[8.2]. From the approximations based on the last strategy I can name a few of the frequently used ones such as $T_s^{LLP}[\rho](\mathbf{r})$[126], $T_s^{PW86}[\rho](\mathbf{r})$[158],$T_s^{PW91}[\rho](\mathbf{r})$[160], $T_s^{T92}[\rho](\mathbf{r})$[191], and $T_s^{LKT}[\rho](\mathbf{r})$[132]. The latest is known as the most successful approximation of this family. The following sub-section explains how the analytical form of the $v^{LKT}[\rho](\mathbf{r})$ is obtained.

8.3.2 The $v^{LKT}[\rho](\mathbf{r})$ from the Functional Derivative of the $T^{LKT}[\rho](\mathbf{r})$

The functional derivation of $T^{approximation}[\rho](\mathbf{r})$ to calculated analytically inverted $v_s[\rho](\mathbf{r})$ could appear to be complicated mathematically based on the definition of $F_s(s)$ included involved in KE functional. The requirement of this inversion is its use in $v_s^{\text{NAD}}[\rho_B, \rho_{tot}](\mathbf{r})$ later on. We base on the work of Wesolowski and Tran[216] in which they formulated a general form for the KE bi-functional of a pair of densities and the functional derivative of

the KE functional of a given density as in Eq.[8.11] and Eq.[8.12]. To calculate $v_s^{\text{NAD/GGA}}[\rho_1, \rho_2](\mathbf{r})$ one can develop $\frac{\delta T_s^{\text{GGA}}[\rho_1,\rho_2](\mathbf{r})}{\delta \rho_i}$ for $i = 1, 2$ depending on the sub-density in question or calculating separately the terms of the $v_s^{\text{NAD/GGA}}[\rho_i, \rho_j](\mathbf{r}) = v_s[\rho_i](\mathbf{r}) - v_s[\rho_j](\mathbf{r})$ from $\frac{\delta T_s^{\text{GGA}}[\rho_{i,j}](\mathbf{r})}{\delta \rho_{i,j}(\mathbf{r})}$ again for i, j being the indices of the sub-densities.

$$
\begin{aligned}
T_s^{\text{GGA}}[\rho_1, \rho_2](\mathbf{r}) = {} & C_{\text{TF}} \int (\rho_1(\mathbf{r}) + \rho_1(\mathbf{r}))^{\frac{5}{3}} F_s(s) \left(\frac{|\nabla(\rho_1(\mathbf{r}) + \rho_1(\mathbf{r}))|}{(\rho_2(\mathbf{r}) + \rho_1(\mathbf{r}))^{\frac{4}{3}}} d\mathbf{r} \right) \\
& - C_{\text{TF}} \int \left[\rho_1^{\frac{5}{3}}(\mathbf{r}) F_s(s) \left(\frac{|\nabla(\rho_1(\mathbf{r}))|}{(\rho_1(\mathbf{r}))^{\frac{4}{3}}} d\mathbf{r} \right) \right. \\
& \left. + \rho_2^{\frac{5}{3}}(\mathbf{r}) F_s(s) \left(\frac{|\nabla(\rho_2(\mathbf{r}))|}{(\rho_2(\mathbf{r}))^{\frac{4}{3}}} \right) \right] d\mathbf{r}
\end{aligned}
\tag{8.11}
$$

$$
\begin{aligned}
\frac{\delta T_s^{\text{GGA}}[\rho](\mathbf{r})}{\delta \rho(\mathbf{r})} = {} & \frac{5 C_{\text{TF}}}{3} \rho^{2/3}(\mathbf{r}) \left[F_s(s) - \frac{|\nabla \rho(\mathbf{r})|}{\rho^{\frac{4}{3}}(\mathbf{r})} F_s'(s) + \frac{4}{3} \left(\frac{|\nabla \rho(\mathbf{r})|}{\rho^{\frac{4}{3}}(\mathbf{r})} \right)^2 F_s''(s) \right] \\
& + C_{\text{TF}} D \frac{\rho^{\frac{1}{3}}(\mathbf{r})}{|\nabla \rho(\mathbf{r})|^3} [F_s'(s) - \frac{|\nabla \rho(\mathbf{r})|}{\rho^{\frac{4}{3}}(\mathbf{r})} F_s''(s)] \\
& - C_{\text{TF}} \frac{F_s'(s) \rho^{\frac{1}{3}}(\mathbf{r})}{|\nabla \rho(\mathbf{r})|} \nabla^2 \rho(\mathbf{r})
\end{aligned}
\tag{8.12}
$$

where $D = \sum_{i=1}^{3} \sum_{j=1}^{3} \partial_i \rho(\mathbf{r}) \partial_i \partial_j \rho(\mathbf{r}) \partial_j \rho(\mathbf{r})$.

The $F_t^{LKT}(s)$ is:

$$
F_t^{LKT}(s) = \frac{1}{\cosh(1.3s)} + \frac{5}{3} s^2
\tag{8.13}
$$

where:

$$
s = \frac{1}{2(3\pi^2)^{1/3}} \frac{|\nabla \rho(\mathbf{r})|}{\rho^{4/3}(\mathbf{r})}
\tag{8.14}
$$

Eq.[8.12] can also be written in simpler way in form of Eq.[8.15].

$$
\begin{aligned}
\frac{\delta T[\rho](\mathbf{r})}{\delta \rho(\mathbf{r})} = \frac{C_{\text{TF}}}{3} \Bigg\{ & 5 \rho^{5/3}(\mathbf{r}) F_s(s) \\
& - \frac{|\nabla \rho(\mathbf{r})|^2}{\rho^2(\mathbf{r})} (F'(s) - 4s F_s''(s)) \\
& - 6 \frac{\nabla^2 \rho(\mathbf{r})}{\rho(\mathbf{r})} \left(F'(s) - 2s F''(s) \right) \Bigg\}
\end{aligned}
\tag{8.15}
$$

where $C_{\text{TF}} = \frac{3^{5/3} \pi^{4/3}}{10}$. In the appendix.E the step-by-step calculation of the $v_s^{LKT}[\rho](\mathbf{r})$ from $T_s^{LKT}[\rho](\mathbf{r})$ is given. For a diatomic model system, I calculated

non-additive kinetic bi-functional for two different pairs of densities as following:

$$v_s^{\text{NAD/LKT}}[\rho_B, \rho_1](\mathbf{r}) = v_s[\rho_B](\mathbf{r}) - v_s[\rho_1](\mathbf{r}) \tag{8.16}$$

where $\rho_1(\mathbf{r}) = 2|\phi_1(\mathbf{r})|^2$ for $\phi_1(\mathbf{r})$ being the solution of the system with the lowest energy and $\rho_B(\mathbf{r})$ is defined in Eq.[3.22] with the help of Eq.[3.21].

$$v_s^{\text{NAD/LKT}}[\rho_B, \rho_{tot}](\mathbf{r}) = v_s[\rho_B](\mathbf{r}) - v_{KS}^{\text{LDA}}(\mathbf{r}) \tag{8.17}$$

In the next section I briefly explain the numerical approach to those calculations.

8.4 Numerical Calculation

The calculations are obtained on accurate numerical grids using the all-electron program package DARSEC [135]. Consequently, I are restricted to computations of molecules with two atomic centres with spherical symmetry. In DARSEC, the Kohn-Sham equations are solved self-consistently using the high-order finite difference approach [52, 11]. In this work, the stencil was set to 12 for the finite difference. A real-space grid based on prolate-spherical coordinates (see Eq.[1.20] and Eq.[1.19]) is used to describe a system with two atomic centres. The grid is very dense near two centres and increasingly sparse farther from the centres. Due to the cylindrical symmetry of diatomic molecules, the problem is reduced to a two–dimensional one. In the calculations for this work, the systems are defined within 15 $Bohr$ of radius and number of 115×121 grid points. The $\rho_{tot}(\mathbf{r})$ is the ground-state density of the systems performed with the LDA [24, 162].

The calculations are down for two different sub-densities: 1) for when $\int \rho_B(\mathbf{r})d\mathbf{r} = 2.0$ and one for the case in which the charge density is not localised into an integer value at the vicinity of the nuclei, $\int \rho_B(\mathbf{r})d\mathbf{r} = 1.5$. For partitioning the ground state density numerically, I use a smooth distribution function $0 \leq F(z) \leq 2$ that has no cusps and respects the smoothness of the function explained in Section[3.3.2]. The choice for such a function used for the reported result is Fermi-Dirac distribution function that changes smoothly from value one to zero (Eq.[3.21]). This latter was realised within binary-search algorithm to localised the density around one nucleus.

 181

8.5   Results and Discussion

The non-additive kinetic potential bi-functional from LKT theory is shown calculated from Eq.[8.17] and compared to the $v^{\mathrm{NAD/LKT}}$ obtained from Eq.[8.16]. The reason to compare these two potentials comes from the fact that from exact analytically inverted potential the second term of both equations must be equal. I previously showed that it comes true for analytically inverted potential in section. 3.3.1 of Chapter 3. In Fig.[8.1] the $v^{\mathrm{NAD/LKT}}$s are compared. It shows them incomparable. To understand such a huge difference between bi-functional potentials, I compare first each inverted potential $v_s[\rho_i](\mathbf{r})$ where $i = 1, B$ (Fig.[8.3]) and then I show how $v_s^{LKT}[\rho_1](\mathbf{r})$ varies from the exact inverted potential $v_s^{\mathrm{EXACT}}[\rho_1](\mathbf{r})$ calculated in Eq.[3.5] (Fig.[8.4]) .
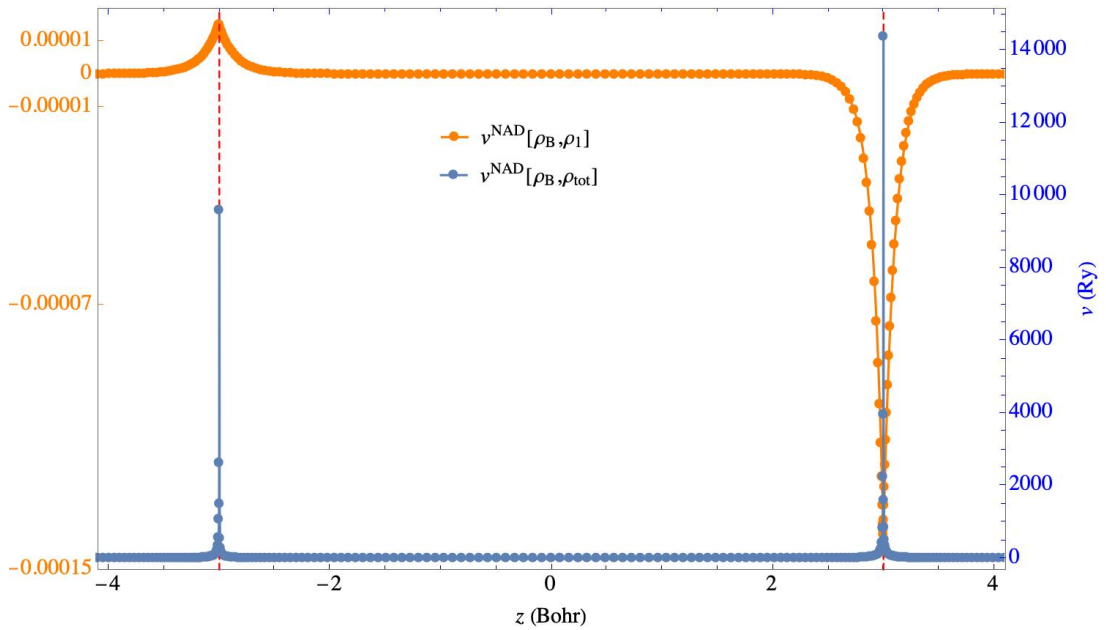
Figure 8.1: System: HeLi$^+$, He is located at $(0,0,-3)$ Bohr (at left) and Li is located at $(0,0,3)$ Bohr (at right). Orange Line: $v^{\mathrm{NAD/LKT}}$ from Eq.[8.16]; Blue Line: $v^{\mathrm{NAD/LKT}}$ from Eq.[8.17]; Vertical dashed lines: The location of the nuclei in space.
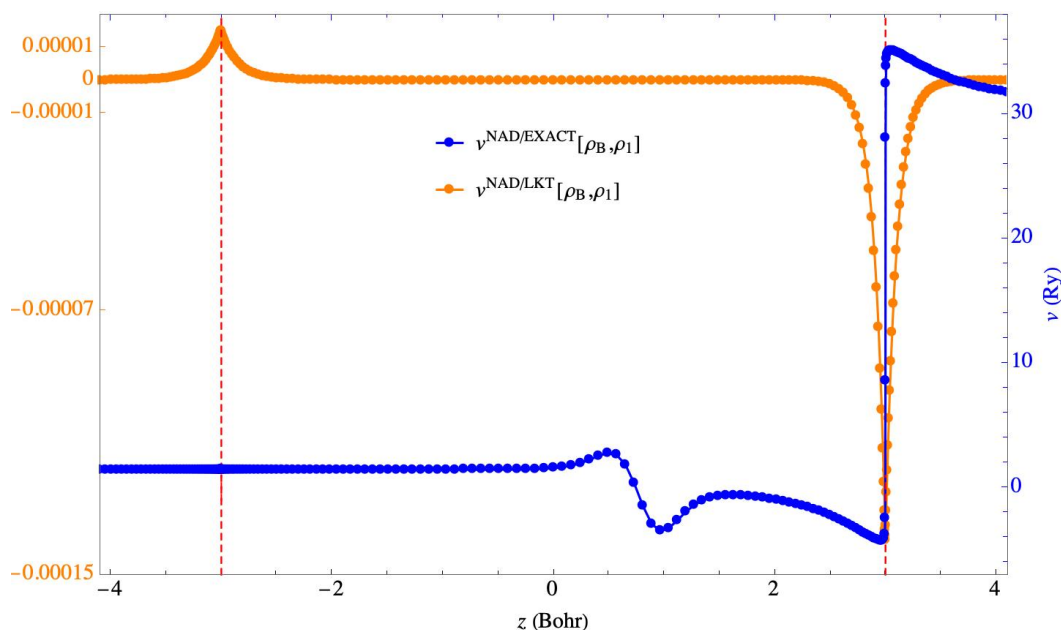
Figure 8.2: System: HeLi$^+$, He is located at $(0, 0, -3)$ Bohr (at left) and Li is located at $(0, 0, 3)$ Bohr (at right). Orange Line: $v^{\text{NAD/LKT}}$ from Eq.[8.16]; Blue Line: $v^{NAD/EXACT}$ from Eq.[3.19]; Vertical dashed lines: The location of the nuclei in space.

In Fig.[8.3] I see both $v_s^{LKT}[\rho_1](\mathbf{r})$ and $v_s^{LKT}[\rho_B](\mathbf{r})$ vary very smoothly in whole space and figure a cusp-like discontinuity at the vicinity of the nuclei. I already showed (see section 3.3) that the exact analytically inverted potential from a charge density that corresponds to the solution of the system ($\rho_i(\mathbf{r}) = 2|\phi_i(\mathbf{r})|^2$; for $i = 1, 2, ...$) must behave exactly as $v_{KS}(\mathbf{r})$. When the localisation of the electron in a diatomic system of four electron respects accurately the equation $\int \rho_B(\mathbf{r}) d\mathbf{r} = 2$, consequently $\rho_B(\mathbf{r})$ corresponds to one of the solutions of the system. Expectantly, the corresponding inverted potential has to be comparable with $v_{KS}(\mathbf{r})$.

When the analytical inversion of the $\rho_B(\mathbf{r})$ and the $\rho_1(\mathbf{r})$ is done from the LKT theory, all small changes in the potential are forced to be suppressed to provide a smooth solution of the system for when it's plugged into the KS equation.
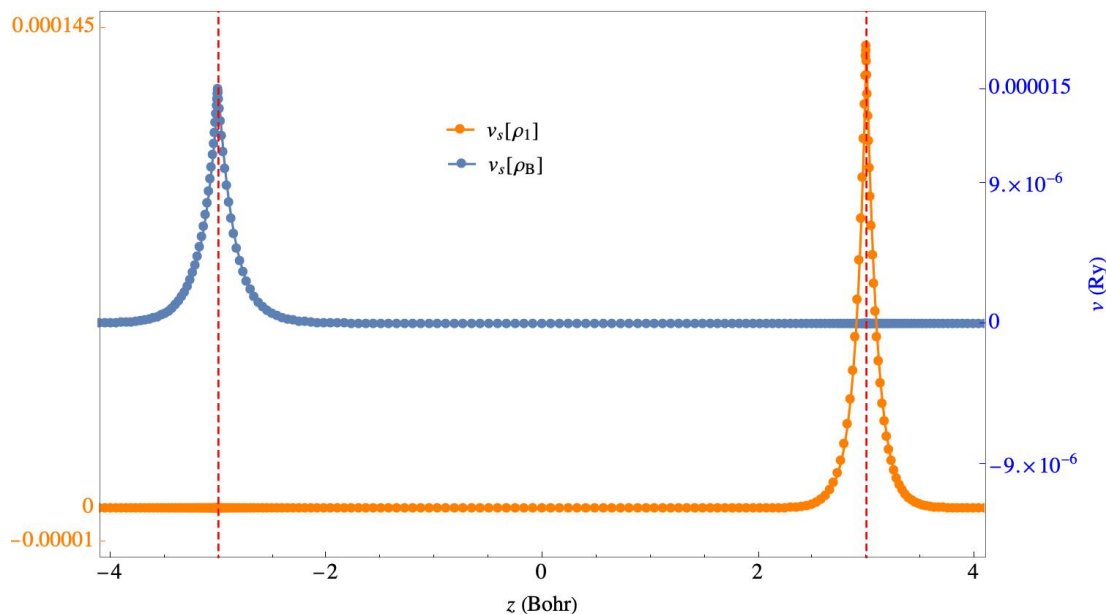
Figure 8.3: System: $HeLi^+$, He is located at $(0,0,-3)$ Bohr (at left) and Li is located at $(0,0,3)$ Bohr (at right). Orange Line: $v_s^{LKT}[\rho_1](\mathbf{r})$; Blue Line: $v_s^{LKT}[\rho_B](\mathbf{r})$; Vertical dashed lines: The location of the nuclei in space.

To clarify better where the theory fails to provide the exact potential, I compared the inverted potential from the solution-charge-density in LKT and Exact inversion and compared them in Fig.[8.4].

The failure of LKT in the calculation of the $v_s^{LKT}[\rho_1](\mathbf{r})$ from the functional derivative of the $T_s^{LKT}[\rho_1](\mathbf{r})$ is more clear when I look at it's difference with the $v_{KS}(\mathbf{r})$. Fig.[8.5] the $\Delta v_s^{LKT}[\rho(\mathbf{r}) = v_s^{LKT}[\rho_1](\mathbf{r}) - v_{KS}^{LDA}(\mathbf{r})$ is plotted and compared with $\Delta v_s^{LKT}[\rho(\mathbf{r}) = v_s^{EXACT}[\rho_1](\mathbf{r}) - v_{KS}^{LDA}(\mathbf{r})$. In exact theory the $\Delta v_s^{LKT}[\rho(\mathbf{r}) = 0$ (taking into account of the actual machine precision which may bring some noises in the curve). In LKT theory the $v_s^{LKT}[\rho_1](\mathbf{r})$ cannot read the total exact potential at all. Such a huge difference between $v_s^{LKT}[\rho_1](\mathbf{r})$ and $v_{KS}(\mathbf{r})$ predict how the uniqueness condition of one-to-one mapping between the potential and ground-state density is violated.
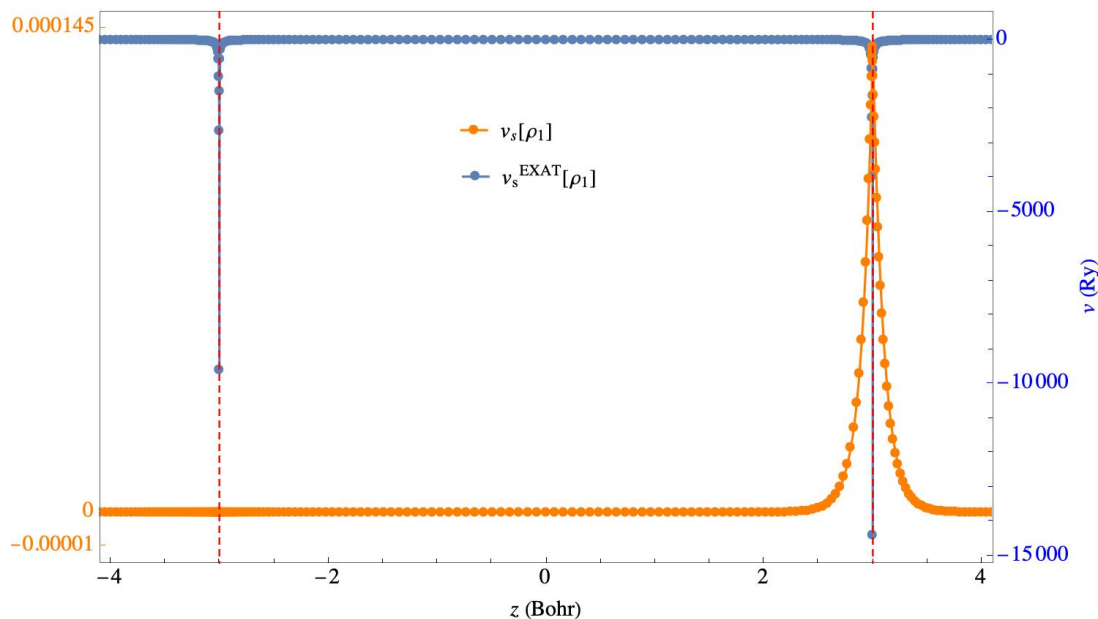
Figure 8.4: System: HeLi$^+$, He is located at $(0, 0, -3)$ Bohr (at left) and Li is located at $(0, 0, 3)$ Bohr (at right). Orange Line: $v_s^{LKT}[\rho_1](\mathbf{r})$; Blue Line: $v_s^{\mathrm{EXACT}}[\rho_1](\mathbf{r})$ from Eq.[3.5]; Vertical dashed lines: The location of the nuclei in space.
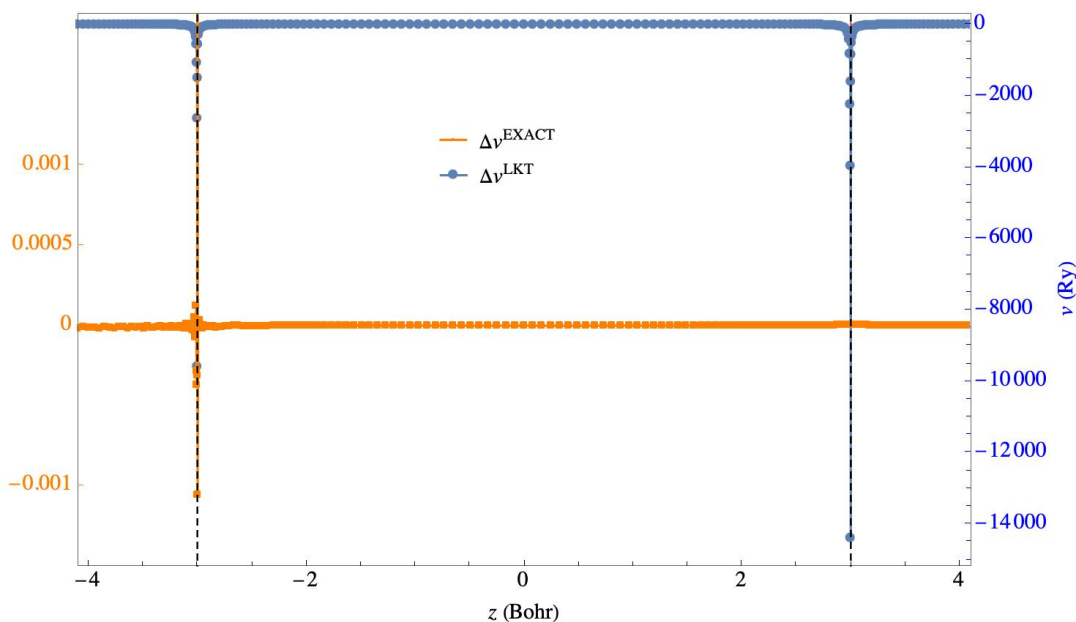
Figure 8.5: System: HeLi$^+$, He is located at $(0, 0, -3)$ Bohr (at left) and Li is located at $(0, 0, 3)$ Bohr (at right). Orange Line: $\Delta v_s^{LKT}[\rho(\mathbf{r}) = v_s^{LKT}[\rho_1](\mathbf{r}) - v_{KS}^{\mathrm{LDA}}(\mathbf{r})$; Blue Line: $\Delta v_s^{EXCAT}[\rho](\mathbf{r}) = v_s^{\mathrm{EXACT}}[\rho_1](\mathbf{r}) - v_{KS}^{\mathrm{LDA}}(\mathbf{r})$ where the $v_s^{\mathrm{EXACT}}[\rho_1](\mathbf{r})$ is calculated in Eq.[3.5]; Vertical dashed lines: The location of the nuclei in space
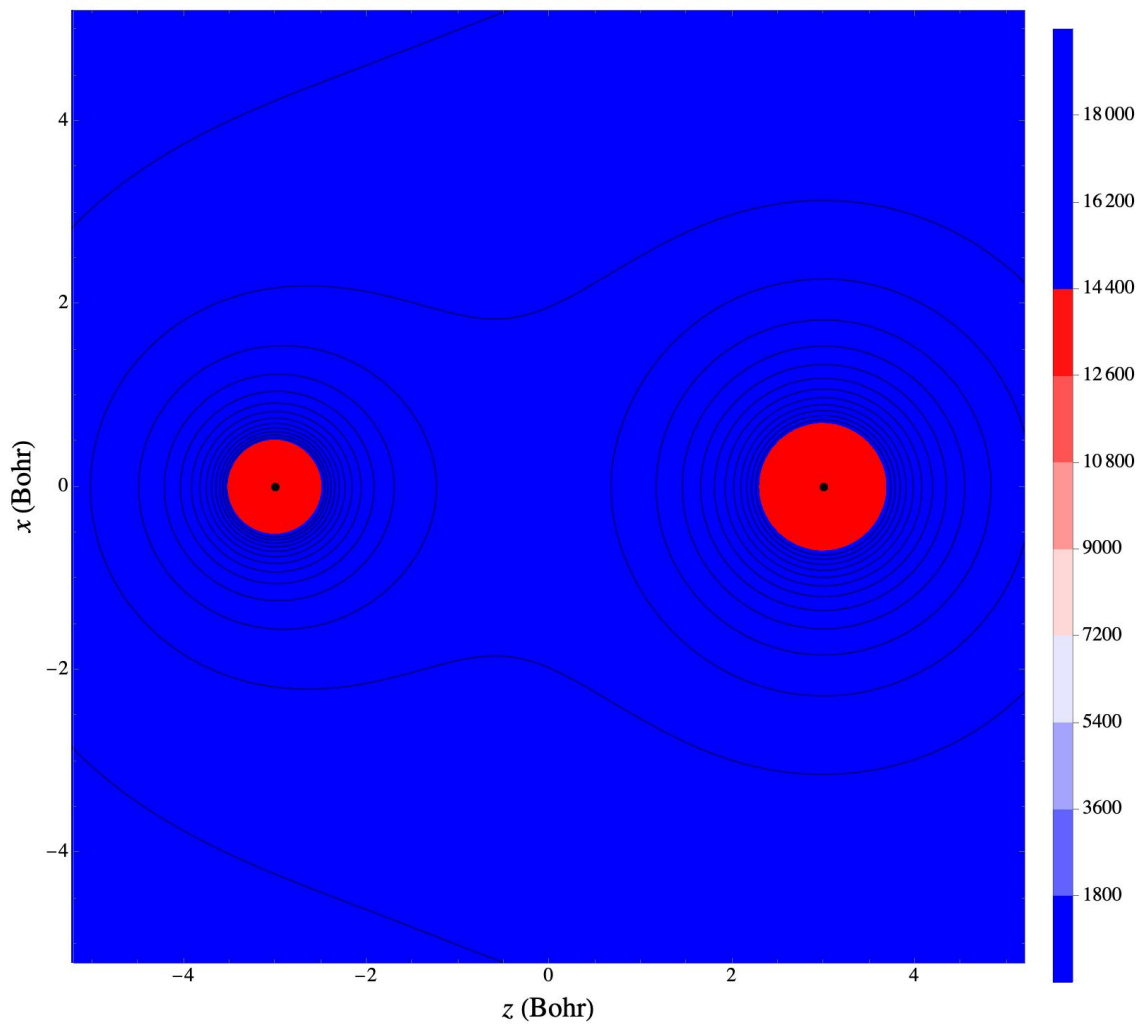
Figure 8.6: 2D representation of the non-additive kinetic potential bi-functional from Eq.[8.17]; System: LiHe$^+$, Two-dimensional representation of $v_s^{\text{NAD/LKT}}[\rho_B, \rho_{tot}](\mathbf{r})$ Ry. Black dots: nuclei.

To understand how the non-additive kinetic potential bi-functional behave in space under, the LKT theory, I showed in Fig.[8.6] and Fig.[8.7] the 2D-representation of the $v_s^{\text{NAD/LKT}}[\rho_B, \rho_{tot}](\mathbf{r})$ and $v_s^{\text{NAD/LKT}}[\rho_B, \rho_1](\mathbf{r})$ consecutively.
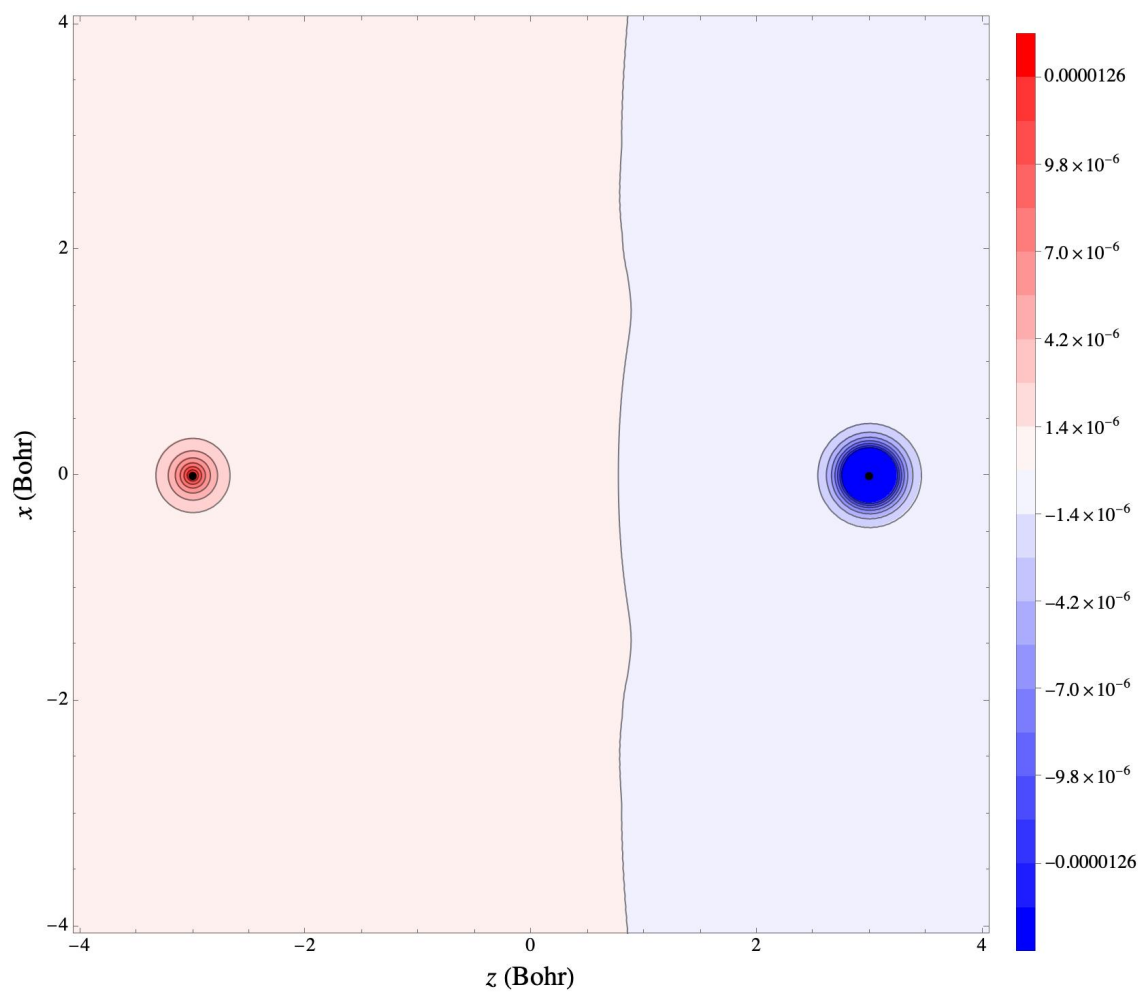
Figure 8.7: 2D representation of the non-additive kinetic potential bi-functional from Eq.[8.16]; System: LiHe$^+$, Two-dimensional representation of $v_s^{\mathrm{NAD/LKT}}[\rho_B, \rho_1](\mathbf{r})$ Ry. Black dots: nuclei.

8.5.1 The $v^{\mathrm{NAD/LKT}}$ for Non-localised Charge Density

Some theories may not provide enough information of the overlap region of two neighbouring sub-densities if this latter is not varying enough from the integer charge density of the whole system. To see how LKT analytically inverted potential behaves in such region, for the same system I localised partially the charge density around He and calculated $v^{\mathrm{NAD/LKT}}[\rho_B, \rho_1](\mathbf{r})$ and $v^{\mathrm{NAD/LKT}}[\rho_B, \rho_{tot}](\mathbf{r})$ for $\int \rho_B(\mathbf{r})d\mathbf{r} = 1.75$ where $\rho_B(\mathbf{r})$ being density localised around the He atom at the left-side of the system.
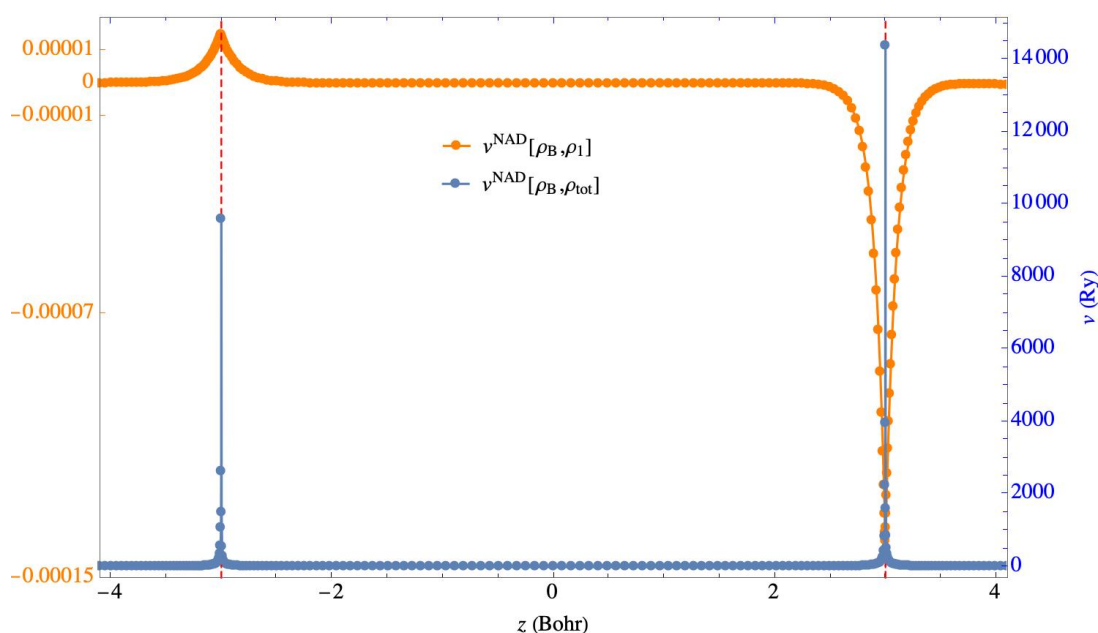
Figure 8.8: Non-additive kinetic potential bi-functionals for the non-integer charge density localisation of $\int \rho_B(\mathbf{r})d\mathbf{r} = 1.75$; System: HeLi$^+$, He is located at $(0,0,-3)$ Bohr (at left) and Li is located at $(0,0,3)$ Bohr (at right). Orange Line: $v^{\mathrm{NAD/LKT}}$ from Eq.[8.16]; Blue Line: $v^{\mathrm{NAD/LKT}}$ from Eq.[8.17]; Vertical dashed lines: The location of the nuclei in space.

One more time these two potentials appear incomparable as it is shown in Fig.[8.8]. Similarly, both inverted potentials $v_s^{LKT}[\rho_1](\mathbf{r})$ and $v_s^{LKT}[\rho_B](\mathbf{r})$ have totally different feature from $v_{KS}(\mathbf{r})$ as I see in Fig.[8.9].
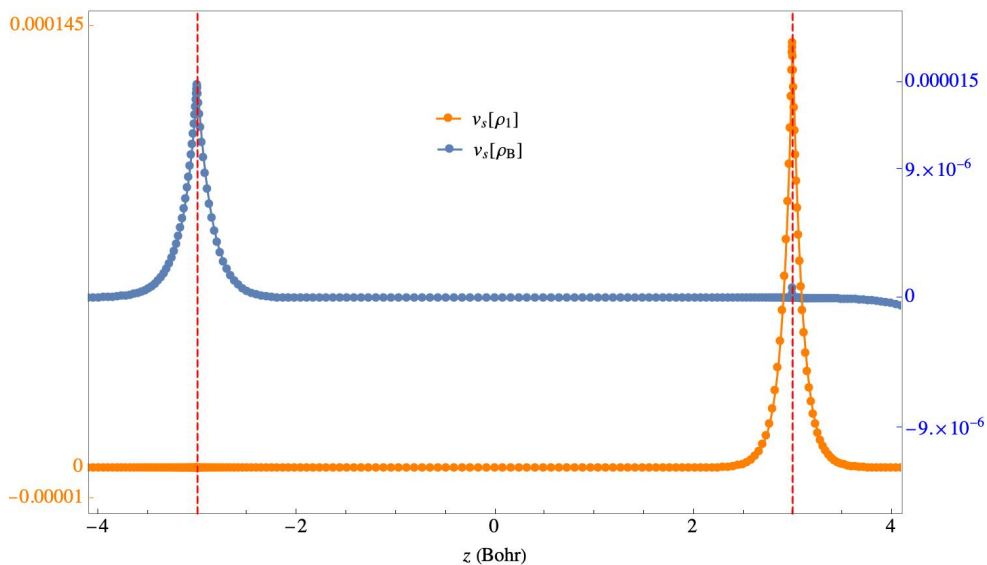
Figure 8.9: Analytically inverted potential functionals for the non-integer charge density localisation of $\int \rho_B(\mathbf{r})d\mathbf{r} = 1.75$ and from orbital density $\rho_1(\mathbf{r}) = 2|\phi_1(\mathbf{r})|^2$; System: HeLi$^+$, He is located at $(0,0,-3)$ Bohr (at left) and Li is located at $(0,0,3)$ Bohr (at right). Orange Line: $v_s^{LKT}[\rho_1](\mathbf{r})$; Blue Line: $v_s^{LKT}[\rho_B](\mathbf{r})$; Vertical dashed lines: The location of the nuclei in space.

Also, the Δvs are:
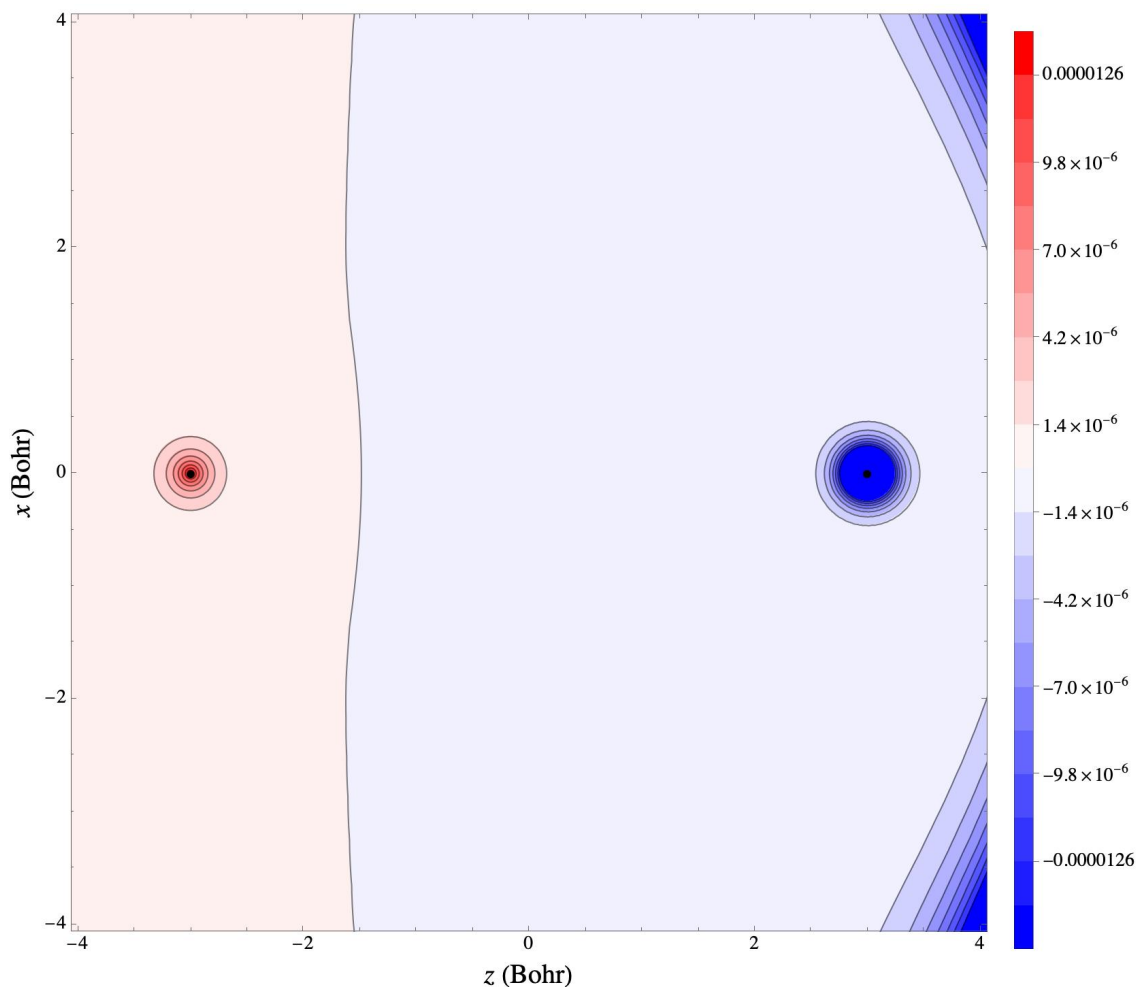
Figure 8.10: 2D representation of the Non-additive kinetic potential bi-functionals for the non-integer charge density localisation of $\int \rho_B(\mathbf{r}) d\mathbf{r} = 1.75$ from Eq.[8.16]; System: LiHe$^+$, Two-dimensional representation of $v_s^{\text{NAD/LKT}}[\rho_B, \rho_1](\mathbf{r})$ Ry. Black dots: nuclei.

Instead, from the 2D representation of $v_s^{\text{NAD/LKT}}[\rho_B, \rho_1](\mathbf{r})$ for non-localised charge density compared to the one from localised density (Fig.[8.7]) I recognised that the negative value of the potential (means the potential being attractive Colombian potential) is shifted to the left for the case of non-localised charge density. This is the expected behaviour of the potential, although the attraction of the potential at the overlap region requires to be tested to see if it can ensure the correct molecular ground state density. This latter is beyond our main goal of this work. However, the 2D representation of $v_s^{\text{NAD/LKT}}[\rho_B, \rho_{tot}](\mathbf{r})$ (Fig.[8.11]) appeared the same as the one for localised charge density around

He nuclei(see Fig.[8.6]).
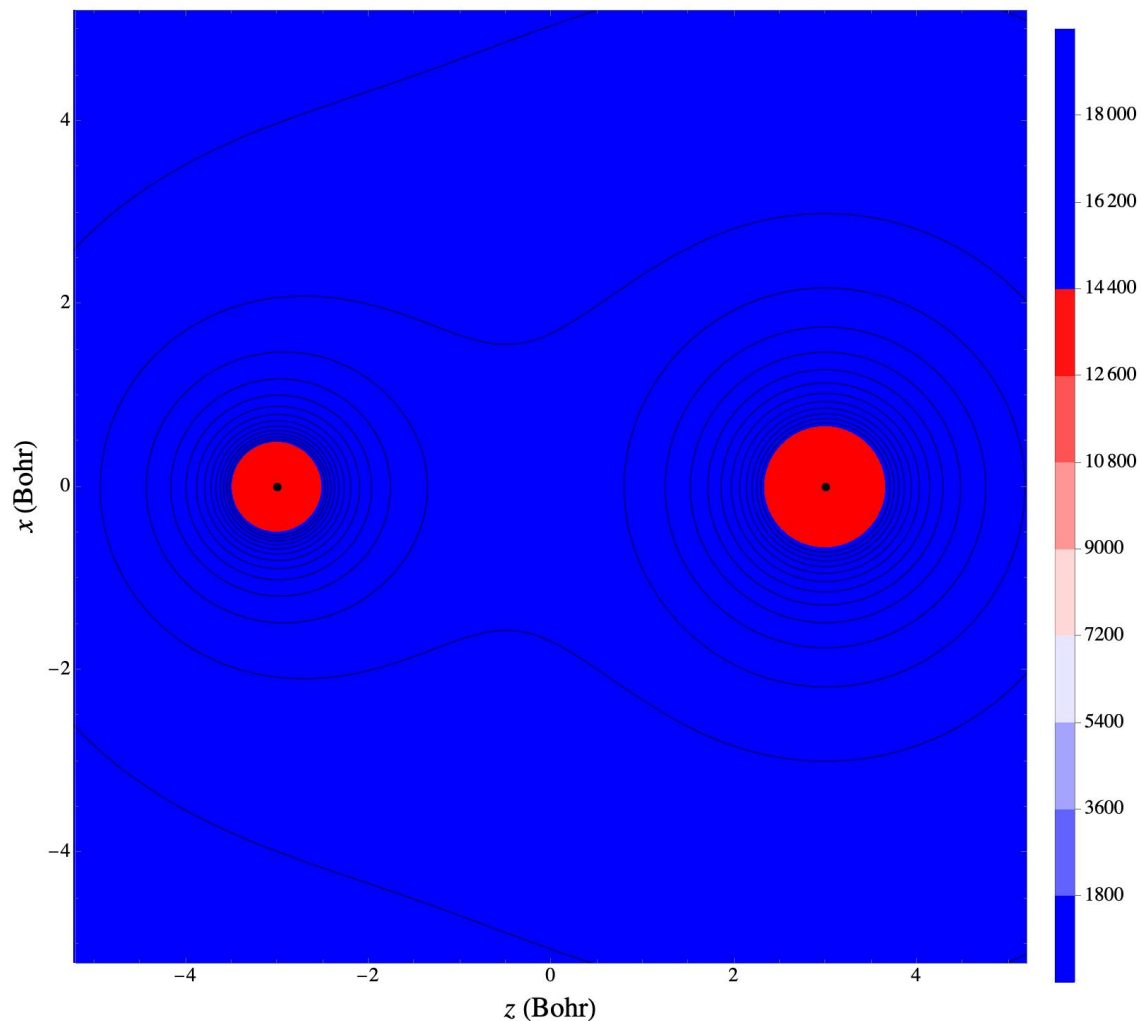
Figure 8.11: 2D representation of the Non-additive kinetic potential bi-functionals for the non-integer charge density localisation of $\int \rho_B(\mathbf{r})d\mathbf{r} = 1.75$ from Eq.[8.17]; System: LiHe$^+$, Two-dimensional representation of $v_s^{\text{NAD/LKT}}[\rho_B, \rho_{tot}](\mathbf{r})$ Ry. Black dots: nuclei.

As the second term in the calculation of the $v_s^{\text{NAD/LKT}}[\rho_B, \rho_i](\mathbf{r})$ for $i = 1, tot$ remains the same for both localised and non-localised charge density cases, I may compare the first term of the equation for both cases to understand more precisely about the accuracy of the theory.

8.5.2 Localised vs non-Localised Charge Density
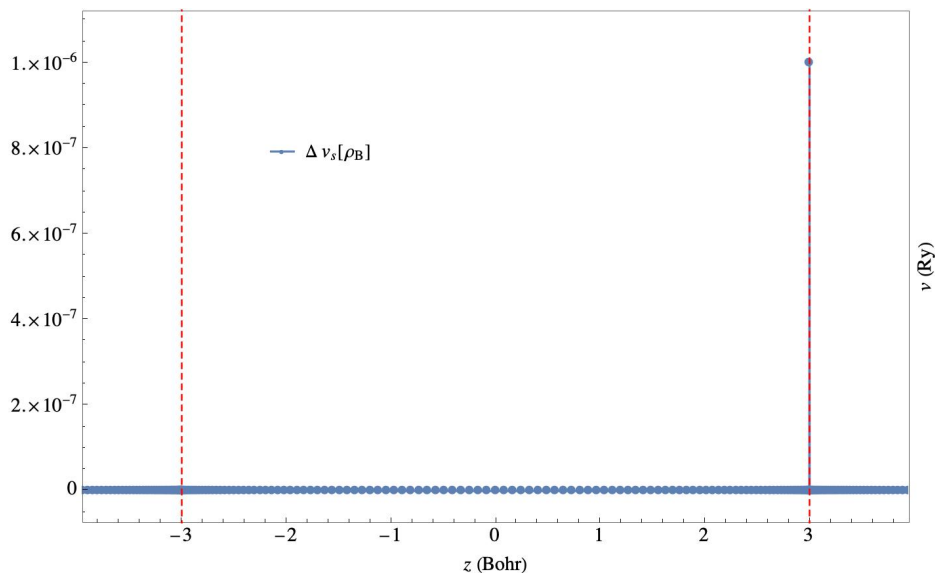
Figure 8.12: Difference between the analytically inverted potential in LKT theorem for localised and non-localised charge density. The localised charge density satisfies $\int \rho_B(\mathbf{r})d\mathbf{r} = 2$, however, in non-localised case $\int \rho_B(\mathbf{r})d\mathbf{r} = 1.75$; System: HeLi$^+$, He is located at $(0, 0, -3)$ Bohr (at left) and Li is located at $(0, 0, 3)$ Bohr (at right). Blue Line: $\Delta v_s^{LKT}[\rho_B](\mathbf{r}) = v_s^{LKT}[\rho_B^{loc}](\mathbf{r}) - v_s^{LKT}[\rho_B^{non-loc}](\mathbf{r})$; Vertical dashed lines: The location of the nuclei in space.

We subtracted $v_s^{LKT}[\rho_B^{non-loc}](\mathbf{r})$ from $v_s^{LKT}[\rho_B^{loc}](\mathbf{r})$ and showed the result in Fig.[8.12]. Except at the location of Li nuclei $((0, 0, 3))$ that a single point comes apart from the rest of the curve, the $\Delta v_s^{LKT}[\rho_B](\mathbf{r}) = 0$ in whole space. That single grid-point with the potential about 1.0×10^{-6} is nothing than numerical taking into account of its orders of magnitude compared to the one from $v_{KS}(\mathbf{r})$.

Some more systems could be chosen to test the accuracy of LKT potential but at this level if fails at different stages.

8.6   Conclusion and Outlook

The $v_s^{LKT}[\rho_i](\mathbf{r})$ for $i = 1, B^{loc}, B^{non-loc}$ so consequently $v_s^{\mathrm{NAD/LKT}}[\rho_B, \rho_1](\mathbf{r})$ and $v_s^{\mathrm{NAD/LKT}}[\rho_B, \rho_{tot}](\mathbf{r})$ failed the accuracy.

The beauty of the exact $v_s^{NAD/EXACT}[\rho_B, \rho_1](\mathbf{r})$ is its potential to improve the other theories by its local application to the region where two neighbouring sub-densities overlap weakly. The failure of the LKT theory in direct analytical inversion of the potential from a given density is no restraint to the overlap region, it fails gravely at nuclei locations as well.

Although the LKT is known as the best approximation in GGA family in providing smooth curve of the penitential yielding acceptable accurate ground state density and computationally being one of the least costly theories, it doesn't have the potential to become close to an exact theory with the help of exact analytical inversion method. So, such modification might not be cost effective.

At the end, I might add that the huge difference of the orders of magnitude between analytically inverted $v_s^{NAD/EXACT}[\rho_B, \rho_1](\mathbf{r})$ and $v_s^{NAD/LKT}[\rho_B, \rho_1](\mathbf{r})$ (also from ρ_{tot}) seems suspicious. It requires more investigation in the numerical implementation to find out the validity of such difference.

8.7 Supplementary Information

Let's understand the homogeneity relationship between two functionals. Assuming a system of spin polarised wave functions. The KE is a bi-functional of the spin polarised densities $T_s[\rho_\uparrow, \rho_\downarrow](\mathbf{r})$. In the spin-polarized scenario of the KS formulation of DFT, the total energy of the ground-state density is given by:

$$E[\rho_\uparrow, \rho_\downarrow](\mathbf{r}) = T_s[\rho_\uparrow, \rho_\downarrow](\mathbf{r}) + J[\rho](\mathbf{r}) + E_{xc}[\rho_\uparrow, \rho_\downarrow](\mathbf{r}) + v_{ne}[\rho](\mathbf{r}) \qquad (8.18)$$

where $E_{xc}[\rho_\uparrow, \rho_\downarrow](\mathbf{r})$ is ex density functional, and

$$J[\rho](\mathbf{r}) = \frac{1}{2} \int \int \frac{\rho(\mathbf{r}_i)\rho(\mathbf{r}_j)}{|\mathbf{r}_i - \mathbf{r}_j|} d\mathbf{r}'_i d\mathbf{r}'_j \qquad (8.19)$$

and

$$v_{ne}[\rho](\mathbf{r}) = \int \rho(\mathbf{r}) v(\mathbf{r}) d\mathbf{r}' \qquad (8.20)$$

which are electron-electron repulsion and nuclear-electron attraction potentials, respectively. The $E_{xc}[\rho_\uparrow, \rho_\downarrow](\mathbf{r})$ contains a contribution of KE functional in terms of the difference between the total KE and the KE of a non-interacting system of electrons: $T[\rho_\uparrow, \rho_\downarrow](\mathbf{r}) - T_s[\rho_\uparrow, \rho_\downarrow](\mathbf{r})$.

The non-interacting KE bi-functional has to read the following Euler- Lagrange equation:

$$\frac{\delta E[\rho_\uparrow, \rho_\downarrow](\mathbf{r})}{\rho_\sigma(\mathbf{r})} = \frac{\delta T_s[\rho_\uparrow, \rho_\downarrow](\mathbf{r})}{\rho_\sigma(\mathbf{r})} + v_{eff,\sigma}(\mathbf{r}) = \mu_\sigma \qquad (8.21)$$

where μ_σ is a Lagrange multiplier (chemical potential), $\sigma \in [\uparrow, \downarrow]$, and $v_{eff,\sigma}(\mathbf{r})$ is the Kohn-Sham effective single-particle potential:

$$v_{eff,\sigma}(\mathbf{r}) = \frac{\delta}{\rho_\sigma(\mathbf{r})}\big\{E[\rho_\uparrow, \rho_\downarrow](\mathbf{r}) - T_s[\rho_\uparrow, \rho_\downarrow](\mathbf{r})\big\} \qquad (8.22)$$

The related Euler-Lagrange equations that determine the $\rho_{i\sigma}(\mathbf{r})$ are given by:

$$-\frac{1}{2}\frac{\nabla^2 \rho_{i\sigma}^{\frac{1}{2}}(\mathbf{r})}{\rho_{i\sigma}^{\frac{1}{2}}(\mathbf{r})} + v_{eff,\sigma}(\mathbf{r}) = \epsilon_{i\sigma} \qquad (8.23)$$

where the $\epsilon_{i\sigma}$ (eigenvalue) are the Lagrange multipliers considered to satisfy $\int \rho_{i\sigma}(\mathbf{r}) d\mathbf{r}' = 1$. Evaluating the functional derivative at the solution points one

needs to read:

$$\frac{\delta T_s}{\delta \rho_\sigma(\mathbf{r})}[\rho_\uparrow, \rho_\downarrow](\mathbf{r}) = -\frac{1}{2}\frac{\nabla^2 \rho_{i\sigma}^{\frac{1}{2}}(\mathbf{r})}{\rho_{i\sigma}^{\frac{1}{2}}(\mathbf{r})} + (\mu_\sigma - \epsilon_{i\sigma}). \tag{8.24}$$

Let's define $T_\Delta[\rho_\uparrow, \rho_\downarrow](\mathbf{r})$ in terms of the vW-KE as following:

$$\frac{\delta T_\Delta[\rho_\uparrow, \rho_\downarrow](\mathbf{r})}{\rho_\sigma(\mathbf{r})} = \frac{\delta}{\delta\rho_\sigma(\mathbf{r})}\{T_s[\rho_\uparrow, \rho_\downarrow](\mathbf{r}) - T_{vW}[\rho_\uparrow, \rho_\downarrow](\mathbf{r})\}. \tag{8.25}$$

In the limit of $r \to \infty$ the following conditions must be respected:

$$\lim_{r \to \infty}\frac{\delta T_s[\rho](\mathbf{r})}{\rho(\mathbf{r})} = \mu - \epsilon_{max} - IP, \tag{8.26}$$

where IP is the ionisation potential, and

$$\lim_{r \to \infty}\frac{\delta T_\Delta[\rho_\uparrow, \rho_\downarrow](\mathbf{r})}{\rho_\sigma(\mathbf{r})} = \mu - \epsilon_{max,\sigma}; \tag{8.27}$$

where $\epsilon_{max,\sigma}$ is the maximum of all the $\epsilon_{\epsilon\sigma}$.

8.7.1 Homogeneity relationships of $T_\Delta[\rho_\uparrow, \rho_\downarrow](\mathbf{r})$ and $T_s[\rho_\uparrow, \rho_\downarrow](\mathbf{r})$

First, I replace the explicit form of the T_{vW} in Eq.[8.25]If the following equations is satisfied:

$$\sum_\sigma \int \rho_\sigma(\mathbf{r})\frac{\delta T_\Delta[\rho_\uparrow, \rho_\downarrow](\mathbf{r})}{\rho_\sigma(\mathbf{r})}d(\mathbf{r}') - \sum_\sigma \int \rho_\sigma(\mathbf{r})\frac{\delta T_s[\rho_\uparrow, \rho_\downarrow](\mathbf{r})}{\rho_\sigma(\mathbf{r})}d(\mathbf{r}')$$
$$= T_\Delta[\rho_\uparrow, \rho_\downarrow](\mathbf{r}) - T_s[\rho_\uparrow, \rho_\downarrow](\mathbf{r}) \tag{8.28}$$

then I conclude that $T_\Delta[\rho_\uparrow, \rho_\downarrow](\mathbf{r})$ and $T_s[\rho_\uparrow, \rho_\downarrow](\mathbf{r})$ are retained to be homogeneous of degree one in ρ because of the existing term of $\sum_\sigma \left\{\sum_i^{N_\sigma} \epsilon_{i\sigma} - \mu_\sigma N_\sigma\right\}$ for $N_\sigma = \int \rho_\sigma](\mathbf{r})d(\mathbf{r}')$in functional derivative of the KE functionals.

We note that $T_{vW}[\rho_\uparrow, \rho_\downarrow](\mathbf{r})$ is homogeneous of degree one in ρ. To verify the homogeneity relationship, one needs to replace the $T_s[\rho_\uparrow, \rho_\downarrow](\mathbf{r})$ with T_s^{appx} and the explained approach needs to be taken.

Chapter 9

Conclusions and Further Work

No matter how big and complicated are the physical and chemical systems in the real world, What makes a system exist is the chemical bonds between its atoms. Good to know that no matter what is the nature of the bonds to form chemical compounds, molecules, crystals, or metals, the bnnding phenomena are nothing more than a friendly relationship between two crazy electrons. Those electrons are part of only two atoms but not more.

So to me, if we want to find exactly what happens in the complicated systems, we need to understand what happens between two funny electrons of two mysterious atoms before everything. That is why I've been looking at only two atoms for years.

9.1 Recap

The main question was how two neighbouring charge densities interact and what kind of kinetic energy can explain this interaction. I tried to find an answer to this question from a potential defined as a functional derivative of such energy as kinetic energy in terms of the charge density. An inverse process was of figuring out the form of that kinetic energy was taken. Within this approach, I tried to study the exact analytical form of the potential of an admissible pair of known charge density and understand the feature and behaviour of the potential together with scratching the physical information from it. To provide the requirements for the potential being analytically exact, I studied the model systems in this work as the first attempt. I studied the larger and

more realistic systems for more advanced levels and tried to re-evaluate other known and frequently used theories with my found potential.

9.2   accomplishments

I managed to provide important information about the feature of an exact potential from the analytical inversion of a given density. I looked more into the results to prepare the physical information carried by the potential. I proved that the potential manifested the properties of the exactitude and explained it in the Chapter Step Structure (Chapter 4). Within this chapter, I showed how the gap energy could be extracted from the potential and showed the high accuracy of the results compared to the other theories. Based on my theoretical understanding, I showed numerically that for what class of the pair densities, the analytically inverted potential bi-functional must not carry a cusp-shape singularity. Through different mathematical and numerical attempts, I justified the results of this work as being free of numerical artifacts. The detailed theoretical and numerical attempts were gathered in chapter 3 to be published.

From my work, those interested in the related research know that the analytically inverted potential bi-functional is exact for specific classes of pair densities. They also know that although the potential includes the singularities at some points in the space, but has to be free of cusp-like singularities at the nuclei when the input densities used to invert the potential are comparable to the orbital densities of the system. The potential is proven to be a reliable candidate to verify the accuracy of the orbital-free theories in the DFT framework.

9.3   Concluded

To make easier the understanding of this hard and amazing work for the readers I itemise the proven facts as following. This work shows:

- Finally the analytically inverted potential bi-functional v^{NAD} was proved numerically to be in agreement with theoretically exact potential for an admissible pair of charge density

- The analytically inverted potential functional from an orbital density is equal to the Kohn-Sham potential

- The analytically inverted potential functional showed expected sensitivity to the change of the input density. This latter is the minimal requirement for a potential respecting the one-to-one relation with the density. With that, I mean, two different densities must corresponds two different potentials and consequently two different potentials have to solve the same system with two different solutions.

- The analytically inverted non-additive potential bi-functional of a pair of charge densities includes the step structure on its curve

- The position of the step structure on the non-additive potential bi-functional is found to be comparable to the step appearing in $v_{\mathrm{xc}}^{\mathrm{OEP\text{-}KLI}}$.

- The exact position of the step was found to be happening where the overlap between two neighbouring charge densities is maximal

- The height of the step structure on the potential curves provide acceptable gap energy

- $v^{\mathrm{Inv/Analyt}}[\rho_B, \rho_{tot}](\mathbf{r})$ provides an accurate E_g even while using the LDA ground state density as input

- The analytically inverted non-additive potential bi-functional of a pair of charge densities behaves well also for large system and its value is precisely accurate for the region in the space the ground state density integrates to a real number between 0 and 2

- For the large system including the orbitals above 1s, The analytically inverted non-additive potential bi-functional carries information about the nodes in the orbitals

- The analytically inverted non-additive potential bi-functional is proven to be a good candidate for the betterment of frequently used and computationally affordable theories within the DFT framework. It was shown in chapter 8 that some theories can be examined by the functional derivative

of their kinetic energy functional compared to the analytically inverted v^{NAD} to see if they provide expected physical feature such the cusp on the position of the nuclei, step structure, etc.

9.4   Outlook and the Applications of this Work

Some of the chapters deserve more investigation as they showed the potential of providing more interesting physical information of the system. It is also good to know for what purpose and how the analytically inverted non-additive potential bi-functional can be applied in the other works. Below, I summarised the possible further investigations of my work.

- It is essential to use the exact ground state density in the analytically inverted potential functional calculation to verify the reliability of the physical properties carried by the potential such as the gap energy.

- Although all attempts and results reported in this work are based on the orbital-free approaches, but it was shown (Chapter 5) that the analytically inverted potential functional carries information about the spatial properties of the orbitals. It is good to seek more to find the relation between the potential and the molecular or atomic orbitals of the large systems.

- It was shown that the theories in local approximations and semi-local approximations don't have the capacity of being improved with the help of the analytically inverted potential functional. By not having the potential I mean such an attempt could appear to be computationally very costly but above that theoretically, it is not intriguing.

- However, the non-local KEFs in DFT could be improved with the help of the analytically inverted non-additive potential bi-functional. It requires to find some theoretical local modifications to those theories using the inverted potential for weakly overlapping densities. It seems more straightforward to do some numerical approaches but those will be less exact and not universal at the end.

- The non-additive kinetic functional was the key issue of FDET and PDFT. Now that the exact form and properties of the analytically inverted non-additive potential bi-functional are known, it's time for insertion of it into the theories of FDET and PDFT. It gives a good hint to better approximation to $T_s[\rho](\mathbf{r})$ in Eq.[3.1].

- Future studies could investigate the association between DFT and average atom models (AAM)[43]. The AAM was first used to calculate the electronic structure of an atom in plasma. Currently, these models are mainly used in studies of understanding the warm dense matter. Warm dense matter points to the phase of the matter with high kinetic energy that brings up the characteristics of plasmas, gases, liquids and solids. Previously KS-DFT has been widely used un WDM. The AAMs compared to KS-DFT are computationally less expensive. It exists some works of using DFT approach for the AAM [23].

9.5   Closure

This work is the result of five years of oscillating between excited states and ground states, up and down, humiliation and pride and feeling helpless and hopeful. Although the negative feelings were longer-lasting, they were dominated by the value and the huge order of magnitudes of the good feelings. Nothing is comparable to that amazing "AHA!" and "WOW!" moments of finding and understanding a new fact. I finished this work happily with satisfaction.

Appendix A

Smooth densities, cusps, and non-singular potentials

This part is with significant contribution of Professor Tim Gould.

Densities of electronic systems are finite, meaning that at any point $\mathbf{R}_N$ I can make a series expansion in small $\mathbf{r}_N = \mathbf{r} - \mathbf{R}_N$. The general formula for expansion of ρ is,

$$
\begin{aligned}
\rho(\mathbf{r}) =& \rho_{0,N} + B_\rho r_N + \boldsymbol{B}_\rho \cdot \mathbf{r}_N \\
&+ r_N \boldsymbol{C}'_\rho \cdot \mathbf{r}_N + \mathbf{r}_N \cdot \mathbf{C}_\rho \cdot \mathbf{r}_N + \ldots
\end{aligned}
\tag{A.1}
$$

where $\boldsymbol{B}$ and $\boldsymbol{C}^{11}$ are vectors and $\mathbf{C}$ is a 3×3 matrix. This includes analytic and non-analytic terms. We may rewrite this as,

$$
\rho(\mathbf{r}) = \rho_{0,N} e^{-2Z r_N} + \rho_{\text{smooth}}(\mathbf{r})
\tag{A.2}
$$

$$
\rho_{\text{smooth}}(\mathbf{r}) = \boldsymbol{B}_\rho \cdot \mathbf{r}_N + r_N \boldsymbol{C}'_\rho \cdot \mathbf{r}_N + \mathbf{r}_N \cdot \mathbf{C}''_\rho \cdot \mathbf{r}_N + \ldots
\tag{A.3}
$$

where $Z = -B_\rho / [2\rho_{0,N}]$ and $\mathbf{C}''_\rho = \mathbf{C}_\rho - 2Z^2 \mathbf{I}$. Here, I focused on a single nucleus – the smooth density must have a similar expansion near every nucleus.

We therefore obtain,

$$
\frac{\nabla^2 \rho(\mathbf{r})}{\rho(\mathbf{r})} = \frac{-4Z}{r_N} + \frac{2\boldsymbol{C}'_\rho}{\rho_{0,N}} \cdot \hat{\mathbf{r}}_N + \text{const}
\tag{A.4}
$$

where $\hat{\mathbf{r}}$ indicates an unit vector. Clearly, the first term dominates, and the second has a radial average of zero. This is how the cusp gives rise to singularities.

The non-singular part, $v_{\text{non-sing}}$, of the potential obeys,

$$\lim_{\mathbf{r}\to\mathbf{R}_N} r_N v_{\text{non-sing}}(\mathbf{r}) = 0, \qquad \forall \mathbf{R}_N \tag{A.5}$$

and contains similar terms to Eq. (A.3). It can also have a constant term, a term $B_v r_N$, and even logarithmic singularities like $L_v \log(r_N)$. Any non-singular potential obeying Eq. (A.5) will not alter any of the conclusions of the main text.

Appendix B

Singularities lead to cusps

Certain parts of this analytical work is due to Professor Tim Gould.

This appendix concerns the properties of the density and potential in the vicinity of a singularity located at $\mathbf{r}_N$. I therefore define, $\mathbf{r}_N = \mathbf{r} - \mathbf{r}_N$, as our coordinate, and use properties of v and ρ to expand around, $\mathbf{r} = \mathbf{r}_N$ and $\mathbf{r}_N \to \mathbf{0}$.

The Kohn-Sham equations [eq. (3.2)] become,

$$
\begin{aligned}
\big[\frac{-\nabla^2_{\mathbf{r}_N}}{2} - \frac{Z_N}{r_N} + v^{(0)} & \\
& + \mathbf{v}^{(1)} \cdot \mathbf{r}_N \\
& + \dots \big] \phi_i(\mathbf{r}_N) = \epsilon_i \phi_i(\mathbf{r}_N) \, .
\end{aligned}
\tag{B.1}
$$

where I have used that v_{Hxc} is smooth and singularity-free to define $v^{(0)} = v_{Hxc}(\mathbf{r}_N) + \sum_{A \neq A'} \frac{-Z_{A'}}{|\mathbf{r}_N - \mathbf{r}_{A'}|}$ and $\mathbf{v}^{(1)}$ to be the next term in the expansion.

We make the similar expansion,

$$
\begin{aligned}
\phi = & \phi^{(0)} + \phi^{(1)}_r r_N \\
& + \{ \boldsymbol{\phi}^{(1)} \cdot \mathbf{r}_N + r_N \mathbf{r} \phi^{(2)}_r \cdot \mathbf{r}_N + \mathbf{r}_N \cdot \boldsymbol{\phi}^{(2)} \cdot \mathbf{r}_N \} + \dots \, .
\end{aligned}
$$

Then,

$$
\begin{aligned}
& -\frac{1}{2} \frac{\partial^2}{\partial r_N^2} [\phi^{(0)} + \phi^{(1)}_r r_N] - \frac{1}{r_N} \frac{\partial}{\partial r_N} [\phi^{(0)} + \phi^{(1)}_r r_N] \\
& - \frac{Z_N}{r_N} [\phi^{(0)} + \phi^{(1)}_r r_N + \boldsymbol{\phi}^{(1)} \cdot \mathbf{r}_N] - \{ 2 \frac{\boldsymbol{\phi}^{(2)} \cdot \mathbf{r}_N}{r_N} + Tr[\boldsymbol{\phi}^{(2)}] \} \\
& + v^{(0)} \phi^{(0)} = \epsilon \phi^{(0)},
\end{aligned}
$$

to leading two orders. Here, I used $\nabla^2 \{ \dots \} = 2 \{ 2 \boldsymbol{\phi}^{(2)} \cdot \hat{\mathbf{r}}_N + Tr[\boldsymbol{\phi}^{(2)}] \}$.

The leading order r_N^{-1} term of eq. (B.2) is then, $-\phi_r^{(1)} - Z_N\phi^{(0)} = 0$, which gives, $\phi_r^{(1)} = -Z_N\phi^{(0)}$. Therefore,

$$
\phi_i \to
\begin{cases}
\phi^{(0)}[1 - Z_N r_N] + \dots & \phi_i(\mathbf{r}_N = \mathbf{0}) \neq 0, \\
\boldsymbol{\phi}_i^{(1)} \cdot \mathbf{r}_N + \dots & \phi_i(\mathbf{r}_N = \mathbf{0}) = 0
\end{cases}
\tag{B.2}
$$

and I finally obtain, [eq. (3.3)]

$$
\rho(\mathbf{r}_N) \approx \sum_i f_i |\phi_i(\mathbf{r}_N = \mathbf{0})|^2 [1 - Z_N r_N]^2
$$
$$
:= \rho_{0,N}[1 - 2Z_N r_N] + O(r_N^2) .
\tag{B.3}
$$

Note, since electronic ground states have a $1s$ orbital which has a value at the nucleus, I always obtain $\rho_{0,N} > 0$ in electronic systems.

Finally, considering all singularities and using $1 - x \approx e^{-x}$ for small x then yields,

$$
\sum_N \frac{-Z_N}{|\mathbf{r} - \mathbf{r}_N|} \longrightarrow \sum_N \rho_{0,N} e^{-2Z_N r_N}
\tag{B.4}
$$

The case of interacting wavefunctions is more complicated, but nevertheless leads to the same result. There, one must consider how, $\Psi(\mathbf{r}_N + \mathbf{r}_N, \mathbf{r}_2, \dots)$, behaves in the vicinity of a nucleus, by recognising that the kinetic energy and potential are the only terms that matter.

Appendix C

Cusps lead to singularities

This part is with significant contribution of Professor Tim Gould.

For two or few electrons it is trivial to show that singularities lead to cusps. The leading terms of our density may be described using, $\rho := e^{-2Z_N r_N}$, where $\mathbf{r}_N = \mathbf{r} - \mathbf{r}_N$ is the distance from the cusp at $\mathbf{r}_N$. The remaining terms begin (by definition) at $O(\mathbf{r}_N)$ and therefore contribute to the potential only at a constant or higher terms.

The von Weizsäcker potential is,

$$v_{vW} = \frac{\partial_{rr}\rho}{4\rho} + \frac{\partial_r \rho}{2r\rho} - \frac{(\partial_r \rho)^2}{8\rho^2} = \frac{Z_N^2}{2} - \frac{Z_N}{r} \tag{C.1}$$

which is clearly dominated by the $\frac{-Z_N}{r_N}$ singularity. This gives our proof for two electrons. To go beyond two electrons, I will show that, v_{vW}, has the same singularities as the KS potential for more than two electrons.

To begin, rewrite, $\rho = \sum_i f_i |\phi_i|^2$, [eq. (3.3)] using,

$$\sqrt{f_i}\phi_i(\mathbf{r}) := \zeta_i(\mathbf{r})\sqrt{\rho(\mathbf{r})} \,, \tag{C.2}$$

where, $\sum_{i \leq h} |\zeta_i(\mathbf{r})|^2 = 1$. The KS orbital equations [eq. (3.2)] yield,

$$\begin{aligned} 0 &= \frac{1}{\sqrt{\rho}}[\frac{-\nabla^2}{2} + v_{KS}[\rho] - \epsilon_i]\zeta_i\sqrt{\rho} \\ &= [\frac{-\nabla^2}{2} - \boldsymbol{g}[\rho] \cdot \nabla + \tilde{v}[\rho] - \delta_i]\zeta_i(\mathbf{r}) \,, \end{aligned} \tag{C.3}$$

for ζ_i. Here, $\tilde{v} := v_{KS}[\rho] - v_{vW}[\rho]$, $\boldsymbol{g}[\rho] := \frac{\nabla\sqrt{\rho}}{\sqrt{\rho}} = \frac{\nabla\rho}{2\rho}$, and δ_i are constants.

Importantly, I recognise that $|\boldsymbol{g}| < \infty$ and is smooth in any nuclear density, while $\tilde{v}$ is singular at nucleii, $N \in \tilde{\boldsymbol{N}}$, where v_{KS} is singular but ρ has no cusp, after making the assumption that v_{Hxc} has no cusps.

204

We show, by contradiction, that no ζ_i can have cusps. Assume, $\zeta_{i \in \boldsymbol{I}_N} = \zeta_{i,0}[1 - Z_N r_N]$, has cusps only for some set of orbitals, $\boldsymbol{I}_N$, near nucleus, N. Then, $\sum_i |\zeta_i|^2 = (1 - C_N) + C_N[1 - Z_N r_N]$, where $C_N = \sum_{i \in \boldsymbol{I}_N} |\zeta_{i,0}|^2 + O(r_N^2)$ and I used that the sum is one at $r_N = 0$. But, unless $C_N = 0$, this cannot be constant due to the $O(r_N)$ cusp term. Therefore, $\sum_{i \in \boldsymbol{I}_N} |\zeta_{i,0}|^2$, means that, $\zeta_{i,0}$ for $\forall i \in \boldsymbol{I}_N$, and that no solution can have a cusp.

Next, I remember that any cusps in $\tilde{v}$ lead either to a solution that is zero near a nucleus, or a solution that has a cusp. The former is forbidden by normalisation while the latter is forbidden by the results in the previous paragraph. Therefore, $\tilde{N}$ must be the empty set and $\tilde{v}$ has no cusps. It follows that the KS potential, v_{KS} has the same cusps as the von Weizsäcker potential, v_{vW}. This extends results to more than two electrons.

Finally, I obtain,

$$\sum_N \rho_{0,N} e^{-2Z_N r_N} \longrightarrow \sum_N \frac{-Z_N}{|\mathbf{r} - \mathbf{r}_N|} \tag{C.4}$$

Appendix D

Inverted potential alternative to von Weizsäcker potential

Here I need to use the expansion for $\nabla^2\sqrt{F(\mathbf{r})}$:

$$\nabla^2\sqrt{F(\mathbf{r})} = \frac{2F(\mathbf{r})\frac{\partial^2 F(\mathbf{r})}{\partial \mathbf{r}^2} - (\frac{\partial F(\mathbf{r})}{\partial \mathbf{r}})^2}{4F^{\frac{3}{2}}(\mathbf{r})} \tag{D.1}$$

replacing $F(\mathbf{r})$ by $\rho(\mathbf{r})$ in Eq.[D.1] I have:

$$\nabla^2\sqrt{\rho(\mathbf{r})} = \frac{2\rho(\mathbf{r})\frac{\partial^2 \rho(\mathbf{r})}{\partial \mathbf{r}^2} - (\frac{\partial \rho(\mathbf{r})}{\partial \mathbf{r}})^2}{4\rho^{\frac{3}{2}}(\mathbf{r})} \tag{D.2}$$

Replacing $\frac{\partial^2 \rho(\mathbf{r})}{\partial \mathbf{r}^2}$ by $\nabla^2\rho(\mathbf{r})$ and $\frac{\partial \rho(\mathbf{r})}{\partial \mathbf{r}}$ by $\nabla\rho(\mathbf{r})$:

$$\frac{1}{2}\nabla^2\sqrt{\rho(\mathbf{r})} = \frac{\rho(\mathbf{r})\nabla^2\rho(\mathbf{r})}{4\rho^{\frac{3}{2}}(\mathbf{r})} - \frac{(\nabla\rho(\mathbf{r}))^2}{8\rho^{\frac{3}{2}}(\mathbf{r})} \tag{D.3}$$

Finally I obtain:

$$
\begin{aligned}
v_s^{Inv}[\rho(\mathbf{r})] &= -\frac{1}{2}\frac{\nabla^2\sqrt{\rho(\mathbf{r})}}{\sqrt{\rho(\mathbf{r})}} \\
&= \frac{(\nabla\rho(\mathbf{r}))^2}{8\rho^{\frac{1}{2}}(\mathbf{r})\rho^{\frac{3}{2}}(\mathbf{r})} - \frac{\rho(\mathbf{r})\nabla^2\rho(\mathbf{r})}{4\rho^{\frac{1}{2}}(\mathbf{r})\rho^{\frac{3}{2}}(\mathbf{r})} \\
&= \frac{1}{8}\left(\frac{\nabla\rho(\mathbf{r})}{\rho(\mathbf{r})}\right)^2 - \frac{1}{4}\frac{\nabla^2\rho(\mathbf{r})}{\rho(\mathbf{r})} = v_s^{vW}[\rho(\mathbf{r})]
\end{aligned}
\tag{D.4}
$$

Appendix E

GGA-LKT

Functional Derivative of GGA-LKT:

$$
\frac{\delta T[\rho](\mathbf{r})}{\delta \rho(\mathbf{r})} = \frac{C_{\mathrm{TF}}}{3} \left\{ {\color{red} 5\rho^{5/3}(\mathbf{r})F(s)} \right.
$$
$$
{\color{green} -\frac{|\nabla \rho(\mathbf{r})|^2}{\rho^2(\mathbf{r})} (F'(s) - 4sF''(s))-}
$$
$$
\left. {\color{blue} 6\frac{\nabla^2 \rho(\mathbf{r})}{\rho(\mathbf{r})} \left(F'(s) - 2sF''(s) \right)} \right\} \tag{E.1}
$$

where $C_{\mathrm{TF}} = \frac{3^{5/3}\pi^{4/3}}{10}$.

The $F_t^{LKT}(s)$ is:

$$
F_t^{LKT}(s) = \frac{1}{\cosh(1.3s)} + \frac{5}{3}s^2 \tag{E.2}
$$

where:

$$
s = \frac{1}{2(3\pi^2)^{1/3}} \frac{|\nabla \rho(\mathbf{r})|}{\rho^{4/3}(\mathbf{r})} \tag{E.3}
$$

Red term:

$$
{\color{red} 5\rho^{5/3}(\mathbf{r})F(s) = 5\rho^{5/3}(\mathbf{r}) \frac{1}{\cosh(1.3s)}}
$$
$$
{\color{red} + \frac{25}{3} \frac{|\nabla \rho(\mathbf{r})|^2}{\rho^{8/3}(\mathbf{r})}.\rho^{5/3}(\mathbf{r}) \left(\frac{1}{2(3\pi^2)^{1/3}} \right)^2} \tag{E.4}
$$
$$
{\color{red} = \frac{5\rho^{5/3}(\mathbf{r})}{\cosh(1.3s)} + \frac{25}{4(3\pi^2)^2 27} \frac{|\nabla \rho(\mathbf{r})|^2}{\rho(\mathbf{r})}}
$$

For the green term of the Eq.[E.1], I go step by step to calculate $F'(s)$ and $F''(s)$:

$$F'(s) = \frac{10s}{3} - 1.3\tanh(1.3s)\operatorname{sech}(1.3s)$$
$$= \frac{10s}{3} - \frac{2(1.3)\sinh(2\times 1.3s)\cosh 1.3s}{(\cosh(2\times 1.3s)+1)^2} \tag{E.5}$$

Taylor expansion of $F'(s)$ for $s \to 0$:

$$F'(s) = (\frac{10}{3}-(1.3)^2)s + \frac{5(1.3)^4 s^3}{6} - \frac{61(1.3)^6 s^5}{120} + \mathcal{O}(s^6) \tag{E.6}$$

$$F''(s) = -(1.3)^2\operatorname{sech}^3(1.3s) + (1.3)^2\tanh^2(1.3s)\operatorname{sech}(1.3s) + \frac{10}{3}$$
$$= -\frac{8(1.3)^2\cosh^3(1.3s)}{(\cosh(2\times 1.3s)+1)^3} + \frac{2(1.3)^2\sinh^2(2\times 1.3s)\cosh(1.3s)}{(\cosh(2\times 1.3s)+1)^3} + \frac{10}{3} \tag{E.7}$$

Taylor expansion of $F''(s)$ for $s \to 0$:

$$F''(s) = (\frac{10}{3}-(1.3)^2) + \frac{5(1.3)^4 s^2}{2} - \frac{61(1.3)^6 s^4}{24} + \mathcal{O}(s^5) \tag{E.8}$$

The green term of Eq.[E.1] become:

$$\color{green}{\frac{|\nabla\rho(\mathbf{r})|^2}{\rho^2(\mathbf{r})}(F'(s)-4sF''(s)) =}$$

$$\frac{|\nabla\rho(\mathbf{r})|^2}{\rho^2(\mathbf{r})} \times \left[\frac{10}{3}\left(\frac{1}{2(3\pi^2)^{1/3}}\frac{|\nabla\rho(\mathbf{r})|}{\rho^{4/3}(\mathbf{r})}\right) - \right.$$
$$\frac{2.6\times\sinh(2.6\frac{1}{2(3\pi^2)^{1/3}}\frac{|\nabla\rho(\mathbf{r})|}{\rho^{4/3}(\mathbf{r})})\left(\frac{|\nabla\rho(\mathbf{r})|}{\rho^{4/3}(\mathbf{r})}\right)\cosh(1.3\frac{1}{2(3\pi^2)^{1/3}}\frac{|\nabla\rho(\mathbf{r})|}{\rho^{4/3}(\mathbf{r})})}{(\cosh(2.6(\frac{1}{2(3\pi^2)^{1/3}}\frac{|\nabla\rho(\mathbf{r})|}{\rho^{4/3}(\mathbf{r})})+1)^2}$$
$$-4\frac{1}{2(3\pi^2)^{1/3}}\frac{|\nabla\rho(\mathbf{r})|}{\rho^{4/3}(\mathbf{r})}\left[\frac{8(1.3)^2\cosh^3(1.3s)}{(\cosh(2\times 1.3s)+1)^3}+\right.$$
$$\left.\left.\frac{2(1.3)^2\sinh^2(2\times 1.3s)\cosh(1.3s)}{(\cosh(2\times 1.3s)+1)^3}+\frac{10}{3}\right]\right] \tag{E.9}$$

It remains to develop the blue term in Eq.[E.1]:

$$6\frac{\nabla^2\rho(\mathbf{r})}{\rho(\mathbf{r})}\Big(F'(s)-2sF''(s)\Big)=$$

$$\frac{6\nabla^2\rho(\mathbf{r})}{\rho(\mathbf{r})}\times\left[\frac{10}{3}\left(\frac{1}{2(3\pi^2)^{1/3}}\frac{|\nabla\rho(\mathbf{r})|}{\rho^{4/3}(\mathbf{r})}\right)-\right.$$

$$\left.\frac{2.6\times\sinh\left(2.6\frac{1}{2(3\pi^2)^{1/3}}\right)\left(\frac{|\nabla\rho(\mathbf{r})|}{\rho^{4/3}(\mathbf{r})}\cosh\left(1.3\frac{1}{2(3\pi^2)^{1/3}}\frac{|\nabla\rho(\mathbf{r})|}{\rho^{4/3}(\mathbf{r})}\right)\right)}{(\cosh\left(2.6\left(\frac{1}{2(3\pi^2)^{1/3}}\frac{|\nabla\rho(\mathbf{r})|}{\rho^{4/3}(\mathbf{r})}\right)+1\right)^2}\right](E.10)$$

$$-2\left[\frac{8(1.3)^2\cosh^3(1.3s)}{(\cosh(2\times1.3s)+1)^3}+\right.$$

$$\left.\frac{2(1.3)^2\sinh^2(2\times1.3s)\cosh(1.3s)}{(\cosh(2\times1.3s)+1)^3}+\frac{10}{3}\right]$$

All I need is insert Eq.[E.4], Eq.[E.9], and Eq.[E.10] into Eq.[E.1].

Bibliography

[1] C. Almbladh and U. von Barth. Density functional methods in physics (nato advanced study institute, series b) vol 123, ed rm dreizler and j da providencia, 1985.

[2] C.-O. Almbladh and A. C. Pedroza. Density-functional exchange-correlation potentials and orbital eigenvalues for light atoms. *Physical Review A*, 29(5):2322, 1984.

[3] C.-O. Almbladh and U. von Barth. Exact results for the charge and spin densities, exchange-correlation potentials, and density-functional eigenvalues. *Physical Review B*, 31(6):3231, 1985.

[4] X. Andrade, J. Alberdi-Rodriguez, D. A. Strubbe, M. J. Oliveira, F. Nogueira, A. Castro, J. Muguerza, A. Arruabarrena, S. G. Louie, A. Aspuru-Guzik, et al. Time-dependent density-functional theory in massively parallel computer architectures: the octopus project. *Journal of Physics: Condensed Matter*, 24(23):233202, 2012.

[5] X. Andrade, D. Strubbe, U. De Giovannini, A. H. Larsen, M. J. Oliveira, J. Alberdi-Rodriguez, A. Varas, I. Theophilou, N. Helbig, M. J. Verstraete, et al. Real-space grids and the octopus code as tools for the development of new simulation approaches for electronic systems. *Physical Chemistry Chemical Physics*, 17(47):31371–31396, 2015.

[6] D. G. Artiukhin, C. R. Jacob, and J. Neugebauer. Excitation energies from frozen-density embedding with accurate embedding potentials. *The Journal of chemical physics*, 142(23):234101, 2015.

[7] F. Aryasetiawan and M. Stott. Effective potentials in density-functional theory. *Physical Review B*, 38(5):2974, 1988.

[8] E. Baerends, O. Gritsenko, and R. Van Meer. The kohn-sham gap, the fundamental gap and the optical gap: the physical meaning of occupied and virtual kohn–sham orbital energies. *Physical Chemistry Chemical Physics*, 15(39):16408–16425, 2013.

[9] M. Banafsheh and T. A. Wesolowski. Nonadditive kinetic potentials from inverted kohn-sham problem. *Int. J. Quantum Chem.*, 118(1):e25410, 2018.

[10] L. Bartolotti and P. Acharya. On the functional derivative of the kinetic energy density functional. *The Journal of Chemical Physics*, 77(9):4576–4585, 1982.

[11] T. L. Beck. Real-space mesh techniques in density-functional theory. *Rev. Mod. Phys.*, 72(4):1041, 2000.

[12] A. D. Becke. Density-functional exchange-energy approximation with correct asymptotic behavior. *Physical review A*, 38(6):3098, 1988.

[13] L. I. Bendavid and E. A. Carter. *Status in Calculating Electronic Excited States in Transition Metal Oxides from First Principles*. Springer, 2014.

[14] A. Benítez and C. Proetto. Kohn-sham potential for a strongly correlated finite system with fractional occupancy. *Physical Review A*, 94(5):052506, 2016.

[15] Y. A. Bernard, M. Dułak, J. W. Kamiński, and T. A. Wesołowski. The energy-differences based exact criterion for testing approximations to the functional for the kinetic energy of non-interacting electrons. *Journal of Physics A: Mathematical and Theoretical*, 41(5):055302, 2008.

[16] S. M. Beyhan, A. W. Götz, C. R. Jacob, and L. Visscher. The weak covalent bond in ngauf (ng= ar, kr, xe): A challenge for subsystem density functional theory. *The Journal of chemical physics*, 132(4):044114, 2010.

[17] D. Bicout and M. Field. Quantum mechanical simulation methods for studying biological systems. *Quantum Mechanical Simulation Methods for Studying Biological Systems*, 4, 1996.

[18] D. J. Bicout and M. J. Field. Stochastic dynamics simulations of macro-molecular diffusion in a model of the cytoplasm of escherichia coli. *The Journal of Physical Chemistry*, 100(7):2489–2497, 1996.

[19] K. Boguslawski, C. R. Jacob, and M. Reiher. Optimized unrestricted kohn–sham potentials from ab initio spin densities. *The Journal of chemical physics*, 138(4):044111, 2013.

[20] M. Brack, B. Jennings, and Y. Chu. On the extended thomas-fermi approximation to the kinetic energy density. *Physics Letters B*, 65(1): 1–4, 1976.

[21] M. Buijse. E. j. baerends, and j. g. snijders. *Phys. Rev. A*, 40:4190, 1989.

[22] F. A. Bulat, T. Heaton-Burgess, A. J. Cohen, and W. Yang. Optimized effective potentials from electron densities in finite basis sets. *The Journal of chemical physics*, 127(17):174101, 2007.

[23] T. J. Callow, S. B. Hansen, E. Kraisler, and A. Cangi. First-principles derivation and properties of density-functional average-atom models. *Physical Review Research*, 4(2):023055, 2022.

[24] D. M. Ceperley and B. J. Alder. Ground state of the electron gas by a stochastic method. *Phys. Rev. letters*, 45(7):566, 1980.

[25] E. Chacón, J. Alvarellos, and P. Tarazona. Nonlocal kinetic energy functional for nonhomogeneous electron systems. *Physical Review B*, 32(12): 7868, 1985.

[26] J.-D. Chai and J. D. Weeks. Orbital-free density functional theory: Kinetic potentials and ab initio local pseudopotentials. *Physical Review B*, 75(20):205122, 2007.

[27] J. R. Chelikowsky, N. Troullier, and Y. Saad. Finite-difference-pseudopotential method: Electronic structure calculations without a basis. *Physical review letters*, 72(8):1240, 1994.

[28] J. Chen, R. Esquivel, and M. Stott. Exchange-correlation potential for small atoms. *Philosophical Magazine B*, 69(5):1001–1009, 1994.

[29] J. Chen, J. Krieger, R. Esquivel, M. Stott, and G. Iafrate. Kohn-sham effective potentials for spin-polarized atomic systems. *Physical Review A*, 54(3):1910, 1996.

[30] D. V. Chulhai and L. Jensen. External orthogonality in subsystem time-dependent density functional theory. *PHYSICAL CHEMISTRY CHEMICAL PHYSICS*, 18(31):21032–21039, AUG 31 2016. ISSN 1463-9076. doi: {10.1039/c6cp00310a}.

[31] A. J. Cohen, P. Mori-Sánchez, and W. Yang. Challenges for density functional theory. *Chemical reviews*, 112(1):289–320, 2012.

[32] F. Colonna and A. Savin. Correlation energies for some two-and four-electron systems along the adiabatic connection in density functional theory. *The Journal of chemical physics*, 110(6):2828–2835, 1999.

[33] L. A. Constantin, E. Fabiano, and F. Della Sala. Modified fourth-order kinetic energy gradient expansion with hartree potential-dependent coefficients. *Journal of chemical theory and computation*, 13(9):4228–4239, 2017.

[34] L. A. Constantin, E. Fabiano, and F. Della Sala. Semilocal pauli–gaussian kinetic functionals for orbital-free density functional theory calculations of solids. *The journal of physical chemistry letters*, 9(15):4385–4390, 2018.

[35] P. Cortona. Self-consistently determined properties of solids without band-structure calculations. *Phys. Rev. B*, 44(16):8454, 1991.

[36] P. de Silva and T. A. Wesolowski. Exact non-additive kinetic potentials in realistic chemical systems. *J. Chem. Phys.*, 137:094110, 2012.

[37] P. De Silva and T. A. Wesolowski. Exact non-additive kinetic potentials in realistic chemical systems. *The Journal of chemical physics*, 137(9): 094110, 2012.

[38] P. De Silva and T. A. Wesolowski. Pure-state noninteracting v-representability of electron densities from kohn-sham calculations with finite basis sets. *Physical Review A*, 85(3):032518, 2012.

[39] P. del Lenguaje Natural. Procesamiento del lenguaje natural. n. 57 (2016). *Sociedad Española para el Procesamiento del Lenguaje Natural*, 2016.

[40] F. Della Sala and A. Görling. Asymptotic behavior of the kohn-sham exchange potential. *Physical review letters*, 89(3):033003, 2002.

[41] F. Della Sala, E. Fabiano, and L. A. Constantin. Kinetic-energy-density dependent semilocal exchange-correlation functionals. *International Journal of Quantum Chemistry*, 116(22):1641–1694, 2016.

[42] A. E. DePristo and J. D. Kress. Kinetic-energy functionals via padé approximations. *Physical Review A*, 35(1):438, 1987.

[43] L. Drska and M. Sinor. Average atom model and eos calculations: Dft approach. *Laser and Particle Beams*, 10(2):277–298, 1992.

[44] M. Dułak and T. A. Wesołowski. Interaction energies in non-covalently bound intermolecular complexes derived using the subsystem formulation of density functional theory. *Journal of molecular modeling*, 13(6-7):631–642, 2007.

[45] M. Dułak, J. W. Kamiński, and T. A. Wesołowski. Equilibrium geometries of noncovalently bound intermolecular complexes derived from subsystem formulation of density functional theory. *Journal of chemical theory and computation*, 3(3):735–745, 2007.

[46] P. Elliott, M. H. Cohen, A. Wasserman, and K. Burke. Density functional partition theory with fractional occupations. *Journal of chemical theory and computation*, 5(4):827–833, 2009.

[47] P. Elliott, K. Burke, M. H. Cohen, and A. Wasserman. Partition density-functional theory. *Physical Review A*, 82(2):024501, 2010.

[48] P. Elliott, K. Burke, M. H. Cohen, and A. Wasserman. Partition density-functional theory. *Physical Review A*, 82(2):024501, 2010.

[49] E. Engel. Orbital-dependent functionals for the exchange-correlation energy: A third generation of density functionals. *A primer in density functional theory*, pages 56–122, 2003.

[50] E. Fermi. Un metodo statistico per la determinzione di alcune prioriet dell'atomo. *Rend. Accad. Naz. Lincei*, 6:602–607, 1927.

[51] E. Fermi. A statistical method for determining some properties of the atoms and its application to the theory of the periodic table of elements. *Z. Phys.*, 48(1-2):73–79, JAN 1928. ISSN 0044-3328. doi: 10.1007/BF01351576.

[52] B. Fornberg. Generation of finite difference formulas on arbitrarily spaced grids. *Math. comput.*, 51(184):699–706, 1988.

[53] J. I. Fuks, A. Rubio, and N. T. Maitra. Charge transfer in time-dependent density-functional theory via spin-symmetry breaking. *Physical Review A*, 83(4):042501, 2011.

[54] S. Fux, K. Kiewisch, C. R. Jacob, J. Neugebauer, and M. Reiher. Analysis of electron density distributions from subsystem density functional theory applied to coordination bonds. *Chemical Physics Letters*, 461(4):353–359, 2008.

[55] S. Fux, C. R. Jacob, J. Neugebauer, L. Visscher, and M. Reiher. Accurate frozen-density embedding potentials as a first step towards a subsystem description of covalent bonds. *The Journal of chemical physics*, 132(16):164101, 2010.

[56] J. M. García-Lastra, J. W. Kaminski, and T. A. Wesolowski. Orbital-free effective embedding potential at nuclear cusps. *J. Chem. Phys.*, 129(7):074107, 2008.

[57] T. L. Gilbert. Hohenberg-kohn theorem for nonlocal external potentials. *Phys. Rev. B*, 12:2111, 1975.

[58] A. Goerling, A. Hesselmann, M. Jones, and M. Levy. Relation between exchange-only optimized potential and kohn-sham methods with finite basis sets; solution of a paradox. *arXiv preprint arXiv:0705.1717*, 2007.

[59] A. S. P. Gomes and C. R. Jacob. Quantum-chemical embedding methods for treating local electronic excitations in complex chemical systems. *Annu. Rep. Prog. Chem., Sect. C: Phys. Chem.*, 108:222–277, 2012.

[60] J. D. Goodpaster, N. Ananth, F. R. Manby, and T. F. Miller. Exact nonadditive kinetic potentials for embedded density functional theory. *The Journal of Chemical Physics*, 133(8):084103, 2010. doi: 10.1063/1.3474575. URL `https://doi.org/10.1063/1.3474575`.

[61] J. D. Goodpaster, N. Ananth, F. R. Manby, and T. F. Miller III. Exact nonadditive kinetic potentials for embedded density functional theory. *The Journal of chemical physics*, 133(8):084103, 2010.

[62] J. D. Goodpaster, T. A. Barnes, and T. F. Miller III. Embedded density functional theory for covalently bonded and strongly interacting subsystems. *The Journal of chemical physics*, 134(16):164108, 2011.

[63] J. D. Goodpaster, T. A. Barnes, F. R. Manby, and T. F. Miller III. Density functional theory embedding for correlated wavefunctions: Improved methods for open-shell systems and transition metal complexes. *The Journal of chemical physics*, 137(22):224113, 2012.

[64] A. Görling. Kohn-sham potentials and wave functions from electron densities. *Physical Review A*, 46(7):3753, 1992.

[65] A. Görling. Exact treatment of exchange in kohn-sham band-structure schemes. *Physical Review B*, 53(11):7024, 1996.

[66] A. Görling and M. Ernzerhof. Energy differences between kohn-sham and hartree-fock wave functions yielding the same electron density. *Physical Review A*, 51(6):4501, 1995.

[67] A. Görling, A. Heßelmann, M. Jones, and M. Levy. Relation between exchange-only optimized potential and kohn–sham methods with finite basis sets, and effect of linearly dependent products of orbital basis functions. *The Journal of chemical physics*, 128(10):104104, 2008.

[68] T. Gould and M. Hellgren. Delocalization-error-free density functional theory via fractional orbital occupations. *arXiv*, pages arXiv–1406, 2014.

[69] N. Govind, Y. Wang, A. Da Silva, and E. Carter. Accurate ab initio energetics of extended systems via explicit correlation embedded in a density functional environment. *Chemical physics letters*, 295(1):129–134, 1998.

[70] N. Govind, Y. A. Wang, and E. A. Carter. Electronic-structure calculations by first-principles density-based embedding of explicitly correlated systems. *The Journal of chemical physics*, 110(16):7677–7688, 1999.

[71] T. Grabo, T. Kreibich, and E. Gross. Optimized effective potential for atoms and molecules. *Molecular engineering*, 7(1):27–50, 1997.

[72] O. Gritsenko and E. J. Baerends. Correct dissociation limit for the exchange-correlation energy and potential. *International journal of quantum chemistry*, 106(15):3167–3177, 2006.

[73] O. V. Gritsenko and E. J. Baerends. Effect of molecular dissociation on the exchange-correlation kohn-sham potential. *Physical Review A*, 54(3): 1957, 1996.

[74] O. V. Gritsenko, R. van Leeuwen, and E. J. Baerends. Molecular kohn-sham exchange-correlation potential from the correlated ab-initio electron-density. *Phys. Rev. A*, 52(3):1870–1874, SEP 1995.

[75] O. V. Gritsenko, R. v. Leeuwen, and E. J. Baerends. Molecular exchange-correlation kohn–sham potential and energy density from ab initio first- and second-order density matrices: Examples for xh (x= li, b, f). *The Journal of chemical physics*, 104(21):8535–8545, 1996.

[76] O. Gunnarsson, M. Jonson, and B. Lundqvist. Descriptions of exchange and correlation effects in inhomogeneous electron systems. *Physical Review B*, 20(8):3136, 1979.

[77] A. W. Götz, S. M. Beyhan, and L. Visscher. Performance of kinetic energy functionals for interaction energies in a subsystem formulation of density functional theory. *Journal of chemical theory and computation*, 5 (12):3161–3174, 2009.

[78] S. Y. Haoyu, L. L. Shaohong, and G. T. Donald. Perspective: Kohn-sham density functional theory descending a staircase. *J. Chem. Phys.*, 145:130901, 2016.

[79] M. K. Harbola. Relationship between the highest occupied kohn-sham orbital eigenvalue and ionization energy. *Physical Review B*, 60(7):4545, 1999.

[80] T. Heaton-Burgess and W. Yang. Optimized effective potentials from arbitrary basis sets. *The Journal of chemical physics*, 129(19):194102, 2008.

[81] T. Heaton-Burgess, F. A. Bulat, and W. Yang. Optimized effective potentials in finite basis sets. *Physical review letters*, 98(25):256401, 2007.

[82] N. Helbig, I. Tokatly, and A. Rubio. Exact kohn–sham potential of strongly correlated finite systems. *The Journal of chemical physics*, 131 (22):224105, 2009.

[83] M. Hellgren and E. Gross. Discontinuities of the exchange-correlation kernel and charge-transfer excitations in time-dependent density-functional theory. *Physical Review A*, 85(2):022514, 2012.

[84] M. Hellgren, D. R. Rohr, and E. Gross. Correlation potentials for molecular bond dissociation within the self-consistent random phase approximation. *The Journal of Chemical Physics*, 136(3):034106, 2012.

[85] F. Herman, J. P. Van Dyke, and I. B. Ortenburger. Improved statistical exchange approximation for inhomogeneous many-electron systems. *Physical Review Letters*, 22(16):807, 1969.

[86] A. Heßelmann, A. W. Götz, F. Della Sala, and A. Görling. Numerically stable optimized effective potential method with balanced gaussian basis sets. *The Journal of chemical physics*, 127(5):054102, 2007.

[87] S. Hirata, S. Ivanov, I. Grabowski, R. J. Bartlett, K. Burke, and J. D. Talman. Can optimized effective potentials be determined uniquely? *The Journal of Chemical Physics*, 115(4):1635–1649, 2001.

[88] C. Hodges. Quantum corrections to the thomas–fermi approximation—the kirzhnits method. *Canadian Journal of Physics*, 51(13):1428–1437, 1973.

[89] M. Hodgson, J. Ramsden, and R. Godby. Origin of static and dynamic steps in exact kohn-sham potentials. *Physical Review B*, 93(15):155146, 2016.

[90] M. J. Hodgson, E. Kraisler, A. Schild, and E. K. Gross. How interatomic steps in the exact kohn–sham potential relate to derivative discontinuities of the energy. *The journal of physical chemistry letters*, 8(24):5974–5980, 2017.

[91] D. Hofmann and S. Kümmel. Integer particle preference during charge transfer in kohn-sham theory. *Physical Review B*, 86(20):201109, 2012.

[92] P. E. Hoggan. *Novel Electronic Structure Theory: General Innovations and Strongly Correlated Systems*. Academic Press, 2018.

[93] P. Hohenberg and W. Kohn. Inhomogeneous electron has. *Phys. Rev. B*, 136:864–871, 1964.

[94] P. Hohenberg and W. Kohn. Inhomogeneous electron gas. *Physical review*, 136(3B):B864, 1964.

[95] A. Holas and N. March. Construction of the pauli potential, pauli energy, and effective potential from the electron density. *Physical Review A*, 44 (9):5521, 1991.

[96] C. Huang, M. Pavone, and E. A. Carter. Quantum mechanical embedding theory based on a unique embedding potential. *The Journal of chemical physics*, 134(15):154110, 2011.

[97] M. Humbert-Droz, X. Zhou, S. V. Shedge, and T. A. Wesolowski. How to choose the frozen density in frozen-density embedding theory-based numerical simulations of local excitations? *Theoretical Chemistry Accounts*, 133(1):1–20, 2014.

[98] Y. L. J. B. Krieger and G. J. Iafrate. *Phys. Rev. A*, 45:101, 1992.

[99] C. R. Jacob. Unambiguous optimization of effective potentials in finite basis sets. *J. Chem. Phys.*, 135(24):244102, 2011. doi: http://dx.doi.org/10.1063/1.3670414. URL `http://scitation.aip.org/content/aip/journal/jcp/135/24/10.1063/1.3670414`.

[100] C. R. Jacob. Unambiguous optimization of effective potentials in finite basis sets. *The Journal of chemical physics*, 135(24):244102, 2011.

[101] C. R. Jacob and J. Neugebauer. Subsystem density-functional theory. *Wiley Interdisciplinary Reviews: Computational Molecular Science*, 4(4): 325–362, 2014.

[102] C. R. Jacob and J. Neugebauer. Subsystem density-functional theory. *Wiley Interdiscip. Rev. Comput. Mol. Sci.*, 4(4):325–362, 2014. ISSN 1759-0884. doi: 10.1002/wcms.1175. URL `http://dx.doi.org/10.1002/wcms.1175`.

[103] C. R. Jacob, S. M. Beyhan, and L. Visscher. Exact functional derivative of the nonadditive kinetic-energy bifunctional in the long-distance limit. *J. Chem. Phys.*, 126(23):234116, 2007.

[104] R. O. Jones. Density functional theory: Its origins, rise to prominence, and future. *Rev. Mod. Phys.*, 87:897–923, 2015.

[105] E. S. Kadantsev and M. J. Stott. Variational method for inverting the kohn-sham procedure. *Physical Review A*, 69(1):012502, 2004.

[106] J. W. Kaminski, S. Gusarov, T. A. Wesolowski, and A. Kovalenko. Modeling solvatochromic shifts using the orbital-free embedding potential at statistically mechanically averaged solvent density. *J. Phys. Chem. A*, 114:6082, 2010.

[107] A. Karolewski, R. Armiento, and S. Kummel. Polarizabilities of polyacetylene from a field-counteracting semilocal functional. *Journal of Chemical Theory and Computation*, 5(4):712–718, 2009.

[108] T. Kato. On the eigenfunctions of many-particle systems in quantum mechanics. *Communications on Pure and Applied Mathematics*, 10(2): 151–177, 1957.

[109] R. Kevorkyants, M. Dulak, and T. A. Wesolowski. Interaction energies in hydrogen-bonded systems: A testing ground for subsystem formulation of density-functional theory. *The Journal of chemical physics*, 124(2): 024104, 2006.

[110] R. A. King and N. C. Handy. Kinetic energy functionals from the kohn–sham potential. *Physical Chemistry Chemical Physics*, 2(22):5049–5056, 2000.

[111] D. Kirzhnits. Quantum corrections to the thomas-fermi equation. *Soviet Phys. JETP*, 5:64–71, 1957.

[112] W. Koch and M. C. Holthausen. *A chemist's guide to density functional theory.* John Wiley & Sons, 2015.

[113] W. Kohn. Density functional and density matrix method scaling linearly with the number of atoms. *Phys. Rev. Lett.*, 76(17):3168, 1996.

[114] W. Kohn and L. J. Sham. Self-consistent equations including exchange and correlation effects. *Phys. Rev.*, 140(4A):1133–1138, 1965.

[115] W. Kohn and L. J. Sham. Self-consistent equations including exchange and correlation effects. *Physical review*, 140(4A):A1133, 1965.

[116] S. V. Kohut, A. M. Polgar, and V. N. Staroverov. Origin of the step structure of molecular exchange–correlation potentials. *Physical Chemistry Chemical Physics*, 18(31):20938–20944, 2016.

[117] C. Kollmar and M. Filatov. Optimized effective potential method: Is it possible to obtain an accurate representation of the response function for finite orbital basis sets. *The Journal of chemical physics*, 127(11):114104, 2007.

[118] D. N. Komsa and V. N. Staroverov. Elimination of spurious fractional charges in dissociating molecules by correcting the shape of approximate kohn–sham potentials. *Journal of Chemical Theory and Computation*, 12 (11):5361–5366, 2016.

[119] E. Kraisler and L. Kronik. Elimination of the asymptotic fractional dissociation problem in kohn-sham density-functional theory using the ensemble-generalization approach. *Physical Review A*, 91(3):032504, 2015.

[120] J. Krieger, Y. Li, and G. Iafrate. Construction and application of an accurate local spin-polarized kohn-sham potential with integer discontinuity: Exchange-only theory. *Physical Review A*, 45(1):101, 1992.

[121] S. Kümmel and L. Kronik. Orbital-dependent density functionals: Theory and applications. *Reviews of Modern Physics*, 80(1):3, 2008.

[122] A. Laio, J. VandeVondele, and U. Rothlisberger. A hamiltonian electrostatic coupling scheme for hybrid car-parrinello molecular dynamics simulations. *J. Chem. Phys.*, 116(16):6941–6947, APR 2002. doi: 10.1063/1.1462041.

[123] A. Laktionov, E. Chemineau-Chalaye, and T. A. Wesolowski. Frozen-density embedding theory with average solvent charge densities from explicit atomistic simulations. *PHYSICAL CHEMISTRY CHEMICAL PHYSICS*, 18(31):21069–21078, AUG 31 2016. ISSN 1463-9076. doi: {10.1039/c6cp00497k}.

[124] S. Laricchia, L. A. Constantin, E. Fabiano, and F. Della Sala. Laplacian-level kinetic energy approximations based on the fourth-order gradient expansion: global assessment and application to the subsystem formulation of density functional theory. *Journal of chemical theory and computation*, 10(1):164–179, 2014.

[125] C. Lee, W. Yang, and R. G. Parr. Development of the colle-salvetti correlation-energy formula into a functional of the electron density. *Physical review B*, 37(2):785, 1988.

[126] H. Lee, C. Lee, and R. G. Parr. Conjoint gradient correction to the hartree-fock kinetic-and exchange-energy density functionals. *Physical Review A*, 44(1):768, 1991.

[127] M. Levy. Electron densities in search of hamiltonians. *Phys. Rev. A*, 26 (3):1200, 1982.

[128] M. Levy and H. Ou-Yang. Exact properties of the pauli potential for the square root of the electron density and the kinetic energy functional. *Physical Review A*, 38(2):625, 1988.

[129] M. Levy and J. P. Perdew. The constrained search formulation of density functional theory. In *Density functional methods in physics*, pages 11–30. Springer, 1985.

[130] M. Levy, J. P. Perdew, and V. Sahni. Exact differential equation for the density and ionization energy of a many-particle system. *Physical Review A*, 30(5):2745, 1984.

[131] C. Li, X. Zheng, A. J. Cohen, P. Mori-Sánchez, and W. Yang. Local scaling correction for reducing delocalization error in density functional approximations. *Physical review letters*, 114(5):053001, 2015.

[132] K. Luo, V. V. Karasiev, and S. Trickey. A simple generalized gradient approximation for the noninteracting kinetic energy density functional. *Physical Review B*, 98(4):041111, 2018.

[133] N. T. Maitra. Undoing static correlation: Long-range charge transfer in time-dependent density-functional theory. *The Journal of chemical physics*, 122(23):234104, 2005.

[134] A. Makmal, S. Kummel, and L. Kronik. Fully numerical all-electron solutions of the optimized effective potential equation for diatomic molecules. *Journal of chemical theory and computation*, 5(7):1731–1740, 2009.

[135] A. Makmal, S. Kummel, and L. Kronik. Fully numerical all-electron solutions of the optimized effective potential equation for diatomic molecules. *J. Chem. Theory Comput.*, 5(7):1731–1740, 2009.

[136] A. Makmal, S. Kümmel, and L. Kronik. Dissociation of diatomic molecules and the exact-exchange kohn-sham potential: The case of lif. *Physical Review A*, 83(6):062512, 2011.

[137] N. H. March, I. A. Howard, A. Holas, P. Senet, and V. E. Van Doren. Nuclear cusp conditions for components of the molecular energy density relevant for density-functional theory. *Phys. Rev. A*, 63:012520, Dec 2000. doi: 10.1103/PhysRevA.63.012520. URL https://link.aps.org/doi/10.1103/PhysRevA.63.012520.

[138] M. A. Marques, A. Castro, G. F. Bertsch, and A. Rubio. octopus: a first-principles tool for excited electron–ion dynamics. *Computer Physics Communications*, 151(1):60–78, 2003.

[139] M. A. Marques, M. J. Oliveira, and T. Burnus. Libxc: A library of exchange and correlation functionals for density functional theory. *Computer physics communications*, 183(10):2272–2281, 2012.

[140] E. Merzbacher. Quantum mechanics. john wiley & sons. *Inc., New York*, 13, 1998.

[141] P. Mori-Sánchez and A. J. Cohen. The derivative discontinuity of the exchange-correlation functional. *Physical Chemistry Chemical Physics*, 16(28):14378–14387, 2014.

[142] M. Mosquera and A. Wasserman. Recovering the integer discontinuity of density functional approximations. In *APS March Meeting Abstracts*, volume 2014, pages J1–009, 2014.

[143] M. A. Mosquera and A. Wasserman. Integer discontinuity of density functional theory. *Physical Review A*, 89(5):052506, 2014.

[144] R. S. Mulliken. Molecular compounds and their spectra. ii. *J. Am. Chem. Soc.*, 74(3):811–824, 1952.

[145] D. Murphy. Sixth-order term of the gradient expansion of the kinetic-energy density functional. *Physical Review A*, 24(4):1682, 1981.

[146] J. Nafziger and A. Wasserman. Density-based partitioning methods for ground-state molecular calculations. *The Journal of Physical Chemistry A*, 118(36):7623–7639, 2014.

[147] J. Nafziger and A. Wasserman. Fragment-based treatment of delocalization and static correlation errors in density-functional theory. *The Journal of chemical physics*, 143(23):234105, 2015.

[148] J. Nafziger, K. Jiang, and A. Wasserman. Accurate reference data for the nonadditive, noninteracting kinetic energy in covalent bonds. *Journal of chemical theory and computation*, 13(2):577–586, 2017.

[149] A. Nagy. Exchange energy in the exact exchange-only density functional theory. *Journal of Physics B: Atomic, Molecular and Optical Physics*, 26 (1):43, 1993.

[150] A. Nagy. Exact and approximate exchange potentials in the density functional theory. *Philosophical Magazine B*, 69(5):779–785, 1994.

[151] A. Nagy and K. Sen. Higher-order cusp of the density in certain highly excited states of atoms and molecules. *J. Phys. B: At. Mol. Opt. Phys.*, 33(9):1745, 2000.

[152] J. Neugebauer. Chromophore-specific theoretical spectroscopy: From subsystem density functional theory to mode-specific vibrational spec-

troscopy. *Phys. Rep.*, 489:1–87, 2010. ISSN 0370-1573. URL `http://www.sciencedirect.com/science/article/pii/S0370157309002853`.

[153] J. Neugebauer. Chromophore-specific theoretical spectroscopy: From subsystem density functional theory to mode-specific vibrational spectroscopy. *Physics reports*, 489(1-3):1–87, 2010.

[154] H. Ou-Yang and M. Levy. Approximate noninteracting kinetic energy functionals from a nonuniform scaling requirement. *International journal of quantum chemistry*, 40(3):379–388, 1991.

[155] R. T. Pack and W. B. Brown. Cusp conditions for molecular wavefunctions. *J. Chem. Phys.*, 45(2):556–559, 1966.

[156] M. C. Payne, M. P. Teter, D. C. Allan, T. Arias, and a. J. Joannopoulos. Iterative minimization techniques for ab initio total-energy calculations: molecular dynamics and conjugate gradients. *Reviews of modern physics*, 64(4):1045, 1992.

[157] J. i. Perdew. Density functional methods in physics. In *NATO Advanced Study Institute, Series B: Physics*, 1985.

[158] J. P. Perdew. Density-functional approximation for the correlation energy of the inhomogeneous electron gas. *Physical Review B*, 33(12):8822, 1986.

[159] J. P. Perdew. Size-consistency, self-interaction correction, and derivative discontinuity in density functional theory. In *Advances in quantum chemistry*, volume 21, pages 113–134. Elsevier, 1990.

[160] J. P. Perdew. Unified theory of exchange and correlation beyond the local density approximation. *Electronic structure of solids' 91*, 11, 1991.

[161] J. P. Perdew and M. Levy. Comment on "significance of the highest occupied kohn-sham eigenvalue". *Physical Review B*, 56(24):16021, 1997.

[162] J. P. Perdew and Y. Wang. Accurate and simple analytic representation of the electron-gas correlation energy. *Phys. Rev. B*, 45(23):13244, 1992.

[163] J. P. Perdew and A. Zunger. Self-interaction correction to density-functional approximations for many-electron systems. *Physical Review B*, 23(10):5048, 1981.

[164] J. P. Perdew, R. G. Parr, M. Levy, and J. L. Balduz Jr. Density-functional theory for fractional particle number: derivative discontinuities of the energy. *Physical Review Letters*, 49(23):1691, 1982.

[165] J. P. Perdew, K. Burke, and M. Ernzerhof. Generalized gradient approximation made simple. *Phys. Rev. Lett.*, 77(18):3865, 1996.

[166] K. Pernal and T. A. Wesolowski. Orbital-free effective embedding potential: Density-matrix functional theory case. *Int. J. Quantum Chem.*, 109 (11):2520–2525, 2009.

[167] F. Perrot. Hydrogen-hydrogen interaction in an electron gas. *Journal of Physics: Condensed Matter*, 6(2):431, 1994.

[168] J. C. Phillips and L. Kleinman. New method for calculating wave functions in crystals and molecules. *Phys. Rev.*, 116(2):287–294, 1959. ISSN 0031-899X. doi: 10.1103/PhysRev.116.287.

[169] J. C. Phillips and L. Kleinman. New method for calculating wave functions in crystals and molecules. *Phys. Rev.*, 116:287–294, Oct 1959. doi: 10.1103/PhysRev.116.287. URL https://link.aps.org/doi/10.1103/PhysRev.116.287.

[170] G. Plindov and S. Pogrebnya. A simple approximation to the kinetic energy functional. *Chemical physics letters*, 143(6):535–537, 1988.

[171] O. Roncero, M. de Lara-Castells, P. Villarreal, F. Flores, J. Ortega, M. Paniagua, and A. Aguado. An inversion technique for the calculation of embedding potentials. *The Journal of chemical physics*, 129(18): 184104, 2008.

[172] O. Roncero, A. Zanchet, P. Villarreal, and A. Aguado. A density-division embedding potential inversion technique. *The Journal of chemical physics*, 131(23):234110, 2009.

[173] O. Roncero, A. Aguado, F. A. Batista-Romero, M. I. Bernal-Uruchurtu, and R. Hernández-Lamoneda. Density-difference-driven optimized embedding potential method to study the spectroscopy of br2 in water clusters. *Journal of chemical theory and computation*, 11(3):1155–1164, 2015.

[174] A. Ruzsinszky, J. P. Perdew, G. I. Csonka, O. A. Vydrov, and G. E. Scuseria. Spurious fractional charge on dissociated atoms: Pervasive and resilient self-interaction error of common density functionals. *The Journal of chemical physics*, 125(19):194112, 2006.

[175] E. Sagvolden and J. P. Perdew. Discontinuity of the exchange-correlation potential: Support for assumptions used to find it. *Physical Review A*, 77(1):012517, 2008.

[176] A. Savin and T. A. Wesolowski. Orbital-free embedding effective potential in analytically solvable cases. In *Advances in the Theory of Atomic and Molecular Systems*, pages 311–326. Springer, 2009.

[177] P. Schipper, O. Gritsenko, and E. Baerends. Kohn-sham potentials corresponding to slater and gaussian basis set densities. *Theoretical Chemistry Accounts: Theory, Computation, and Modeling (Theoretica Chimica Acta)*, 98(1):16–24, 1997.

[178] G. Senatore and K. Subbaswamy. Nonlinear response of closed-shell atoms in the density-functional formalism. *Physical Review A*, 35(6):2440, 1987.

[179] S. Sharifzadeh, P. Huang, and E. Carter. Embedded configuration interaction description of co on cu (111): Resolution of the site preference conundrum. *The Journal of Physical Chemistry C*, 112(12):4649–4657, 2008.

[180] R. Sharp and G. Horton. A variational approach to the unipotential many-electron problem. *Physical Review*, 90(2):317, 1953.

[181] S. Śmiga, E. Fabiano, L. A. Constantin, and F. Della Sala. Laplacian-dependent models of the kinetic energy density: Applications in subsystem density functional theory with meta-generalized gradient approximation functionals. *The Journal of Chemical Physics*, 146(6):064105, 2017.

[182] V. N. Staroverov, G. E. Scuseria, and E. R. Davidson. Effective local potentials for orbital-dependent density functionals. *The Journal of chemical physics*, 125(8):081104, 2006.

[183] V. N. Staroverov, G. E. Scuseria, and E. R. Davidson. Optimized effective potentials yielding hartree-fock energies and densities, 2006.

[184] E. V. Stefanovich and T. N. Truong. Embedded density functional approach for calculations of adsorption on ionic crystals. *J. Chem. Phys.*, 104(8):2946–2955, FEB 1996. doi: 10.1063/1.471115.

[185] E. Steiner. Charge densities in atoms. *J. Chem. Phys.*, 39(9):2365–2366, 1963.

[186] J. Sun, A. Ruzsinszky, and J. P. Perdew. Strongly constrained and appropriately normed semilocal density functional. *Physical review letters*, 115(3):036402, 2015.

[187] J. D. Talman and W. F. Shadwick. Optimized effective atomic central potential. *Physical Review A*, 14(1):36, 1976.

[188] P. K. Tamukong, Y. G. Khait, and M. R. Hoffmann. Density differences in embedding theory with external orbital orthogonality. *J. Phys. Chem. A*, page DOI:10.1021/jp5062495, 2014.

[189] N. Tancogne-Dejean, M. J. Oliveira, X. Andrade, H. Appel, C. H. Borca, G. Le Breton, F. Buchholz, A. Castro, S. Corni, A. A. Correa, et al. Octopus, a computational framework for exploring light-driven phenomena and quantum dynamics in extended and finite systems. *The Journal of chemical physics*, 152(12):124119, 2020.

[190] D. G. Tempel, T. J. Martinez, and N. T. Maitra. Revisiting molecular dissociation in density functional theory: A simple model. *Journal of chemical theory and computation*, 5(4):770–780, 2009.

[191] A. J. Thakkar. Comparison of kinetic-energy density functionals. *Physical Review A*, 46(11):6920, 1992.

[192] L. H. Thomas. The calculation of atomic fields. In *Mathematical proceedings of the Cambridge philosophical society*, volume 23, pages 542–548. Cambridge University Press, 1927.

[193] L. H. Thomas. The calculation of atomic fields. In *Mathematical proceedings of the Cambridge philosophical society*, volume 23, pages 542–548. Cambridge University Press, 1927.

[194] D. Tozer, N. Handy, and W. Green. Exchange-correlation functionals from ab initio electron densities. *CHEMICAL PHYSICS LETTERS*, 273(3-4):183–194, JUL 18 1997. ISSN 0009-2614. doi: {10.1016/ S0009-2614(97)00586-1}.

[195] F. Tran, J. Weber, and T. A. Wesołowski. Theoretical study of the benzene dimer by the density-functional-theory formalism based on electron-density partitioning. *Helvetica Chimica Acta*, 84(6):1489–1503, 2001.

[196] S. Trickey, V. Karasiev, and R. Jones. Conditions on the kohn–sham kinetic energy and associated density. *International Journal of Quantum Chemistry*, 109(13):2943–2952, 2009.

[197] J. P. Unsleber, J. Neugebauer, and C. R. Jacob. No need for external orthogonality in subsystem density-functional theory. *Physical Chemistry Chemical Physics*, 2016.

[198] R. Van Leeuwen and E. Baerends. Exchange-correlation potential with correct asymptotic behavior. *Physical Review A*, 49(4):2421, 1994.

[199] R. Van Leeuwen, O. Gritsenko, and E. J. Baerends. Step structure in the atomic kohn-sham potential. *Zeitschrift für Physik D Atoms, Molecules and Clusters*, 33(4):229–238, 1995.

[200] C. von Weizsäcker. Zur theorie der kernmassen. *Zeitschrift für Physik*, 96(7-8):431–458, 1935.

[201] C. F. von Weizsäcker. Regarding theory of nuclear masses. *Z. Phys.*, 96: 431, 1935.

[202] O. A. Vydrov, G. E. Scuseria, J. P. Perdew, A. Ruzsinszky, and G. I. Csonka. Scaling down the perdew-zunger self-interaction correction in many-electron regions. *The Journal of chemical physics*, 124(9):094108, 2006.

[203] L.-W. Wang. A brief comparison between grid based real space algorithms andspectrum algorithms for electronic structure calculations. Technical report, Lawrence Berkeley National Lab.(LBNL), Berkeley, CA (United States), 2006.

[204] Y. Wang and R. G. Parr. Construction of exact kohn-sham orbitals from a given electron density. *Physical Review A*, 47(3):R1591, 1993.

[205] Y. A. Wang, N. Govind, and E. A. Carter. Orbital-free kinetic-energy functionals for the nearly free electron gas. *Physical Review B*, 58(20): 13465, 1998.

[206] Y. A. Wang, N. Govind, and E. A. Carter. Erratum: Orbital-free kinetic-energy functionals for the nearly free electron gas [phys. rev. b 58, 13 465 (1998)]. *Physical Review B*, 60(24):17162, 1999.

[207] S. H. Werden and E. R. Davidson. On the calculation of potentials from densities. In *Local Density Approximations in Quantum Chemistry and Solid State Physics*, pages 33–42. Springer, 1984.

[208] T. Wesolowski. One-electron equations for embedded electron density: Challenge for theory and practical payoffs in multi-level modelling of complex polyatomic systems. *Computational chemistry: reviews of current trends*, 10:1–82, 2006.

[209] T. A. Wesolowski. Density functional theory with approximate kinetic energy functionals applied to hydrogen bonds. *The Journal of chemical physics*, 106(20):8516–8526, 1997.

[210] T. A. Wesolowski. Hydrogen-bonding-induced shifts of the excitation energies in nucleic acid bases: an interplay between electrostatic and electron density overlap effects. *Journal of the American Chemical Society*, 126(37):11444–11445, 2004.

[211] T. A. Wesolowski. Hydrogen-bonding-induced shifts of the excitation energies in nucleic acid bases: an interplay between electrostatic and electron density overlap effects. *Journal of the American Chemical Society*, 126(37):11444–11445, 2004.

[212] T. A. Wesolowski. Chemistry: Reviews of current trends; leszczynski, j., ed. *World Scientific, Singapore*, 10:1–82, 2006.

[213] T. A. Wesołowski. Embedding a multideterminantal wave function in an orbital-free environment. *Phys. Rev. A*, 77(1):012504, 2008.

[214] T. A. Wesolowski and A. Savin. Non-additive kinetic energy and potential in analytically solvable systems and their approximated counterparts. *Recent Prog. Orbital-free Density Funct. Theory*, 6:275, 2013.

[215] T. A. Wesolowski and A. Savin. Non-additive kinetic energy and potential in analytically solvable systems and their approximated counterparts. *Recent Progress in Orbital-free Density Functional Theory*, 6:275, 2013.

[216] T. A. Wesolowski and F. Tran. Gradient-free and gradient-dependent approximations in the total energy bifunctional for weakly overlapping electron densities. *The Journal of chemical physics*, 118(5):2072–2080, 2003.

[217] T. A. Wesolowski and A. Warshel. Frozen density functional approach for ab initio calculations of solvated molecules. *The Journal of Physical Chemistry*, 97(30):8050–8053, 1993.

[218] T. A. Wesolowski and J. Weber. Kohn-sham equations with constrained electron density: an iterative evaluation of the ground-state electron density of interacting molecules. *Chemical physics letters*, 248(1):71–76, 1996.

[219] T. A. Wesolowski and J. Weber. Kohn-sham equations with constrained electron density: The effect of various kinetic energy functional parametrizations on the ground-state molecular properties. *International journal of quantum chemistry*, 61(2):303–311, 1997.

[220] T. A. Wesolowski, H. Chermette, and J. Weber. Accuracy of approximate kinetic energy functionals in the model of kohn–sham equations with constrained electron density: The fh...nch complex as a test case. *The Journal of chemical physics*, 105(20):9182–9190, 1996.

[221] T. A. Wesolowski, S. Shedge, and X. Zhou. Frozen-density embedding strategy for multilevel simulations of electronic structure. *Chemical reviews*, 115(12):5891–5928, 2015.

[222] Q. Wu and W. Yang. A direct optimization method for calculating density functionals and exchange–correlation potentials from electron densities. *The Journal of chemical physics*, 118(6):2498–2509, 2003.

[223] J. Xia and E. A. Carter. Density-decomposed orbital-free density functional theory for covalently bonded molecules and materials. *Physical Review B*, 86(23):235109, 2012.

[224] J. Xia and E. A. Carter. Single-point kinetic energy density functionals: A pointwise kinetic energy density analysis and numerical convergence investigation. *Physical Review B*, 91(4):045124, 2015.

[225] Z. Yan, J. P. Perdew, T. Korhonen, and P. Ziesche. Numerical test of the sixth-order gradient expansion for the kinetic energy: Application to the monovacancy in jellium. *Physical Review A*, 55(6):4601, 1997.

[226] W. Yang and Q. Wu. Direct method for optimized effective potentials in density-functional theory. *Physical Review Letters*, 89(14):143002, 2002.

[227] W. Yang, A. J. Cohen, and P. Mori-Sanchez. Derivative discontinuity, bandgap and lowest unoccupied molecular orbital in density functional theory. *The Journal of chemical physics*, 136(20):204111, 2012.

[228] Q. Zhao, R. C. Morrison, and R. G. Parr. From electron densities to kohn-sham kinetic energies, orbital energies, exchange-correlation potentials, and exchange-correlation energies. *Physical Review A*, 50(3):2138, 1994.

[229] B. Zhou, Y. A. Wang, and E. A. Carter. Transferable local pseudopotentials derived via inversion of the kohn-sham equations in a bulk environment. *Physical Review B*, 69(12):125109, 2004.

Index